Faculty of Sciences

Department of Physics and Astronomy

Exploring galaxies through stellar kinematics and globular clusters

Dissertation

to obtain the degree of

Doctor in Astronomy

by

Joachim Vanderbeke

Promotor:

Prof. Dr. Maarten Baes
Universiteit Gent
Vakgroep Fysica en Sterrenkunde

Reading committee:

Prof. Dr. Michael West
Maria Mitchell Association, USA
Maria Mitchell Observatory

Prof. Dr. Alessandro Boselli
Laboratoire d'Astrophysique de Marseille, France

Prof. Dr. Sven De Rijcke
Universiteit Gent
Vakgroep Fysica en Sterrenkunde

Other members of examination board:

President:

Prof. Dr. Freddy Callens
Universiteit Gent
Vakgroep Vaste-stofwetenschappen

Prof. Dr. Maarten Baes
Universiteit Gent
Vakgroep Fysica en Sterrenkunde

Prof. Dr. Herwig Dejonghe
Universiteit Gent
Vakgroep Fysica en Sterrenkunde

Prof. Dr. Gianfranco Gentile
Vrije Universiteit Brussel
Vakgroep Fysica en Sterrenkunde

Prof. Dr. Jan Ryckebusch
Universiteit Gent
Vakgroep Fysica en Sterrenkunde

Acknowledgements

It would have been impossible to write this doctoral thesis without the tremendous support of the kind people around me. I want to start by thanking everyone who helped me during the last couple of years and have contributed to the finishing of this PhD thesis.

First of all, I want to thank my supervisor, Prof. Dr. Maarten Baes, who made this all possible and gave me the opportunity to discover the beautiful world of astronomy. I am grateful for the opportunities to attend conferences and to visit ESO/Chile, where Linda Schmidtobreick taught me the skills to work with astronomical software. During the first year of my PhD, I could count on the nice colleagues at Ghent University to vent the first frustrations.

After the first year at Ghent University, I started a studentship at ESO/Chile, where I worked under the supervision of Prof. Dr. Michael West. I am grateful for the opportunities he provided me to grow as a scientist and for being the guide for what would become the bulk of this PhD thesis. Another person who definitely deserves a special mention is Prof. Dr. Roberto De Propris, who shared his passion for science with me and was a huge support (both during my stay in Chile and afterwards), discussing his never-ending original ideas that resulted in successful observing proposals and the interesting views on the various projects. Moreover, I want to thank all colleagues who contributed to G2C2 (observing, writing proposals, commenting on the different manuscripts of the papers). Your support was indispensable. Also the people contributing to the technical feasibility of the VLT/FORS2 project deserve a special thanks.

However, not only astronomers contributed to this doctoral thesis. Both at Ghent University and ESO/Chile, I could count on motivated people in the administration and software departments, which was highly appreciated.

Because the last years and especially the last few months have often been hectic and stressful, I want to thank my family and friends for their patience. I want to give special thanks to my parents, who always help, support and encourage me. I also want to thank my sister and Cata, who sometimes had to suffer my bad moods and I could always count on. Moreover, I want to thank the housemates of Casa Coleta and Casa Mágica for being great at making me forget the daily grind and making the last few years some of the best so far. Finally, I want to thank Kristof Braekevelt for designing an artist impression of the thesis content, which resulted in an appealing cover.

Contents

List of Figures

List of Tables

1 Introduction: Galaxies and Globular Clusters

1.1 Galaxies

When looking at images at different wavelengths, galaxies appear as a gravitationally bound system of millions of stars. They come in a variety of shapes and sizes.

The best-known morphological classification scheme was proposeded by Hubble (1926) and is shown in Fig. 1.1. Some galaxies have irregular shapes (like the Magellanic Clouds), but the remaining galaxies (which were still believed to be nebulae about a century ago) fall into distinct sequences depending on their form which is characterised by rotational symmetry. The scheme is generally called the Tuning-fork diagram, because of its sequences of elliptical (E) and spiral (S) galaxies (with and without bar) merging into each other. Lenticular galaxies are denoted S0 in Fig. 1.1. Elliptical and lenticular galaxies are often denoted as 'early-type' galaxies (ETG), while spiral galaxies are often called 'late-type' galaxies. Over the years, many refinements of this general scheme were published (e.g. de Vaucouleurs 1955, 1959; Sandage et al. 1975; Kormendy & Bender 1996). Also more recently, the galaxy classification scheme was refined depending on the rotational properties of the systems (Emsellem et al. 2007; Cappellari et al. 2007; Kormendy et al. 2009; Krajnović et al. 2013; Cappellari et al. 2013; Cappellari 2013). Although the classification scheme has some shortcomings, it is still the standard scheme used in extragalactic astronomy. Moverover, the morphological classification of galaxies (the so-called Hubble type) show correlations with other physical galaxy properties like luminosity, colour, mass and star formation rates (for more details, see e.g. the review by Roberts & Haynes 1994).

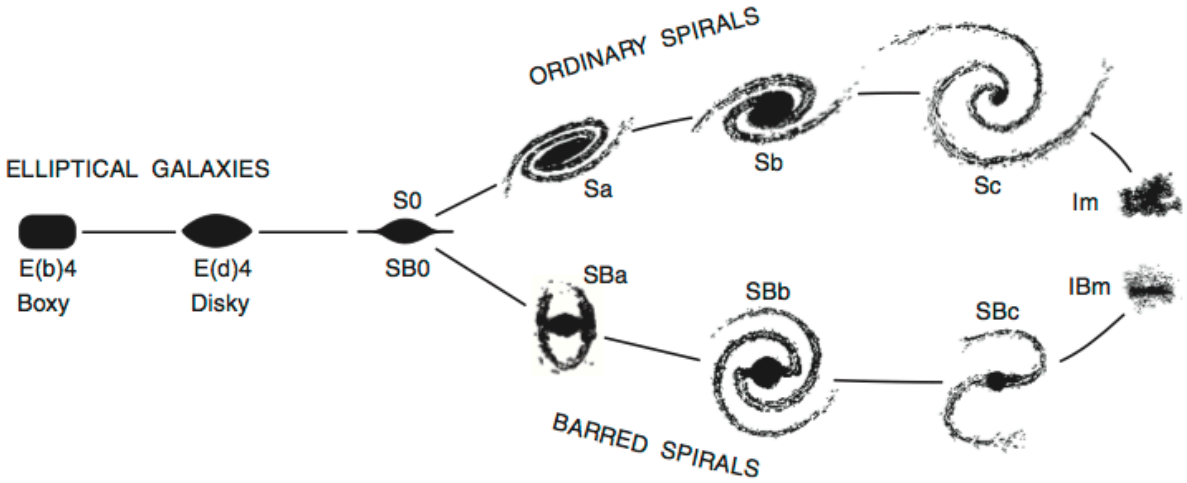

Figure 1.1: Tuning-fork classification scheme invented by Edwin Hubble, in a revision proposed by Kormendy & Bender (1996).

Our own galaxy, the Milky Way (MW), is a barred spiral galaxy of the SBc type (Gerhard 2002). However, it is not easy to classify our own galaxy, because it is hard to infer how it looks like

for an outside observer. However, the Milky Way has several advantages compared to other galaxies: because we are part of this stellar system, we can easily resolve substructures, which will be of fundamental importance throughout this PhD thesis.

Stars are not the only constituent of galaxies. They also contain an interstellar medium (ISM), which consists of gas and dust. The ISM is dominated by the gaseous component, which mainly consists of hydrogen and helium, with a small contribution of more massive elements (indicated as metals by astronomers). The gas exists in different forms (ionized, atomic, molecular,...) and can be traced by line and continuum emission at different wavelength regimes, ranging from the radio to X-rays. The majority of the dust grains are thought to form in the atmospheres of asymptotic giant branch (AGB) stars and are ejected in the ISM due to the radiation pressure of those stars. Although the dust component only accounts for about 1% of the total ISM mass, it plays a crucial role in the star formation: while the gas reservoir is required to form stars, the dust enables the gas to cool by shielding it from other heath sources. As a result of this complex interplay of the galactic components, the gas in galaxies is able to condense and to form stars.

In optical observations, the dust can hamper observations by scattering and absorbing the stellar radiation. To study the dust properties in detail and to uncover their physical contribution to galaxy formation and evolution processes, observations at infrared and submillimeter wavelengths are indispensable. Unfortunately, the Earth's atmosphere is opaque over almost the entire infrared-submm wavelength range, and as a result, observations from space are required. While observations of such previous generation space satellites were limited by a poor resolution and wavelength coverage, the recent Herschel Space Observatory (Pilbratt et al. 2010) has overcome many of these issues and finally has enabled a profound study of the dusty ISM.

At this point, we summarised the different galactic components which are observable directly based on images of different wavelengths. However, the mass of a galaxy is probably dominated by a component called dark matter, which is not directly observable as it does not interact with photons (Trimble 1987). Its properties are still poorly constrained and can only be studied indirectly, using for example rotation curves of galaxies (Rubin & Ford 1970; Rubin et al. 1978; but see also Begeman et al. 1991) or gravitational lenses (Massey et al. 2010; Zitrin et al. 2011). The currently more favoured theory of galaxy formation is based on this dark matter component and assumes that galaxies grow in size during their evolution by devouring/accreting smaller objects (so-called merger trees). Many issues still remain open (e.g. the missing satellite problem). For a recent discussion on the astrophysical implications of dark matter, we refer to Silk (2012), while Sofue (2012) present a study on the dark matter content of the Milky Way. Nevertheless, alternative competing gravitational theories exist (e.g. Milgrom 1983; Moffat 2005; Moffat & Toth 2008).

Yet, there is another component present in the centre of most –and possibly all– galaxies: super-

massive black holes (SMBH), which have masses from thousands to billions of solar masses. These black holes can be observed as active galactic nuclei (AGN) in X-rays when they accrete surrounding matter. Observations of distant luminous quasars indicate that SMBH already formed in the first galaxies, when the Universe was still very young (less than one billion years old). As such they play a key role in our understanding of the assembly of galaxies. Moreover, feedback from SMBHs heats up the cold gas reservoirs, which has as a consequence that less gas is converted into stars (LaMassa et al. 2012; Silk et al. 2013). The construction of these giant structures remains still a puzzle to astronomers, who are currently seeking their building blocks (which are believed to be intermediate-mass black holes) in globular clusters (e.g. Lützgendorf et al. 2013).

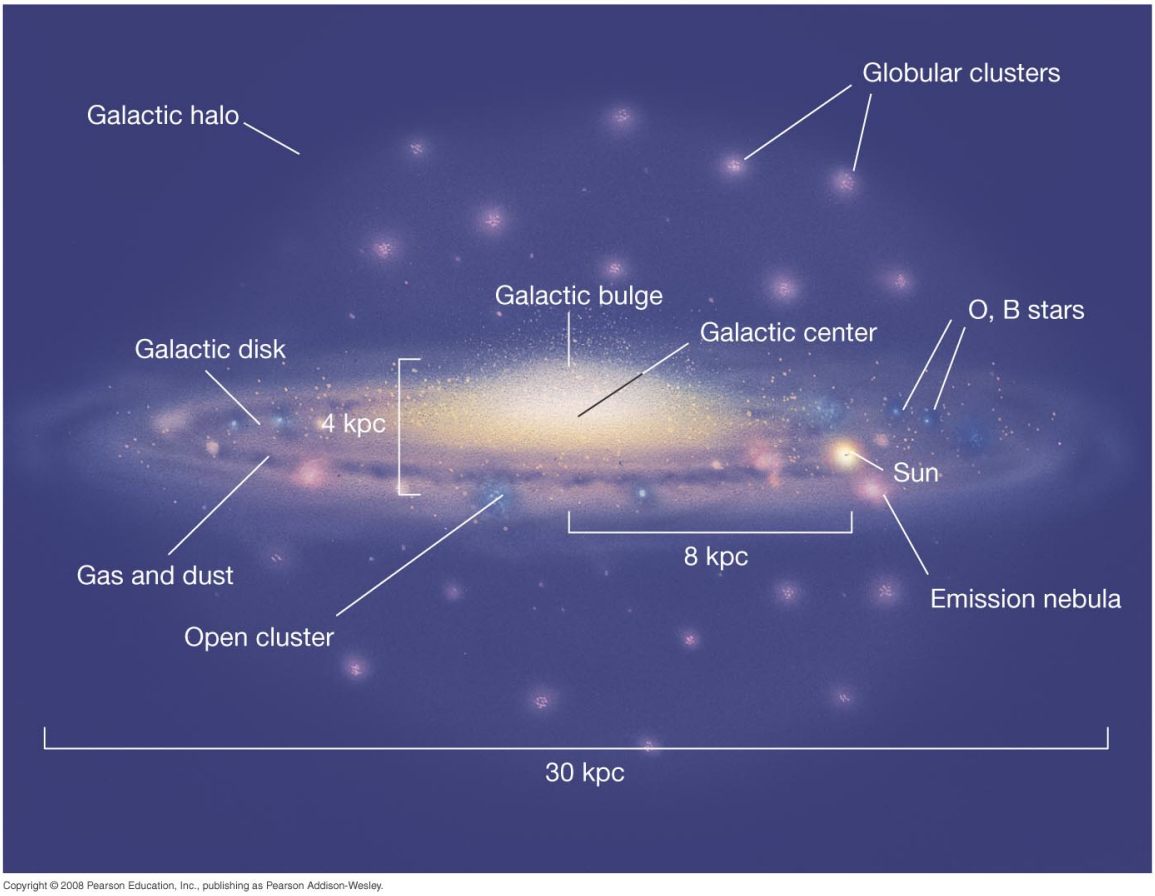

Figure 1.2: Structure of the Milky Way. The main Galactic components (bulge, halo and disk) are indicated, as well as the gas and dust residing in the disk. Globular clusters are located throughout the Galaxy. Copyright of 2008 Pearson Education, Inc., publishing as Pearson Addison-Wesley.

Fig. 1.2 represents the visible matter of a spiral galaxy like the Milky Way. It consists of three components. The central bulge is composed of old (population II) and young stars (population I). The disk with spiral arms contains population I and II stars together with gas and dust. The Galactic halo has a spherical shape, contains only old population II stars and is free of gas and dust. Globular clusters (GC) are spread over the entire galaxy. These intriguing objects are

introduced in section 1.3 and will prove to be invaluable tools to unravel the formation and evolution histories of galaxies. Therefore, GCs will be the main objects of study in this PhD thesis. However, several approaches exist to study properties of galaxies: section 1.2 introduces an alternative approach based on the velocity dispersion of galaxies, which is an observable that is well-known to correlate with hard-to-constrain physical properties like the black hole mass of a galaxy.

1.2 Velocity dispersions in ETGs

Stars in galaxies do not have fixed positions but move constantly on orbits through the system. For our own galaxy, the Milky Way, it is possible to resolve the individual stars and to scrutinise their positions and velocities. Nevertheless, this is impossible for most extragalactic objects. For these systems, we can only study the line-of-sight velocity distribution (LOSVD) of the radial velocities based on spectroscopic observations of the integrated stellar radiation. The most basic properties of a galactic LOSVD are the average speed at which the system moves with respect to the observer (determined by the Doppler shift of the spectral lines) and the velocity dispersion, which is a measure of the stellar speeds within the galaxy and is directly related to the broadening of the spectral features. In theory, astronomers could determine the LOSVDs for many different positions within the projection on the sky of the galaxy. However, in practice astronomers generally confine themselves to the centre of the galaxies. These regions are much brighter than the outskirts and therefore more suitable to obtain good quality spectra with high resolution, which are indispensable to accurately constrain the LOSVDs. Note that a global galaxy spectrum is dominated by the central region because of its brightness increase. Therefore the global velocity dispersion is a good proxy for the central velocity dispersion of these systems.

The velocity dispersion parameter turns out to be very important in a number of extragalactic scaling relations for ETGs. The Faber & Jackson (1976) relation describes how the velocity dispersions correlate with the galactic luminosities ($L_V \propto \sigma^4$) and reveals that stars move faster in more massive galaxies, as illustrated in Fig. 1.3. Although the correlation is clear, the scatter is substantial, which can be an indication that another parameter influences the luminosity at fixed velocity dispersion.

The scatter in the Faber-Jackson relation can indeed be significantly reduced when introducing the effective radius R_e as a third parameter (and substituting the total luminosity L by the average effective surface brightness $\langle\mu\rangle_e$). In the three-dimensional parameter space formed by log σ, log R_e and $\langle\mu\rangle_e$, ETGs nearly fall on a plane (as illustrated in Fig. 1.4), which is denoted as the Fundamental Plane (Djorgovski & Davis 1987). This relation proved to be very useful for theories on the formation and evolution of galaxies (regarding structural properties

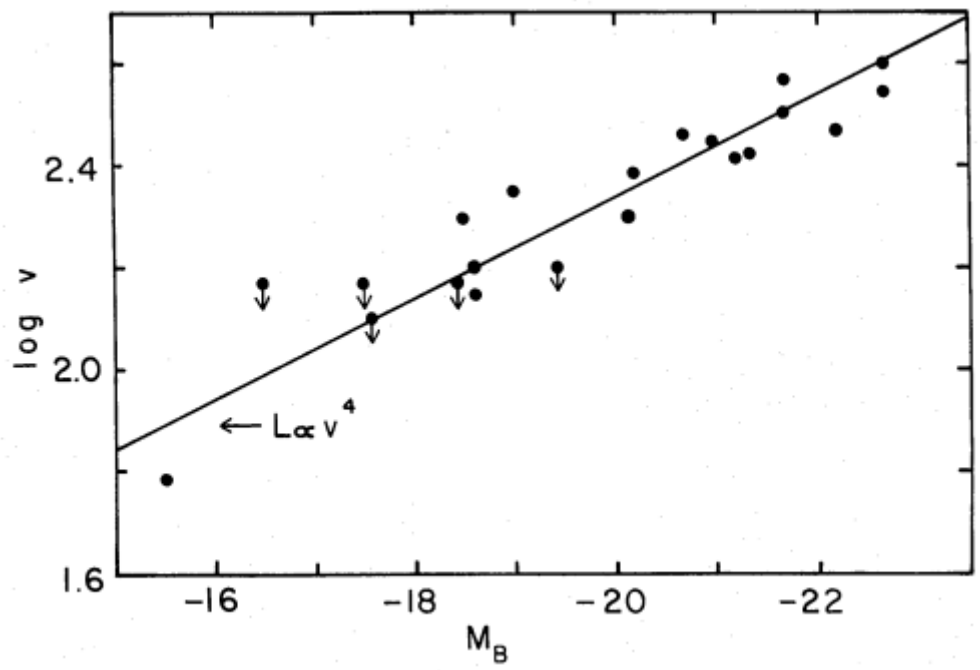

Figure 1.3: Correlation between the line-of sight velocity dispersions and the absolute magnitudes for ETGs (taken from Faber & Jackson 1976). Note that in this figure, the authors use "v" to represent the velocity dispersions; σ is the generally accepted notation, which is also used throughout this PhD thesis.

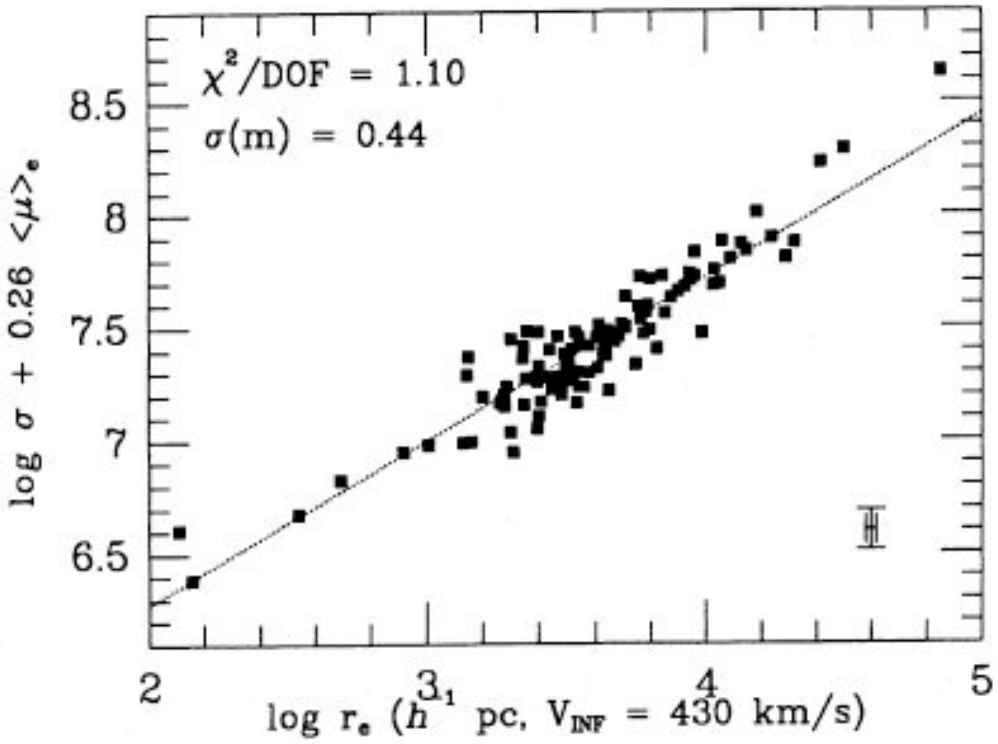

Figure 1.4: A projection of the Fundamental Plane (taken from Djorgovski & Davis 1987) showing a linear combination of the surface brightness and the logarithm of the velocity dispersion as a function of the logarithm of the effective radius.

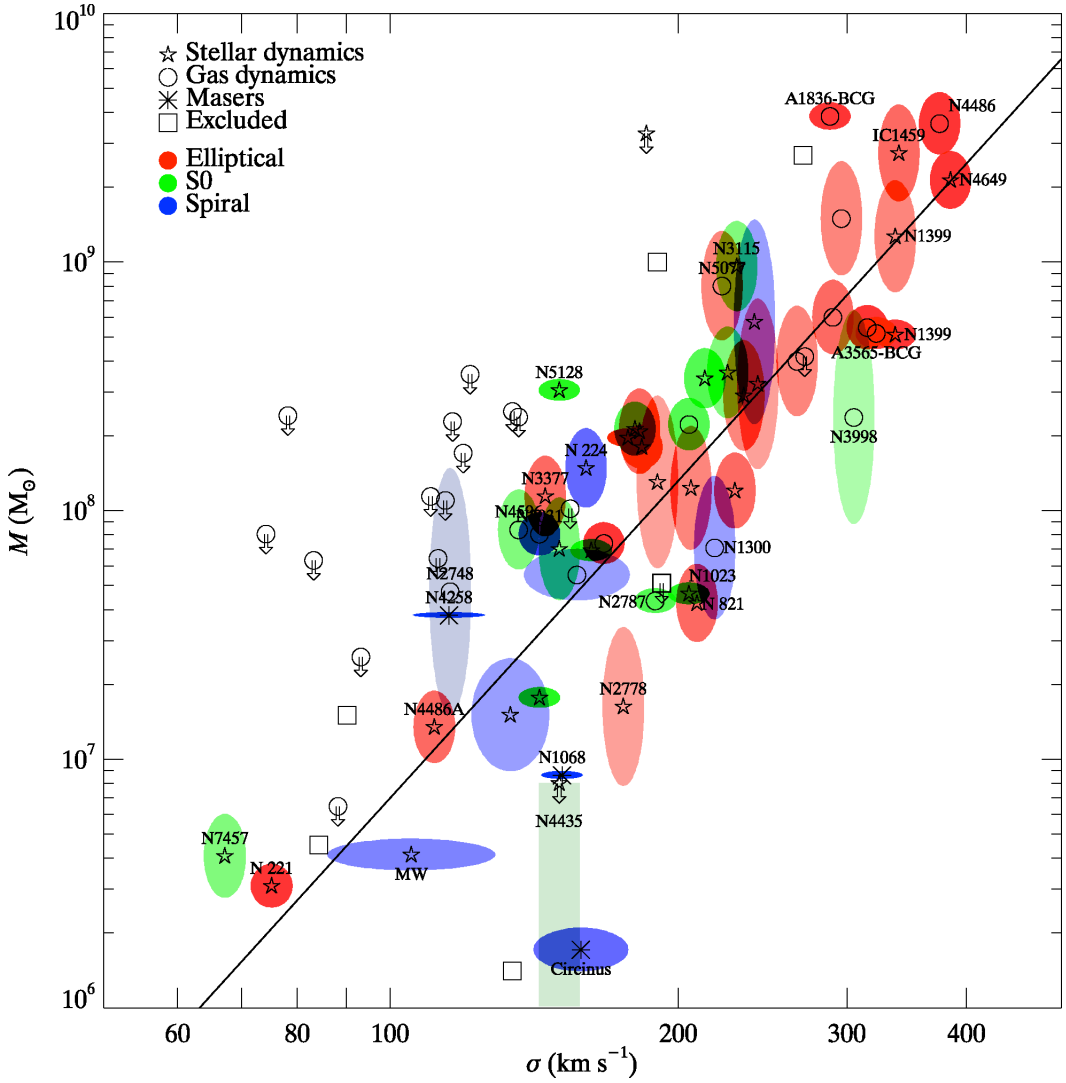

Figure 1.5: $M_{BH} - \sigma$ relation (taken from Gültekin et al. 2009). The different symbols indicate the method of the BH mass measurement, different galaxy morphologies are represented with different colours (as indicated in the legend).

and mass-to-light ratios). Moreover, it can be applied to determine astronomical distances: both σ and $\langle\mu\rangle_e$ are distance independent, while R_e does depend on the distance to the galaxy. If we are able to determine these three parameters, we can determine the distance to the galaxy by assuming it obeys the Fundamental Plane relation.

Finally, velocity dispersions also scale with the black hole mass of the galaxy (e.g. Gültekin et al. 2009). This relation is known as the $M_{BH} - \sigma$ relation and is shown in Fig. 1.5.

Generally the velocity dispersions are obtained based on optical data, a wavelength regime that is known to be highly susceptible to dust absorption and scattering. Therefore, dust in ETGs could complicate and bias the determination of the velocity dispersion, which could have vast consequences for the physical relations described above. As an example, dust could lower the

stellar velocity dispersion profile along the line of sight, as some stellar light is blocked in optical observations. This would result in an underestimation of the velocity dispersion.

Dust in early-type galaxies was first observed in the form of dust lanes and patches (Hawarden et al. 1981; Ebneter & Balick 1985; Veron-Cetty & Veron 1988). Later HST observations revealed that dust extinction features exist in a large fraction of early-type galaxies (van Dokkum & Franx 1995). Fig. 1.6 shows an HST image of NGC 1316 (also known as Fornax A), which is a giant elliptical galaxy in the Fornax cluster. The prominent dust lanes clearly block some of the stellar light, which could alter the measured velocity dispersions along the line of sight.

Figure 1.6: HST image of NGC 1316, a giant elliptical galaxy with clear dust lanes in the Fornax cluster. Credit: NASA and The Hubble Heritage Team (STScI/AURA)

Nonetheless, the optical dust features could not explain the high far-infrared fluxes found by

Goudfrooij & de Jong (1995) (based on *Infrared Astronomical Satellite* (IRAS) observations). Their results estimated the total dust masses to be about ten times higher than the dust masses based on the optical extinction, which indicates that the bulk of the dust is diffusely distributed. Moreover, their dust mass estimates are only a lower limit for the true dust masses, because IRAS is not sensitive to cold dust (which emits at wavelengths longer than 250 μm). Subsequent FIR and sub millimetre observations of ETGs provided further evidence of large amounts of diffuse and cold dust (e.g. Temi et al. 2004).

Nevertheless, as indicated in section 1.1, the Herschel Space Observatory is crucial for detecting the missing cold dust component and, as a consequence, for making accurate dust estimates in ellipticals (Boselli et al. 2010). Science Demonstration Phase results for the Herschel Virgo Cluster Survey (Davies et al. 2010) did not confirm the diffuse dust thesis in elliptical galaxies: Clemens et al. (2010) found no detection for passively evolving early-type galaxies and Baes et al. (2010) did not find evidence for a diffuse dust component in M87. Smith et al. (2012) detected dust (although generally in small amounts) for a significant fraction of their ETG sample (with dust detections for about a quarter of the ellipticals and more than half of the lenticular galaxies). Cortese et al. (2012) and Smith et al. (2012) show that ETGs generally contain up to hundred times less dust per unit stellar mass than late-type galaxies. Nevertheless, Rowlands et al. (2012) demonstrate that ETGs exist containing as much dust as typical spirals. The last word on the dust content of ETGs is definitely not said yet. With a large quantity of Herschel data still being reduced and analysed at the moment, it can only be hoped that a clearer and more uniform picture will emerge in the coming years.

It is clear from Fig. 1.6 that dust affects optical images. The influence of dust on the optical and NIR photometry of early-type galaxies was studied by Michard (2005) and modelled by e.g. Wise & Silva (1996). The SKIRT (Stellar Kinematics Including Radiative Transfer) group at the University of Ghent were the first to model the influence of dust on the observed stellar kinematics (see e.g. Baes & Dejonghe 2000). They showed that dust may bias optical observations through absorption and scattering, thus influencing the photometric and kinematic data. Such effects would have widespread consequences for studies of early-type galaxies, as velocity dispersions play a key role in tracking the mass evolution of early-type galaxies (van der Marel & van Dokkum 2007) and in other extragalactic scaling relations described above.

One way to investigate the effect of dust on the kinematics is to compare the optical and NIR velocity dispersions, because NIR observations are much less affected by the intervening dust. Comparative studies about NIR and optical velocity dispersions were performed in the past, but their conclusions were not in agreement (Silge & Gebhardt 2003; Silva et al. 2008). A homogeneous velocity dispersion study of a well-balanced sample of ETGs is highly needed in order to investigate these discrepant results. Without a decent reliability check of velocity dispersions based on optical observations, it is potentially dangerous to use their values in fundamental relations to approximate other physical properties of ETGs.

1.3 Globular clusters

Globular clusters (hereafter GCs) are dense spherical groups of hundreds of thousands to millions of stars that form during the earliest episodes of star formation in galaxies. They are found in all but the tiniest dwarf galaxies, with massive galaxies hosting systems of hundreds or thousands of such clusters.

A nice example of a supergiant elliptical galaxy is shown in Fig. 1.7. M 87 is a galaxy that looks very different than our own Milky Way: it is ellipsoidal in shape (it has no spiral structure, hence stars are moving by random orbital motions) and has only very little gas and dust (Baes et al. 2010). Although it is very different galaxy, M 87 also hosts globular clusters, visible as faint blobs in the image, swarming like bees around the galactic centre. Even for an elliptical galaxy, M 87 is particular. It is much bigger than the average galaxy, located close to the centre of the Virgo cluster of galaxies and shows an unusually high number of globular clusters (Harris 1991). It also hosts a SMBH at the galactic centre, resulting in a powerful AGN emitting relativistic jets (Doeleman et al. 2012).

Figure 1.7: Image of M 87. This supergiant elliptical galaxy in the Virgo cluster has no clear dust lanes. It hosts a SMBH at the core, resulting in a powerful AGN emitting relativistic jets. M 87 also hosts a peculiarly high number of GCs, which are visible as faint spots surrounding the bright centre of M 87. Image credit: Canada-France-Hawaii Telescope, J.-C. Cuillandre, Coelum.

A major reason why studying globular clusters is important, is their vital link to formation and evolution of galaxies. One way to reconstruct the cosmic history of galaxy formation is to study galaxies at different redshifts, which corresponds to different cosmic epochs due to the finite speed of light. However, galaxies at large redshifts are difficult to observe (they are faint and tiny on the plane of the sky). An alternative approach to galaxy formation and evolution that is not affected by these observational difficulties is based on studying GCs of nearby galaxies. These old objects are survivors of an ancient epoch of galaxy formation and give a snapshot of conditions prevailing at that time (Harris 1991). Moreover, they witnessed the evolution of galaxies, traced their merger histories and star formation histories and form as such the fossil records of galaxies. This way, GCs intrinsically lead to galaxy formation (see e.g. West et al. 2004; Brodie & Strader 2006; Leaman et al. 2013).

Several indications exist that galaxy formation and globular clusters are tightly related:

- The correlation between the number of globular clusters and the luminosity of their parent galaxies (specific frequency S_N– Harris & van den Bergh 1981). In general, elliptical galaxies have $S_N \sim 3.5$, larger than disk galaxies by factors of 2 to 3. Note that M 87 has an even higher specific frequency: $S_N \gtrsim 10$ (Harris et al. 1998). Miller et al. (1998) demonstrated that nucleated dwarf elliptical galaxies (dE), which are distributed like giant elliptical galaxies in galaxy clusters, have $S_N \sim 6.5$, while non-nucleated dE (distributed like late-type galaxies) have $S_N \sim 3.1$. This implies that some galaxies are much more effective in creating or holding their GCs, often referred to as the "specific frequency problem". The specific frequencies in different types of galaxies are constraining galaxy formation theories, as will be described in section 1.3.1.
- The ubiquitous bimodality in their colour distributions (e.g., Zepf & Ashman 1993; Ostrov et al. 1993; Whitmore et al. 1995; Mieske et al. 2006; Peng et al. 2006; Strader et al. 2006; Mieske et al. 2010; Faifer et al. 2011; Yoon et al. 2011b and references therein), with 2 peaks at approximately the same colour in every galaxy, which might even indicate that the formation of GCs predated formation of galaxies themselves (e.g. Spitler & Forbes 2009). A typical example of such a colour distribution is given in Fig. 1.8. The colour of a stellar population is largely determined by age and metallicity. Because GCs are old stellar populations with colours dominated by the red giant branch stars, their broadband colours are closely related to metallicity (e.g. Peng et al. 2006). One of the remaining issues is whether the bimodal colour distribution (bimodality of observables) corresponds to a bimodal metallicity distribution (bimodality in physical properties): some studies claim that the colour bimodality is caused by a metallicity difference between two old populations (Brodie & Strader 2006 and references therein), while other studies ascribe it to the non-linearity of the colour-metallicity relation (Yoon et al. 2006; Richtler 2006). Chapter 4 will address this issue studying relations between the colours and the chemical properties of GCs.

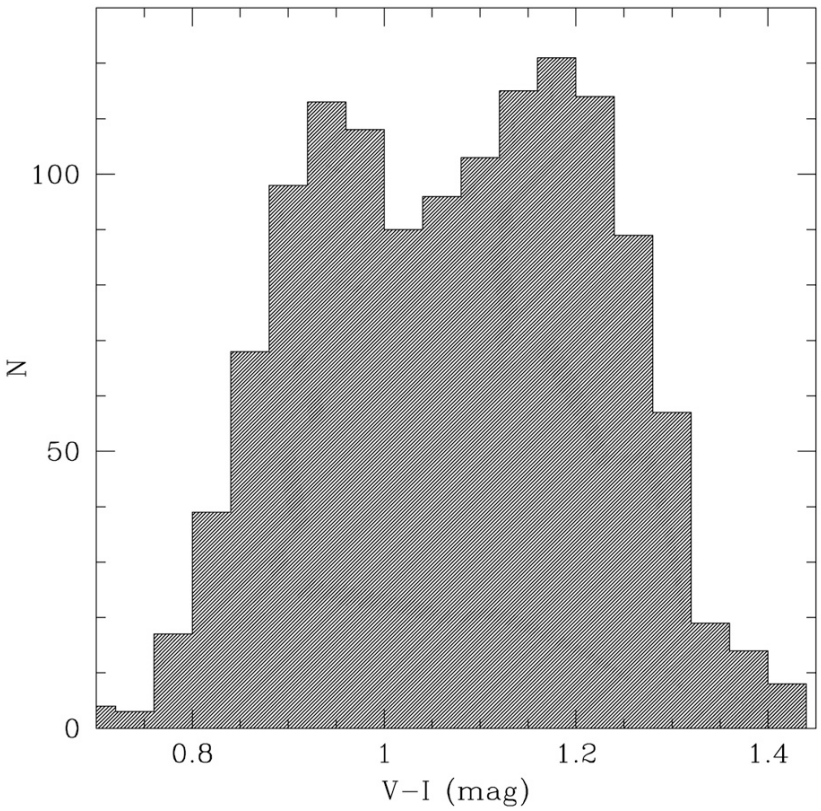

Figure 1.8: $V - I$ colour histogram of the M87 GC system, demonstrating clear bimodality (from Brodie & Strader 2006, based on a study by Larsen et al. 2001).

- The metal-rich GC subpopulation of galaxies is generally more centrally concentrated and closely follows the underlying galaxy light (Brodie & Strader 2006), while the metal-poor GCs dominate at large radii (e.g. the giant elliptical galaxy NGC 1399, presented in Bassino et al. 2006). This might indicate that the metal-rich GCs formed together with the galaxy field stars, while the metal-poor GCs could be used as a tracer for the assembly history of the galaxy. Also in the Milky Way, the metal-rich GCs are related to the bulge, while the metal-poor GCs are associated with the halo. This is an important constraint for galaxy formation models.
- The existence of a nearly universal globular cluster luminosity function (see review by Rejkuba 2012). Fig. 1.9 presents an example of the Galactic GC luminosity function, taken from this review.
- The number of GCs is related to the SMBH mass of the host galaxy (e.g. Burkert & Tremaine 2010; Rhode 2012), which is expected as both S_N and M_{BH} correlate with parent galaxy mass.
- Spitler & Forbes (2009) presents evidence for a direct correlation between the total GC system mass and the host galaxy halo mass (including dark matter).

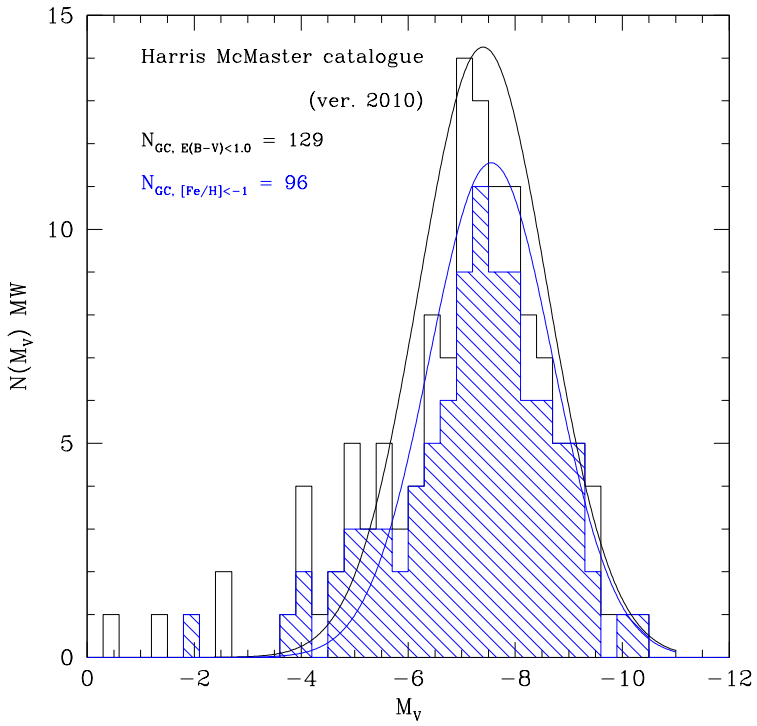

Figure 1.9: The Galactic GC luminosity function, as presented by Rejkuba (2012), for GCs with moderate reddening (E(B-V)< 1). The histogram for a subset of these cluster with low metallicities ([Fe/H]< -1)) is plotted in blue.

- The GC mass of about 10^6 $M_\odot$ corresponds well to the Jeans mass (which is the minimum mass that can collapse at recombination, i.e. gas can become gravitationally bound at that mass (Peebles & Dicke 1968)). Moreover, the globular gas clouds have about the right dimensions (Jeans length) to end up as star clusters with the GC radius. These authors argue that GCs originated as gravitationally bound gas clouds before galaxies formed, suggesting that the first bound systems to have formed in the expanding Universe were gas clouds with mass and shape quite similar to GCs.
- These GCs are believed to survive galaxy mergers, which enables us to study the assembly history of galaxies (Brodie & Strader 2006). As an example, Searle & Zinn (1978) suggested that the Milky Way halo was formed by accreting proto-galactic star-forming regions. Nevertheless, the survival of GCs during galaxy mergers is still a topic of debate. Recent models of Kruijssen et al. (2012) show that both cluster formation and disruption play a role during galactic mergers, and, that the total number of star clusters decreases.

The above list of links between GCs and galaxies provides compelling evidence that studying GCs contributes to our general understanding of galaxy formation.

1.3.1 Formation of Globular Clusters

The ubiquitous colour bimodality observed in the GC systems of nearly all ETGs puts strong constraints on the formation histories of these galaxies. Several competing scenarios, which are not necessarily mutually exclusive, have been proposed to account for the bimodality, which will be briefly summarised in this section. For a more extensive discussion, we refer to the reviews of West et al. (2004) and Brodie & Strader (2006).

The three most important scenarios are (i) major disk-disk mergers, (ii) in situ formation by multiphase dissipational collapse of gas clouds and (iii) dissipationless accretion (i.e. accretion of systems with formed GCs, not of gas clouds which could form GCs during the merging process).

Major disk-disk mergers

In the major merger scenario, GCs are formed during starbursts when gas-rich disk progenitors are merging to form elliptical galaxies. The major merger model, which was predicting the GC bimodality before it was observationally confirmed (Ashman & Zepf 1992), could also be applied to explain the young massive clusters (YMCs) in merging galaxies (e.g. YMCs in the Antennae galaxy merger Whitmore & Schweizer 1995 - as shown in Fig. 1.10), making the model increasingly important. Some of these YMC have masses and sizes similar to GCs, making them possible progenitors of old GCs (e.g. Goudfrooij et al. 2004), although it is still not clear if these young systems will be consistent with old GC systems after a Hubble time of evolution (Brodie & Strader 2006).

One of the issues for the major merger scenario is the so-called "S_N problem". Elliptical galaxies have $S_N \sim 2-5$, while disk galaxies only have $S_N \sim 1$. Note that mergers will only increase S_N if GCs form with a higher efficiency than field stars. Another issue is the presence of fewer metal-rich than metal-poor GCs in ellipticals, which is in conflict with the major merger prediction (Brodie & Strader 2006 and references therein).

Note that this scenario cannot be applicable to the Milky Way: any major merger would destroy the Galactic disk and would transform the Galaxy into an elliptical galaxy (e.g., Toomre 1978; Schweizer 1982), hence, we would not longer pertain to a spiral galaxy.

Forbes et al. (1997) encountered problems with the major merger model predictions when scrutinizing the number and colour distributions of GCs in elliptical galaxies. The results of their study favoured a scenario based on multiphase dissipational collapse, described below.

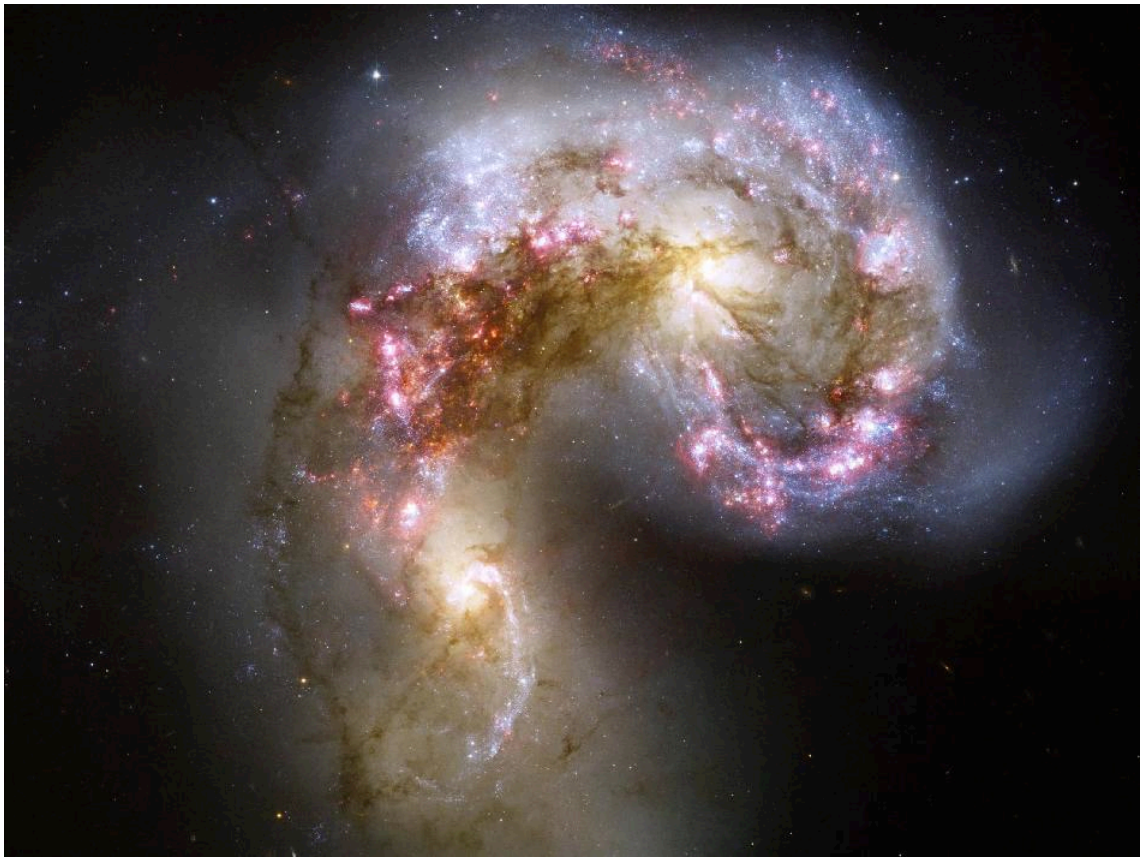

Figure 1.10: The Antennea galaxies: merging pair of galaxies with billions of stars formed during the collision. The most dense regions of star formation form young massive clusters. Most of these clusters will disperse and their stars will become part of the galaxy. However, the most massive clusters are believed to evolve into regular GCs.
Image Credit: NASA, ESA, and the Hubble Heritage Team (STScI/AURA)-ESA/Hubble Collaboration

In situ/multiphase collapse

To account for the bimodal GC distributions, Forbes et al. (1997) proposed an in-situ scenario with GCs forming during two distinct phases from gas of differing metallicity. In the first phase, metal-poor GCs are formed in the collapse of the protogalactic cloud. However, feedback processes expel the gas and abort the star formation. After a period of a few Gyr lacking GC formation, the enriched gas falls back into the gravitational potential of the galaxy and is converted into metal-rich GCs and galactic field stars.

So far, little observational evidence against this scenario has been found, which is at least partly due to the fact that the scenario makes only few specific predictions of observable quantities (Brodie & Strader 2006).

To explain the GC populations in the outer parts of cD galaxies, Forbes et al. (1997) do not exclude the tidal stripping of GCs from nearby galaxies, which is the principle that underlies the dissipationless accretion, which described in the next section.

Dissipationless accretion

In the scenario proposed by Côté et al. (1998), metal-rich GCs are not produced during gas-rich mergers. They propose that these metal-rich clusters are the intrinsic GC population of the massive seed galaxy, while the metal-poor subpopulation originates from the capture induced by mergers or tidal stripping from other lower-mass galaxies. This assembly mechanism was also proposed by Hilker et al. (1999) and reflects the relation between the mean metallicity of the GC system and the mass of the host galaxy (van den Bergh 1975; Brodie & Huchra 1991). Remark that it is possible to strip GCs without the accompanying galaxy light (Côté et al. 1998), because the GC distribution is more extended than the field stars of the galaxy. As a result, the capture of GCs through tidal stripping, unlike mergers, does not necessarily conserve the specific frequency.

To reproduce the observed bimodality, galaxies need to accrete large numbers of metal-poor GCs residing in dwarf galaxies: models of Côté et al. (1998, 2000, 2002b) require that each galaxy has an intrinsic population of GCs (whose metallicity increases with the galaxy's mass, following the mass-metallicity relation) and that the primordial galactic mass function for low-mass galaxies is a rather steep power law (i.e. large numbers of low-mass galaxies are needed for accretion). The slope is consistent with the halo mass functions predicted by standard ΛCDM models, but much steeper than that actually observed for present-day low-mass galaxies (Brodie & Strader 2006).

Elaborating the same principles of dissipationless accretion, Tonini (2013) proposed another theoretical model based on the hierarchical galaxy assembly scenario. Based on their mass-metallicity relation as a function of redshift, together with the assumption that GCs share the metallicity of their parent galaxy at the time of formation, they create GCs in the merger tree that constructs the galaxy. The metallicity bimodality in their models is based on hierarchical clustering, with metal-rich clusters forming at $z \sim 2$ in the main progenitor of the galaxy, while the metal-poor clusters originate from less massive satellite galaxies, with GC systems forming at $z \sim$ 3-4.

It is clear the scenarios described above are not mutually exclusive. Moreover, differences between the scenarios become more vague if they occur at high redshift. One of the key questions is how much gas there is involved in the merger/accretion (see review by Brodie & Strader 2006 and references therein for extended discussion).

The prevailing theory for galaxy formation is based on the merger hypothesis. Nevertheless, some issues with this formation model are still matter of debate. Milky Way GCs are known to show the Oosterhoff dichotomy (which is a classification based on the luminosity, periodicity and metallicity of their RR Lyrae stars – see e.g. Catelan 2009), while all GC systems of dwarf galaxies are generally Oosterhoff intermediate (Mackey & Gilmore 2003a). Although it is not clear yet what causes the Oosterhoff effect, it does imply that present-day dwarf galaxies do

not resemble whatever the Galactic building blocks were or that the MW halo was not built up accreting these objects (hence not based on minor mergers). The study of the Oosterhoff dichotomy in the Andromeda spiral galaxy (and its related dSphs) is still in a very early stage: it is very difficult to obtain the required measurements to study the Oosterhoff effect in these systems (e.g. Pritzl et al. 2002, 2004, 2005; Mancone & Sarajedini 2008; Contreras Ramos et al. 2013).

Moreover, Bochanski et al. (2013) claim that no more than two Sagitarrius dSph-like accretion events can have contributed to the hierarchical build-up of the Milky Way's outer halo: since the halo relaxation time is larger than the Hubble time, we would still be able to detect previous mergers. If their findings are confirmed, other formation scenarios are required, as it is impossible for one or two such dwarf galaxies to build the whole Galactic GC system.

In the previous section, galaxies were described as stellar systems dominated by a dark matter component. In contrast, current GCs are largely considered to be dark matter free (Heggie & Hut 1996; Moore 1996; Mashchenko & Sills 2005a; Bradford et al. 2011). Nevertheless, Mashchenko & Sills (2005b) demonstrate that primordial dark matter Burkert halos around GCs can be removed by tidal stripping. Moreover, Ibata et al. (2013) cannot rule out the presence of a small dark matter halo around NGC 2419.

1.3.2 Globular clusters as laboratories for stellar evolution

The stars in Galactic globular clusters can be relatively easily resolved, which enables to classify the cluster stars according to their colour (hence temperature or spectral class) and magnitude (or brightness) in a colour-magnitude diagram (CMD). This classification of stars is also known as the Hertzsprung-Russell diagram, as shown in Fig. 1.11, and is essential to understand the evolution of stars in clusters. The figure indicates the main sequence, which collects hydrogen-burning stars like our Sun. The giant stars are located on the upper-right side of the diagram: these stars are very luminous but have relatively low temperatures. The white dwarfs are located at the lower-left and are very compact remnants of stars not massive enough to become a neutron star.

CMDs can be used as well to estimate the age of the stellar population by fitting isochrones (with the corresponding metallicity) to the principal stellar sequences. As shown by Vandenberg et al. (2013), it is essential to accurately recover the main-sequence turn-off to obtain a reliable age estimate.

The stars in globular clusters were long believed to share a common age and chemical composition (so-called single stellar populations). Nevertheless, recent discoveries of multiple sequences in colour-magnitude diagrams (Bedin et al. 2004; Piotto et al. 2007) and anti-correlations in abundances of light elements (Gratton et al. 2012b) reveal multiple successive epochs of star

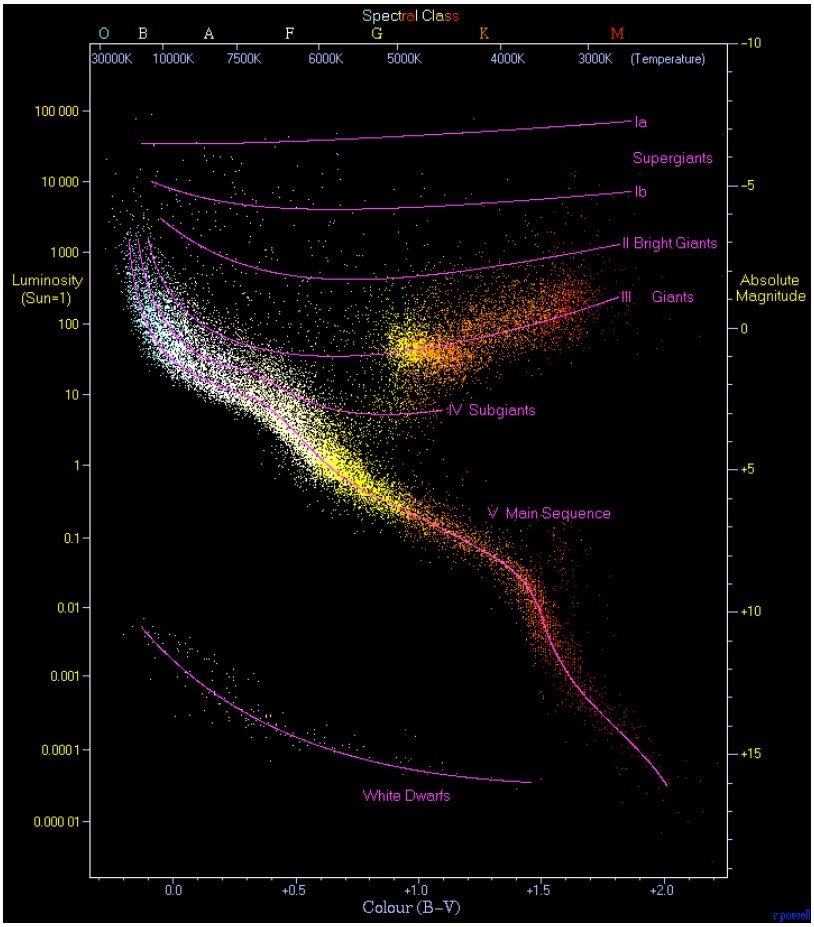

Figure 1.11: Hertzsprung-Russel diagram, showing the luminosity (or absolute magnitude) as a function of the stellar colour for stars ranging from hot blue-white stars (on the left side) to low temperature red stars on the right side. Image credit: Richard Powell.

formation and show evidence for extended enrichment histories (see review by Gratton et al. 2012a). These new developments are illustrated by Fig. 1.12 (taken from Piotto et al. 2007), which presents an HST/ACS CMD of NGC 2808, revealing three separate branches.

CMDs are not only interesting to study the stellar populations of GCs. Alonso-García et al. (2011) used CMDs of GCs near the Galactic centre to study the differential foreground extinction. Correcting for these differential reddening effects allows to construct high-quality CMDs with tighter sequences. This leads to a more accurate determination of ages, metallicities and distances based on isochrone fitting, which are important for models of the formation and evolution of the Milky Way.

1.3.3 Structural parameters of globular clusters

The structural properties of GCs reveal features of their formation and interactions with the galactic environment (Brodie & Strader 2006). Moreover, their high stellar concentrations and

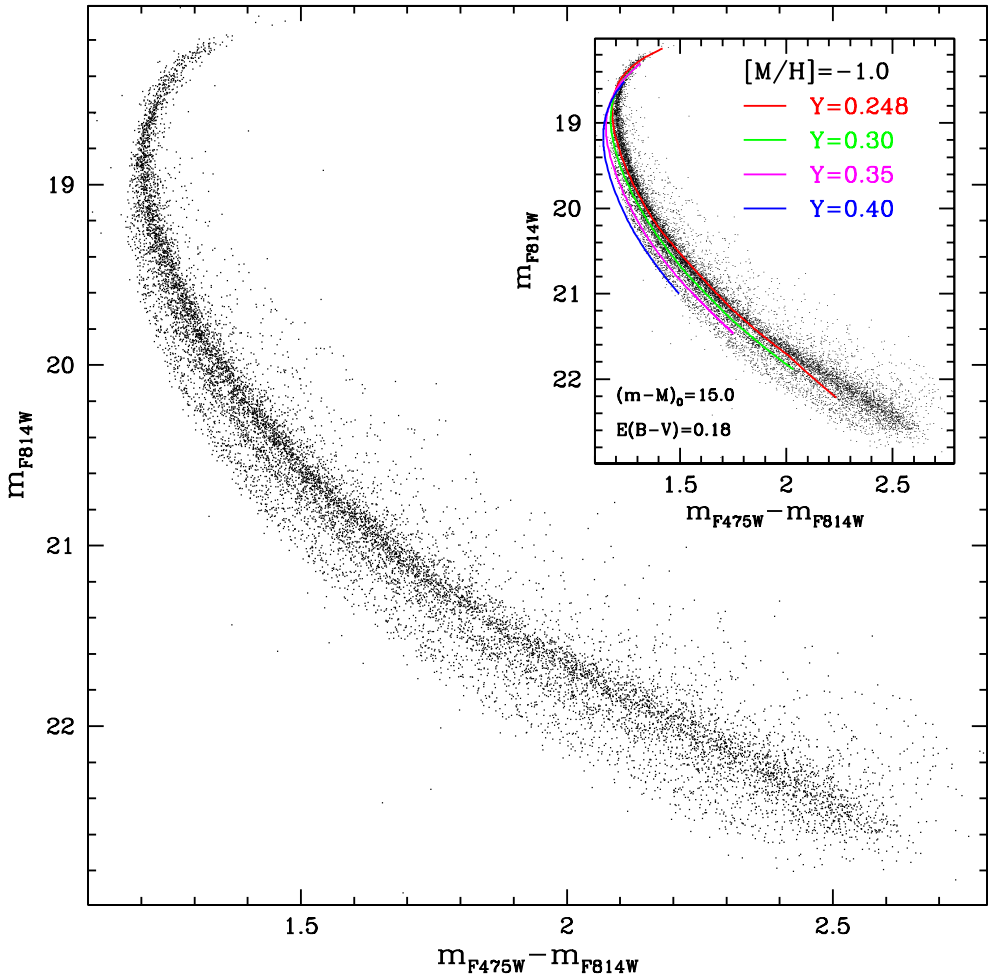

Figure 1.12: CMD of NGC 2808 based on HST/ACS photometry (taken from Piotto et al. 2007). The main sequence splits into three separate branches, which are attributed to successive epochs of star formation, with different helium abundances.

the absence of a dark matter halo make GCs excellent objects to study N-body dynamics (e.g., Elson et al. 1987; Heggie & Hut 2003; Trenti et al. 2010; Hurley & Shara 2012). These extreme dense environments take part in the formation of several stellar exotica, such as blue stragglers (Ferraro & Lanzoni 2009), extreme horizontal branch stars (Fusi Pecci et al. 1992; Catelan et al. 2001), cataclysmic variables and millisecond pulsars (Benacquista & Downing 2013). Moreover, they can host intermediate-mass black holes (Lützgendorf et al. 2013), which might serve as building blocks for the SMBHs and black hole binaries (Lin et al. 2013).

Structural parameters for globular clusters are needed to explore correlations between stellar populations, dynamics and the Galactic environment. The Milky Way is the only galaxy where these questions can be explored in detail, as we can resolve clusters to the level of individual stars on the main sequence and we will soon be able to obtain their internal kinematics and proper motions (e.g., Bianchini et al. 2013).

It is known that the cluster sizes depend on the position in the Galaxy: van den Bergh et al. (1991) found that the cluster diameters correlate with Galactocentric distance. Another main result regarding the formation of GCs was discovery that metal-poor GCs are significantly larger than metal-rich GCs (Kundu & Whitmore 1998). This result has been attributed to a variety of possible solutions, including (i) projection effects (metal-rich clusters are more centrally concentrated, and, as stated above, clusters that are closer to the galactic centre are smaller), (ii) different formation scenarios (with metal-rich GCs forming in higher-pressure environments) or (iii) mass segregation, based on the observation that the brightest stars in metal-rich GCs are more massive than in metal-poor GCs (see review by Brodie & Strader 2006 and references therein).

1.4 Scope of this thesis

In this PhD thesis, we consider two different aspects of galaxies, both of which hold important clues about their structure, formation and evolution.

Chapter 2 will focus on the effects dust can have on the velocity dispersion determination in ETGs. It is important to have a reliable estimate of the velocity dispersions in ETGs, because they appear in important scaling relations, as illustrated in section 1.2. We determine the velocity dispersions of ETGs in the Fornax cluster, based on near-infrared spectra obtained with the ISAAC instrument on the VLT. For the first time, we are able to make a homogeneous comparison between NIR velocity dispersions and optical values from the literature (Vanderbeke et al. 2011). Moreover, we discuss the influence of dust on the velocity dispersion determination in these largely optically-thin systems.

From Chapter 3 onwards, we choose another approach to study the formation and evolution of galaxies. We leave the distant extra-galactic objects behind and will fully concentrate on the Milky Way with its globular cluster system of approximately 150 GCs. Although limited in number when compared to the GC systems of distant giant galaxies, the study of our Milky Way GC system has several advantages over these distant galaxies. The Galactic GCs are close enough we can resolve the stars and determine accurate chemical abundances (tracing early enrichment histories), while they show what the formation conditions were like more than 10 Gyr ago (Krauss & Chaboyer 2003; Forbes & Bridges 2010). Milky Way GCs are far enough we can also study their integrated properties with current CCD technology. These are indispensable as they provide calibration data for the study of more distant early-type galaxies with predominantly old populations, as well as the GCs of distant galaxies for which only the integrated light can be observed (Harris 1991; West et al. 2004; Brodie & Strader 2006; Cohen et al. 2007).

Because these clusters are excellent calibrators, we want our calibration relations based on

the new standardised filter system provided by the Sloan Digital Sky Survey (SDSS – York et al. 2000). SDSS has now homogeneously imaged over a quarter of the Northern sky (about 14500 square degrees) in five passbands. Together with upcoming imaging surveys in the South, SDSS will completely replace the older Schmidt plate atlases of the sky, and at the same time provide, for the first time, a standardised system of photometry in the optical for astrophysics (theoretically, with calibrators in every field). Yet, most work in both Galactic and extragalactic GCs is still based on the older photometric systems (such as Johnson-Cousins, Washington, etc.). Several authors have remarked on the lack of calibrating studies of globular clusters in the SDSS system (Jordán et al. 2005; Sinnott et al. 2010; Peacock et al. 2011; Vickers et al. 2012); as most such objects are in the South, the vast majority of Galactic GCs have not been imaged by the SDSS survey. Harris (1996) (2010 edition) lists $UBVRI$ colours for 81 of the 150 Galactic GCs. Moreover, this photometry is inhomogeneous, as it is taken from different papers spanning decades, using different methods and instruments. With this motivation, the main goal of this PhD thesis was to collect reliable photometry for a large sample of Galactic GCs using the SDSS filter system.

Chapter 3 describes the observational campaign needed to build our data set and gives an overview of the basic data reduction steps applied to our data. Moreover, it discusses issues related to the cluster centroids and the sky determination, which can be complicated in these crowded fields. In order to obtain clean representative GC colours, which are essential in the next chapter, we clean contaminating foreground stars by a technique involving the cluster colour-magnitude diagrams and the stellar proper motions. It is the first time this technique was applied for such an ample GC sample. As the main result of this chapter, we present the currently largest homogeneous SDSS photometry catalog of the Galactic Globular Cluster system (Vanderbeke et al. 2014a).

In chapter 4, we improve existing colour-metallicity relations (CMRs) using the clean colours obtained in the previous chapter. We do not only use the standard [Fe/H] metal abundance, but also present CMRs based on the Calcium Triplet metallicity scale, a new metallicity indicator currently gaining interest in the astronomical community (e.g. Foster et al. 2010; Usher et al. 2012). We find that the CMRs are non-linear for both metallicity indicators. We discuss the origin of the scatter in the CMR and look for links with other GC properties like the HB morphology, the age and the initial mass function. We find a clear correlation between the CMR scatter and the extinction estimates, which can be poorly defined especially close to the Galactic plane. Finally, we discuss the colour bimodality and its link to metallicity bimodality, which is complicated by the non-linear nature of the CMRs. These results were published in Vanderbeke et al. (2014b).

Most structural parameters for Galactic globular clusters are still measured from surface brightness profiles derived from an inhomogeneous compilation of older CCD and photographic data (Trager et al. 1995; McLaughlin & van der Marel 2005). In chapter 5 we extend the homoge-

neous photometric Galactic GC catalog with structural parameters. We first study the influence of a limited field-of-view to the determination of the King model parameters. Thereafter, we compare our derived parameters with the literature, based on both SB profiles and stellar count density profiles. We give a new definition for core-collapsed clusters and find a clear correlation with the position in the Galaxy. This was predicted by theoretical models (Gnedin et al. 1999; Madrid et al. 2012), but not confirmed yet by observations. Further, we seek correlations between the obtained structural parameters and other cluster properties that are related to the high stellar densities in GCs (including HB morphology, milli-second pulsars and X-ray sources). Finally, we show that colour gradients can be vastly affected by a few central RGB stars, which makes it hard to interpret the gradients and relate them to stellar subpopulations in GCs.

In chapter 6 some projects based on the colour-magnitude diagrams (CMDs) are presented as an illustration of the scientific output we expect from these diagrams. Although this is still work in progress, some preliminary results are presented regarding the double HB discovered by Mauro et al. (2012) in NGC 6569, our cumulative fraction approach on the the long-standing second-parameter problem and the mass-loss in RGB and AGB stars.

For distant galaxies, where stars are not resolved, the only possible way to determine the age of the stellar population is by interpreting integrated spectra. These spectra can be biased by the emission of hot HB stars, which makes an accurate age determination very difficult. Chapter 7 presents a large observational campaign started during the course of this PhD thesis. We obtained VLT/FORS2 drift-scan spectra for the bulk of the southern GCs, making it the largest homogeneous spectroscopic sample to date of such objects. We plan to use these spectroscopic data to obtain spectroscopic age estimates, which are biased due to the effects of extremely hot HB stars. However, using the unbiased age estimates based on the CMDs, we will be able to calibrate this effect using FUV/NUV-optical colours. This relation will enable to improve current age estimates of unresolved elliptical-like stellar populations.

Finally, in chapter 8 we summarise the main results of this PhD thesis. The Dutch summary is given in chapter 9.

Optical and near-infrared velocity dispersions of early-type galaxies

2

The results described in this chapter are based on Vanderbeke et al. (2011).

2.1 Introduction

The dust content of early-type galaxies (ellipticals and lenticulars), and the effects on galaxy parameters inferred from optical observations, is still unclear and a hot topic of debate.

Dust in early-type galaxies was first observed in the form of dust lanes and patches (Hawarden et al. 1981; Ebneter & Balick 1985; Veron-Cetty & Veron 1988). Later HST observations revealed that dust extinction features exist in a large fraction of early-type galaxies (van Dokkum & Franx 1995). Nonetheless, the optical dust features could not explain the high far-infrared (FIR) fluxes found by Goudfrooij & de Jong (1995) (based on *Infrared Astronomical Satellite* (IRAS) observations). Their results implied dust masses exceeding the values from optical extinction by nearly an order of magnitude, indicating that the major part of the dust is diffusely distributed. Furthermore, the dust mass estimates based on IRAS flux densities are only a lower limit for the true dust masses, because IRAS is not sensitive to cold dust. FIR observations of early-type galaxies selected from the *Infrared Space Observatory* (ISO) archive found that the colder dust component dominates the total dust mass, which is typically more than 10 times larger than the dust masses previously estimated using IRAS observations (Temi et al. 2004). Recent FIR Spitzer observations of elliptical galaxies show evidence of diffuse dust (Temi et al. 2007) and ground-based submillimetre continuum observations with SCUBA have already revealed that galaxies indeed contain large amounts of cold dust, but that the submm emission of some of the elliptical galaxies may be synchrotron rather than dust emission (Vlahakis et al. 2005). Nevertheless, the Herschel Space Observatory is crucial for detecting the missing cold dust component and, as a consequence, for making accurate dust estimates in ellipticals (Boselli et al. 2010).

Science Demonstration Phase results for the Herschel Virgo Cluster Survey (Davies et al. 2010) did not confirm the diffuse dust thesis in elliptical galaxies: Clemens et al. (2010) found no detection for passively evolving early-type galaxies and Baes et al. (2010) did not find evidence for a diffuse dust component in M87, explaining the FIR emission by a synchrotron model.

The influence of dust on the optical and NIR photometry of early-type galaxies was studied by Michard (2005) and models to predict the effect of dust were developed by Witt et al. (1992) and Wise & Silva (1996, 1997). Baes & Dejonghe (2000, 2001, 2002) and Baes et al. (2000) were the first to include the influence of dust on the observed stellar kinematics in their models. They showed that dust may bias optical observations through absorption and scattering, thus influencing the photometric and kinematic data. Such effects would have widespread ramifications for studies of early-type galaxies, as velocity dispersions play a significant role in tracking the mass evolution of early-type galaxies (van der Marel & van Dokkum 2007), and appear in empirical relationships such as the the M_{BH}-σ relation (Ferrarese & Merritt 2000; Gebhardt et al. 2000; Graham 2008; Gültekin et al. 2009; Kormendy & Bender 2009), the Faber-Jackson

relation and the Fundamental Plane relation (Djorgovski & Davis 1987; Dressler et al. 1987; Guzman et al. 1993; Pahre et al. 1995; Prugniel & Simien 1996; Gavazzi et al. 1999; Graham 2002; Bernardi et al. 2003; Michard & Prugniel 2004; Desroches et al. 2007; Fraix-Burnet et al. 2010; Ribeiro & Dantas 2010).

One way to investigate the effect of dust on the kinematics is to compare the optical and NIR velocity dispersions. The *K*-band is the optimal region to perform a study on NIR velocity dispersions: the extinction by dust in the *K*-band is only 7% of that in the *B*-band (where dust is very opaque) and the wavelengths are short enough to evade dilution of the stellar continuum by hot dust (Gaffney et al. 1995). In the *K*-band, one can use the 2.29μm (2$-$0) ^{12}CO absorption band head as a kinematical tracer. It is the strongest absorption feature in galactic spectra in the 1$-$3 μm range and increases in strength with decreasing effective temperature or increasing radius of the underlying stars (Silge & Gebhardt 2003). This late-type star feature can be used to probe the kinematics of the red stellar population of galaxies (Gaffney et al. 1993) and is intrinsically sharp and deep, spectrally isolated from other strong absorption and emission features and is located in a dark part of the infrared sky spectrum (Lester & Gaffney 1994). The advent of efficient NIR spectrographs and detectors on large telescopes has made the CO absorption band a generally available tool for kinematic studies (e.g. Silge et al. 2005; Nowak et al. 2007, 2008; Lyubenova et al. 2008).

Comparative studies about NIR and optical velocity dispersions were performed in the past. Silge & Gebhardt (2003) were the first to perform a systematic study, but their sample was biased to lenticulars (it contained 25 galaxies, of which 7 ellipticals and 18 lenticulars) and was based on inhomogeneous optical velocity dispersions, obtained from different papers with different instruments, methods and extraction windows. They found that the velocity dispersion decreases with wavelength, opposite to the theoretical expectations of Baes & Dejonghe (2002). Silva et al. (2008) studied the stellar populations in early-type galaxies, using the strong spectral features near 2.2 μm. They found a one-to-one correspondence between the optical and NIR velocity dispersions, based on a homogeneous set of 4 lenticular and 7 elliptical galaxies. 10 out of the 11 galaxies are part of our new, extended sample, in which we excluded NGC1344, because this galaxy was not included in the sample of Kuntschner (2000).

To investigate the disagreement between the different velocity dispersion studies, we embarked on a project, for the first time using a complete and well-balanced sample of 22 early-type galaxies (comprising 11 ellipticals and 11 lenticulars). All galaxies are members of the Fornax cluster, the nearest galaxy cluster after the Virgo cluster. Fornax is considerably more compact and regular in shape than Virgo, doubling the central density of galaxies but having a total mass of nearly an order of magnitude lower. This makes the Fornax cluster a good representative of the groups and poor clusters in which most galaxies in the universe reside (Jordán et al. 2007). Nevertheless, the main reason for the choice of our sample was the availability of uniform spectroscopic optical data, obtained by Kuntschner (2000). In his paper, velocity dispersion,

age, metallicity and line strength are discussed for all galaxies in the sample.

2.2 Observations and data reduction

2.2.1 Data sample

This study is based on the complete magnitude-limited sample of Kuntschner (2000). This sample, presented in Table 2.2, has been selected from the catalogue of Fornax galaxies of Ferguson (1989), in order to obtain a complete sample down to $B_T = 14.2$ or $M_B = -17$ and contains 11 elliptical and 11 lenticular galaxies. Recent measurements of B_T were taken from the NASA/IPAC Extragalactic Database.

2.2.2 Observations

The observations were performed between 20 October 2008 and 26 January 2009 with the VLT using the SW arm of ISAAC (Moorwood et al. 1998) in spectroscopic medium resolution mode (SWS-MR). The characteristics of the detector and the instrumental set-up are given in Table 2.1.

We used the nod-on-slit mode (double subtraction technique). Every observational sequence was started with the galaxy centered on the slit near one end and an individual spectrum was taken. The galaxy was then moved $60''$ or $90''$ towards the other end of the slit and two more integrations were executed. Then the galaxy was placed again at the original slit position where another spectrum was taken. This ABBA sequence was repeated a number of times, resulting in multiple individual two-dimensional spectroscopic images. In order to remove properly the sky background for the observations of big and bright galaxies (i.e. for NGC 1399, NGC 1316, NGC 1380, NGC 1404 and NGC 1427 in particular), we observed separate sky spectra. That way, only half of the frames contained the galaxy spectrum, resulting in an observing sequence of the form OSSO (O=object integration, S=sky integration). Total on source exposure times were between 900 and 2400s [see Table 2.2 for a detailed listing, with '(1/2)' denoting OSSO observations]. The seeing was generally sub-arcsecond, reaching as low as $\sim 0.5''$ in the best cases.

To be able to remove the telluric lines, we observed B-type standard stars with the same observing sequence we have used for our science targets. These hot stars do not have any spectral features in the wavelength interval we are considering. Moreover, their continuum in the *K*-band is well approximated by the Rayleigh-Jeans part of the blackbody spectrum (Silva et al. 2008). To remove the stellar signature, we divide the spectrum by a template of the corresponding type of star (Pickles 1998). All the remaining variation in the spectra is due to observational features and is caused by the telluric lines and the instrument response, so, by dividing the galaxy

Table 2.1: The instrumental set-up.

Telescope	VLT UT1/Antu
Dates	20 October 2008 - 26 January 2009
Instrument	ISAAC
Spectral range	$0.98 - 2.5\ \mu m$
Grating	MR
Dispersion	1.22 Å pixel^{-1}
Resolution (FWHM)	8.196 Å
Spatial Scale	0.1484 arcsec pixel^{-1}
Slit Width	1 arcsec
Detector	Hawaii
Gain	4.6 e$^-$ ADU^{-1}
Read-out noise	~ 10 e$^-$
Seeing	$< 1''$
Pixel Size	$18.5 \mu m$

spectra by this residual template spectrum, we remove the telluric lines and the detector signature. Because of the variability of the NIR sky, we impose the conditions that the difference in observing time between the target and the standard star has to be less then 2 hours and that the difference in airmass between the observations has to be less than 0.2.

Galaxy	Type	B_T [mag]	Exposure time [s]	PA [°]	$\sigma_{\rm opt}$ [km s^{-1}]	$\sigma_{\rm NIR}$ [km s^{-1}]	$\sigma_{\rm NIR,23\ templates}$ [km s^{-1}]	EW$_{\rm CO}$ [Å]	S/N
NGC 1316	S0 pec	9.4	1800 (1/2)	47	221.0 ± 11.0	237.7 ± 11.1	218.6 ± 9.9	13.56	89
NGC 1336	E4	13.1	2400	10	96.0 ± 5.0	119.0 ± 8.2	126.9 ± 7.0	13.04	66
NGC 1339	E5	12.5	1200	159	158.0 ± 8.0	182.4 ± 9.2	175.2 ± 9.4	14.41	57
NGC 1351	E5	12.5	1200	140	157.0 ± 8.0	153.0 ± 6.6	148.4 ± 5.5	9.58	73
NGC 1373	E3	14.1	2400	130	75.0 ± 4.0	79.8 ± 4.7	72.5 ± 4.0	11.26	66
NGC 1374	E0	12.0	1200	120	185.0 ± 9.0	206.8 ± 10.0	193.9 ± 9.7	13.72	72
NGC 1375	S0	13.2	1800	90	56.0 ± 10.0	64.1 ± 4.2	58.2 ± 3.8	11.66	68
NGC 1379	E0	11.8	1200	65	130.0 ± 7.0	130.0 ± 6.8	123.3 ± 5.3	12.02	90
NGC 1380	S0	10.9	1800 (1/2)	7	219.0 ± 11.0	189.8 ± 16.6	199.8 ± 20.8	12.19	59
NGC 1380A	S0	13.3	2400	178	55.0 ± 9.0	59.9 ± 9.1	51.2 ± 8.6	11.41	33
NGC 1381	S0	12.4	1200	139	153.0 ± 8.0	155.2 ± 5.7	148.3 ± 4.6	11.70	129
NGC 1399	E0, cD	10.6	1800 (1/2)	175	375.0 ±19.0	405.5 ± 33.1	409.0 ± 34.2	11.87	40
NGC 1404	E2	11.0	1800 (1/2)	163	260.0 ± 13.0	246.9 ± 21.6	240.9 ± 19.0	13.30	84
NGC 1419	E0	13.5	2400	125	117.0 ± 6.0	125.4 ± 5.0	119.2 ± 3.7	10.45	108
NGC 1427	E4	11.8	1800 (1/2)	76	175.0 ± 9.0	154.9 ± 17.5	150.3 ± 14.6	9.87	62
IC 1963	S0	12.9	2400	83	58.0 ±10.0	48.6 ± 5.6	40.3 ± 4.7	9.97	57
IC 2006	E	12.2	1800	10	136.0 ± 7.0	125.4 ±10.2	118.7 ± 8.1	14.18	50
ESO 359-G02	S0	14.2	1800	50	45.0 ± 8.0	...	...	...	7
ESO 358-G06	S0	13.9	1800	31	57.9 ± 10.8	55.1 ± 25.0	52.8 ± 24.8	13.20	13
ESO 358-G25	S0 pec	13.8	1800	60	58.0 ± 10.0	...	...	...	8
ESO 358-G50	S0	13.9	1800	172	49.0 ± 8.0	...	...	...	17
ESO 358-G59	S0	14.0	1800	160	54.0 ± 9.0	70.0 ± 20.4	65.0 ± 14.9	10.83	29

Table 2.2: Galaxy sample. Morphological type and optical velocity dispersions taken from Kuntschner (2000), B_T from NASA/IPAC Extragalactic Database. Empirical S/N estimates were determined for the extracted spectra as described in §2.2.3.

2.2.3 Data reduction

The basic data reduction steps were performed with the ISAAC pipeline and MIDAS. The sky subtraction, bias subtraction, flat fielding and wavelength calibration (based on the OH-lines) were done by the ISAAC pipeline. The removal of telluric lines (using our standard star observations) was done with MIDAS. If possible and appropriate, we increased the S/N of the telluric profile by averaging different observations of telluric stars. For NGC 1380, telluric lines have not been removed, because of a problem with the wavelength calibration of the standard star. For all spectra we had some problem around 2.3 μm to correct a telluric absorption line with a very sharpe edge. As a result, a spike-like emission feature remains in the corrected spectra.

We choose not to remove cosmic rays, but will ignore any contaminated pixel when fitting the stellar template. An average of the 25 central rows was taken to obtain an effective aperture of 1×3.7 arcsec^2, choosing a slit width of 1 arcsec to obtain the needed spectral resolution and approximating the spatial width of the 2.3×3.85 arcsec^2 optical aperture used by Kuntschner (2000). We do not increase the extraction width to obtain a better S/N, because the velocity dispersion can be strongly aperture-dependent (as shown in Fig. 2.1), and it is important to be well-matched to Kuntschner (2000). As a final step, the spectra were rebinned to a common wavelength increment (2.43 Å/pix), approximately doubling the original step size. To illustrate the effect of the different data reduction steps, we refer to Fig. 2.2, where a central $3.7''$ extraction of NCG 1381 is shown for the different data reduction steps: the ISAAC pipeline result, after removing the telluric lines and after rebinning to the 2.43Å/pix wavelength increment. For each extracted spectrum, we have derived an empirical S/N following the method described by Stoehr et al. (2007). The resulting S/N per rebinned element ranges from ~ 7 for the faintest galaxies to more than 100 for the brightest ones and is listed in Table 2.2.

The instrumental set-up, as described in Table 2.1, gives a FWHM resolution of approximately 107 km s^{-1}, producing an instrumental contribution to the dispersion of ~ 45 km s^{-1}.

2.2.4 Velocity dispersion determination

The sharp blue edge of the CO band head allows us to measure the kinematics accurately (Silge & Gebhardt 2003). There are several techniques to obtain the internal kinematical information, e.g. the Fourier correlation quotient (FCQ) method, developed by Bender et al. (1994) and used by Kuntschner (2000). We use the pPXF technique developed by Cappellari & Emsellem (2004). This method rebins the spectrum logarithmically and fits it directly in pixel space. We correct the template continuum shape using additive second degree Legendre polynomials and use a pure Gaussian to model the LOSVD. An alternative LOSVD is inspected in § 2.3.2, where Gauss-Hermite coefficients h_3 and h_4 are included to model the LOSVD. We apply pPXF to a wavelength range of $\sim 2.23 - 2.345\,\mu$m, fitting not only the CO band head, but also including

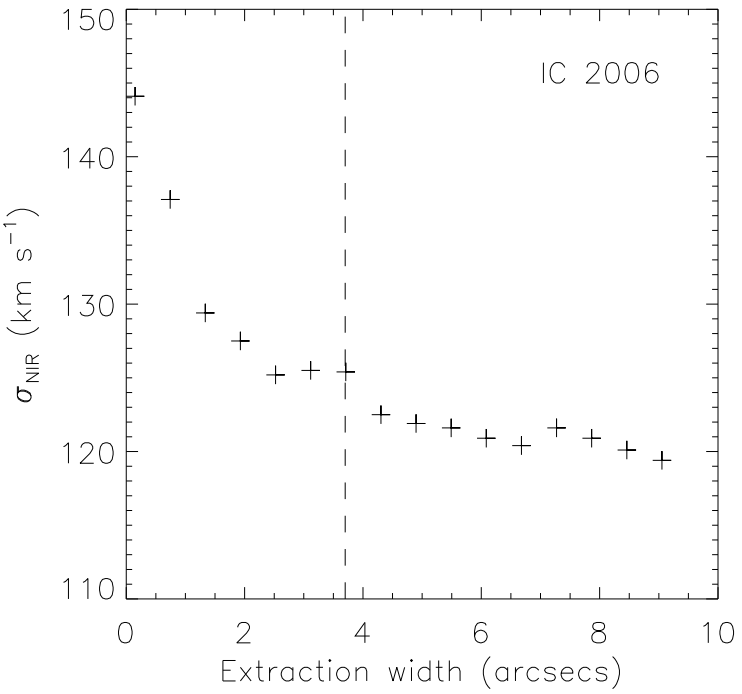

Figure 2.1: Central velocity dispersion of IC 2006 as a function of the extraction width. The dashed line shows the standard extraction aperture of 3.7 arcsecs.

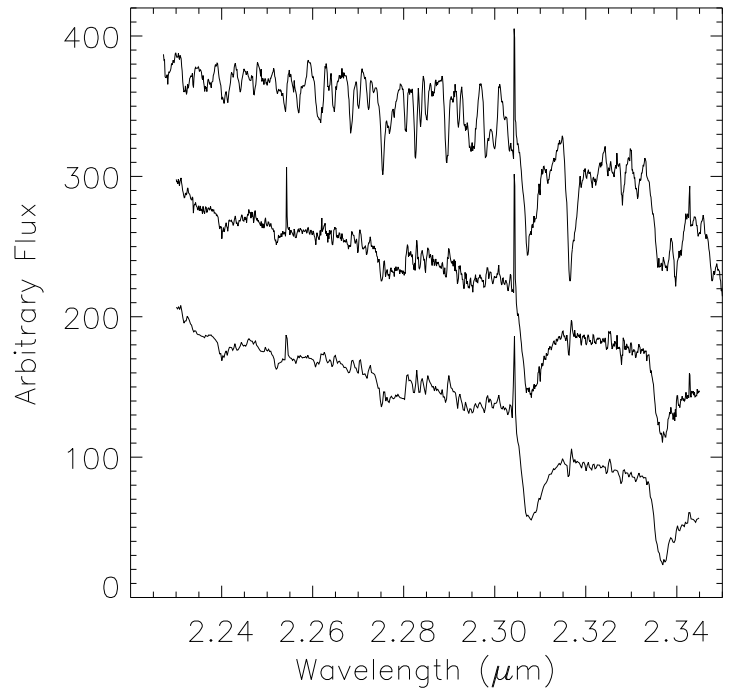

Figure 2.2: Data reduction steps applied to a central 3.7″ extraction of NGC 1381 are shown (from top to bottom) before corrections for telluric absorption (the pipeline result), after correction for telluric absorption and instrument sensitivity and after rebinning to ∼2.43Å/pix. The sharp emission feature around 2.3 μm is a remnant of the telluric correction.No correction for redshift has been applied. The middle and the bottom spectra have been separated by an arbitrary additive offset; otherwise, they would be on top of each other.

a part of the spectrum bluewards of it. To illustrate the effect of the velocity dispersion on the CO band head, we refer to Fig. 2 of Silge & Gebhardt (2003).

The choice of the template stars, which we obtained from the GNIRS and NIFS libraries (Winge et al. 2009), is an important aspect when determining the velocity dispersion: Silge & Gebhardt (2003) showed that the equivalent width of the template used for the fit is important, not the details of the spectral type. To account for the spectral resolution differences between ISAAC and the template libraries, we have logarithmically rebinned the latter to the same velocity scale as the ISAAC spectra, under the assumption that the shape of the instrumental spectral profiles can be well approximated by a Gaussian. Fig. 2.3 presents the measured central velocity dispersion as a function of the equivalent width of the input template, with equivalent widths ranging from $\sim$ 1.5 to $\sim$ 15Å. One concludes that the larger the EW of the CO band of the template, the lower the resulting velocity dispersion required to reproduce the galaxy spectrum. The relative values of the velocity dispersion are only comparable, if a fixed template is used to generate the fits. The filled squares are the results for an average template of K giants (HD206067, HD218594, HD39425 and HD4730 from the GNIRS library) and M giants (HD27796, HD30354, HD23574, HD234791 from the NIFS library). To be consistent with Kuntschner (2000), we choose the average K giant spectrum to fit the galaxy spectra in a homogeneous way. An alternative template scheme is explored in § 2.3.2, where velocity dispersions have been determined using all the templates of Fig. 2.3 as input templates for pPXF. The asterisks in Fig. 2.3 represent the EWs of the galaxies in the sample, given in Table 2.2. This shows that the stellar library spans the range of the observed CO strength in the galaxies.

Table 2.2 presents the resulting NIR velocity dispersion $\sigma_{\rm NIR}$ and the optical velocity dispersions $\sigma_{\rm opt}$ taken from Kuntschner (2000). The optical velocity dispersions have been used as the initial value in the pPXF method. After trying several approaches, we have used a bootstrap method to estimate the uncertainties on the velocity dispersions, resampling the residuals of the initial fit. For ESO 359-G02, ESO 358-G25 and ESO 358-G50 we did not get a reliable fit, as a consequence of the low S/N for these galaxies and the low expected velocity dispersions (based on the optical values). We decided to exclude these galaxies from the sample. Afterall, their optical velocity dispersions are not reliable either; they suffered an instrumental broadening of $\sim$ 105 km s^{-1}, which introduces optical systematic errors for $\sigma < 90$ km s^{-1} [as stated in Kuntschner (2000)].

The spectral fits are presented in Figs. 2.4 and 2.4: the thick smooth line is the resulting fit, the thin noisy line represents the galaxy spectrum. Cosmic rays, sharp features and poorly removed telluric features were flagged as bad pixels and were not used by the pPXF method to generate the fit. If we estimate the error on the fit by the dispersion of the residuals, we obtain $\chi^2/DOF < 1$ for all galaxies, which indicates that we obtain good fits.

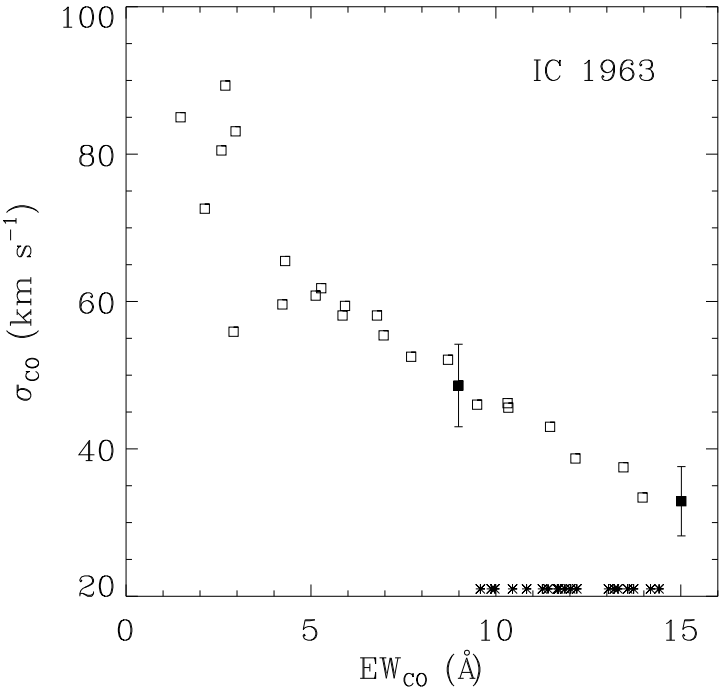

Figure 2.3: Dispersion measured by the pPXF method for IC 1963 as a function of the equivalent width of the input template star. The two filled squares are the results for an average template of K giants ($EW_{CO} = 8.99$, $\sigma_0 = 48.6 \pm 5.6$) and M giants ($EW_{CO} = 15.01$, $\sigma_0 = 32.9 \pm 4.7$). The asterisks represent the EWs of the galaxies in the sample.

2.3 Results and discussion

2.3.1 Comparing NIR velocity dispersions

The line strength study of Silva et al. (2008) had 4 S0 and 6 E galaxies in common with our galaxy sample [of which 8 are observed with ISAAC and 2 (NGC 1316 and NGC 1399) with SINFONI at the VLT]. For their ISAAC observations in SWS-MR mode, they also used a $120'' \times 1''$ slit and had total exposure times of 3000s or 3200s. This resulted in extracted spectra with a S/N ranging from 48 to 280, based on the S/N determination of Stoehr et al. (2007). However, they applied a procedure derived from the processing of optical long-slit spectra and did not use a simple AB subtraction, because this could cause inaccurate dark and background correction in the lower surface brightness parts of the luminosity profiles. They periodically observed velocity template standard stars, covering the range K5 III to M1 III. Those templates were fitted to the galaxy spectra applying the pPXF method, extracting the NIR velocity dispersions $\sigma_{\mathrm{NIR,Silva}}$. Unfortunately, no uncertainties on the velocity dispersions were given. They used $1'' \times 1/8R_e$ for the extraction window, which results in spatial widths ranging from 0.15 to 0.61 arcsec (extracted R_e for NGC 1404 equals 2.9 arcsecs, kindly provided by Dr. Kuntschner, private communication). For the SINFONI observations, Silva et al. (2008) extracted a slit of $2'' \times 3''$ from the data cube.

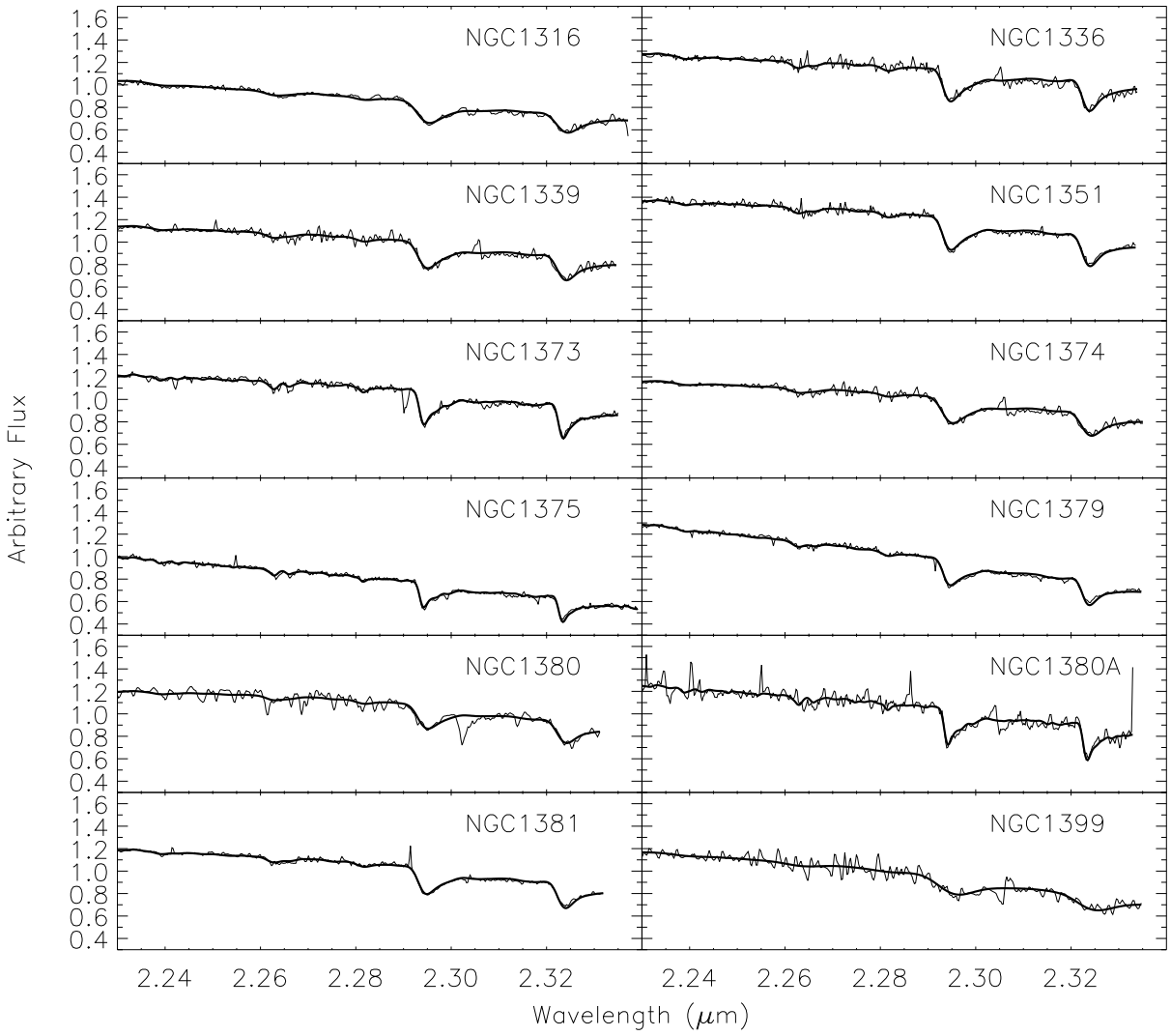

Figure 2.4: Rest-frame spectra of galaxies (noisy thin curves) and spectra of the average KIII stellar spectrum convolved with the derived velocity distribution (smooth thick curves). Cosmic rays and poorly removed telluric features were flagged as bad pixels and not used to generate the fit. No removal of telluric lines was done for NGC 1380.

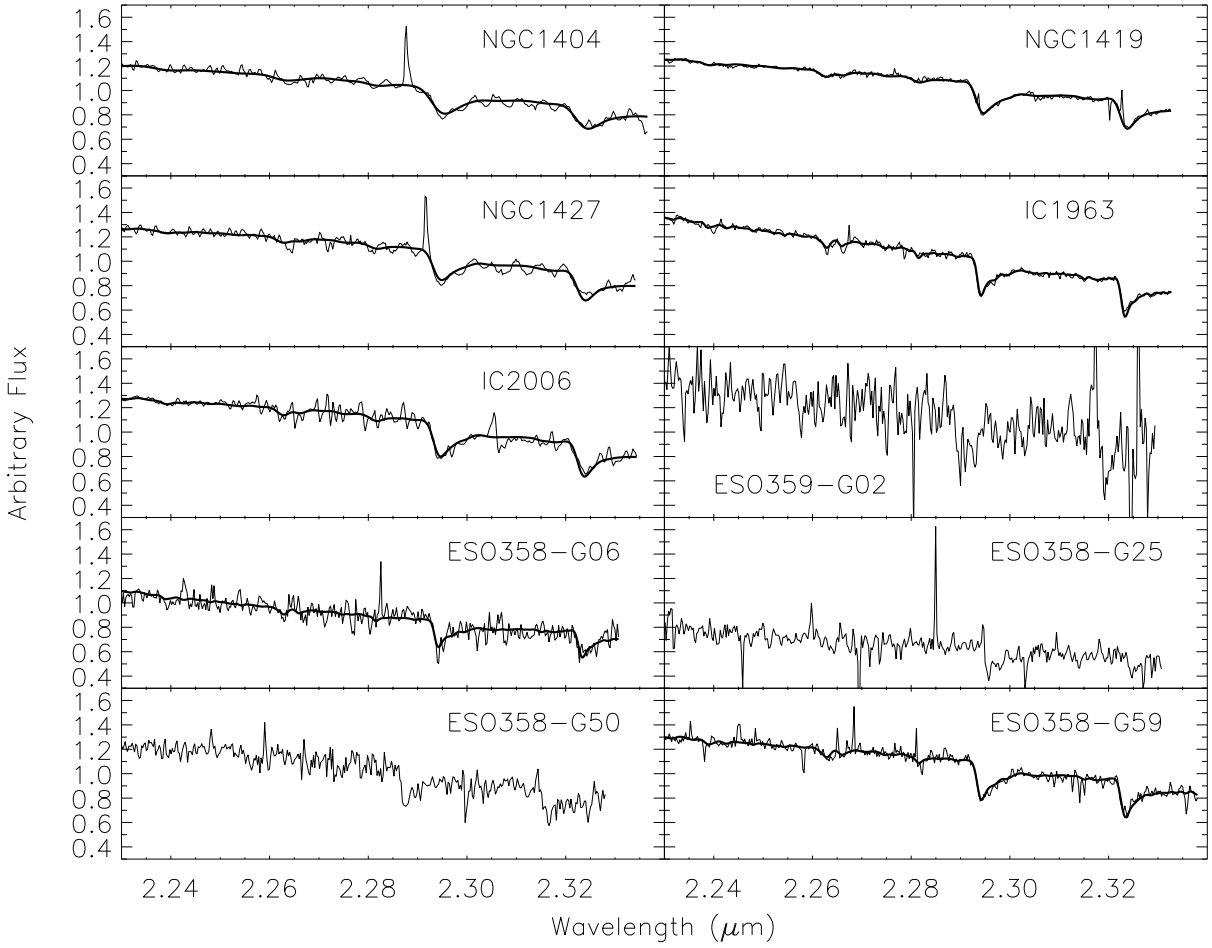

Figure 2.4: (continued)

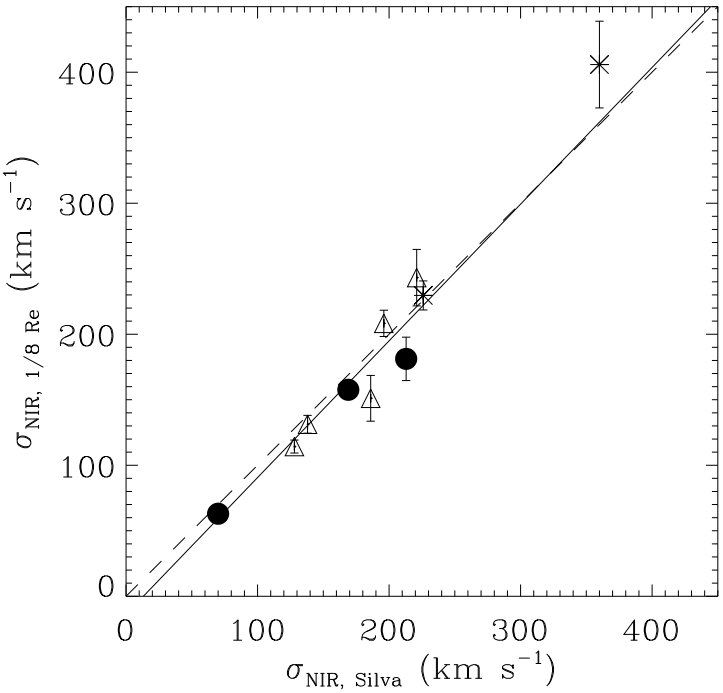

Figure 2.5: Correlation between the velocity dispersions determined with an extraction window of 1/8 R_e and the NIR velocity dispersions from the literature (Silva et al. 2008). The dashed line has a slope of unity, the solid line is the best fit, given by equation 2.1. Here and in the following plots, the filled circles are S0 galaxies, while the open triangles are E galaxies. The two galaxies observed with SINFONI (Silva et al. 2008) are represented with an asterisk.

In Fig. 2.1 it is shown that the velocity dispersion can depend on the extraction width. In order to compare our measurements with Silva et al. (2008), we have redetermined the velocity dispersion for the 10 galaxies in common, adopting an extraction width of $1'' \times 1/8R_e$ ($1'' \times 3''$ for NGC 1316 and NGC 1399) and fitting the average K giant template to the galaxy spectra. The measurements are denoted as $\sigma_{\rm NIR,1/8\ Re}$. The results are presented in Fig. 2.5, where the derived velocity dispersions $\sigma_{\rm NIR,1/8\ Re}$ are compared to the values $\sigma_{\rm NIR,Silva}$, derived by Silva et al. (2008). In this and following figures, true elliptical galaxies are represented as open triangles, lenticular galaxies as filled circles. However, to distinguish the 2 galaxies observed with SINFONI by Silva et al. (2008), we have marked those galaxies with asterisks in Fig. 2.5. We have used the uncertainties on $\sigma_{\rm NIR}$ as an estimate for the uncertainties on $\sigma_{\rm NIR,1/8\ Re}$. The best-fitting line, which is given by

$$\sigma_{\rm NIR,1/8\ Re} = (1.04 \pm 0.05)\sigma_{\rm NIR,Silva} - (13.78 \pm 9.52), \tag{2.1}$$

has a slope consistent with 1, an intercept marginally inconsistent with 0 and a reduced χ^2 of 1.89. Using the velocity dispersions obtained with the fixed extraction width of $3.7''$ ($\sigma_{\rm NIR}$) instead of $\sigma_{\rm NIR,1/8\ Re}$ does not change the fit significantly. Thus, our NIR results generally compare well to those of Silva et al. (2008) for the same galaxies.

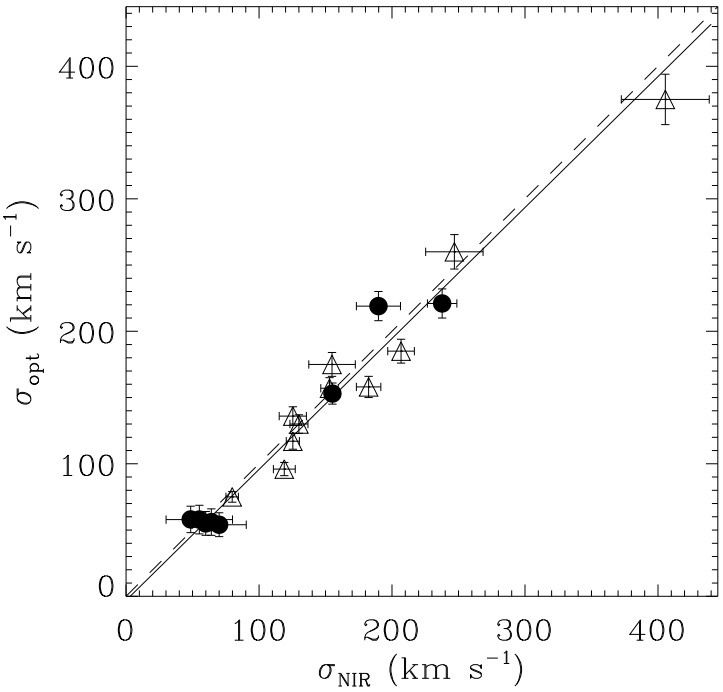

Figure 2.6: Correlation between the dispersion measured from the CO band head and the optical dispersion (Kuntschner 2000). The dashed line shows where two measurements are equal, the solid line is the best-fitting line, given by equation 2.2.

2.3.2 Comparing NIR and optical dispersions

Fig. 2.6 presents the correlation between the optical and NIR central velocity dispersions for 19 galaxies of our sample. The solid line

$$\sigma_{\rm opt} = (0.99 \pm 0.06)\sigma_{\rm NIR} - (3.76 \pm 8.72) \tag{2.2}$$

shows the best fit, with a slope consistent with 1, an intercept consistent with 0 and a reduced χ^2 of 1.09. This result confirms the findings by Silva et al. (2008) and further generalizes their results due to the statistical completeness of this study, but does not agree with Silge & Gebhardt (2003). Their best-fitting line had a slope of 1.189 ± 0.084 and an intercept of -8.6 ± 12.4.

Kuntschner (2000) had difficulties in determining the velocity dispersions for galaxies with $\sigma_{\rm opt} < 70$ km s^{-1} and noted that the results of $\sim 50 - 60$ km s^{-1} are only rough estimates. However, excluding the galaxies with $\sigma_{\rm opt} < 70$ km s^{-1} does not change the results significantly.

Fig. 2.7 presents a histogram of the fractional difference between NIR and optical measurements of dispersion. The median fractional difference between the optical and the NIR velocity dispersions is 6.4%, the mean fractional difference is 3.9%. Silge & Gebhardt (2003) found a median difference of -11%, opposite to theoretical expectations (Baes & Dejonghe 2002) and

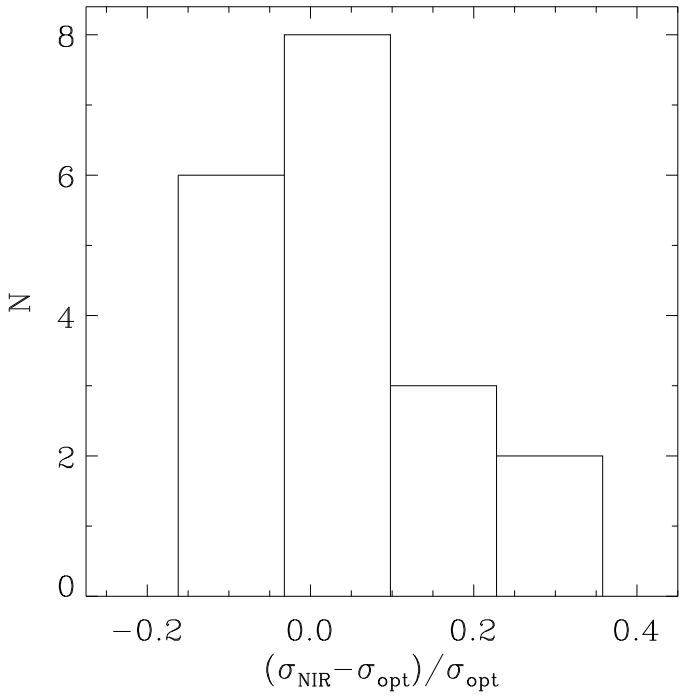

Figure 2.7: Histogram showing the number of galaxies in each bin of fractional difference between infrared and optical measurements. The median fractional difference is 6.4%, the mean fractional difference is 3.9%.

to our results.

It is not immediately clear why Silge & Gebhardt (2003) found that NIR velocity dispersion measurements are lower than optical dispersion measurements. One possible reason could be the different spatial range used by Silge & Gebhardt (2003): Fig. 2.1 indicates that velocity dispersions can decrease for higher spatial ranges. The average spatial width in Silge & Gebhardt (2003) is $\sim 12''$, which may be the reason for their difference between NIR and optical velocity dispersions. In order to investigate this possibility, we recalculated the NIR velocity dispersions for all galaxies in our sample, now using an extraction window of $1'' \times 12''$. The best-fitting line, with a reduced χ^2 of 1.35, is

$$\sigma_{\rm opt} = (1.03 \pm 0.07)\sigma_{\rm NIR,1\times 12 arcsec^2} - (3.35 \pm 9.16), \tag{2.3}$$

fully consistent with Eq. 2.2. Fig. 2.1 suggests an increase of the slope of $\sim$ 4%, which is indeed what we find. Nonetheless, a $\sim$ 20% effect is needed to explain the results found by Silge & Gebhardt (2003), so we exclude that the extraction width is responsible for the discrepancy.

Another possible explanation for the discrepancy could be the choice of the templates: Fig. 2.3 showed that the measured velocity dispersion depends strongly on the equivalent width of the CO band of the template. Silge & Gebhardt (2003) used templates with equivalent widths rang-

ing from less than 5 to over 20 Å. So far, we have only used the average K giant template with an equivalent width of 8.99 Å. In order to investigate this possibility, we have provided the 23 templates we have used in Fig. 2.3 as input templates for pPXF. The resulting velocity dispersions are given in Table 2.2. For every galaxy separately, pPXF gives weights to the different templates to obtain the best fit, delivering stellar population information. pPXF favoured HD113538 (KV), HD2490 (MIII) and HD63425B (KIII), which indicates that the light is dominated by cool giants and dwarfs. The best linear fit is given by

$$\sigma_{\rm opt} = (0.99 \pm 0.07)\sigma_{\rm NIR,23\ templates} + (2.92 \pm 9.05) \tag{2.4}$$

and has a reduced χ^2 of 1.70. It is fully consistent with equation 2.2, indicating that template mismatch does not affect our velocity dispersion determination.

Silge & Gebhardt (2003) used a nonparametric LOSVD. To investigate whether this could account for the discrepancy, we included the h_3 and h_4 Gauss-Hermite coefficients, using the average K giant template as input spectrum and the default pPXF parameter λ to penalize both parameters. The resulting values for h_3 (and h_4) are between -0.05 and 0.11 (-0.01 and 0.08, respectively) with a median value of 0.012 (0.020, respectively). The best-fitting line is given by

$$\sigma_{\rm opt} = (0.99 \pm 0.05)\sigma_{\rm NIR,G\text{-}H} - (2.40 \pm 7.58) \tag{2.5}$$

with a reduced χ^2 of 0.93. Again, the slope is consistent with 1 and the intercept is consistent with 0, so we exclude that the parametrization of the LOSVD is accountable for the discrepancy.

One remaining possibility for the difference between our results and Silge & Gebhardt (2003) is that the sample selection is important. Our Fornax sample represents only a cluster environment, while the Silge & Gebhardt (2003) sample ranges from cluster to isolated field galaxies and there are known correlations between environment and velocity dispersion (e.g. Zhu et al. 2010; La Barbera et al. 2010b).

2.3.3 Correlation with IRAS dust masses

According to Silva et al. (2008), at least two galaxies (NGC 1316 and NGC 1380) from our sample show clear central dust features. We need to know how much dust there is in the galaxies to study the effects of dust on the observed kinematics. In this section, we derive the dust masses (M_d) for our galaxies based on IRAS flux densities at 60 and 100μm. We apply the technique of Goudfrooij & de Jong (1995), using a distance D=19.3 Mpc for all galaxies (Jordán et al. 2007). For 5 galaxies of our sample, both S(60) and S(100) were given. In that case both T_d and M_d were determined. If only S(100) was given, which was the case for 5 galaxies of our sample, we used the average dust temperature $\overline{T}_d = 25.9K$ of our galaxy sample as a representative value

Table 2.3: IRAS flux densities and dust characteristics.

Galaxy	S(60μm) [Jy]	S(100μm) [Jy]	$\log(M_d)$ $[M_\odot]$	T_d [K]	$\log(M_d/L_B)$ $[M_\odot/L_\odot]$
NGC 1316	3.070 ± 0.030	8.110 ± 1.900	6.11 ± 0.25	27.2 ± 2.2	-4.64
NGC 1336	...	0.260 ± 0.095	4.73	...	-4.54
NGC 1339	0.2298 ± 0.14	0.670 ± 0.058	5.09 ± 0.25	26.5 ± 2.1	-4.42
NGC 1351	0.090 ± 0.021	0.510 ± 0.042	5.41 ± 0.24	22.4 ± 1.5	-4.10
NGC 1379	...	0.140 ± 0.047	4.46	...	-5.33
NGC 1380	1.040 ± 0.042	3.440 ± 0.107	5.88 ± 0.24	25.6 ± 1.9	-4.27
NGC 1399	...	0.300 ± 0.082	4.79	...	-5.48
NGC 1404	...	0.270 ± 0.056	4.75	...	-5.36
IC 2006	0.120 ± 0.015	0.320 ± 0.047	4.71 ± 0.25	27.2 ± 2.2	-4.92
ESO 358-G59	...	0.380 ± 0.060	4.90	...	-4.01

to compute the dust mass. Table 2.3 presents the resulting dust masses M_d, T_d and the IRAS flux densities for 10 galaxies in our sample. For six galaxies (NGC1374, NGC1375, NGC1381, NGC1419, NGC1427, ESO358-G06) the IRAS Faint Source Catalog lists only upper limits, the three remaining galaxies (NGC1373, NGC1380A, IC1963) are not listed in the catalog.

Fig. 2.8 presents the fractional difference of the infrared and the optical dispersions as a function of the relative amount of dust in a galaxy, which is estimated in Silge & Gebhardt (2003) by the ratio of the IRAS dust mass to the B-band luminosity. The estimates for the relative amount of dust are given in Table 2.3. Note that the IRAS dust mass estimates are a lower limit for the true dust masses, because IRAS is not sensitive to cold dust (which emits the bulk of its radiation longwards of 100μm.). A negligible trend is visible (confirmed by the Spearman rank-order correlation coefficient equal to 0.21). The best-fitting solid line is given by equation

$$\frac{\sigma_{\rm NIR} - \sigma_{\rm opt}}{\sigma_{\rm opt}} = (0.008 \pm 0.056)\log(\frac{M_d}{L_B}) + (0.068 \pm 0.266), \tag{2.6}$$

with both the slope and the intercept consistent with 0 and a reduced χ^2 of 1.76. This implies that warm dust does not affect optical dispersions. We cannot yet make the same conclusion for colder dust, but Fig. 2.6 indicates that the typical effect is very weak.

2.4 Conclusions

In this chapter, we investigated a complete magnitude-limited and unbiased sample of 22 early-type galaxies in the Fornax cluster and were able to determine the kinematics based on the 2.29μm ^{12}CO(2-0) feature for 19 of those galaxies. We related the NIR velocity dispersions

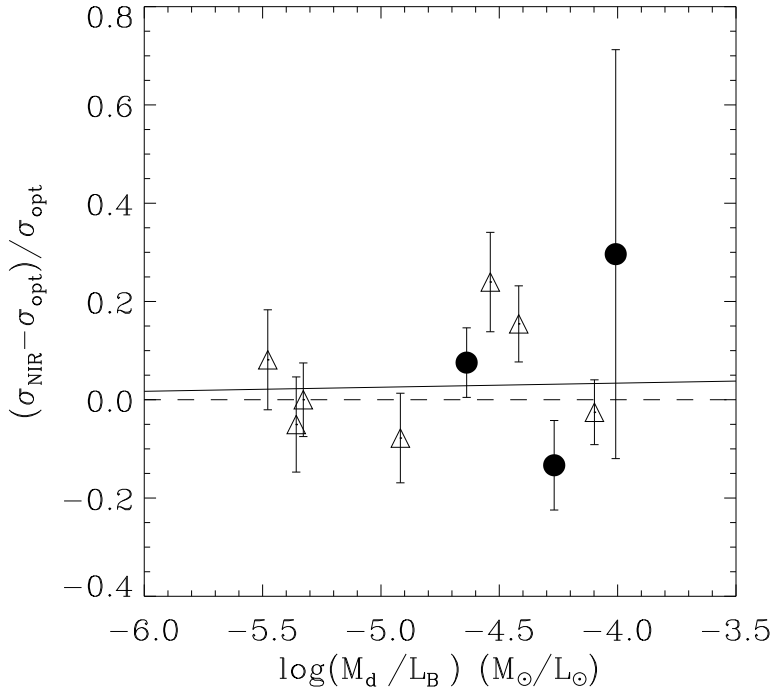

Figure 2.8: Fractional difference between the infrared and optical dispersions as a function of the ratio of dust mass to *B*-band luminosity. The solid line is the best fit, given by Eq. 2.6. The Spearman rank-order correlation coefficient is 0.21 at a significance level of 0.56.

with the optical dispersions of Kuntschner (2000) and found a 1-to-1 correspondence for the ellipticals as well as for the lenticulars. Our results agree with a previous smaller study of Silva et al. (2008), but not with Silge & Gebhardt (2003). We investigated this disagreement by providing a variety of input templates to pPXF with a large range of EWs, by changing the spatial width of the extraction window and by introducing Gauss-Hermite coefficients in the LOSVD, but we were not able to clarify this discrepancy.

We have computed the dust masses based on IRAS flux densities for 10 galaxies of our sample and investigated the influence of diffuse dust on the observed kinematics, which turned out to be negligible.

The one-to-one correspondence between the optical and the NIR velocity dispersions found for this homogeneous set of early-type galaxies implies that velocity dispersions measured at optical wavelengths are reliable kinematic parameters for early-type galaxies and hence that no bias is introduced in statistical relations that build on such dispersions (such as the M_{BH}-σ relation or the Fundamental Plane).

Combined with the simulations by Baes & Dejonghe (2000, 2002), it also supports the traditional point of view on the dust content of early-type galaxies, namely that they are virtually optically thin. While some observational studies hinted towards the existence of a substantial diffuse dust component in early-type galaxies (e.g. Temi et al. 2004, 2007; Leeuw et al. 2004; Vlahakis et al. 2005), the Science Demonstration results from the recently launched Her-

schel Space Observatory indicate a dearth of diffuse dust in the few elliptical galaxies studied (Clemens et al. 2010; Baes et al. 2010; Gomez et al. 2010). Smith et al. (2012) presented a subsequent study using a larger sample of ETGs as part of the Herschel Reference Survey (Boselli et al. 2010). They detected dust in only a quarter of the elliptical galaxies, while more than half of the lenticular galaxies contain generally low but detectable amounts of cold dust. De Looze et al. (2012) excluded the presence of a massive cold dust component in the brightest early-type dwarf satellite of the Andromeda galaxy. However, Rowlands et al. (2012) demonstrate that some but relatively few ETGs exist which contain as much dust as typical spirals based on their submillimetre-selected sample (hence preferentially selecting dusty galaxies) and Wilson et al. (2013) give another example of an elliptical galaxy which contains large amounts of cold dust.

Whereas our results support the optically-thin scenario, we must be careful for two caveats. On the one hand, our results only set limits on the presence of a smooth, diffusely distributed dust component, which one would expect if the dust has an internal origin. If the dust has an external origin, it is not necessarily coincident with the stellar body. An example is the nearby Virgo Cluster elliptical M86, where the dust is clearly related to stripping from a nearby spiral galaxy and is concentrated some 10 kpc to the south-east of the nucleus (Gomez et al. 2010).

On the other hand, the comparison of optical and NIR velocity dispersions might not be the most sensitive way to measure the optical thickness of early-type galaxies. The simulations of Baes & Dejonghe (2000, 2002) indicate an effect of a few percent only for optical depths of order unity. Combined with the measurement errors and other possible effects such as different stellar populations dominating the kinematics at optical and NIR wavelengths, our results should be considered only in a statistical sense and one should take care not to directly interpret results on individual galaxies in terms of optical thickness. A clear example is the case of NGC1380: in spite of a clear dust lane in optical images (Jordán et al. 2007) and a significant IRAS dust mass of $7.6 \times 10^5\,M_\odot$, the NIR velocity dispersion is lower than the optical dispersion.

The data reduction of the recent Herschel data is still ongoing, which will hopefully provide a definite and irrevocable picture on the optical thickness of early-type galaxies in the near future. Moreover, these upcoming results contain promising information to gain more insight on the origin of the ISM (Rowlands et al. 2012), the star formation histories and the galactic build-up based on minor mergers (Kaviraj et al. 2013). Of particular interest for our study on ETGs in the Fornax cluster is the Herschel Fornax Cluster Survey (HeFoCS; Davies et al. 2013). The first results of this project further point at largely optically thin ETGs (with a mean optical depth $\tau = 0.4$), in agreement with the results from the Herschel Virgo Cluster Survey (Davies et al. 2010) and with our results. Preliminary HeFoCS results of Fuller et al. (in prep.) further confirm this picture: they have 16 ETGs in common with our sample, and, only four of these galaxies were detected by the Herschel Space Observatory.

Homogeneous photometry for Galactic Globular Clusters in SDSS passbands

3

The results presented in this chapter are based on Vanderbeke et al. (2014a).

3.1 Introduction

Globular clusters (hereafter GCs) formed during the earliest episodes of star formation in galaxies. They are found in all but the smallest dwarf galaxies, with massive galaxies hosting systems of hundreds or thousands of clusters. The properties of globular clusters appear to be very homogeneous from one galaxy to the other (in terms of colour, luminosity distribution, etc.) and this implies that the formation of these objects has been intimately related to the assembly of their parent galaxies (e.g., Harris 1991). Globular clusters are living fossils of the Universe at high redshift (their mass is similar to the Jeans mass at the epoch of recombination) and therefore give a snapshot of conditions as prevailed at early epochs (see West et al. 2004; Brodie & Strader 2006 for reviews). The integrated properties of globular clusters therefore provide us with information on the earliest stages of galaxy formation; the high intrinsic luminosities of clusters means that they can be studied in detail well beyond the Local Group, while the bright end of the globular cluster luminosity function has been detected around a $z \sim 0.2$ elliptical galaxy (Alamo-Martínez et al. 2013).

Most work in both Galactic and extragalactic GCs is still based on the older photometric systems (such as Johnson-Cousins, Washington, etc.). Several authors have remarked on the lack of calibrating studies of globular clusters in the SDSS system (Jordán et al. 2005; Sinnott et al. 2010; Peacock et al. 2011; Vickers et al. 2012); as most such objects are in the South, the vast majority of Galactic GCs have not been imaged by the SDSS survey. The latest edition of the Harris (1996) compilation (2010 edition, this is the version we refer to in the remainder of the thesis) lists $UBVRI$ colours for about half of the 150 Galactic GCs. Nevertheless, this photometry is inhomogeneous, as it is taken from different papers, using different methods and instruments (including photomultipliers, photographic plates and modern CCDs).

The Sloan Digital Sky Survey (SDSS – York et al. 2000) has now imaged over a quarter of the Northern sky (about 14500 square degrees) in five passbands. Together with upcoming imaging surveys in the South, SDSS will completely replace the older Schmidt plate atlases of the sky, and at the same time provide a standardised system of photometry in the optical for astrophysics (theoretically, with calibrators in every field). With this motivation, our team embarked on the Galactic Globular Cluster Catalog (G2C2) project, with an ultimate goal of collecting reliable photometry using the SDSS filter system for a large sample of Galactic GCs. In the current chapter, we present g' and z' magnitudes for about two-thirds of the Galactic GCs and r' and i' magnitudes for about one-third of all Galactic GCs.

Here we discuss the buildup of the photometric database: imaging of 96 Galactic clusters in at least 2 SDSS bands (as well as 2 more for a subset of 56 objects). We describe our observations and basic data reduction: we give details about the samples, determination of cluster centres, aperture photometry, estimation of the sky level, removal of outliers, photometric errors and

Table 3.1: The instrumental set-up.

Telescope	CTIO 0.9m
Dates	2003 May - 2012 March
Filter set	$g'r'i'z'$
Spatial scale	$0.396\,''pixel^{-1}$
Field Size	$13.6' \times 13.6'$
Gain	3.0 e^- ADU^{-1}
Read-out noise	5 e^-
Detector	2048×2046 Tek2K CCD

correction for extinction. To assess the quality of our data we compare these with previous work and carry out a similar analysis on globular clusters in common with the SDSS footprint.

3.2 Observations and data reduction

3.2.1 CTIO

We selected Galactic GCs from the latest versions of the Harris (1996) catalog, which includes about 150 GCs. Observations were carried out between 2003 May 10 and 2012 June 9 using the CTIO 0.9 m and 1 m telescopes with the USNO $g'r'i'z'$ filter set. Because the Galactic bulge and hence the bulk of the Galactic GCs are best observable during the Chilean winter, cirrus and bad weather were a real issue during the observing runs: many nights were totally lost due to clouds or strong winds, while other nights were disturbed by cirrus and were not photometric.

For the results in this chapter, we reduced 13 nights of observations. Several clusters were observed multiple times and it became clear that only 4 nights (all of which used the 0.9 m telescope, with an instrumental set-up as shown in Table 3.1) could be considered (largely) photometric. During these nights, we collected g' and z' observations for 81 GCs, about half of which we also observed using r' and i' filters.

For the vast majority of the clusters, we have 60 s exposures in g' and z' taken in June 2004. During the run performed on 2003 May 10 short (between 5 and 30 s) and long (270 s in g', 410 s in z') exposures were obtained. Both shorter and longer exposures were used separately to determine magnitudes. Some of the clusters have very bright stars close to their centres. These very bright stars saturated the CCD even for the short exposures. For these clusters (NGC 6397, 47 Tuc, NGC 6121) we obtained additional 1 s exposures. The observations discussed in this chapter were performed between 2003, May 10 and 2005, September 26 under seeing conditions varying between $1''$ and $\sim 2''$.

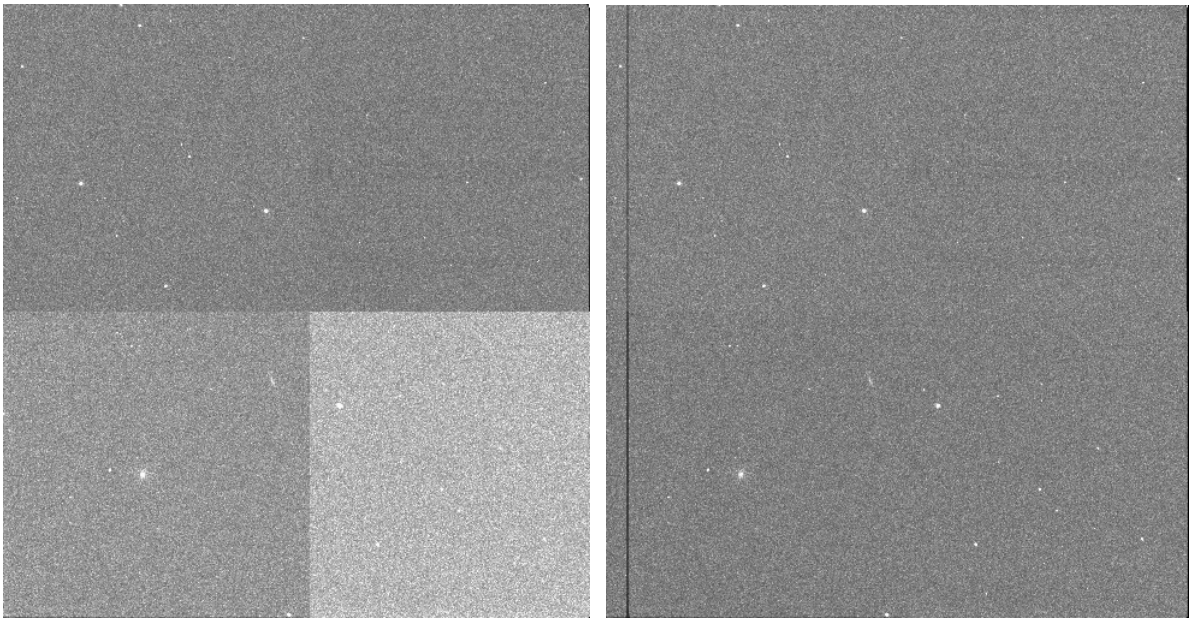

Figure 3.1: Figure illustrating the bias subtraction based on zero second exposures (left panel) and based on the bias section (right panel) for a frame observing standard stars. Scaling parameters are the same in both panels.

The basic data reduction was performed via a dedicated IDL pipeline which I developed. The procedure largely follows conventional CCD reduction processes.

Fig. 3.1 illustrates two possible ways to perform the bias subtraction. A standard way to account for the bias in astronomical observations is taking zero second exposures, which are subtracted from the raw images before flat-fielding. However, this method did not result in satisfying results for our data. As is illustrated in the left panel of Fig. 3.1, using this method produces frames with a sky offset between different quadrants, which is obviously not physical.

Another method to remove the bias from the data was tested. The bias level was estimated separately for each quadrant computing the median of the corresponding bias section, which was then subtracted for each quadrant. The right panel of Fig. 3.1 presents the resulting reduced image of the same field, using the same scaling parameters for both panels. It is clear that the latter method gives more satisfying results.

After the bias subtraction, the frames were flat-fielded by the median of the twilight flats taken each night and corrected for bad columns. To identify and robustly remove cosmic rays, we used the L.A. Cosmic (imaging version) method (van Dokkum 2001).

One additional complication was the incorrect information in the fits headers of the clusters observed from 2005 onwards. John Subasavage (private communication) confirmed that, since the TCS upgrade in early 2005, the header values (including RA, DEC, airmass and epoch) are not correct. Based on the coordinates obtained from Harris (1996) and the header values (date and time of observation), we computed automatically the airmasses for the observations taken

after 2005. Comparison with observation log sheets showed excellent agreement.

During the course of each observing night a minimum of several dozen photometric standard stars, selected from Smith et al. (2002), were observed at different airmasses. Photometric calibration (i.e., determination of zeropoints, colour terms and atmospheric extinction values, as well as removal of other instrumental signatures) was carried out as in Patat & Carraro (2001). Foreground (Galactic) extinction was estimated for each position using the most recent values from the recalibration of Schlafly & Finkbeiner (2011).

3.2.2 SDSS Data Release 9

We also considered a sample of 21 northern hemisphere clusters from the ninth data release of SDSS (Ahn et al. 2012), 6 of which have also been observed by us with the CTIO 0.9m telescope. However, NGC 6838 and NGC 6254 were only partly covered by SDSS and were not included in this study, as our procedure (see below) requires us to cover at least the half-light radius in each object. Bright foreground stars outshine GLIMPSE01, Ko 1 and Ko 2. We do not consider these clusters further.

For some other clusters, several SDSS stripes needed to be assembled into mosaics using Montage[1], although this may lead to issues with variable sky levels. Although SDSS data have the considerable advantage of being photometrically homogeneous and uniform, the 53.9 s standard exposure in SDSS saturates bright red giant branch (RGB) stars in some GCs, an effect which becomes clear when comparing the colour magnitude diagrams and which is further discussed in Section 3.3.7. Note that the 'SDSS' filters at the APO 2.5m telescope (and the CTIO 0.9m) have significantly different effective central wavelengths from the calibrating filters at the USNO 1m telescope, where the $u'g'r'i'z'$ photometric system was defined (Fukugita et al. 1996) and extended with secondary standards by Smith et al. (2000, 2002). The conversion between the $u'g'r'i'z'$ and $ugriz$ system is given on the SDSS website[2]. These result in negligible changes to the GC colours when compared to the magnitude uncertainties.

For NGC 6341 and NGC 5904 the saturation of the SDSS chip was so severe that almost the entire RGB is brighter than the saturation limit of the CCD. It was nearly impossible to select non-saturated stars to construct the PSF for the CMDs, which are indispensable in the reduction process (see Section 3.3.3). We decided to discard these clusters from the sample. Nevertheless, good quality data for NGC 6341 is highly desirable, as this GC is one of the most metal-poor GCs of the Milky Way.

[1] http://montage.ipac.caltech.edu/

[2] http://www.sdss.org/dr6/algorithms/jeg_photometric_eq_dr1.html

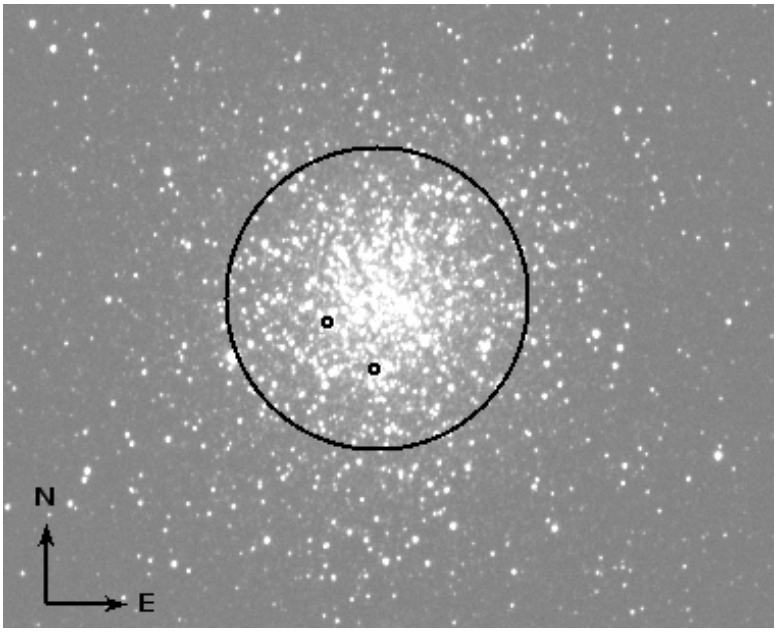

Figure 3.2: g'-band observation of NGC 5986. The half-light radius is indicated with the big circle, while the small circles indicate two stars that are likely non-members (contaminants) as selected from their position in the cluster colour-magnitude diagram.

3.3 Integrated Photometry of Globular Clusters

Galactic GCs are generally too large on the sky to be completely included within a single CCD frame (see Figure 3.2 for an example from our own data). Although we experimented with fitting King models to the surface brightness profiles of the GCs to measure total magnitudes (we discuss this in chapter 5), we ultimately chose to derive aperture magnitudes within the clusters' half-light radii (e.g., Peng et al. 2006) to determine integrated colours. As long as the clusters show no strong colour gradients in their outskirts, the integrated colours we present here should be suitable proxies for studies of extragalactic systems as well.

We measured the aperture magnitude within the half-light radius r_h obtained from Harris (1996) where the original values are drawn largely from Trager et al. (1993, 1995) and McLaughlin & van der Marel (2005). As the largest r_h is 5 arcminutes, it does not completely fill the CCD field-of-view and therefore enables us to determine magnitudes for all clusters in a homogeneous manner (as in Peng et al. 2006). To obtain a total magnitude for the clusters, we would need imaging reaching well beyond the tidal radius. However, the largest tidal radius for the Galactic GCs is 53.8 arcminutes, much bigger than our field-of-view. As long as colour gradients in the cluster outskirts are not very strong, the integrated colours determined within the 1/2 light radius aperture should be representative of the total colours. To illustrate this for a cluster with a tidal radius r_t which fits the CTIO 0.9m telescope field-of-view, we compared the $g' - z'$ colour based on r_h and r_t apertures for NGC 5694. After correcting for contaminants (as will

be described in Section 3.3.3) the colour difference between r_h and r_t apertures is 0.002 mag for this cluster, which is negligible compared to the magnitude uncertainties.

NGC 6287 and NGC 6553 are other clusters with a tidal radius small enough to be entirely covered by the CTIO field-of-view. However, NGC 6287 was not centred properly on the chip and was not entirely covered as a consequence . The observations of NGC 6553 included some saturated stars within the tidal radius, which is complicating the cleaning of the contaminants and impeding a proper comparison of the colours within the half-light and tidal radii.

Our first step will be to determine the cluster centres for the apertures, followed by estimation of the sky values, removal of contaminants (foreground stars) and measurement of the total flux within the 1/2 light radius. We then discuss extinction, photometric errors and compare our results with previous work and SDSS.

3.3.1 Cluster Centroids

Our first step is to determine an accurate cluster centroid for the apertures. For the CTIO data, we followed the method of Bellazzini (2007). We calculated the aperture fluxes in a grid of 25 points around the initial (visual) guess for the cluster centre: the size of the grid is 125 pixels or $60''$. The 'centre' position at which the aperture flux is maximal is adopted as the cluster centroid and used as the reference point for aperture photometry. This was performed separately for all frames, because of inconsistent coordinates in the headers. For the SDSS data, the coordinates listed in Harris (1996) were adopted together with the SDSS astrometric solution. The error in the photometry introduced by the uncertainty in the centre position is estimated in the following way (both for SDSS and CTIO data): magnitudes were computed for apertures centered at four grid points separated by 5% of the stated half-light radius; we calculated the magnitude difference between the aperture magnitudes centered on these positions and the 'true' centre we determined above. The median of this difference is used as the estimate of the uncertainty introduced by the centre determination and is summed in quadrature to the photometric and other errors to obtain the total magnitude error, assuming these errors are independent. The median contribution of the centre determination to the total magnitude uncertainty is 0.006 mag.

To provide a consistency check, we have compared the centroids in the g'-band to the more accurate central coordinates for each cluster as determined by Goldsbury et al. (2010) with HST/ACS data. The median difference between both centre determinations is 0.086 r_h. Using $8.6\% r_h$ instead of $5\% r_h$ to determine the magnitude uncertainty due to the centre determination results in a median additional error of 0.004 mag, which is negligible when compared to the systematic error introduced in Section 3.3.6.

3.3.2 Sky values

Determination of the sky value proved challenging, as several clusters fill the 0.9m CCD and in most cases the images do not cover the clusters out to their tidal radius. We used MMM (Mean, Median, Mode), a routine available at the IDL astronomy library which was developed to estimate the sky background in a crowded field and was adapted from the DAOPHOT routine with the same name. The algorithm consists of several steps: it first computes the mean and standard deviation of the sky flux, which is used to eliminate outliers. MMM repeats the first step in up to 30 iterations recomputing the sky (eliminating outliers of the previous iteration). As a next step, MMM estimates the amount of stellar contamination by comparing the mean, mode and median of the remaining sky pixels. If the mean is less than the mode and the median, then the contamination is slight and the sky is estimated by the mean. If the mean is larger, indicating severe contamination (as the program assumes positive departures from the true sky value in crowded fields), then the true sky value is estimated by $3 \times \text{median} - 2 \times \text{mean}$. We applied the MMM method to the four corners of each frame in a 100 by 100 pixel area, summing up about 40000 pixels (as some pixels will be identified as outliers by MMM and will not contribute to the sky determination). We regard these regions are the best approximation for the sky value.

The SDSS pipeline processing the data includes the sky subtraction, hence the sky value for these frames is always about zero. For consistency, we did determine the sky value running MMM on the entire mosaic.

Photometric uncertainties introduced when determining the sky level are further discussed in Section 3.3.6.

3.3.3 Removing foreground stars

Contamination from foreground bulge or disk stars can be severe at low Galactic latitudes and a number of methods have been proposed to tackle this issue. In their study on the integrated 2MASS photometry of Galactic GCs, Cohen et al. (2007) considered stars brighter than the tip of the RGB by 1.5 mag as non-members and excluded them. However, it is difficult to use this approach close to the cluster centre (at least from the ground) because of crowding and the low spatial resolution of their (and our) data. Peng et al. (2006), for example, disregarded this correction.

Contaminating stars can be excluded in two ways: from their abnormal position in the cluster colour-magnitude diagram, which implies they are unlikely to be cluster members (e.g., if they lie well outside the cluster principal sequences), or from their measured proper motions, as cluster stars are unlikely to show detectable motions because of their great distances.

Although our data suffer from crowding, average seeing and poor spatial resolution, we were able to derive colour-magnitude diagrams to identify likely foreground stars and clean the aper-

ture magnitudes. We carried out stellar photometry with DAOPHOT and ALLSTAR (Stetson 1987, 1994). As a first step, up to 50 isolated and bright stars were selected to model a point spread function (PSF), accounting for variation over the field by allowing quadratic variability. We used a PSF radius depending on the seeing: generally we used $4\times$FWHM but adopted a maximum of 15 pixels when the seeing was bad or the focus was mediocre. This aperture is large enough to remove the bulk of the contaminating star light but small enough to enable DAOPHOT to resolve the stars. DAOMATCH and DAOMASTER were used to crossmatch the different filters.

As a consequence of the low resolution of our data ($0.396''$ pixels and a seeing between $1''$ and $\sim 2''$), crowding does obviously affect the final CMDs, which are not complete, especially close to the centre. However, these cover large fields, extending well beyond the half-light radius where crowding is not as important. A detailed analysis of these colour-magnitude diagrams will be presented in chapter 6.

As an example, Fig. 3.3 shows the CMD for NGC 5986: open circles represent stars within the half-light radius, dots are stars from the entire field. This GC is located at a Galactic latitude of $b = 13.27^{\circ}$, so some contamination from the disk may be expected, and is visible as a blue plume of stars above the turnoff. As mentioned above we use the half-light radius to measure the aperture magnitudes of the cluster, so stars in this area (represented as open circles) that lie outside of the principal sequences are possible contaminants. For confirmation, we checked the bright outliers, indicated by red circles in Fig. 3.3, for proper motions in the USNO-B1.0 catalog (Monet et al. 2003) and the NOMAD catalog (Zacharias et al. 2005), although in many cases these are not fully conclusive (e.g., see McDonald et al. 2013 for a similar approach to the bright AGB stars in NGC 4372). Once we are convinced that the star is a true non-member, the star is cleaned from the cluster photometry by subtracting its flux, based on the DAOPHOT PSF magnitudes, from the flux in the cluster aperture. Removing these stars in NGC 5986 results in magnitude corrections of 0.06 (0.03, 0.02, 0.02) in g' (r', i', z', respectively). It is interesting to note that the contaminating stars in NGC 5986 would not have been removed if we had followed Cohen et al. (2007) as they are fainter than the RGB tip.

The magnitude corrections for foreground contamination may sometimes be very large, especially in poor clusters: for Pal 10 these corrections are 1.33 (0.62, 0.39, 0.33) mag. in g' (r', i', z'). This yields a ~ 1 mag correction for contamination in $g' - z'$.

A caveat is that differential reddening may shift foreground stars into the cluster principal sequences: this can be significant for clusters at low galactic latitude, where extinction may be patchy (Alonso-García et al. 2012). While we discuss reddening related issues extensively in our study on the colour-metallicity relation, specifically as these affect the colour-magnitude relation, we believe that a few such outliers will not significantly affect the derived colours.

For the CTIO data, an extract of the magnitudes and the applied contamination corrections

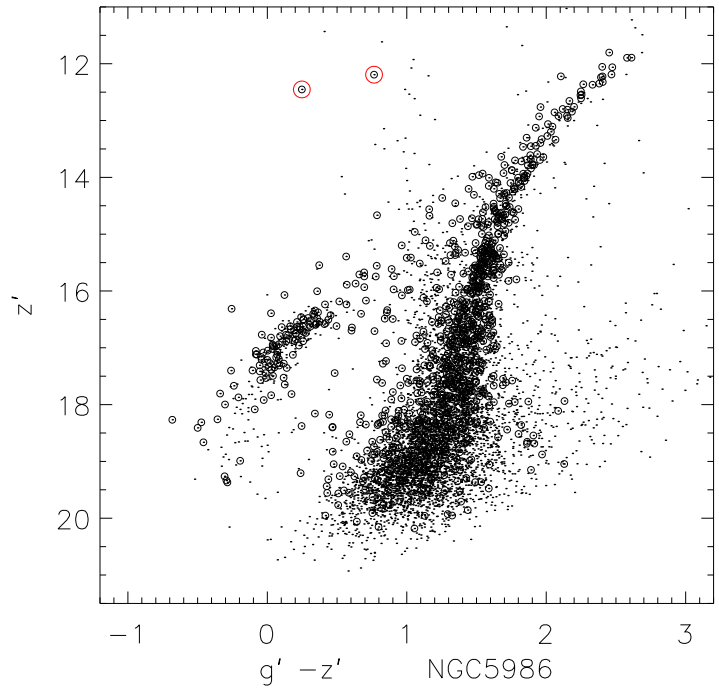

Figure 3.3: NGC 5986: open circles are stars within r_h, dots are stars from the entire field. The two bright isolated stars in the CMD (indicated with red circles) are selected as candidate outliers and were checked for proper motions. See text for more details.

(denoted as CMD$_{g',r',i',z'}$) is listed in Table 3.2. The complete table is available in the electronic version of Vanderbeke et al. (2014a) or on the G2C2 website[3]. Magnitudes and contamination corrections for the SDSS data are given in Table 3.3.

[3] www.G2C2.ugent.be

Table 3.2: Extract of the GC $g'r'i'z'$ magnitudes and errors based on CTIO observations. $\mathrm{CMD}_{g',r',i',z'}$ presents the magnitude corrections based on the CMDs. The complete table is available in the online version of Vanderbeke et al. 2014a or on the G2C2 website.

ID	g'	$\sigma_{g'}$	r'	$\sigma_{r'}$	i'	$\sigma_{i'}$	z'	$\sigma_{z'}$	$\mathrm{CMD}_{g'}$	$\mathrm{CMD}_{r'}$	$\mathrm{CMD}_{i'}$	$\mathrm{CMD}_{z'}$
NGC104	4.912	0.030	...	...	...	...	3.677	0.044	0.00	...	...	0.00
NGC288	9.080	0.032	8.600	0.045	8.295	0.044	8.139	0.044	0.00	0.00	0.00	0.00
NGC362	7.471	0.030	6.925	0.043	6.618	0.043	6.419	0.043	0.01	0.02	0.02	0.03
NGC1261	9.474	0.031	8.995	0.045	8.744	0.045	8.582	0.045	0.03	0.05	0.06	0.06
AM1	15.958	0.035	15.582	0.046	15.219	0.047	15.159	0.056	0.07	0.13	0.14	0.16
NGC1851	8.280	0.031	7.703	0.044	7.413	0.044	7.194	0.044	0.03	0.04	0.05	0.05
NGC1904	9.006	0.030	8.570	0.044	8.351	0.044	8.178	0.044	0.02	0.04	0.05	0.05
NGC2298	9.650	0.039	9.287	0.050	9.036	0.052	8.865	0.054	0.06	0.10	0.10	0.10
NGC2808	6.695	0.030	6.194	0.044	5.916	0.044	5.725	0.044	0.00	0.00	0.00	0.00

Table 3.3: GC *griz* magnitudes and errors based on data from SDSS (Data Release 9). $\mathrm{CMD}_{g,r,i,z}$ presents the magnitude corrections based on the CMDs.

ID	g	σ_g	r	σ_r	i	σ_i	z	σ_z	CMD_g	CMD_r	CMD_i	CMD_z
Whiting1	16.637	0.083	16.162	0.069	15.953	0.060	15.854	0.060	0.00	0.00	0.00	0.00
Pal1	15.118	0.042	14.769	0.033	14.615	0.030	14.522	0.032	0.46	0.62	0.67	0.69
NGC2419	11.198	0.009	10.727	0.009	10.473	0.009	10.371	0.010	0.01	0.01	0.01	0.01
Pal3	15.389	0.046	14.824	0.036	14.585	0.033	14.304	0.043	0.01	0.03	0.04	0.04
Pal4	15.284	0.052	14.636	0.058	14.293	0.083	14.074	0.107	0.00	0.00	0.00	0.00
NGC4147	11.185	0.010	10.823	0.008	10.670	0.007	10.443	0.005	0.00	0.00	0.00	0.00
NGC5024	8.518	0.003	8.122	0.004	7.991	0.003	7.676	0.003	0.00	0.00	0.00	0.00
NGC5053	10.734	0.012	10.379	0.008	10.164	0.007	10.062	0.005	0.00	0.00	0.00	0.00
NGC5272	7.071	0.002	6.712	0.002	6.555	0.001	6.135	0.002	0.00	0.00	0.00	0.00
NGC5466	10.180	0.013	9.725	0.011	9.466	0.009	9.413	0.009	0.00	0.00	0.00	0.00
Pal5	12.383	0.069	11.941	0.067	11.800	0.056	11.483	0.136	0.07	0.10	0.14	0.14
Pal14	14.654	0.028	13.937	0.047	13.689	0.044	13.641	0.052	1.02	0.58	0.79	0.81
NGC6205	6.903	0.005	6.667	0.003	6.397	0.004	6.076	0.002	0.00	0.00	0.00	0.00
NGC6229	10.419	0.007	9.876	0.005	9.751	0.005	9.489	0.004	0.00	0.00	0.00	0.00
Pal15	13.618	0.032	13.072	0.043	12.769	0.060	12.527	0.057	0.19	0.16	0.14	0.12
NGC6535	10.274	0.030	9.901	0.029	9.773	0.033	9.470	0.040	0.11	0.08	0.06	0.06
NGC6934	9.446	0.003	9.059	0.003	8.858	0.003	8.576	0.003	0.00	0.00	0.00	0.00
NGC7006	11.320	0.012	10.817	0.012	10.554	0.012	10.436	0.012	0.02	0.02	0.02	0.02
NGC7078	7.230	0.006	6.876	0.004	6.802	0.004	6.289	0.008	0.00	0.00	0.00	0.00
NGC7089	7.298	0.003	6.854	0.004	6.758	0.004	6.407	0.002	0.00	0.00	0.00	0.00
Pal13	15.736	0.060	15.392	0.050	15.270	0.048	15.147	0.049	0.00	0.00	0.00	0.00

3.3.4 Comparing different nights

Because the Galactic bulge and hence the bulk of the Galactic GCs are best observable during the Chilean winter, cirrus and bad weather were a real issue during the observing runs: many nights were totally lost due to clouds or strong winds, while other nights were disturbed by cirrus and were not photometric.

To determine the photometric nights, we compared magnitudes of the clusters observed during different nights and checked the log-sheets of the observations for additional indications. Mutual comparison of magnitudes showed that 4 nights (May 10 2003, June 5 and 6 2004, September 26 2005) could be considered (largely) photometric. During these nights, we collected g' and z' observations for 80 GCs, about half of these clusters we also observed using r' and i' filters.

The comparison process is illustrated in Fig. 3.4. In this figure, magnitude differences for observations performed on February 14 2005 are compared with the reference nights. On perfectly photometric nights, there should be no magnitude difference. At this point, accounting for possible systematics and errors induced by the centre determination, we assume that the magnitude differences for bright clusters during photometric nights are not larger than 0.05 mag (indicated as dashed lines in the figure). For this comparison, g' and z' filters are used, because the overlap between the different nights is largest for these filters. More than 20% of the g'-band magnitudes obtained on February 14 2005 have differences larger 0.05 mag, almost 50% of the z'-band magnitude differences are not within this limits. This night was clearly not photometric.

As a reference, we compare in Fig. 3.5 the magnitudes obtained on May 10 2003, which is one of the reference nights, with the other reference nights. Note that there are no overlapping clusters with the September 26 2005 observations. As can be seen in this figure, not all magnitude differences are within 0.05 mag: in the g'-band, 11% of the clusters are outliers, in the z'-band 14%. This illustrates well that entire nights being perfectly photometric are very scarce, and, that one has to be cautious handling magnitudes obtained on a single night. However, if a cluster has the same magnitude on several nights, one can be positive that the observations were taken under perfect conditions.

By taking the median magnitude of clusters observed on multiple nights, one can restrict the effect of spurious observations. NGC 6426 is the strong g'-band outlier in Fig. 3.5. This cluster was observed on three out of four reference nights, and, the magnitude difference between the observations performed on June 5 and 6 2004 was only 0.03 mag. Hence, when taking the median magnitude over the different nights, the non-photometric observation on May 10 2003 will not affect the final catalogue magnitude.

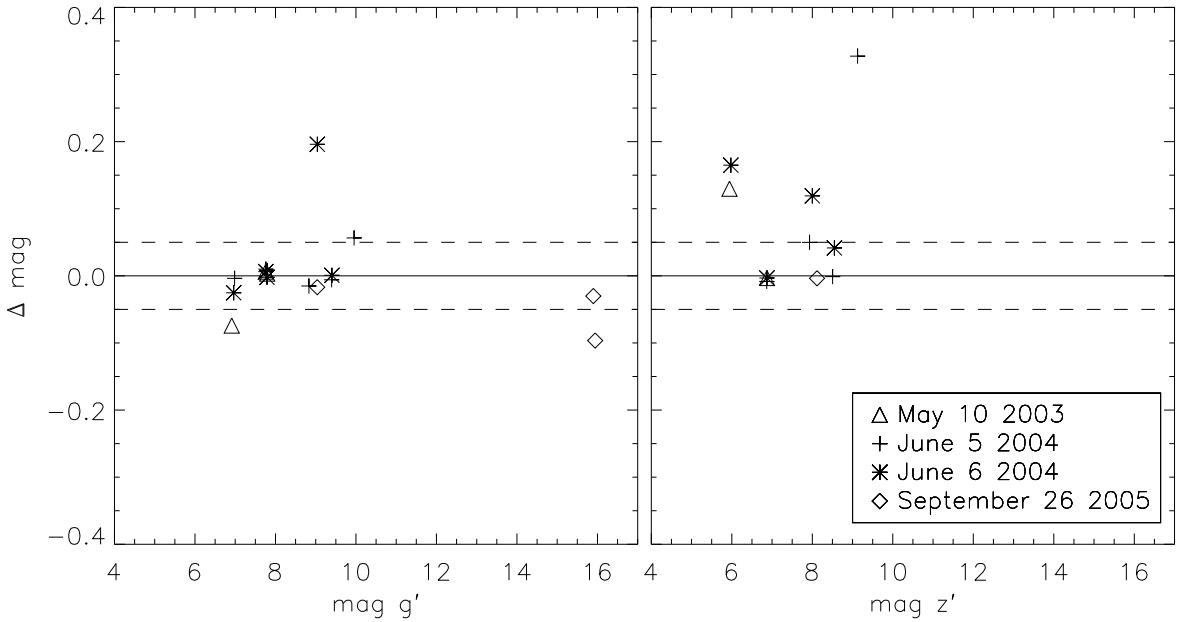

Figure 3.4: Comparison of g' and z' magnitudes obtained on February 14 2005 with the reference nights (indicated in the legend), which are considered photometric. The dashed lines indicate a magnitude difference of 0.05 mag. See text for more details.

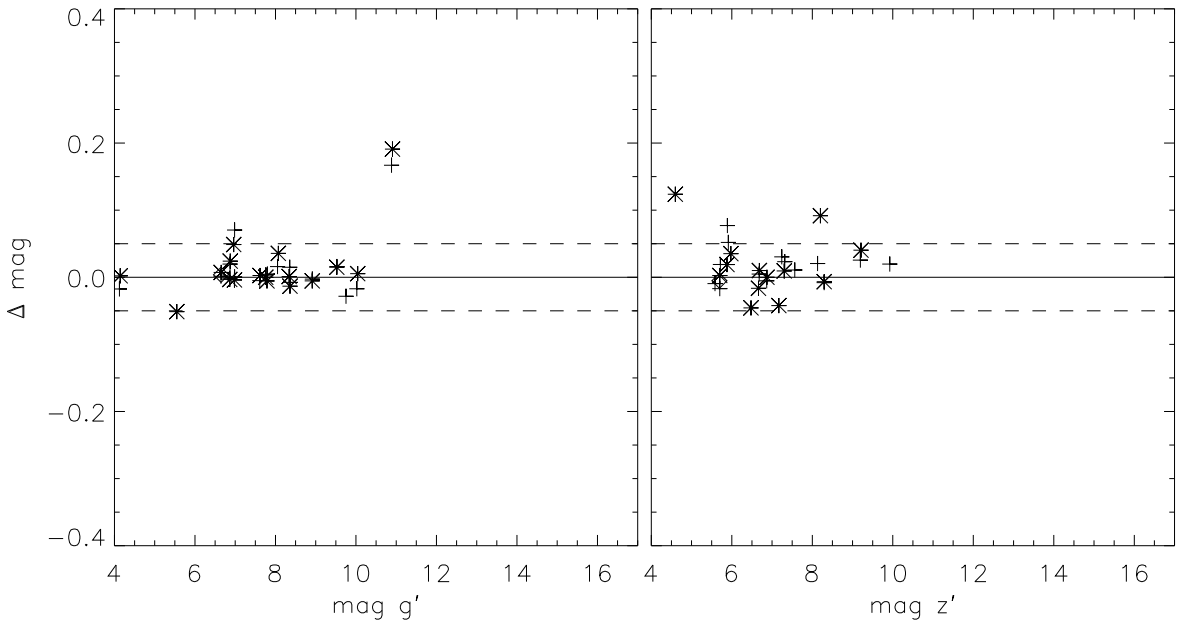

Figure 3.5: Comparison of g' and z' magnitudes obtained on May 10 2003 with the reference nights. Legend as in Fig. 3.4. See text for more details.

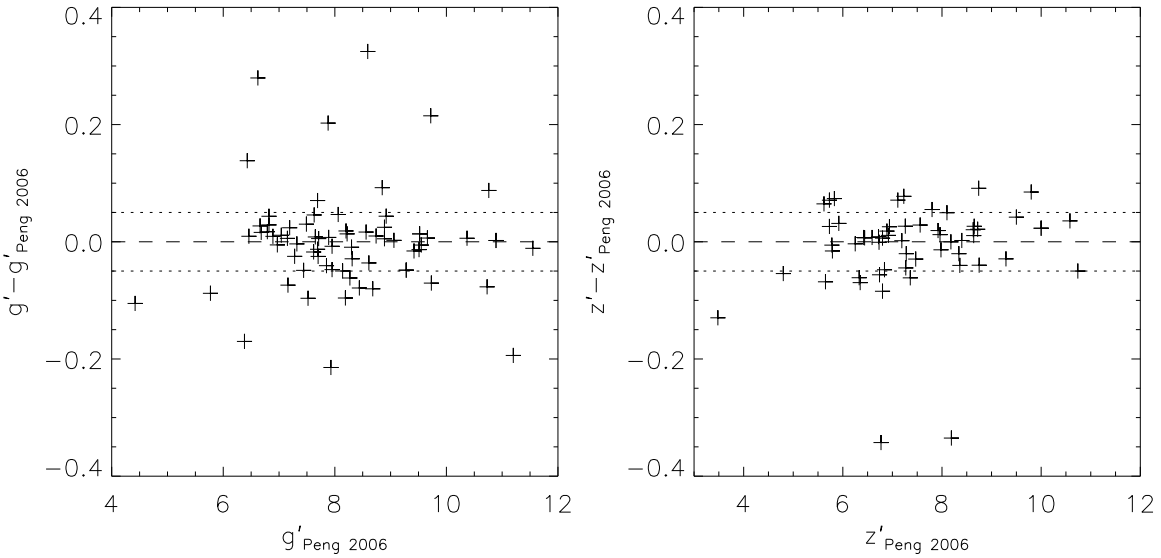

Figure 3.6: Comparison of the g' and z' magnitudes with the literature magnitudes (Peng et al. 2006).

3.3.5 Comparison with previous work

To test the reliability of our approach we compare our g' and z' magnitudes with Peng et al. (2006), which also uses the half-light radius. Moreover, their Galactic GC data was based on the observations performed on 2004 June 5 and 6, so there is a considerable overlap with our sample. We match our apertures to theirs (some measurements of structural parameters have since changed) and we use the $E(B-V)$ values from Harris (1996) which were used by Peng et al. (2006) and a Cardelli et al. (1989) reddening law instead of the reddening values from Schlafly & Finkbeiner (2011), for the sake of consistency in these comparisons. These are shown in Fig. 3.6: while there is no systematic offset, there are a couple of outliers, for which the magnitude difference with the earlier results (Peng et al. 2006) is larger than expected. It is unclear what the origin of the discrepancy is. In the next section, we discuss the origin of the photometric errors in more detail. It will become clear that the sky determination can strongly affect the final magnitudes, which we raise as possible cause for the variance when comparing to Peng et al. (2006). At least for NGC5927 the observing log of the original Peng et al. (2006) hints at clouds or cirrus and this may be another possible reason for the difference. The RMS scatter of our photometry, compared with Peng et al. (2006), is 0.08 (0.07, 0.09) for g' ($z', g'-z'$).

3.3.6 Photometric errors

Except for some poor clusters, the integrated magnitudes over the half-light radius have small random errors. The main contributions to the photometric error budget come from uncertainties in the photometric calibration and the centre determination (discussed above). For several clus-

ters we have g' and z' data available from consecutive short and long exposures or from observations obtained during different nights. In this case the median magnitude of all observations is taken as the final magnitude in Table 3.2. In Fig. 3.7 we compare the magnitude differences between different observations (both performed on different nights or subsequent observations performed during the same night). The magnitudes in general compare well. However, there are some exceptions which will be treated later in this section.

First, we introduce some parameters that will be used to describe the details of these clusters. The standard way adopted in this study to estimate the sky level was described in Section 3.3.2. We now refer to this sky determination as method A. To test the influence of the sky determination on the cluster magnitude, we estimate the sky contribution using a sky band, centred in the cluster centre, with an inner radius of 900 pixels and a width of 100 pixels. We refer to the latter as method B. The resulting magnitude difference between method A and method B is denoted as Δ^*_{AB} (with '*' indicating the filter). Tests on SDSS data did not result in significantly different sky estimates using methods A and B.

Another parameter used in the remainder of this section is $R_{GC/Sky,*}$, which is the ratio of the sky-subtracted cluster flux to the sky flux (both measured within a half-light radius). Hence, when $R_{GC/Sky,*} = 1$, the sky contribution is as strong as the cluster contribution to the flux within r_h. $R_{GC/Sky,*} < 1$ when the sky contribution is higher than the pure (sky-subtracted) cluster contribution.

E 3 is a faint old cluster (12.8 Gyr, Marín-Franch et al. 2009) that may have been truncated by tidal forces (van den Bergh et al. 1980). Observations of 60 s were performed on both June 5 2004 and September 26 2005, with magnitude differences between both nights of 0.17 mag in g' and 0.02 mag in z'. It is suspicious that the magnitudes compare well for the z' filter, while they do not for the g' filter. In the latter filter, the average cluster surface brightness within a half-light radius is much lower than the brightness of the sky. Moreover, for the observations performed on June 5 2004, $R_{GC/Sky,g} = 0.18$, while on September 26 2005 $R_{GC/Sky,g} = 0.07$. This is a first indication the magnitude difference could be attributable to the sky uncertainty. Using method B (with the sky radius) instead of method A (with the four corners) results in an absolute g' magnitude difference $|\Delta^{g'}_{AB}| \sim 0.1$ mag, while the magnitude uncertainty is about 0.01 mag. This shows that the contribution of the sky uncertainty to the magnitude uncertainty is underestimated. Remark that the magnitude resulting using method B instead of method A was 0.1 mag brighter for the June 5 2004 observation ($\Delta^{g'}_{AB} \sim 0.1$ mag), while it was 0.1 mag fainter for the September 26 2005 observation ($\Delta^{g'}_{AB} \sim -0.1$ mag). For the z' filter, $R_{GC/Sky,z}$ is about 0.02 for both nights. The z' magnitudes are differing for both nights by $\Delta^{z'}_{AB} \sim -0.1$ mag when using a sky band instead of the 4 corner approach. Peng et al. (2006) did not include E 3 in their analysis because of the significant reddening ($E(B-V) \sim 0.3$, Harris 1996).

NGC6426, a high-reddening cluster with $E(B-V) \sim 0.36$, was observed on May 10, 2003

and on June 5 and 6, 2004. The g'-band magnitudes show significant variations between the nights: magnitudes obtained on May 10, 2003 were about 0.1 mag brighter than for the observations performed in June 2004. Taking the median of the observations performed on the different nights resulted in a g' magnitude consistent with all the June 2004 observations. The resulting z' magnitudes are all within 0.04 mag. Again, we want to pinpoint the influence of the sky determination on the magnitude discrepancies. The ratio $R_{GC/Sky,g}$ is about 0.6 for the observations performed on May 10 2003, while it is about 0.05 for the June 5 and 6 2004 observations. $\Delta_{AB}^{g'} \lesssim 0.02$ mag for the May 10 2003 observations, while these differences are as high as 0.34 mag (0.24 mag) for the June 5 (6, respectively) 2004 observations. For the 75 s and 410 s z' observations taken on May 10 2003, the ratio $R_{GC/Sky,z} \sim 0.1$, with $\Delta_{AB}^{z'} < 0.03$. For the 60 s observation performed on June 5 2004, $R_{GC/Sky,z} \sim 0.14$ and $\Delta_{AB}^{z'} \sim 0.24$, while for the 410 s observation taken on June 6 2004, $R_{GC/Sky,z} \sim 0.08$ and $\Delta_{AB}^{z'} \sim 0.15$. However, pure Poisson magnitude errors are smaller than 0.01. It is clear that some of the variation over the different nights can be attributed to the sky determination for this cluster.

Pal 3 is a low-reddening cluster ($E(B-V) \sim 0.04$) and was observed on June 5 and 6 2004. The magnitude difference in g' was about 0.19 mag (and 0.01 mag in z'). A bright star on the edge of the aperture complicates the determination of the magnitude. $R_{GC/Sky,g}$ amounts about 0.05 on both nights, while $R_{GC/Sky,z}$ varies between 0.002 and 0.02, so again the cluster is much fainter than the sky level. Using a sky band with MMM to estimate the sky value, results in g' (z') magnitude differences up to $\Delta_{AB}^{g'} \sim 1$ mag ($\Delta_{AB}^{z'} \sim 3.4$ mag, respectively). The sky values obtained with MMM in the corners (as described in Section 3.3.2) and the sky band are consistent within the large uncertainties. However, the photometric magnitude uncertainties given by the routine are large (up to $\sigma_{z'} \sim 0.23$), but not as large as the differences invoked by different sky estimation methods.

NGC 6584 was observed on May 10 2003 and June 5 2004. While g' magnitudes compare well for both nights, z' magnitudes show larger differences. For the z' observations performed on June 5, $R_{GC/Sky,z}$ is 0.86, while for the observations taken on May 10 it amounts to 0.60. $\Delta_{AB}^{z'} \sim 0.04$ mag for the June 2004 observation, while $\Delta_{AB}^{z'} \sim -0.02$ mag for the May 2003 observation. For this cluster, the sky determination seems not to be responsible for the magnitude offset. As a reference, we give some details on the g' observations as well. For the 37 s and 270 s observations performed on May 10 2003, $R_{GC/Sky,g} \sim 6$ and $\Delta_{AB}^{g'} < 0.01$ mag. For the observation obtained on June 5 2004, $R_{GC/Sky,g} \sim 0.53$ and the magnitude difference (using a sky band instead of the corners) is about $\Delta_{AB}^{g'} \sim 0.03$ mag.

Another cluster with a large difference between different observations is Terzan 7. This faint cluster was only observed on May 10 2003, but consecutive z'-band 79 s and 410 s observations showed magnitude variations about 0.1 mag. Because it is unlikely that, during a night that is considered photometric, the observing conditions change drastically in a ten minute timespan,

Table 3.4: Median magnitude differences of clusters in common on different nights. Observations on September 26, 2005 had only few observations in common with other nights.

Δ Nights	g'	z'
5/10/03 − 6/5/04	−0.004	0.015
5/10/03 − 6/6/04	−0.008	0.007
6/5/04 − 6/6/04	−0.002	−0.002
6/5/04 − 9/26/05	−0.004	0.001

this magnitude difference is surprising and deserves some special attention. This cluster, at a Galactic latitude of $b \sim -20°$, is associated with the Sagittarius stream, hence located in a crowded field. This obviously complicates the sky determination: there is a difference of 0.7% between both sky determinations. However, as the surface brightness of the cluster is much lower than the sky level ($R_{GC/Sky,z} \sim 0.06$), this sky level difference results in a magnitude difference as stated above. This example again stresses the difficulty and importance of obtaining a reliable sky value. Nevertheless, the resulting magnitude errors are lower than 0.01 mag, hence the magnitude uncertainty is underestimated for this cluster. $|\Delta^{z'}_{AB}| \lesssim 0.01$ for both observations.

NGC 6121 is a bright high-reddening ($E(B-V) \sim 0.35$) cluster showing a z' magnitude difference of ~ 0.1 mag between the short 1 s exposure obtained on May 10 2003 ($z' \sim 4.37$) and the 11 s exposure performed on June 6 2004 ($z' \sim 4.47$). This cluster is located in a very crowded field ($l \sim 351°, b \sim 16°$), with a vast number of stars saturating the 60 s exposures. Nevertheless, for the short exposures, only few counts are collected to determine a reliable sky value. In the case of the 1 s exposure, the sky uncertainty obtained by MMM was larger than the sky value itself, with $R_{GC/Sky,z} \sim 1.2$ and $\Delta^{z'}_{AB} \sim -0.07$ mag, while for the 11 s exposure, $R_{GC/Sky,z} \sim 1.2$ and $\Delta^{z'}_{AB} \lesssim 0.01$ mag. On May 10 2003, the short 1 s exposure was followed by a long 410 s exposure, which could obviously not be used to determine the aperture magnitude of the cluster because of saturation issues. However, when using the long exposure to determine a more reliable sky value and then applying this sky value to the 1 s exposure, we obtain a magnitude 0.05 mag fainter than the value obtained above. Note that this value is fully consistent with the median value of the magnitudes obtained on both May 10 2003 and June 6 2004.

The scatter in Fig. 3.7 is larger than we would expect given the known error budget (photometric, centroiding, etc). We add a systematic contribution of 0.03 mag for g' and 0.0435 mag for z'), for the remainder of this analysis, to reduce the derived χ^2 to 1 and account for the additional photometric uncertainty. We cannot estimate this error for the other bands and we therefore adopt the z' error.

To demonstrate this error is not caused by a systematic photometric shift of certain nights, we

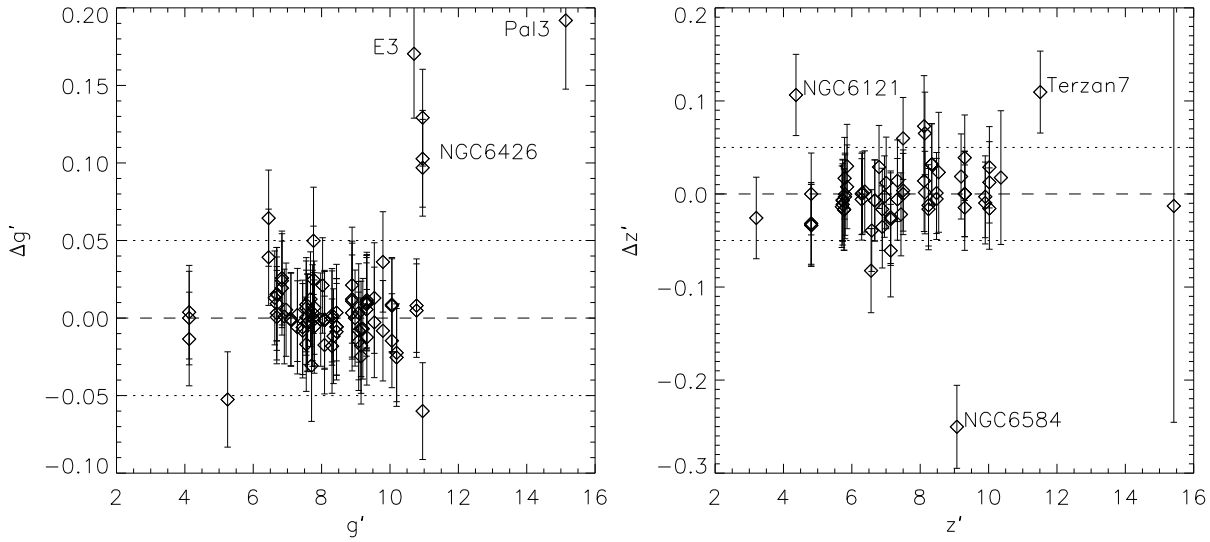

Figure 3.7: Comparison of g' and z' magnitudes, based on observations performed on different nights or performed subsequently during the same night). Error bars are including the systematic error.

present in Table 3.4 the median differences for clusters in common for the given nights.

3.3.7 Comparing CTIO and SDSS DR9

The CTIO and SDSS subsamples have 6 clusters in common for the g- and z-band and 4 GCs for r- and i-band. In Fig. 3.8 we compare the different magnitudes for the different filters. The included error bars are the combined errors of both magnitudes. The RMS for the magnitude difference between CTIO and SDSS data is 0.10, 0.18, 0.21 and 0.53 mag. for the g, r, i and z band respectively. NGC 7078 and NGC 7089 are the outliers in the i-band, Pal 3 and Pal 13 are the two z-band outliers. These objects contribute most to the high scatter.

Pal 3 has uncertain CTIO photometry, as was discussed in Section 3.3.6. It should be noted that the CTIO g' magnitude, based on the observations performed on June 6 2004, is consistent with the SDSS magnitude (within the large photometric uncertainty for this faint cluster). However, z' magnitudes based on CTIO observations on both June 5 and 6 2004 do not compare well with the SDSS magnitude for this filter. The issues regarding the sky determination for CTIO observations of this cluster were discussed in Section 3.3.6.

Pal 13 was only observed on September 26 2005 and has one of the highest specific frequencies of blue stragglers in any known GC (Clark et al. 2004). Based on the SDSS CMDs, one candidate outlier was identified. However, the star did not have proper motions, hence was not removed from the aperture photometry. This candidate outlier cannot explain the $g-z$ colour difference between SDSS and CTIO: removing the star would have resulted in a $g-z$ colour correction of -0.04. In Section 3.3.6 it became clear that a small variation in the CTIO sky determination can result in a large magnitude difference, especially for faint clusters which have a lower surface brightness than the sky itself. Motivated by the latter argument, we reinspected

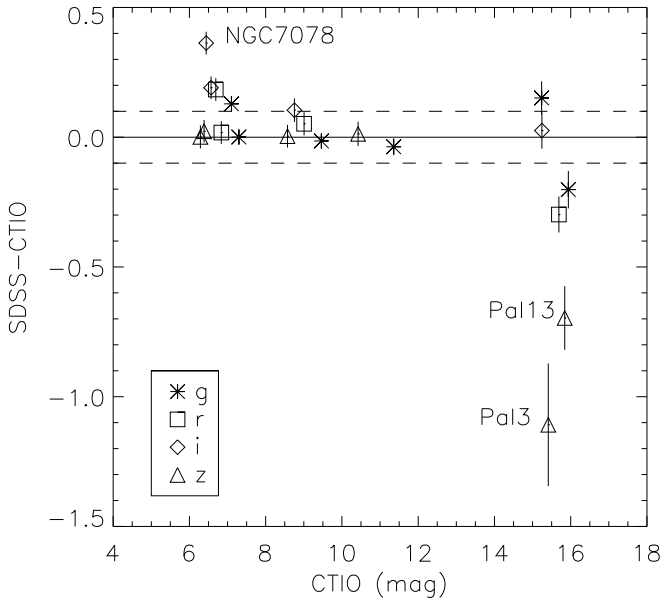

Figure 3.8: Comparison of magnitudes based on the CTIO observations and the SDSS DR9 survey. Error bars are the combined errors on both magnitudes.

the CTIO sky determination for Pal 13. The $R_{GC/Sky,g} \sim 0.12$, while $R_{GC/Sky,z} \sim 0.01$, so the cluster flux contribution is much smaller than the sky contribution within a half-light radius. Using MMM on a sky ring of 900 to 1000 pixels (referred to as method B in Section 3.3.6) instead of the four corner approach (method A) results in magnitude differences of $\Delta^{g'}_{AB} \lesssim 0.003$ mag, while these rise to $\Delta^{z'}_{AB} \sim 0.35$ mag in the z' band. The large photometric uncertainties are reflected in the magnitude errors, though these are smaller than the difference invoked by using the different sky estimation methods.

Fig. 3.9 presents CMDs for NGC 6934 based on CTIO and SDSS data. It is clear that the RGB in the SDSS CMD suffers from saturation (it is known SDSS saturation starts at $r \sim 14$). Moreover, more blue stragglers are found in the CTIO CMD and the blue HB is more extended than in the SDSS CMD. Further analysis of the CMDs will be presented in a subsequent chapter. Nevertheless, when comparing the integrated magnitudes of NGC 6934, the agreement is excellent in grz while in the i-band magnitudes show a larger difference.

The SDSS data for NGC 7078 is also saturated for the RGB stars. Only for the z-band the difference between SDSS and CTIO data is smaller than 0.01 mag, for the other filters the differences are much larger. We observed this cluster with the CTIO 0.9m telescope on 3 different nights in the g' and z' filters. These 3 observations deviate less than 0.01 mag from each other in both filters. The cluster was also observed with the r' and i' filters but only for one night.

For the future work, we use the CTIO-based magnitudes whenever GCs have magnitudes from both subsamples, except for Pal 3 and Pal 13, which are low-reddening clusters with very exceptional CTIO colours ($g' - z' \sim 0$), compared to $g' - z'$ colours of the other low-reddening clusters ranging between 0.4 and 1.4. We suspect issues with the sky determination for the

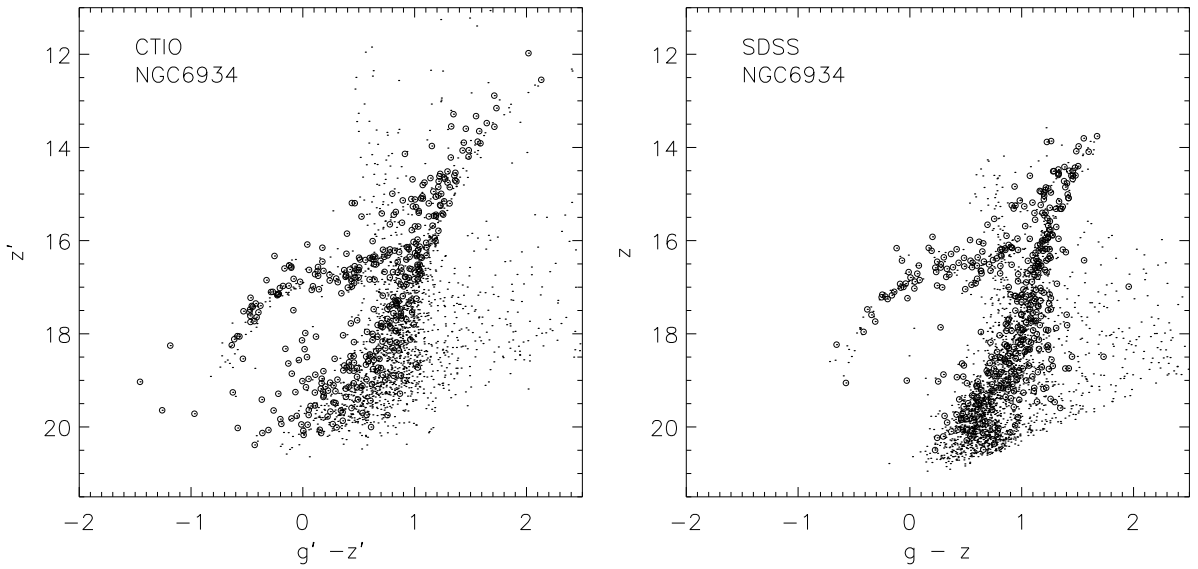

Figure 3.9: CMDs for NGC 6934 based on CTIO and SDSS data, using open circles for stars within r_h, dots for stars from the entire field. It is clear that saturation issues in the SDSS data sweep out the tip of the RGB. See text for more details.

CTIO data are causing the offsets with the SDSS data for these faint clusters.

3.4 Summary

In the current chapter we presented integrated photometry for 96 Galactic GCs. We discuss a variety of issues, such as dealing with incomplete imaging (CCD cameras do not image the whole cluster), sky removal, calibration, the cleaning of contamination based on CMDs and proper motions and systematic errors. We obtained g' and z' magnitudes for about two-thirds of the Galactic GC system, making this the largest homogeneous optical sample based on the SDSS filter system. For about half of these clusters, we also present r' and i' photometry.

In the next chapter, we will use the obtained colours to improve the relations between colour and metallicity.

Integrated colour-metallicity relations for Galactic Globular Clusters in SDSS passbands

4

The results described in this chapter are based on Vanderbeke et al. (2014b).

4.1 Introduction

Globular clusters (hereafter GCs) form during the earliest stages of galaxy formation. In nearly all galaxies that have been studied, GCs follow a nearly universal luminosity function (e.g., Rejkuba 2012), exhibit a bimodal colour distribution (e.g., Zepf & Ashman 1993; Ostrov et al. 1993; Whitmore et al. 1995; Mieske et al. 2006; Peng et al. 2006; Strader et al. 2006; Mieske et al. 2010; Faifer et al. 2011; Yoon et al. 2011b and references therein) and a strong correlation between the number of globular clusters and the luminosity of their parent galaxies (specific frequency –Harris & van den Bergh 1981). These all imply that the formation of globular clusters has been intimately related to the early assembly history of galaxies (Harris 1991). Therefore, the properties of globular clusters allow us to use them as fossil tracers of the initial stages of galaxy formation and evolution (see West et al. 2004 and Brodie & Strader 2006 for reviews).

Although most globular clusters show evidence of extended star formation and enrichment histories (see review by Gratton et al. 2012a), the vast majority are nevertheless almost homogeneous in iron (Marino et al. 2013) and have large ages (> 10 Gyr, Chaboyer et al. 1998; Strader et al. 2005; Puzia et al. 2005), making them still the best available approximation of single stellar populations. Their integrated colours are largely dominated by light from K-giants and this allows for a more straightforward interpretation (in terms of age, metallicity, etc.) than the more complex stellar populations of galaxies.

The bimodal distribution of GC colours corresponds, at least in our Galaxy, to a bimodal distribution of metallicities (e.g. Zinn 1985), with blue clusters being more metal poor than their red counterparts. Moreover, these two GC populations are also kinematically distinct (Sharples et al. 1998; Zepf et al. 2000; Côté et al. 2001, 2003; Peng et al. 2004; Strader et al. 2011; Pota et al. 2013). However, it is still uncertain whether the bimodal distributions of GC colours observed in more distant galaxies can be generalized into bimodal *metallicity* distributions (Cantiello & Blakeslee 2007; Galleti et al. 2009; Foster et al. 2010, 2011; Alves-Brito et al. 2011; Caldwell et al. 2011; Chies-Santos et al. 2011a,b; Usher et al. 2012). There is no colour that yields a univocal mapping to metallicity. Yoon et al. (2006) and Richtler (2006) showed that a non-linear relation between metallicity and integrated colour can transform a unimodal metallicity distribution into a bimodal colour distribution. Vice versa, Yoon et al. (2011a) demonstrated that the bimodal colour distributions could be transformed into metallicity distributions consisting of a sharp peak with a metal-poor tail, similar to the metallicity distribution functions of resolved field stars in nearby elliptical galaxies (e.g. Harris & Harris 2002).

Colour-metallicity relations (CMR), calibrated to objects of known metal abundance are essential to correctly interpret the colour distributions in external galaxies. The first empirical relationships between colour and [Fe/H] were approximately linear (Brodie & Huchra 1990;

Couture et al. 1990; Kissler-Patig et al. 1997, 1998), while more recent studies tend to prefer non-linear CMRs (Peng et al. 2006; Blakeslee et al. 2010; Sinnott et al. 2010; Usher et al. 2012). Faifer et al. (2011) find a linear CMR, but their sample was lacking in metal-poor GCs, which are the clusters invoking the non-linearity of the CMRs.

Some stellar population models also predict a non-linear CMR (Yoon et al. 2006, 2011a,b; Cantiello & Blakeslee 2007) and studies based on optical-NIR colours (Chies-Santos et al. 2012; Blakeslee et al. 2012) provide further evidence that the non-linearity of the CMR is unavoidable even in the presence of unimodal metallicity distributions. Moreover, the metallicity distributions seem usually less bimodal than the optical colour distributions, which suggests that at least part of the observed colour bimodality is caused by the nonlinearity of the CMR (Blakeslee et al. 2012). Although most of these studies agree on the non-linear form of the CMR, further data sets are indispensable to extend the metallicity range, to better calibrate the CMR and to capture its details.

In the previous chapter we have presented integrated photometry for 96 globular clusters in SDSS passbands g' and z', as well as r' and i' photometry for a subset of 56 clusters. Here we use these data to construct the Galactic colour-metallicity relation. We discuss the CMRs for the different colour combinations in Section 4.2 and study the influence of (differential) reddening, horizontal branch (HB) morphology, age, present-day mass function variations, structural parameters and contamination correction on the scatter in the CMR. In Section 4.3 we investigate the colour bimodality of our sample, and summarize the results in Section 4.4.

4.2 The colour-metallicity relation for Globular Clusters

We use the photometry described in detail in the previous chapter to refine the colour-metallicity relations for GCs. For some clusters, both SDSS and CTIO magnitudes were obtained. Motivated by the findings of the investigation of the GC photometry, we use CTIO magnitudes in all cases, except for Pal 3 and Pal 13. For Galactic clusters, metallicities are taken from the compilation of Harris (1996), using the latest version, and are based on the Carretta et al. (2009) scale supplemented with data from Armandroff & Zinn (1988). However, our Galaxy lacks the high metallicity (solar or more) GCs that are encountered in bright cluster ellipticals; following Peng et al. (2006) and Blakeslee et al. (2010) we will supplement our data with photometry (and metallicities) for globular clusters in M 49 and M 87, taken from the SDSS and the ACS Virgo Cluster Survey (Côté et al. 2004) in Section 4.2.3. There is also a lack of very metal-poor clusters in both the Galactic and extragalactic samples; some globular clusters in dwarf spheroidals appear to be more metal-poor than the most extreme such objects in our Galaxy.

In Fig. 4.1 we present [Fe/H] as a function of $g' - z'$ for 96 Galactic GCs. Red filled circles represent CTIO photometry, blue filled circles are used for clusters with SDSS data. The previ-

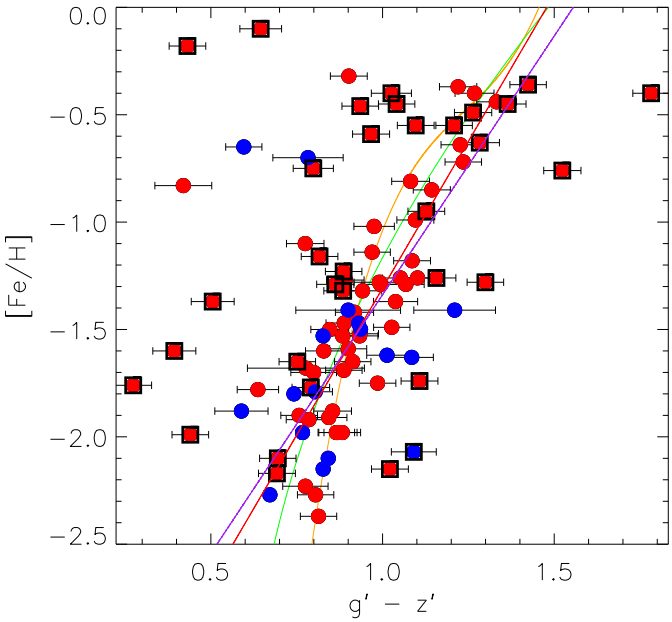

Figure 4.1: [Fe/H] as a function of $g' - z'$ for 96 Galactic GCs. Red circles represent clusters with CTIO data, blue circles are used for clusters with SDSS data. Clusters with $E(B-V) \geqslant 0.35$ are indicated with boxes and are excluded to make the fits. The purple line is a linear robust fit to all the data, while the red line is fitting only the CTIO data. As a reference, CMRs from the literature (Sinnott et al. 2010; Blakeslee et al. 2010) are also presented as green and grey lines (resp.). The four metal-rich low-reddening GCs that are offset the CMRs are E 3 and Terzan 7 (CTIO data) and Whiting 1 and Pal 1 (SDSS data). See text for more details.

ous CMRs from Blakeslee et al. (2010) and Sinnott et al. (2010) are shown as grey and green lines. For completeness, we show all clusters in Fig. 4.1, but only the clusters with extinction $E(B-V) < 0.35$ (Harris 1996) are used to fit the CMR.

We fit a straight line to the data using the method of least absolute deviation (robust fitting) as this is less sensitive to outliers (Armstrong & Tam Kung 1978). The best robust fit to the CTIO data only is given by:

$$[\text{Fe/H}] = (-4.04 \pm 0.04) + (2.74 \pm 0.04) \times (g' - z') \tag{4.1}$$

and is represented by a red line in the figure, while the best fit to both SDSS and CTIO data is given by:

$$[\text{Fe/H}] = (-3.75 \pm 0.04) + (2.41 \pm 0.05) \times (g' - z'), \tag{4.2}$$

which is the purple line in Fig. 4.1. The errors on the coefficients are computed by a bootstrap method. We note that the CMR of Blakeslee et al. (2010) seems to overestimate [Fe/H] for the relatively more metal-rich clusters, while our linear relations do not fit well the metal-poor end of the metallicity range. There is considerable scatter around the relation, more than would be expected simply from photometric errors. This appears to be related to foreground reddening

and is discussed in detail in Section 4.2.4.

SDSS data for low-reddening clusters show more scatter around the existing relations than the corresponding CTIO data. When computing the horizontal RMS for these two subsamples with respect to the CMR of Blakeslee et al. (2010), we find a RMS of 0.14 for the low-reddening CTIO subsample, but a RMS of 0.20 for the low-reddening SDSS subsample. This might be due to the saturation issues for SDSS data discussed in the previous chapter. On the metal-rich side, four low-reddening clusters are offset from the relation. These clusters are E 3 and Terzan 7 (CTIO data) and Whiting 1 and Pal 1 (SDSS data). In the chapter on the GC photometry we raised some sky determination issues which affect the obtained magnitudes of E 3 and Terzan 7. For the position in colour-metallicity space of these and other clusters, we refer to Fig. 4.5. These and other outliers are discussed in Section 4.2.1.

Due to the sizable scatter, the limited metallicity range and the low sample size, it is not justifiable to fit a higher-order polynomial to the Galactic data. The linear fit is a reasonable approximation for the Galactic data only, when considering the limitations of the sample. The fit however is not satisfactory, thus we will address this issue again in Section 4.2.3, where we will include extragalactic data from the literature to extend the metallicity range and the sample size.

Fig. 4.2 shows the CMR for the $g' - i'$ colour. As a reference, the CMRs published in Sinnott et al. (2010) and Usher et al. (2012) are presented as green and cyan lines. Sinnott et al. (2010) presented a $g' - i'$ CMR for clusters in NGC 5128, using Milky Way clusters to convert their [MgFe]$'$ index to [Fe/H], but their CMR has not been compared to $g' - i'$ colours for Galactic GCs. It is generally assumed that Galactic GCs are not intrinsically different from extragalactic GCs (e.g. Foster et al. 2010), although Usher et al. (2012) note that differences in the CMR could be driven by differences in the age or the IMF of GCs between galaxies. These possibilities will be further discussed in Sections 4.2.6 and 4.2.7.

Galactic GC colours based on CTIO data compare well to the extragalactic CMR of Sinnott et al. (2010). Only clusters suffering severe reddening are outliers. The two low-reddening metal-rich GCs based on SDSS data are Whiting 1 (associated to the Sagittarius system) and Pal 1. For E 3 and Terzan 7, discussed above, no i'-band observations were performed. Nevertheless, it is clear again that the low-reddening SDSS data has more scatter around the Sinnott et al. (2010) CMR than the low-reddening CTIO data. NGC 5272 and NGC 6205 are the low-reddening outliers at $[Fe/H] \sim -1.5$ with small photometric uncertainties. This reinforces the suspicion that the SDSS magnitudes of bright clusters are affected by saturation of their bright stars (as discussed in chapter 3).

The best robust fit for the CTIO data only is given by

$$[\mathrm{Fe/H}] = (-3.94 \pm 0.05) + (3.21 \pm 0.06) \times (g' - i'), \tag{4.3}$$

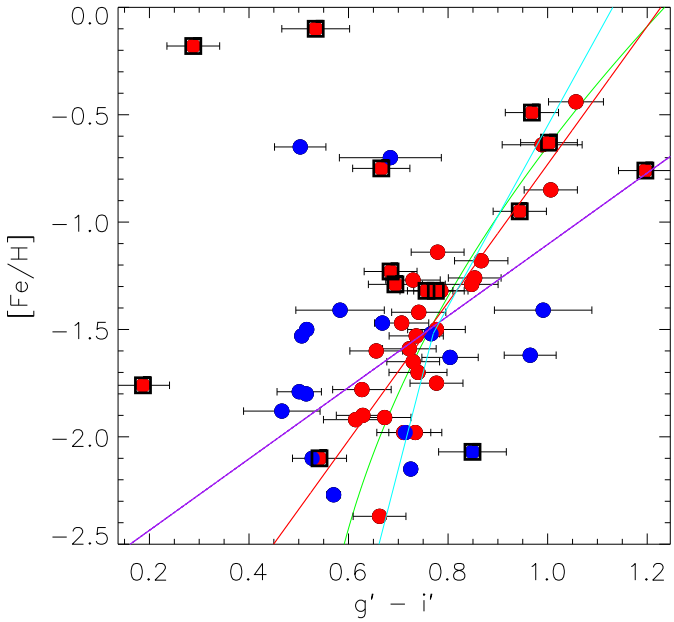

Figure 4.2: [Fe/H] as a function of $g' - i'$ for 56 Galactic GCs. Legend as in Fig. 4.1. The cyan line is another CMR from the literature (Usher et al. 2012). The two low-reddening metal-rich GCs based on SDSS data are Whiting 1 and Pal 1. The SDSS outliers at $[Fe/H] \sim -1.5$ with small photometric uncertainties are NGC 5272 and NGC 6205.

while including the SDSS data results in

$$[\mathrm{Fe/H}] = (-2.77 \pm 0.02) + (1.66 \pm 0.03) \times (g' - i'). \tag{4.4}$$

Errors on this relation were determined using a bootstrap method. It is clear that the relation based on CTIO data only compares well to the extragalactic relation published by Sinnott et al. (2010), while the scatter in the SDSS data results in an inconsistent fit when using all available data. The relative lack of metal-poor clusters makes it hard to constrain the metal-poor part of the CMR.

Usher et al. (2012) proposed a broken line fit as their [Z/H]-$(g - i)$ relation (their Eq. 10) and give a conversion between [Z/H] and [Fe/H] (their Eq. 1). Plotting this relation as a cyan line on Fig. 4.2 we find that their relation predicts slightly redder colours for metal-poor clusters than our observed $g' - i'$ colours. Nevertheless, our sample has only a couple of metal-poor objects with available $g' - i'$ colours.

Fig. 4.3 presents [Fe/H] as a function of $g' - r'$ for 58 GCs. Again, the more significant outliers are affected by high foreground reddening, and, the scatter for low-reddening GCs in the SDSS data is significantly larger than for the CTIO data. When robustly fitting the low-reddening CTIO data, we find:

$$[\mathrm{Fe/H}] = (-3.44 \pm 0.06) + (4.10 \pm 0.12) \times (g' - r'), \tag{4.5}$$

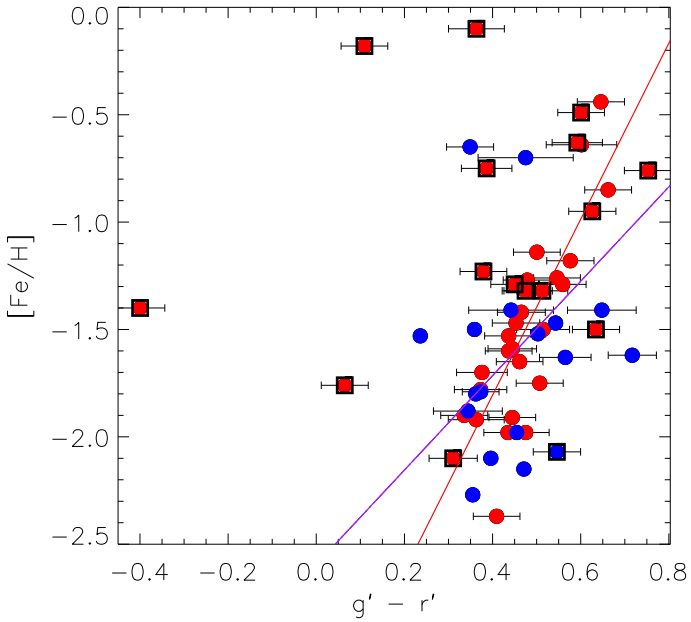

Figure 4.3: [Fe/H] as a function of $g' - r'$ for 58 Galactic GCs. Legend as in Fig. 4.1. The two low-reddening metal-rich GCs based on SDSS data are Whiting 1 and Pal 1. The fitted relations are given by Eqs. 4.5 and 4.6.

while including the SDSS data results in

$$[\mathrm{Fe/H}] = (-2.59 \pm 0.03) + (2.20 \pm 0.06) \times (g' - r'). \tag{4.6}$$

In this colour the CMR is even closer to being linear, which is expected when considering the limited wavelength baseline of $g' - r'$ and hence its relatively weak sensitivity to metal abundance.

4.2.1 Outliers in the CMR

We here discuss briefly the properties of some of the most significant low-reddening outliers from the Galactic CMR.

As discussed in chapter 3, E 3 and Terzan 7 are very poor clusters and were both observed with the CTIO 0.9 m telescope during conditions with the sky having a higher surface brightness than the average cluster surface brightness (sky-subtracted, within the half-light radius). As a consequence, small variations in the sky determination can significantly affect the obtained magnitudes. Moreover, E 3 suffers from considerable extinction along the line of sight ($E(B-V) \sim 0.3$).

Pal 4, a GC initially suspected to be a dwarf galaxy (Wilson 1955), is one of the only low-reddening globular clusters which has a $g - z$ colour redder than expected based on its metallicity. However, this offset can be partly explained by its large colour uncertainty ($\sigma_{g-z} \sim$

0.12).

Both Whiting 1 and Pal 1 are faint clusters, resulting in very poor CMDs. For the sake of completeness, we provide more details on the photometric analysis performed in the previous chapter for the latter clusters. For Whiting 1, one candidate non-member star was selected in the CMD but had no proper motions, so the star was not removed. Pal 1 is located at a Galactic latitude of 19.03° (resulting in a foreground reddening of $E(B-V) \sim 0.15$), so some foreground stars are expected. Based on the CMD, seven candidate outliers were selected in the same colour-magnitude region, five of which had known proper motions in the NOMAD catalog (Zacharias et al. 2005), including the four brightest candidates. We decided to remove all seven candidate outliers (because all candidates are in the same CMD region), which resulted in magnitude corrections as presented in chapter 3. Not performing the magnitude corrections would result in $g-z = 0.82$, thus moving the cluster towards the CMR (to a position close to Whiting 1).

Despite the photometric uncertainties, it is interesting to discuss these clusters in some more detail. In their study of the Galactic outer halo, van den Bergh & Mackey (2004) found several similarities for the properties of Pal 1 and Terzan 7 (e.g. $r_h < 7pc, [Fe/H] > -0.7$), suggesting that these clusters have similar formation and evolutionary histories. These authors explain the existence of such metal-rich GCs in the outer Galactic halo by a formation in dwarf spheroidal galaxies. This appears probable for Terzan 7, a cluster often associated with the Sagittarius system (e.g. Geisler et al. 2007). Moreover, these clusters have estimated ages lower than 8 Gyrs (Rosenberg et al. 1998; Geisler et al. 2007). Hence, it is possible that these clusters are outliers on the CMR, because they have a different formation history. Forbes & Bridges (2010) associated Pal 1 as a probable member of the Canis Major dwarf and confirm the similarities between Pal 1 and the Sagittarius dSph GCs in their age-metallicity relation. Nevertheless, other GCs associated by Forbes & Bridges (2010) to the Canis Major system (including NGC 1851, NGC 1904, NGC 2298, NGC 2808, NGC4590 and Rup 106) are very close to the CMR of Blakeslee et al. (2010).

Whiting 1 is another young ($\sim$ 6.5 Gyr) GC associated with the Sagittarius dwarf spheroidal galaxy, hence another object that originated in a dwarf galaxy that has since been disrupted by the tidal forces of the Milky Way (Carraro 2005; Carraro et al. 2007). This intermediate-metallicity object is clearly offset of the CMR presented in Fig. 4.1.

Lotz et al. (2004) find that dE GC candidates are as blue as the metal-poor GCs of the Milky Way. In the discussion, these authors assume that their sample of dE GCs is dominated by old and metal-poor GCs. However, in the above analysis, Pal 1, Whiting 1 and Terzan 7 are younger GCs at intermediate metallicities, associated with dSph galaxies. This again stresses the peculiarity of these objects.

In Sections 4.2.6 to 4.2.10 we will reevaluate the position in colour-metallicity space of these

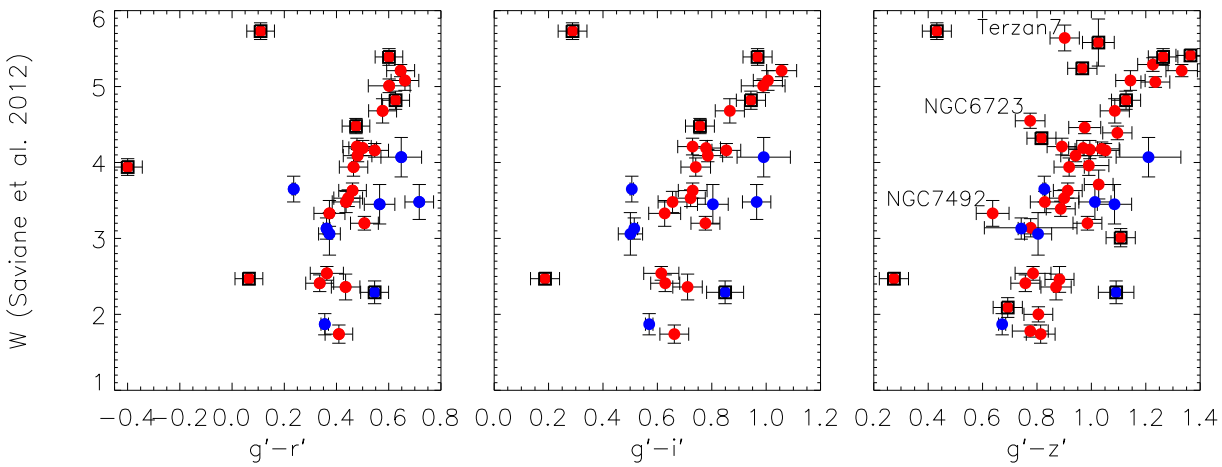

Figure 4.4: Colour-metallicity relations for CaT W' and $g'r'i'z'$ colours. Legend as in Fig. 4.1. Black boxes indicate clusters with $E(B-V) \geqslant 0.35$. It is clear the CaT metallicity indicator behaves non-linear when compared to the $g'-i'$ and $g'-z'$ colours.

clusters.

4.2.2 Calcium Triplet metallicity scale

Though gaining importance and attention, the infrared Calcium Triplet (CaT) is not yet generally accepted as a metallicity indicator (e.g. Foster et al. 2010; Usher et al. 2012, and references therein). Nevertheless, homogeneous CaT measurements from Saviane et al. (2012) allow us to produce a CMR based on our $g'r'i'z'$ colours and metallicity based on this indicator.

In this section we compare our colours with W', which is the sum of the equivalent widths of the two strongest CaT lines (λ8542, λ8662) corrected for the HB level ($W' = W_{8542} + W_{8662} - a(V - V_{HB})$, Armandroff & Da Costa 1991). Fig. 4.4 presents the CMR for the CaT W' parameter as a function of the $g'r'i'z'$ colours. Some of the findings of the previous section are confirmed: the scatter for the SDSS data is larger than for the CTIO data and for the CTIO data, the scatter is closely related to the reddening estimate. Although the metallicity range is limited, the figure suggests that W' is non-linear with $g'-i'$ and $g'-z'$. Even for $g'-r'$ the relation seems slightly non-linear. Nevertheless, it is again clear that this latter colour has a relatively weak sensitivity to metal abundance, as a consequence of its limited wavelength baseline.

Based on the transmission curves, one would expect that $g'-z'$ is the colour most sensitve to W', because both λ8542 and λ8662 fall within z'. Indeed, for the clusters with available photometry, $g'-z'$ shows the largest dynamic range.

Terzan 7, one of the GCs associated to the Sagittarius system, is the metal-rich low-reddening cluster which is the outlier with respect to the general relation in $g'-z'$. Note that Terzan 7 was also an outlier in the $(g'-z')$-[Fe/H] CMR presented in Fig. 4.1.

4.2.3 The colour-metallicity relation including Extragalactic Globular Clusters

The Milky Way lacks both very metal-poor and very-metal rich GCs. Here we address the issues raised in the previous sections by including extragalactic GCs from the literature. Peng et al. (2006) presented colours for GCs in the giant ellipticals M 49 and M 87, for which spectroscopic metallicities were published in Cohen et al. (1998, 2003). These clusters are added to our Galactic sample; they provide extra leverage especially at the metal-rich end of the relation.

We present all available data in Fig. 4.5. Several Galactic GCs suffer from high reddening ($E(B-V) \geqslant 0.35$) and are indicated with boxes in the figure. For clarity, no error bars are presented in this figure. We also show, in the same figure, CMRs from the literature.

In the previous sections it became clear that most of the scatter in the CTIO data is caused by the uncertainty in the reddening correction, which will be scrutinised in Section 4.2.4 (while for SDSS data saturation may also play a role). Therefore we exclude clusters with high reddening to make the fits. Because the scatter in colour is still significant, we binned the data points in bins of 0.2 dex in metallicity. We then computed the median colour for each bin, obtaining a representative colour for each metallicity bin and fitted a cubic polynomial to the binned data. This resulted in a CMR:

$$\begin{aligned}[\text{Fe/H}] = -22.69 \pm 1.54 + (47.81 \pm 4.02) \times (g' - z') \\ - (35.27 \pm 3.44) \times (g' - z')^2 + (9.01 \pm 0.96) \times (g' - z')^3 \end{aligned} \quad (4.7)$$

which is plotted as a black solid line in Fig. 4.5. Note that the uncertainties on the coefficients are large because of the small number of degrees of freedom and because we use the bin size as the metallicity uncertainty in the bootstrapping routine. Using the homogeneous Saviane et al. (2012) [Fe/H] values where possible does not significantly change the fitted relation. Compared to Blakeslee et al. (2010) we find good agreement over the metallicity range considered. When comparing our CMR to Sinnott et al. (2010), there are larger differences on both the metal-poor and metal-rich end. This is partly due to the fact that Sinnott et al. (2010) used a different metallicity range for their fit ($-2.2 <$ [Fe/H] < -0.5). Nevertheless the two CMRs compare reasonably well up to [Fe/H]$\sim$ 0. On the blue end of the relation, the difference is somewhat larger, stressing the importance of obtaining additional data at the low metallicity end.

As has been discussed in Section 4.2.1, some clusters are strong outliers: Whiting 1, Terzan 7 (clusters associated with the Sagittarius dSph) and Pal 1 (probably related to the Canis Major system). Another outlier is E 3, an old cluster with uncertain photometry. We make a new subset, excluding these clusters from the low-reddening sample. Using this subset, we performed an optimization algorithm in PYTHON, minimizing the orthogonal distance to the CMR. This

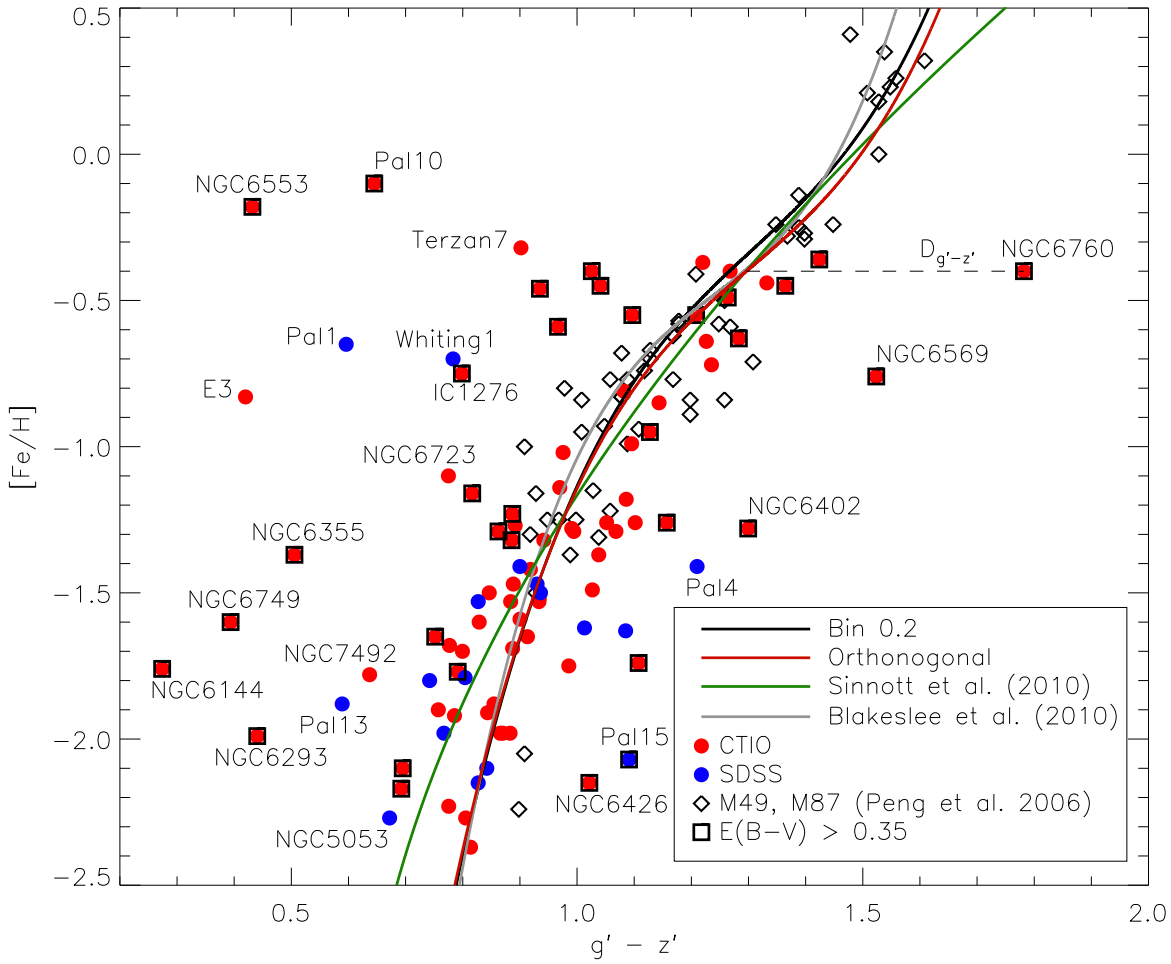

Figure 4.5: [Fe/H] as a function of $g' - z'$ for our sample of Galactic GCs and data of extragalactic GCs from the literature. Clusters from our CTIO and SDSS samples are represented with filled circles, while literature data of M 49 and M 87 (Peng et al. 2006) is represented by diamonds. The black line presents the CMR derived for all low-reddening GCs, fitting colours binned by metallicity bins of 0.2 (as given by Eq. 4.7). The red line is the final CMR (given by Eq. 4.8) obtained by minimizing the orthogonal distance. The grey and green lines present CMRs from the literature (Blakeslee et al. 2010; Sinnott et al. 2010). The black dashed line presents the distance $D_{g'-z'}$, as defined in Eq. 4.9. See text for more details.

resulted in our final CMR:

$$[\text{Fe/H}] \;=\; -22.68 + 48.04 \times (g' - z') - 35.63 \times (g' - z')^2 + 9.12 \times (g' - z')^3, \quad (4.8)$$

presented as a red line in Fig. 4.5. This relation compares very well to the binned relation given by Eq. 4.7, with all coefficients within the error bars. Compared to the CMR of Sinnott et al. (2010), there is a significant offset at both the metal-rich and metal-poor end.

Visual inspection might suggest that the [Fe/H] range of -1 to -0.5 reveals a larger spread in $g - z$ for the M 49 and M 87 GCs than for the MW GCs. However, this is misleading, as the overall RMS for the extragalactic GCs is 0.069, while the RMS for the extragalactic GCs with [Fe/H] between -1 and -0.5 equals 0.074. Note that the RMS for the low-reddening Galactic GCs amounts 0.16.

4.2.4 Colour uncertainties due to Reddening

It is clear from Fig. 4.1 that most of the CMR outliers, which are not related to dSph galaxies or do not have uncertain photometry, suffer from high reddening. Note that not only Galactic studies suffer from this issue: Kim et al. (2013) also indicate that colours of M 31 GCs are very susceptible of reddening uncertainties. This resulted in colour scatter so large that no meaningful comparison could be made with their models.

To get a handle on the error introduced by the reddening estimates, we define a new parameter, which is the colour difference between the final CMR (Eq. 4.8) assuming the metallicity is accurately known and the observed colour:

$$D_{g'-z'} = CMR^{-1}([\text{Fe/H}]) - (g' - z')_{observed}, \quad (4.9)$$

as indicated in Fig. 4.5. This new parameter is positive (negative) when the observed colour is bluer (redder) than the colour predicted by our final CMR. In Fig. 4.6 we plot the distance $|D_{g'-z'}|$ to the CMR as a function of the reddening $E(B-V)$ (from Harris 1996 (2010 edition), which is a compilation of Reed et al. 1988; Webbink 1985 and Zinn 1985). It is clear that a significant part of the scatter is caused by the uncertainties in the reddening estimates. Note that the scatter is relatively larger for low-reddening clusters with SDSS data than with CTIO data.

To get a better notion of the uncertainty on the reddening estimate, we present in Fig. 4.7 the absolute difference between the reddening corrections based on Cardelli et al. (1989) (C89) and

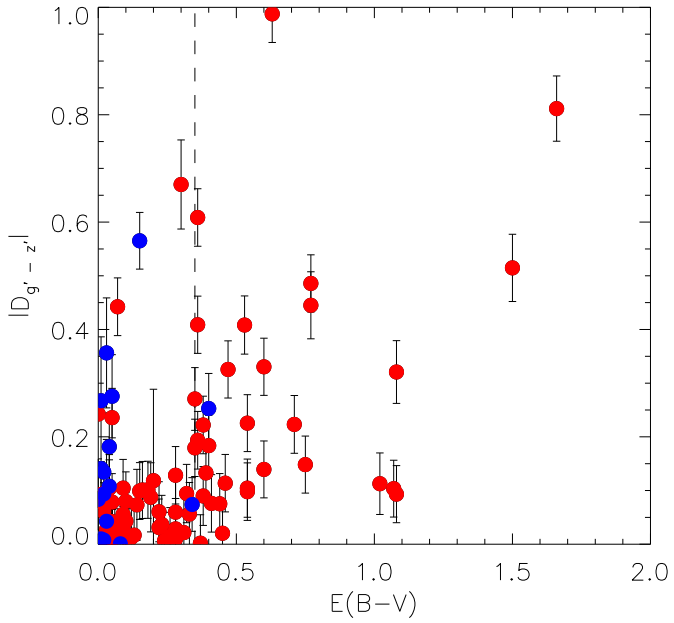

Figure 4.6: Absolute colour difference $|D_{g'-z'}|$ (as defined in Eq. 4.9) as a function of $E(B-V)$ (Harris 1996). Legend as in Fig. 4.1. The vertical dashed line indicates $E(B-V) = 0.35$.

Schlafly & Finkbeiner (2011) (S11, which was used in chapter 3) with:

$$\Delta A_{g'} = A_{g',\mathrm{C89}} - A_{g',\mathrm{S11}} \quad (4.10)$$

$$\Delta A_{z'} = A_{z',\mathrm{C89}} - A_{z',\mathrm{S11}}. \quad (4.11)$$

We find, as expected, that the reddening corrections and uncertainties are much larger in the g'-band than in the z'-band and that both reddening estimates generally compare well for $A_{g'} \lesssim 1$ and $A_{z'} \lesssim 0.4$. Higher reddenings are more unreliable, probably reflecting the patchiness of the extinction and irregular distribution of dust clouds. For NGC 6144, NGC 6256, NGC 6544 and NGC 6553 we find $|\Delta A_g| > 1$ and $|\Delta A_z| > 0.4$.

To further scrutinize the reddening issue, we introduce another new parameter:

$$\Delta A_{g'-z'} = (A_{g'} - A_{z'})_{\mathrm{C89}} - (A_{g'} - A_{z'})_{\mathrm{S11}}. \quad (4.12)$$

In practice, $\Delta A_{g'-z'} < 0$ results in $g'-z'$ colours which are redder if we would use the Cardelli et al. (1989) reddening law instead of the updated maps by Schlafly & Finkbeiner (2011) to correct for the reddening.

In the left panel of Fig. 4.8 we compare the absolute scatter in the CMR as a function of the absolute value of this new parameter. The clusters with low $|\Delta A_{g'-z'}|$ and large $|D_{g'-z'}|$ are Pal 1, Whiting 1, Terzan 7 and E 3. The origin of these large offsets was discussed in more detail in Section 4.2.1.

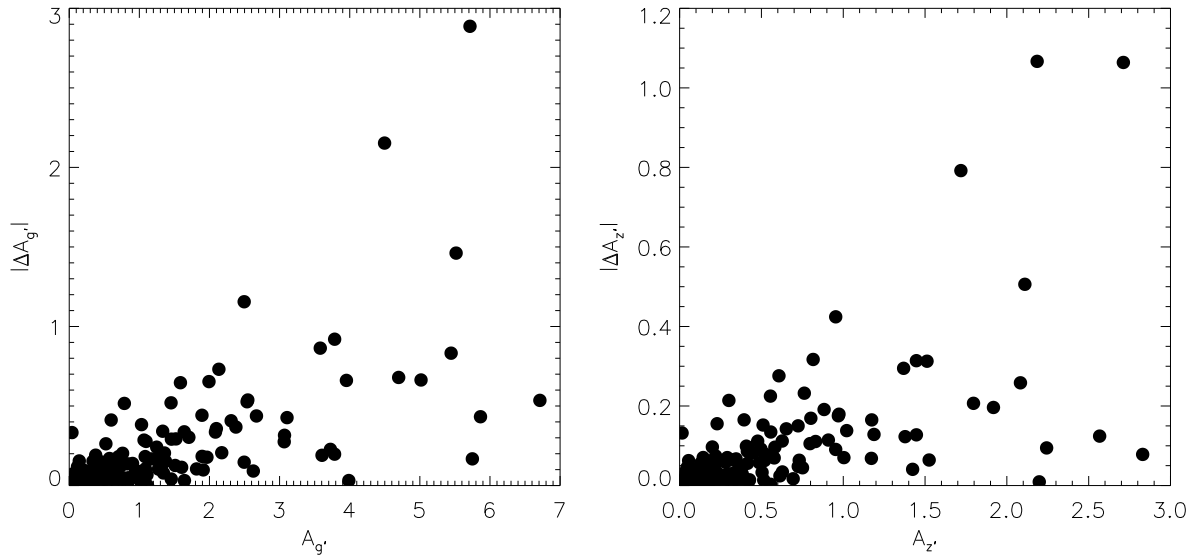

Figure 4.7: Absolute reddening correction difference (defined in Eqs. 4.10 and 4.11) as a function of the reddening coefficient for g' and z' (Schlafly & Finkbeiner 2011). The uncertainty on $A_{g'}$ is much larger than on $A_{z'}$.

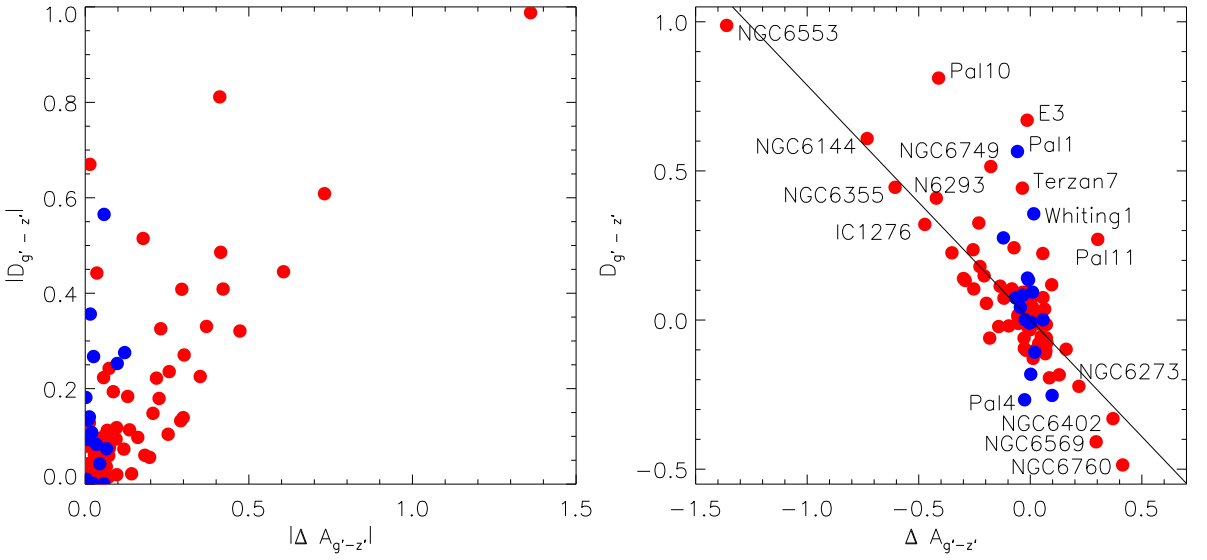

Figure 4.8: Left panel: Absolute scatter around the CMR vs. the absolute reddening coefficient difference as defined in Eq. 4.12. It is clear that the uncertainty in the reddening estimate scales with the distance to the CMR. — Right panel: Scatter around the CMR vs. the reddening coefficient difference. The black line is a robust fit to the data, as given by Eq. 4.13. Legend as in Fig. 4.1. Some particular clusters are indicated: these include Pal 1, E 3, the GCs associated with the Sagittarius system (Whiting 1, Terzan 7) and some GCs suffering severe differential reddening (NGC 6144, NGC 6273, NGC 6355, NGC 6402, NGC 6553). See text for more details.

The right panel of Fig. 4.8 presents the scatter about the CMR as a function of $\Delta A_{g'-z'}$. Surprisingly, $D_{g'-z'}$ correlates with $\Delta A_{g'-z'}$. This is unexpected: in fact it predics that, when:

$$(A_{g'} - A_{z'})_{\rm C89} < (A_{g'} - A_{z'})_{\rm S11},$$

the $g' - z'$ colour (based on the Schlafly & Finkbeiner 2011 extinction coefficients) is too blue and results in $D_{g'-z'} > 0$. This demonstrates that the scatter around the CMR and the reliability of the extinction estimate are intimately related. Moreover, GCs located at Galactic latitude $|b \lesssim 5|$ (including Pal 10, NGC 6553, NGC 6355 and NGC6760) are known to have unreliable extinction estimates (Schlafly & Finkbeiner 2011).

Again, E 3, Pal 1, Terzan 7 and Whiting 1 do not follow the general trend. Nevertheless, some other clusters also do not follow the relation either: Pal 10, Pal 11 and NGC 6749 all suffer high extinction ($E(B-V) = 1.66$, 0.35 and 1.50, respectively). For these clusters, it is not the difference between the reddening estimates of Cardelli et al. (1989) and Schlafly & Finkbeiner (2011) that causes the offset in the CMR. However, as these are high reddening clusters, it does illustrate again that the scatter in the CMR scales with the reddening.

We made a robust fit of $D_{g'-z'}$ as a function of $\Delta A_{g'-z'}$ and obtain

$$D_{g'-z'} = -0.78 \times \Delta A_{g'-z'} - 0.02, \tag{4.13}$$

plotted as a black line in Fig. 4.8. We can use this relation to correct the $g' - z'$ colours:

$$(g' - z')^* = (g' - z') + (-0.78 \times \Delta A_{g'-z'} - 0.02)$$

or

$$(g' - z')^* \; = \; \hat{g} - \hat{z} - 0.78 \times (A_{g'} - A_{z'})_{\rm C89} - 0.22 \times (A_{g'} - A_{z'})_{\rm S11} - 0.02, \tag{4.14}$$

with $\hat{g}$ and $\hat{z}$ the calibrated but not reddening corrected magnitudes.

Fig. 4.9 presents a CMR for $(g' - z')^*$, which are represented as black circles. For reference, the $g' - z'$ colours are given as red crosses. Note the huge difference for e.g. NGC 6553, a high-metallicity cluster with a colour correction of more than 1 magnitude. It is clear that the scatter is significantly reduced: the horizontal RMS for the $g' - z'$ colour is 0.24, while it is 0.16 for the corrected $(g' - z')^*$ colour. This suggests that a combination of the C89 and S11 reddening laws results in a better extinction estimate. Moreover, the horizontal RMS for the $g' - z'$ colour is also 0.16 when we limit the sample to GCs with $E(B-V) < 0.35$. Nevertheless, not all GCs are moved towards the CMR by applying the reddening correction of Eq. 4.14. Pal 11 is a high-reddening 10.4 Gyr old GC (Lewis et al. 2006) that scatters off the CMR when applying this correction. E 3, Pal 1, Terzan 7 and Whiting 1 are not affected by the reddening correction.

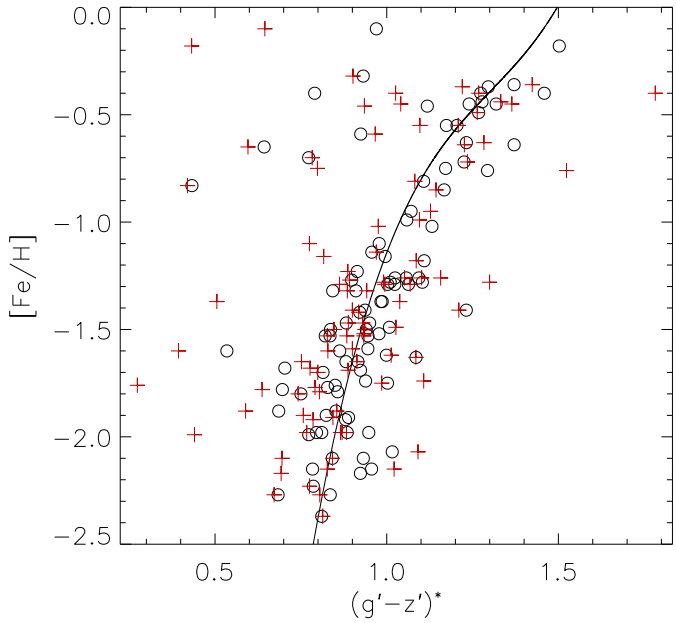

Figure 4.9: [Fe/H] as a function of $(g' - z')^*$, a colour corrected for the reddening uncertainty (defined in Eq. 4.14). Corrected colours are indicated with black circles. As a reference, red crosses represent the $(g' - z')$, which were also given in Fig. 4.1. The solid line presents the CMR as given by Eq. 4.8.

Again, their position in the figure suggests another evolutionary history and younger ages.

Pal 10, another high reddening GC ($E(B-V) \sim 1.66$) in the Sagittarius constellation, is moved towards but not on the CMR by the reddening correction. It is notable that the difference between the corrected $(g' - z')^*$ colour and the CMR is similar to the difference for Terzan 7 and Whiting 1, which are associated to the Sgr dSph.

Some GCs suffer from substantial differential reddening (Heitsch & Richtler 1999; Alonso-García et al. 2012). To estimate the contribution of the differential reddening to the photometric error and to the scatter in the CMR, we present in Fig. 4.10 the absolute distance to the CMR as a function of the differential reddening $\Delta E(B-V)$ (obtained from Alonso-García et al. 2012, supplemented with data from Contreras Peña et al. 2013 for NGC 6402). Some of the clusters with $\Delta E(B-V) > 0.15$ show large offsets from the CMR, while clusters with relatively low differential reddening ($\Delta E(B-V) < 0.15$) are all close to the CMR. NGC 6553, NGC 6144 and NGC 6355 are clusters with $\Delta A_{g'-z'} > 0.5$. NGC 6287 has $\Delta A_{g'-z'} = -0.3$, but lies remarkably close to the CMR. The large $\Delta A_{g'-z'}$ values could suggest that the differential reddening is affecting the reddening estimate for the entire cluster. Nevertheless, NGC6402, NGC 6273, NGC 6553, NGC 6144 and NGC 6355 are right on the relation presented in the right panel of Fig. 4.8, suggesting that combining both Cardelli et al. (1989) and Schlafly & Finkbeiner (2011) reddening laws could resolve the issue.

Future work will determine the reddening by fitting isochrones to the colour-magnitude diagrams and further discuss this issue.

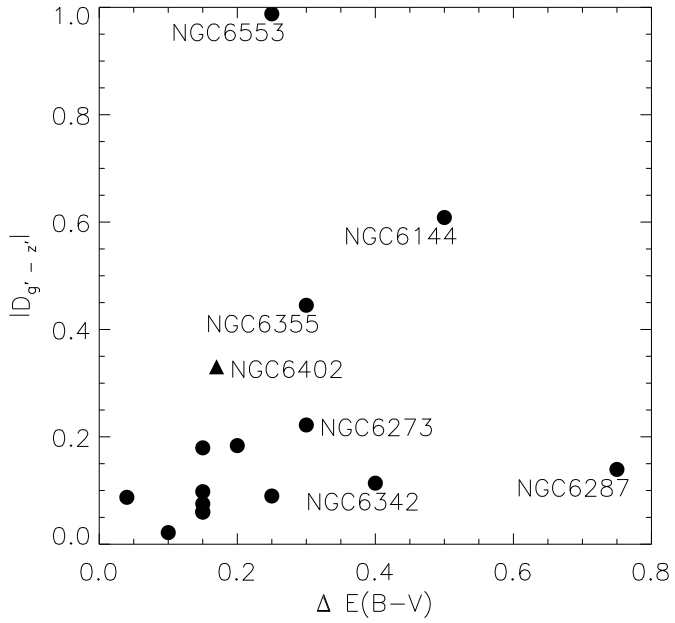

Figure 4.10: Absolute colour difference $|D_{g'-z'}|$ (as defined in Eq. 4.9) as a function of the differential reddening $\Delta E(B-V)$ (Alonso-García et al. 2012; Contreras Peña et al. 2013). Some of the clusters with $\Delta E(B-V) > 0.15$ show large offsets from the CMR, while clusters with relatively low differential reddening ($\Delta E(B-V) < 0.15$) are all close to the CMR.

4.2.5 The Effects of Horizontal Branch morphology

Yoon et al. (2006) studied the influence of HB morphology on GC colours and indicated that HB stars are the main drivers behind the non-linearity of the CMR. The CMR presented in Eq. 4.8 is clearly non-linear and should account for the influence of the HB stars. However, to check whether the HB morphology contributes to the scatter around the CMR we plot in Fig. 4.11 the colour difference $D_{g'-z'}$ as function of the HB morphology index ($\frac{B-R}{B+V+R}$, Lee 1990; Lee et al. 1994) of Mackey & van den Bergh (2005) for 78 GCs. The best fit relation

$$D_{g'-z'} = (0.058 \pm 0.023) - (0.014 \pm 0.029) \times \frac{B-R}{B+V+R} \tag{4.15}$$

is not statistically significant and is given by the solid line in Fig. 4.11. The HB index becomes insensitive to the HB morphology for very blue and very red HBs (Catelan et al. 2001, and references therein), which are the ranges which are best populated in our GC sample. Motivated by this argument, we restrict the HB index range to $[-0.9, 0.9]$ to fit the data and find

$$D_{g'-z'} = (0.01 \pm 0.02) + (0.05 \pm 0.04) \times \frac{B-R}{B+V+R}, \tag{4.16}$$

presented by the dash-dot line in the same figure. Again, this relation is statistically not significant, which indicates that the non-linear CMR does account well for the influence of the HB morphology on the cluster colour.

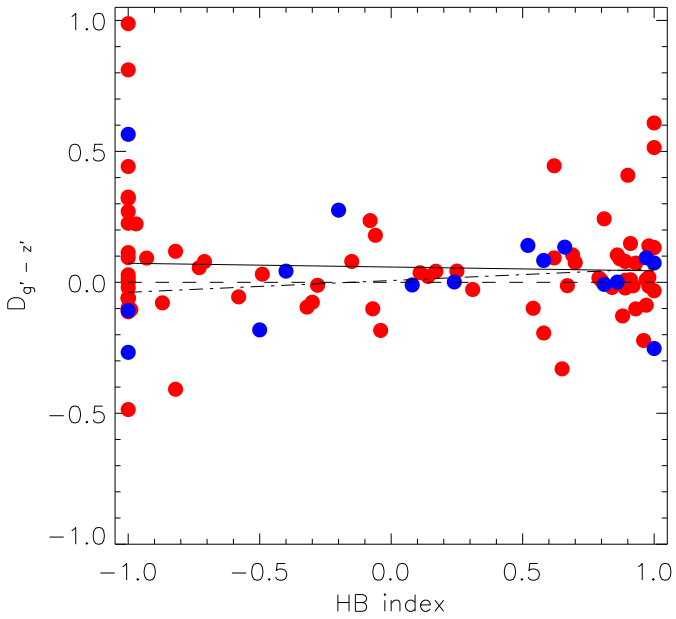

Figure 4.11: Colour difference $D_{g'-z'}$ (as defined in Eq. 4.9) as a function of HB index (Mackey & van den Bergh 2005). The best fit is given as a solid line, the dashed line indicates the $D_{g'-z'} = 0$. The dash-dot line is the best fit for clusters with HB index between -0.9 and 0.9. Legend as in Fig. 4.1. See text for more details.

Table 4.1: HB morphology (taken from Mackey & van den Bergh 2005), [Fe/H] and distance to the CMR (as defined in Eq. 4.9) for some crucial clusters regarding the second parameter problem.

	HB index	[Fe/H]	$D_{g'-z'}$
NGC 288	0.98	−1.32	0.019
NGC 362	−0.87	−1.26	−0.078
NGC 5272 (M 3)	0.08	−1.50	−0.010
NGC 6205 (M 13)	0.97	−1.53	0.094
NGC 7006	−0.28	−1.52	−0.011

To further investigate the effects of the HB morphology we list in Table 4.1 some clusters with similar metallicities but different HB structure, the so-called 'second parameter objects' (e.g. Catelan et al. 2001; Caloi & D'Antona 2005). For NGC 288 and NGC 362, one of the best studied 'second parameter pairs' of GCs, we find a blue (red, respectively) offset from the CMR, as could be expected from the HB morphology of these clusters. The same holds for NGC 6205 and NGC 7006, while this is not the case for NGC 5272. In most cases $|D_{g'-z'}|$ is smaller than the colour uncertainties; therefore, we conclude that the effect of the HB morphology on the integrated colour is reasonably well accounted for by the non-linear CMR.

4.2.6 Age as possible cause for the scatter in CMR

In Section 4.2.1, discussing the young GCs associated to the Sagittarius and Canis Major system, we already considered age as possible contributor to the scatter in the CMR. In this section, we will discuss this issue in some more detail, concentrating on both high-reddening and low-reddening clusters. Recently, Forbes & Bridges (2010) made a compilation of the most reliable ages published to date (based on results of Salaris & Weiss 1998; Bellazzini et al. 2002; Catelan et al. 2002; De Angeli et al. 2005; Carraro et al. 2007; Marín-Franch et al. 2009). We add new ages for IC4499, Pal 15 and NGC7006 from Dotter et al. (2011), NGC6293 (Lee & Carney 2006), NGC6402 (Paust & Chaboyer 2011), NGC6553 (Ortolani et al. 1995), Pal 11 (Lewis et al. 2006) and Pal 13 (Trouille & Chaboyer 2002). Note that Vandenberg et al. (2013) do not give an age estimate for Pal 1, Terzan 7 and E 3, because of the poor quality of the available CMDs.

Fig. 4.12 presents [Fe/H] as a function of the $g' - z'$ colour, with the clusters being colour-coded depending on their age. Three young low-reddening GCs (Terzan 7, Pal 1 and Whiting 1) were associated with the Canis Major and Sagittarius systems. For the old GC E 3, we discussed in Section 4.2.1 the photometric uncertainties for the observations of this faint cluster, which suffers significant foreground extinction ($E(B-V) \sim 0.3$).

To pinpoint the influence of age on the $g - z$ colour for the younger GCs, we integrated PARSEC (v1.1) isochrones from Bressan et al. (2012) with a Kroupa (1998) IMF corrected for binaries[1]. For Pal 1 and Whiting 1 (with [Fe/H]~ -0.7 and an age about 7 Gyr), we used a metallicity $Z \sim 0.004$ and obtained Single Stellar Population (SSP) integrated $g - z \sim 1.1$, much redder than the observed $g - z \sim 0.6$ and ~ 0.8 (respectively). For Terzan 7 (with [Fe/H]~ -0.32 and age of 7.3 Gyr) we adopted $Z \sim 0.008$. For this combination, the models predict $g - z \sim 1.2$, much redder than $g - z \sim 0.9$ based on our observations. The models confirm that the colours of GCs, older than a few Gyrs, are totally dominated by the RGB, which is populous and bright. At old-enough ages it is only the metal abundance that sets the colour of the RGB, suggesting that Pal 1, Whiting 1 and Terzan 7 are peculiar clusters with a different chemical enrichment history. This will be further discussed in Section 4.2.10.

It is clear that age is not the main contributor to the scatter in the CMR. Several old high-reddening clusters are offset of the relation (e.g. NGC 6144, NGC 6293, NGC 6402). Pal 15 and NGC 6426 are distant, high-reddening GC (with signs of differential reddening) and are coeval with all other metal-poor GCs, with ages estimated about 13 Gyrs (Dotter et al. 2011). The metal-rich outlier with an age of 12 Gyr is NGC6553, suffering significant differential reddening, as was described in Section 4.2.4.

[1] http://stev.oapd.inaf.it/cgi-bin/cmd

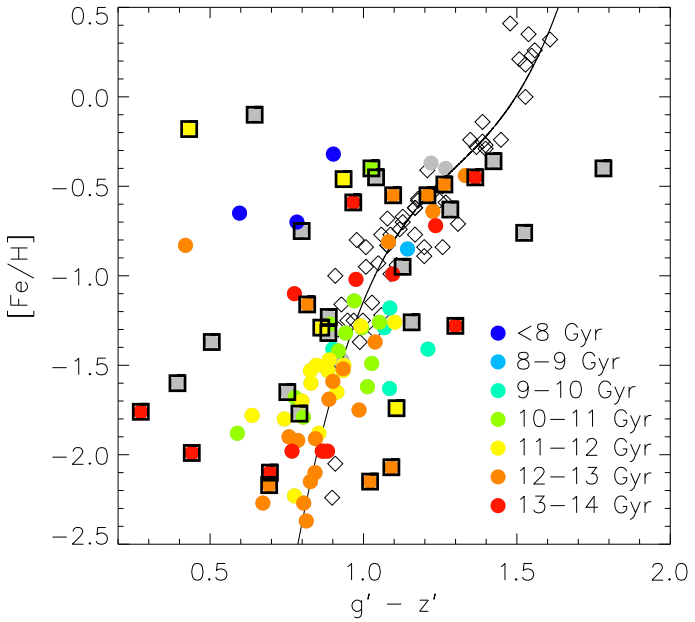

Figure 4.12: [Fe/H] as a function of $g' - z'$, colour-coded by the ages of the GCs. Grey symbols are used for the clusters without age estimate, open diamonds are the M 49 and M 87 GCs. Black boxes indicate high-reddening GCs. As a reference, the CMR (given by Eq. 4.8) is presented by the black solid line. See text for more details.

4.2.7 Do mass function variations play a role?

In Section 4.2.6, we quietly assumed that the GC initial mass function (IMF) is well represented by a Kroupa (1998) IMF. Although the IMF of the Milky Way field stars is mostly consistent with Salpeter (1955) or Kroupa IMFs (Bochanski et al. 2010), recent studies discuss the possibility of IMF variations (e.g. Conroy & van Dokkum 2012 and references therein). Paust et al. (2010) suggested that the observed variations of GC present-day mass functions (MF) are related to dynamical evolution, while Marks et al. (2012) claim IMF correlations with cluster density and metallicity.

Recently, Hamren et al. (2013) gathered the MF slopes published to date (based on results of Paust et al. 2010; Rosenberg et al. 1998; Bellazzini et al. 2012; Frank et al. 2012; Pulone et al. 2003; Dotter et al. 2008; Cote et al. 1991; Grillmair & Smith 2001; Jordi et al. 2009; De Marchi et al. 2007; Capaccioli et al. 1991; Grabhorn et al. 1991; Paust et al. 2009; Saviane et al. 1998; Milone et al. 2012). These authors used a single-sloped power law MF in the form $dN/dm \sim m^{-(1+\alpha)}$ (implying $\alpha = +1.35$ for the classic Salpeter (1955) MF) and cover masses $M \lesssim 0.8 M_{\odot}$ of the present day mass function, which are the stellar masses remaining in old clusters.

In Fig. 4.13 we plot the colour difference $D_{g'-z'}$ (defined in Eq. 4.9) as a function of the MF power law slope for 34 GCs. The clusters are colour-coded with age as in Fig. 4.12. Pal 5 is indicated with an arrow, because only an upper limit for the MF slope was given. Making a

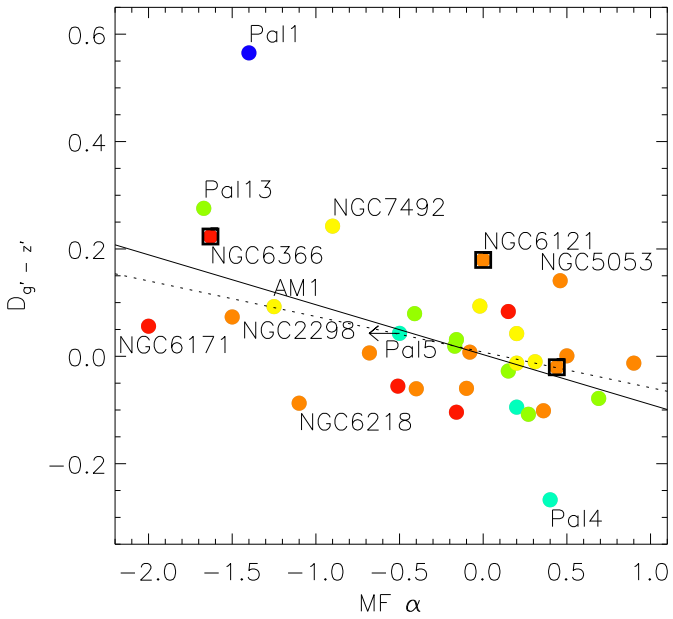

Figure 4.13: Colour difference $D_{g'-z'}$ (as defined in Eq. 4.9) as a function of the GC MF slope α. Legend as in Fig. 4.12. The solid line, given by Eq. 4.17 represents the best robust fit to all the data. The dotted line, given by Eq. 4.18, shows the best robust fit excluding Pal 1 and Pal 4. The slope of the MF of Pal 5 is only an upper limit. See text for more details.

robust fit to the data results in

$$D_{g'-z'} = 0.00 \pm 0.01 - (0.09 \pm 0.03) \times \alpha, \tag{4.17}$$

which is represented by the solid line in Fig. 4.13. Limiting the fit to the low-reddening ($E(B-V) < 0.35$) clusters does not alter the fit and using the extinction corrected $(g'-z')^*$ colours (defined in Section 4.2.4) confirms the correlation.

Despite the significant scatter among the relation, Pal 1 and Pal 4 are the strongest outliers. Both clusters are faint, resulting in $\sigma_{g-z} \sim 0.05$ for Pal 1 and $\sigma_{g-z} \sim 0.12$ for Pal 4. Remark that the magnitudes obtained for Pal 1 and Pal 4 are based on SDSS data. Therefore, their colours did not suffer from the complications regarding the CTIO sky determination (as discussed in chapter 3). Excluding these clusters to make a robust fit we find

$$D_{g'-z'} = 0.01 \pm 0.01 - (0.07 \pm 0.02) \times \alpha, \tag{4.18}$$

fully consistent with Eq. 4.17. Nevertheless, if we use the $(g'-z')^*$ colours excluding Pal 1 and Pal 4, the slope of the relation does become more shallow and is only different from zero at the 1.6 σ level.

The MF slope for Whiting 1 is not given by Hamren et al. (2013). Nevertheless, Carraro et al. (2007) found that the luminosity function of Whiting 1 is remarkably flat and suggest that the cluster has experienced tidal stripping by the Milky Way. If the mass function is confirmed to

be approximately flat, this cluster would be located close to Pal 1 in Fig. 4.13 and would follow the general trend given by Eq. 4.17: GCs with more bottom-light MFs show a blue offset to the CMR.

Other GCs showing evidence for tidal stripping by the Milky Way include Pal 5 (Koch et al. 2004) and Pal 13 (Côté et al. 2002a). Remark that both clusters follow the general trend (given by Eq. 4.17), although the slope of the MF for Pal 5 is just an upper limit.

Remark that NGC 5053, a GC likely associated with the Sgr dSph by Law & Majewski (2010), shows a blue offset to the CMR, while Eq. 4.17 predicts a negligible colour difference based on the MF slope found by Paust et al. (2010). Nevertheless, the colour offset for this metal-poor GC is smaller than for the CMR outliers related with the Sgr dSph.

Although the coefficients in Eqs. 4.17 and 4.18 are significantly different from zero, we are cautious to conclude any correlations between MF variations and the CMR offset are real. These correlations would not imply the MF varies with metallicity, they only suggest the colour offset to the CMR is related to the MF.

4.2.8 Influence of structural parameters in the CMR scatter

In this section, we study the CMR scatter and its relation to the structural parameters, which relate to the evolutionary history of the GCs.

Fig. 4.14 presents the colour difference $D_{g'-z'}$ and absolute colour difference $|D_{g'-z'}|$ (as defined in Eq. 4.9) as a function of the concentration c (obtained from the compilation of Harris 1996 (2010 version), which is based on values taken from Trager et al. 1993, 1995 and McLaughlin & van der Marel 2005). In this figure, green symbols are used for core-collapsed clusters.

It is remarkable that, ignoring Pal 1 and all high-reddening GCs, only low-concentration GCs are offset from the CMR. However, all these clusters are faint and we cannot exclude that this is the principal cause of the scatter with respect to the CMR. Note that NGC 6723, a GC in the Sagittarius constellation, has a similar concentration and metal abundance to Whiting 1 and Terzan 7. However, it has an estimated age of 13.06 Gyr (Marín-Franch et al. 2009), hence this GC is much older than Whiting 1 and Terzan 7.

Pal 1, the GC which might be associated to the Canis Major dSph, has a very different concentration and is the only low-reddening cluster with a concentration $c > 1$ that is an outlier in the CMR.

Note that low-reddening core-collapsed clusters (with the exception of NGC 6723) are all close to the CMR. This suggests that the $g' - z'$ colours of GCs are not altered during or after the core-collapse.

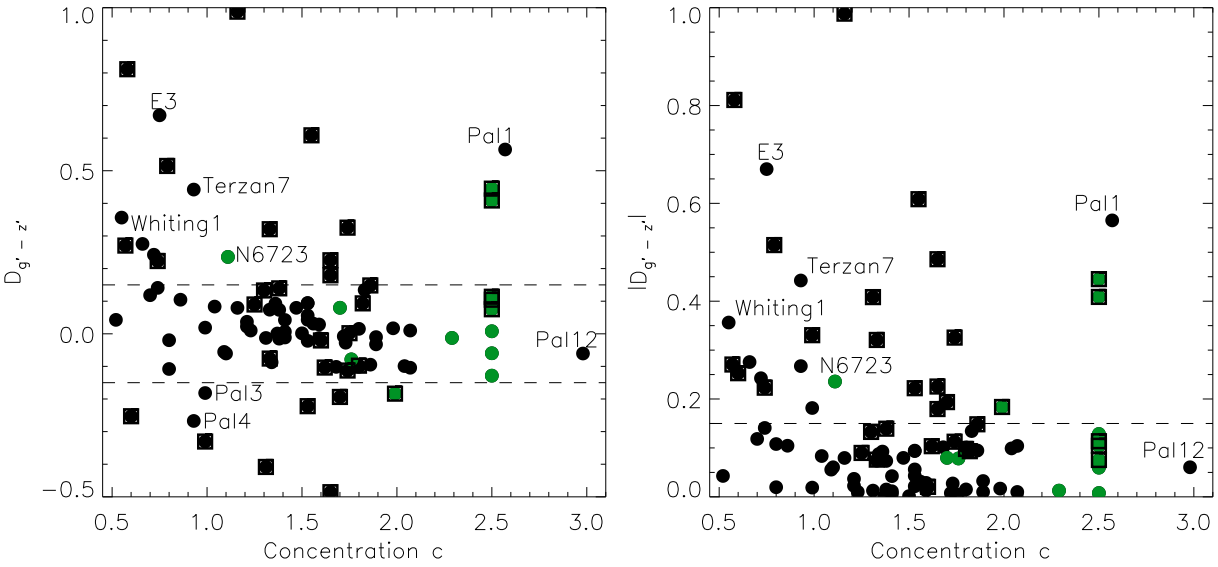

Figure 4.14: Colour difference $D_{g'-z'}$ and absolute colour difference $|D_{g'-z'}|$ (as defined in Eq. 4.9) as a function of the concentration c (Harris 1996). Green circles are used for core-collapsed clusters, black circles for other clusters. Black boxes indicate high-reddened clusters. The four low-reddening clusters with low concentration ($c < 1$) and $|D_{g'-z'}| > 0.15$ that are not indicated in the right panel are Pal 3, Pal 4, Pal 13 and NGC 7492. See text for more details.

4.2.9 A Note on the influence of the contamination correction on the scatter in the CMR

In chapter 3 we described how we used CMDs and proper motions to clean out the aperture magnitudes. In this section we check how effective this correction is and what its influence is on the scatter in the CMR.

Fig. 4.15 presents the absolute colour difference $|D_{g'-z'}|$ (defined in Eq. 4.9) as a function of the g' magnitude correction and the $(g'-z')$ colour correction. Only three low-reddening clusters deviate strongly from the CMR. These clusters (E 3, Pal 3 and Pal 13) are very faint which is reflected in their magnitude errors. It was not possible to obtain a decent CMD for these clusters so no magnitude correction was applied.

The need to clean out the contamination, especially for faint clusters, is illustrated well by Pal 12. For this halo cluster, only one very bright foreground star was identified in the CMD and removed from the aperture photometry. This resulted in magnitude corrections of 1.38 (1.20, 1.15, 1.06) mag. in g' (r', i', z'), yielding a 0.32 mag. correction for the contamination in $g'-z'$. Note that for this cluster $|D_{g'-z'}| = 0.06$, so the magnitude correction significantly moved the GC towards the CMR relation.

Nevertheless, as was discussed in Section 4.2.4, the main source of the scatter in the CMR is the reddening uncertainty.

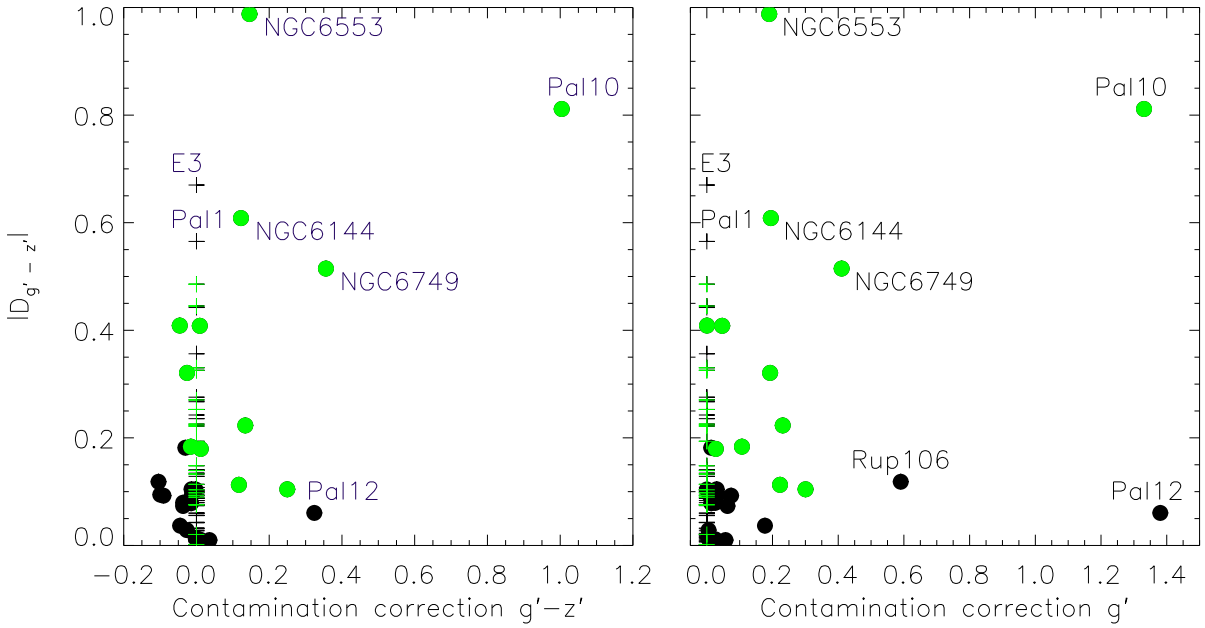

Figure 4.15: Absolute colour difference $|D_{g'-z'}|$ as a function of the contamination correction in g' and $g'-z'$. Crosses indicate clusters without contamination correction based on the CMDs, filled circles represent the GCs for which contamination corrections were applied. Green symbols are used for clusters with $E(B-V) \geqslant 0.35$.

4.2.10 GCs with a different chemical evolution?

In Section 4.2.1 we discussed the particular position in colour-metallicity space of Whiting 1, Pal 1, E 3 and Terzan 7. In the previous sections, we excluded age and HB morphology as the origin for the offset for these low-reddening clusters. For E 3 and Terzan 7, we cannot exclude photometric uncertainties cause the offset. In this section, we reexamine the issue, but also include NGC 6723, NGC 7492 and Pal 13, which are other low-reddening GCs showing similar blue offsets to the [Fe/H] CMR (see Fig. 4.5).

NGC 6723 is a low-reddening cluster in the Sagittarius constellation, which was also discussed in Section 4.2.8. However, Forbes & Bridges (2010) listed this cluster among the Milky Way GCs and did not include this cluster in their subsample associated to the Sagittarius dSph. With an age of about 13 Gyr, it is much older than Terzan 7 and Whiting 1. Note that NGC 6723 and NGC 7492 also show a similar offset to the CaT CMR as Terzan 7 (see Fig. 4.4). Pal 13 is a sparse distant halo cluster which is about to be devoured by the Milky Way (Siegel et al. 2001).

Only age and chemical composition determine the intrinsic colours of the RGB stars which dominate the magnitudes of the GCs, hence it is not unreasonable to consider the chemical history as the possible origin for the colour offset. Moreover, Sakari et al. (2011) show that Pal 1, a low surface brightness cluster with a sparse red giant branch, has a very unusual chemistry: the cluster does not show the Na-O anti-correlation and the neutron-capture elements show

different abundances than for standard Galactic GCs.

Whiting 1 and Terzan 7 are two GCs associated with the Sgr dSph that are offset the CMR, the latter cluster being formed during the main episode of star formation in the Sgr system (Bellazzini et al. 1999). Smecker-Hane & McWilliam (2002) show that not only the GCs associated to the Sgr system can be peculiar: the red giant stars in the Sgr dSph galaxy span a wide range of metallicities and show very unusual abundance variations (both for α abundances as for neutron-capture elements), inferring an extended period of star formation and chemical enrichment with considerable mass loss.

Mackey & Gilmore (2004) suggested an extragalactic origin for the old outer halo cluster NGC 7492, a cluster located at $R_{GC} = 25$ kpc. Majewski et al. (2004) find that it is unlikely that this cluster is a Sagittarius remnant, though these authors do not fully exclude this possibility. Based on a sample of four RGB stars, Cohen & Melendez (2005) recover the well-known Na-O anti-correlation and find evidence for a chemical history (including neutron capture processes) similar to that of inner halo GCs with similar [Fe/H].

Several GCs associated to the Canis Major dSph (NGC 1851, NGC 1904, NGC 2298, NGC 2808, NGC 4590 and Rup 106) are on the CMR. In our sample, Pal 1 is the only GC related to the Canis Major system (Forbes & Bridges 2010) that is offset the CMR. However, the existence of the Canis Major structure is under debate. It is not clear whether this system is produced by a collision with a dSph satellite galaxy or if it is caused by a warp in the Galactic disk, combined with the spiral arm populations of the Milky Way (see e.g. Mateu et al. 2009).

If the latter turns out to be true, it is even more remarkable that several clusters linked to the Sagittarius stream, which is then the only genuine dSph stream being accreted to the Milky Way, are outliers in the CMR. However, other GCs associated to the Sagittarius system by Forbes & Bridges (2010) also fall close the CMR (including NGC 6715, Pal 12, NGC 4147 and NGC 5634), thus not all GCs related to dSph galaxies have somehow particular colours.

Bellazzini et al. (1999) claimed that the stellar content and the star formation history of the Sgr dSph appears very similar to those of other dSph galaxies. Most of the GCs that are consistently off the CMR are related to the Sagittarius dSph in some way. Accurate colours and metallicities for GCs residing in dwarf galaxies are highly desirable to check our findings. If it is true that dwarf galaxies host a number of peculiar GCs, we should be able to find these GCs as well in massive galaxies, which are assembled by accreting such objects according to CDM theories. However, these peculiar clusters are faint, thus detecting them will be observationally challenging.

Note that not all clusters with particular chemical properties are offset from the CMR. Cohen (2004) demonstrate the chemical peculiarities of Pal 12, another GC associated to the Sagittarius system (Forbes & Bridges 2010). Due to the large contamination correction (as shown

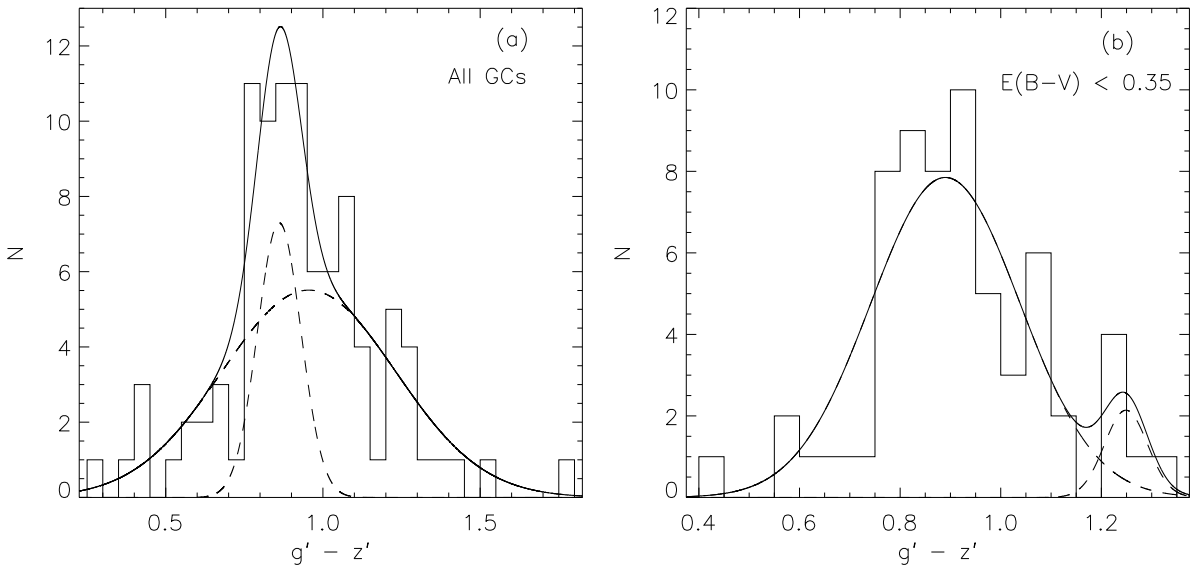

Figure 4.16: $(g' - z')$ colour distribution for different subsamples of the Galactic GCs. The GMM parameters describing the fits of the Gaussian distributions are tabulated in Table 4.2. The solid line is the sum of the two Gaussians obtained with GMM. In general, the distributions are not strongly bimodal, which is unexpected when bearing in mind the bimodal metallicity distribution of the MW.

in Fig. 4.15), this cluster falls right on the CMR. NGC 2419, another outer halo cluster with chemical peculiarities (Cohen & Kirby 2012), is not off the CMR.

4.3 Colour bimodality

It is widely known that the metallicity distribution of Galactic GCs is bimodal. If the $g' - z'$ colour is representative of the metallicity then one would expect to find bimodality in the distribution of $g' - z'$ colour. However, we ran a Gaussian mixture modelling algorithm (GMM – Muratov & Gnedin 2010) on the full Galactic $g' - z'$ distribution and did not find evidence for a bimodal distribution (Fig. 4.16, panel (a)).

The GMM parameters for the colour distribution and the corresponding [Fe/H] distribution of the full GC sample are listed in Table 4.2. It is clear that the colour distributions are not strictly bimodal and could just be skewed unimodal distributions. It would imply that the bimodal Galactic metallicity distribution transforms into a skewed unimodal distribution as a result of the non-linear CMR. This is in fact the opposite case of a unimodal metallicity distribution transforming into a bimodal colour distribution (which was studied in Yoon et al. 2006). Moreover, about half of the metal-poor clusters are attributed to the metal-rich peak based on their colours. Note that more than half of the smaller ACSVCS galaxies from Peng et al. (2006), hosting a similar number of GCs as our current sample, did not exhibit strong colour bimodality either.

Table 4.2: The results of the GMM analysis for the distributions shown in the different panels of Fig. 4.16: (a) all GCs, (b) $E(B-V) < 0.35$. Case (c) shows the GMM results for the colour distribution (presented in Fig. 4.17) for low-reddening GCs, excluding two Sagittarius GCs (Terzan 7 and Whiting 1), Pal 1 and GCs with $\sigma_{g-z} > 0.1$. Cases (a)* and (c)* present the corresponding [Fe/H] distributions for cases (a) and (c) (presented in Fig. 4.18). See text for more details.

	(a)	(b)	(c)	(a*)	(c*)
μ_1	0.86 ± 0.12	0.89 ± 0.053	0.86 ± 0.04	-1.59 ± 0.05	-1.65 ± 0.08
μ_2	0.96 ± 0.27	1.25 ± 0.11	1.07 ± 0.03	-0.52 ± 0.05	-0.52 ± 0.20
μ_3	...	...	1.25 ± 0.03	...	...
σ_1	0.07 ± 0.07	0.14 ± 0.03	0.10 ± 0.02	0.38 ± 0.04	0.38 ± 0.041
σ_2	0.28 ± 0.13	0.06 ± 0.03	0.03 ± 0.01	0.19 ± 0.04	0.16 ± 0.041
σ_3	...	...	0.04 ± 0.01	...	...
N	96	63	56	96	56
D	0.47 ± 1.76	3.28 ± 0.94	5.11 ± 1.49	3.59 ± 0.36	3.67 ± 0.81
$p(\chi^2)$	0.06	0.45	0.23	0.001	0.055
$p(DD)$	0.88	0.21	0.29	0.11	0.003
$p(kurt)$	0.98	0.87	0.66	0.01	0.583
Ratio	26 : 74	93 : 7	80 : 11 : 9	75 : 25	83:17
$kurt$	1.14	0.34	-0.09	-0.97	-0.18

As our sample is not large (compared to massive galaxies with extensive GC systems) and there are some outliers in the CMR, with colour determinations affected by high reddening, we decided to analyse a subsample limited to clusters with low reddening. The distribution for this subset is presented in panel (b) of Fig. 4.16. In spite of the imposed constraints, no colour bimodality is found. The corresponding GMM parameters are listed in Table 4.2.

It is known GMM is susceptible to outliers, especially long tails (Muratov & Gnedin 2010; Blakeslee et al. 2012). In a final attempt to recover the $g' - z'$ Galactic colour distribution, we make a new subset of Galactic GCs, excluding GCs with a colour error larger than 0.1 mag, two Sagittarius CMR outliers (Terzan 7 and Whiting 1) and Pal 1 (for reasons described above). Fig. 4.17 presents the $g' - z'$ colour distribution for this subset, which is trimodal ($D > 2$ and $kurt < 0$, although the p value suggests that it is not very statistically significant). GMM parameters are listed in Table 4.2.

The clusters in the reddest peak of the histogram (NGC 104, NGC 6356, NGC 6352, NGC 6624 and Pal 8) are all bulge or thick disk clusters. Heasley et al. (2000) proposed NGC 104 (47 Tuc), NGC 6352, NGC 6624 had a common origin, but Gao et al. (2007) did not assign the GCs to the same accretion streams. Vandenberg et al. (2013) found a bifurcation in their age-metallicity diagram of clusters with disk-like kinematics. It is remarkable that NGC 104, NGC 6352 and NGC 6624 all pertain to the second branch in their diagram. No age estimate was obtained in the

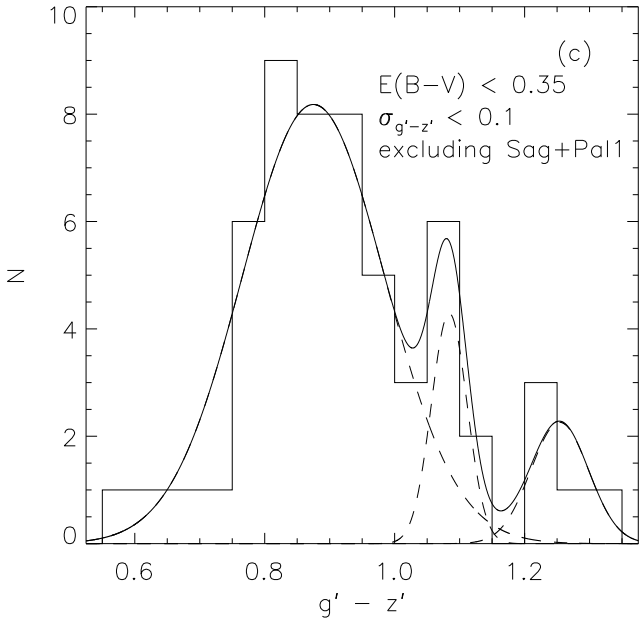

Figure 4.17: Trimodal $(g' - z')$ colour distribution for a Galactic GC low-reddening subsample with small colour errors and excluding Whiting 1, Terzan 7 and Pal 1. The GMM parameters describing the fits of the Gaussian distributions are tabulated in Table 4.2. The solid line is the sum of the Gaussians obtained with GMM. See text for more details.

latter study for NGC 6356 and Pal 8, which are subject to considerable reddening ($E(B-V) \sim 0.3$).

Peng et al. (2006) found VCC 798 (NGC 4382/M 85) as the best candidate for a trimodal colour distribution. This galaxy is classified as $T = -1$ in the RC3 (Corwin et al. 1994), indicating pure S0, and has a very strong disk component, although the inclination angle makes it appear less obvious. It is tempting to speculate that the trimodal colour distribution is linked with the disk component. Nevertheless, the giant elliptical galaxy NGC 4365 also hosts three subpopulations of GCs (Brodie et al. 2005; Blom et al. 2012a,b), making a link with the disk less probable. For M 31, a spiral galaxy, some evidence for a trimodal distribution was found, although it is not completely clear how many subpopulations are present (Perrett et al. 2002).

In Fig. 4.18 we present the [Fe/H] distributions of the different subsamples. It is clear that the [Fe/H] distribution for all GCs (case (a)) is bimodal, which is confirmed by the GMM results given in Table 4.2. It is clear that the strong [Fe/H] bimodality vanishes limiting the sample to the low-reddening clusters, because a significant fraction of the metal-rich GCs is located towards the bulge of the Galaxy, where the reddening is significant. Note that the GMM parameters for the [Fe/H] distribution associated to case (c) are not conclusive: the peak separation D favours a bimodal distribution, while the second peak is not clearly apparent in Fig. 4.18. The rather large p values favour a unimodal distribution. It was not possible with GMM to fit a trimodal distribution to the case (c) [Fe/H] distribution. Therefore it is rather normal no bi-

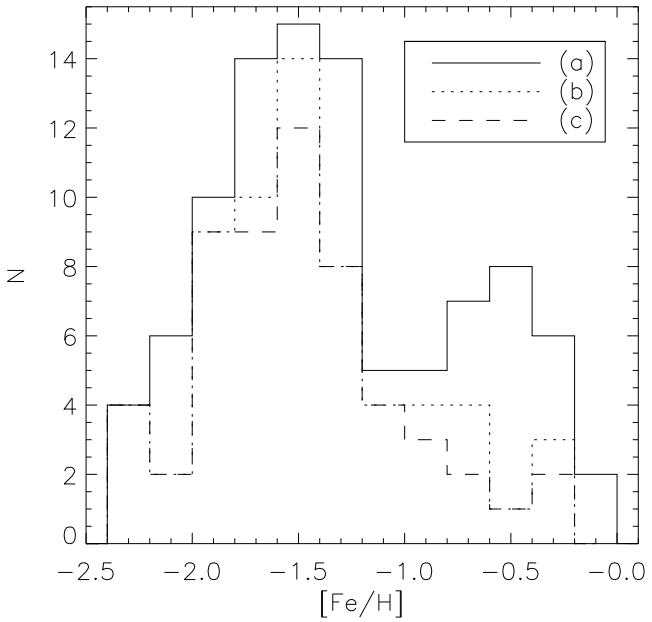

Figure 4.18: [Fe/H] distribution of the different subsamples. Case (a) presents all GCs, case (b) is limited to low-reddening clusters with $E(B-V) < 0.35$ and case (c) is limited to low-reddening clusters with small colour errors and excludes GCs associated to Sagittarius. It is clear that the strong [Fe/H] bimodality disappears when limiting the sample to low-reddening clusters.

modal colour distributions were found for the different subsamples and it nicely illustrates that selection effects can complicate the correct interpretation of the colour and metallicity distributions.

4.4 Summary

In the current study we used our integrated optical photometry (presented in chapter 3) to confirm and improve existing CMRs. For the $(g'-z')$-[Fe/H] relation we double the number of Galactic GCs used in the fit when comparing to the earlier studies by Peng et al. (2006) and Blakeslee et al. (2010). Moreover, these authors relied on pure aperture photometry and did not correct for foreground contamination. Nevertheless, we rely on the same extragalactic data to extend the metallicity range. Furthermore, we confirm the $(g'-i')$-[Fe/H] relation of Sinnott et al. (2010), for the first time with Galactic GCs. However, we find an offset at both the metal-rich and metal-poor end of their $(g'-z')$-[Fe/H] CMR. We also demonstrate that the CaT metallicity indicator behaves non-linear when compared to the $(g'-i')$ and $(g'-z')$ colours.

We scrutinise the influence of the reddening estimate on the scatter in the CMR and demonstrate that this scatter can be significantly reduced by combining Cardelli et al. (1989) and Schlafly & Finkbeiner (2011) reddening laws. We also discuss how the scatter in the CMR is influenced

by the contamination correction, differential reddening, HB morphology, age, present-day mass function variations and structural parameters.

We find a group of clusters which lie conspicuously off the Galactic CMR: with one possible exception, all these objects are associated with the Sagittarius dwarf or the proposed Canis Major dwarf. This might imply that a subset of globular clusters belonging to dwarf spheroidal galaxies are a different population from those found in the Milky Way and other bright local group members. If so, it will not be possible to build our globular cluster system from mergers of dwarf galaxies with the early Milky Way, unless such objects are radically different from present-day dwarf spheroidals in the Local Group.

Structural King model parameters for Galactic GCs in SDSS colours

5

5.1 Introduction

Globular clusters are ancient stellar systems (formed beyond $z \sim 3$), containing of O(10^5) stars within a volume of ~ 100 pc^3. They provide essential information on the formation and evolution of the Galaxy (e.g., Forbes & Bridges 2010) and are natural laboratories for theories of stellar structure (Vandenberg et al. 2013, and references therein). The structure and properties of globular clusters bear the imprint of the initial conditions of their formation and interactions with the galactic environment (Brodie & Strader 2006). The high stellar densities (without a dark matter halo) make globular clusters invaluable objects for the study of N-body dynamics (e.g., Elson et al. 1987; Heggie & Hut 2003; Trenti et al. 2010; Hurley & Shara 2012). We also expect that these complex environments are involved in the formation of several stellar exotica, such as blue stragglers (Ferraro & Lanzoni 2009), extreme horizontal branch stars (Fusi Pecci et al. 1992), cataclysmic variables and millisecond pulsars (Benacquista & Downing 2013), intermediate-mass black holes (Lützgendorf et al. 2013), and black hole binaries (Lin et al. 2013). Structural parameters for globular clusters are needed to explore correlations between stellar populations, dynamics and the Galactic environment. The Milky Way is the only object where these questions can be explored in detail, as we can resolve clusters to the level of individual stars on the main sequence and we will soon be able to obtain their internal kinematics and proper motions (e.g., Bianchini et al. 2013).

Most structural parameters for Galactic globular clusters are still measured from surface brightness profiles derived from an inhomogeneous compilation of older CCD and photographic data (Trager et al. 1995). The most extensive compilation (McLaughlin & van der Marel 2005) fits these to the classical King (1962, 1966) profile for self-gravitating systems or to Wilson (1975). More recently, Miocchi et al. (2013) have derived structural parameters based on star counts from HST and ground-based photometry for 26 clusters: this latter method is arguably the most accurate (e.g., Ferraro et al. 1999, 2003) but it is observationally expensive (e.g., Salinas et al. 2012) and cannot be applied to unresolved systems such as clusters in all but the nearest galaxies (Wang & Ma 2013). As long as the clusters are bright, we expect that surface brightness profiles will perform adequately (Noyola & Gebhardt 2006). However, in nearly all instances (and almost irrespective of methodology) it is difficult to decide on a 'radius' where globular clusters 'end'. In several cases, clusters are seen to contain 'extra-tidal' stars (e.g., NGC 1851 – Olszewski et al. 2009; NGC 5694 – Correnti et al. 2011), while tidal tails and other debris are relatively common (e.g., Grillmair et al. 1995; Odenkirchen et al. 2001; Sollima et al. 2011). A further complication is that many clusters do not fit smooth King-like models, but exhibit a central density enhancement or core-collapse (Cohn 1980). Given the large ages of these objects, this is expected to have occurred in most clusters (Djorgovski & Piotto 1993; Harris 1996), but the formation of hard binaries is expected to halt this process (Vesperini & Chernoff

1994; Fregeau & Rasio 2007).

In this chapter we use the imaging presented in chapter 3 to produce surface brightness profiles and derive structural parameters by fitting King models to our homogeneous survey of the Galactic globular cluster system. We supplement these data with clusters from the SDSS (York et al. 2000; Ahn et al. 2012), where we also use the much larger images to explore the limitations of our dataset. We use the derived structural parameters to explore internal colour gradients and the interactions between clusters and the Galaxy. In the next section we describe the data and our analysis. We present structural parameters and compare these with previous work: at this stage we also explore how smaller CCD imaging (from our CTIO observations) affects our measurements, by comparison with clusters in common with the SDSS (which theoretically can be studied to any radius). We then discuss our results and explore their significance for stellar populations and the interactions of clusters with our Galaxy.

5.2 Dataset

For several GCs in chapter 3 we were unable to perform aperture photometry because bright red giants within the cluster half light radius saturated the CCD. Our purpose in that chapter was to provide a conservative set of aperture magnitudes and colours and we therefore excluded a number of clusters from our analysis. Here, we fit King models to the surface brightness profiles and we are able to apply an iterative clipping method and profile fitting to derive 'model' magnitudes. We have a total of 111 clusters with g and z photometry and 61 with r and i data, plus several more with SDSS data. In the latter case, we built large images with MONTAGE[1] and in theory we can follow these clusters over areas of degrees on the sky, but we caution that stitching together several SDSS stripes often leads to variable sky levels (as illustrated in Fig. 5.1).

5.3 Surface Brightness Profiles

We derive radial surface brightness profiles for all clusters and all passbands by using conventional aperture photometry, in annuli of increasing radius, as in building a curve of growth for extended systems. For the CTIO 0.9m data, where the field of view is $13'$ on the side, the annuli are 15 pixels wide, or approximately 4 times the seeing disk. We integrated to the edges of the images, although in some cases we were forced to stop at smaller radii for small or faint clusters, where we reached the sky limit. We applied a similar technique to SDSS data out to $6.5'$ (for consistency with the analysis of CTIO data) and subsequently expanded the annuli to reach the tidal radius of each object.

[1] http://montage.ipac.caltech.edu/

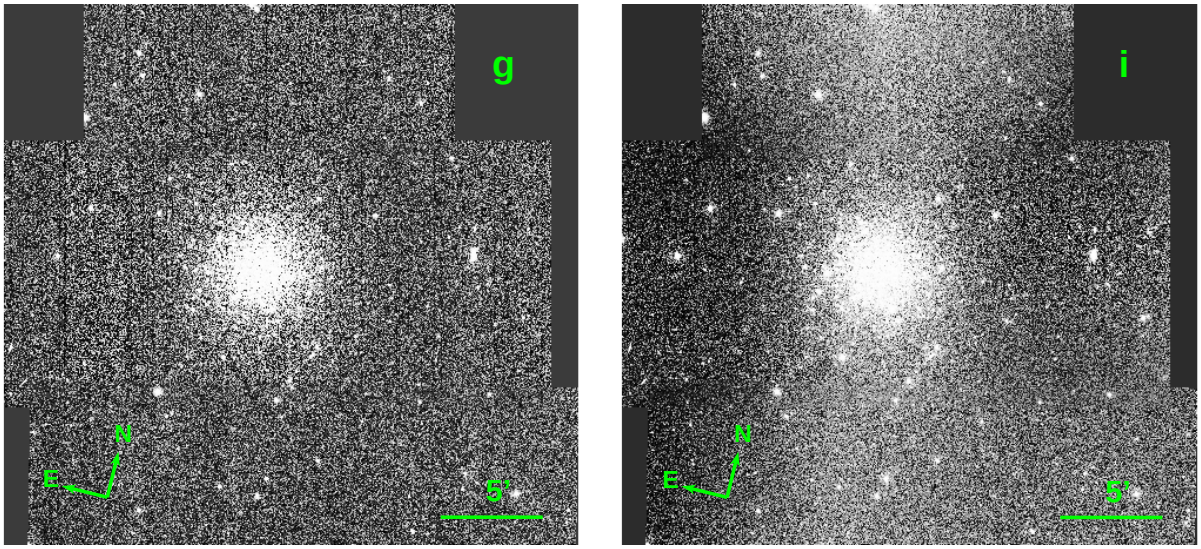

Figure 5.1: Mosaicked SDSS g and i band images of NGC 5466. It is clear that the sky of the i band image is problematic, resulting in a less accurate i-band SB profile.

An essential element in this procedure is the choice of an appropriate centroid for the apertures. We use the centre determination carried out in section 3.3.1 as the standard approach: by using a series of small apertures surrounding the optical centre and choosing the aperture where the flux is maximal (Noyola & Gebhardt 2006; Bellazzini 2007). Because the distribution of bright stars is stochastic and the central surface brightness distributions of King models are flat, errors in the centring may lead to artificially flat profiles (Mackey & Gilmore 2003b). However, as will become clear further in this chapter, sometimes the centring can also lead to artificially peaked profiles. When fitting King profiles we found it sometimes necessary to reduce the influence of the central aperture as described below.

Determination of an accurate sky value is also paramount. Small errors in sky values propagate because of the large areas of the apertures, especially in the outer regions of each cluster. We have used the MMM algorithm to measure the sky flux in apparently blank regions in the corners of the CCD images: the routine is adapted from DAOPHOT (Stetson 1987) specifically for crowded fields as in our globular clusters. In our case, exposure times are relatively short to preserve the dynamic range between the bright central regions and the low surface brightness wings of the cluster profile; this leads to more uncertain sky determinations. Peng et al. (2002, 2010) point at similar issues when determining surface brightness profiles for galaxies: in some cases the outskirts of extended systems are barely above the sky noise and even the areal increase in the apertures is offset by the increasing noise from the sky, flat field and detector read. This may lead to a bias in favour of low effective radii. The problem may be complicated by our assumption of circular symmetry, whereas there is evidence of changing ellipticity and position angles in the outer regions of globular clusters (Bianchini et al. 2013). Additionally, some clusters have stars beyond the tidal radius, while others under-fill their tidal region (Gieles et al.

2010; Alexander & Gieles 2013). Peng et al. (2002, 2010) advises for the solution we have eventually chosen, to estimate the sky independently and hold it fixed for the estimate.

We then fit the surface brightness profile to a King (1962) model of the form:

$$SB(r) = k\left(\frac{1}{[1+(r/r_c)^2]^{1/2}} - \frac{1}{[1+(r_t/r_c)^2]^{1/2}}\right)^2, \tag{5.1}$$

where r is the aperture radius, r_c is the core radius and r_t the tidal radius. The constant k is related to the central surface brightness μ as

$$\mu = k\left(1 - \frac{1}{[1+(r_t/r_c)^2]^{1/2}}\right)^2.$$

We fit these using a Levenberg-Marquardt non-linear least squares algorithm (Press & Schechter 1974; Bevington & Robinson 1992). We define a concentration index $c' = r_t/r_c$ to simplify our numerical work, while $c \equiv log(r_t/r_c)$ as in McLaughlin & van der Marel (2005). We iterated the fit with 3σ clipping about each point to remove the effects of bright contaminating stars. We do not adopt this within the core radius, to avoid biases against core-collapsed clusters. However, we found that in many cases the fit gave excessive strength to the central aperture, as the (small) photometric error results in a large weight being given to this data point. Especially for clusters with core collapses or central cusps (Vesperini & Trenti 2010), we found it necessary to artificially increase the error bars for the central aperture in order to lower its weight in the fitting process. An example of this is given for the z-band profile of NGC 288 in Fig. 5.2. The centre of the cluster appears to coincide with a bright red giant. All clusters where this procedure was needed are clearly marked in subsequent figures. In some instances, we found that the concentration c became very high and dominated the fit, and we set this to infinity.

Since the field of view of CTIO data does not reach to the tidal radius, it is inherently difficult to measure this quantity. We then used an *ad hoc* measure, adopting as the tidal radius the radius at which the best fit King profiles had flux comparable to the mean sky noise. For some very poor and sparse clusters we limited the tidal radius to $200''$ or $1000''$.

We show an example King profile for the classical rich cluster NGC104 (47 Tucanae) in Fig. 5.3. Fits for all other objects are placed in an on-line appendix. We tabulate an extract of the derived parameter values in Table 5.1. We estimated the errors on these parameters by bootstrapping the derived fits with 100 random points (assuming Poisson errors) and deriving new King model fits to these artificial data. The errors in the table are the 1σ conditional errors on each parameter. Where we have more than one observation in one or more filters, we computed parameters independently and then adopted their median value for Table 5.1. The entire table is placed in an on-line appendix.

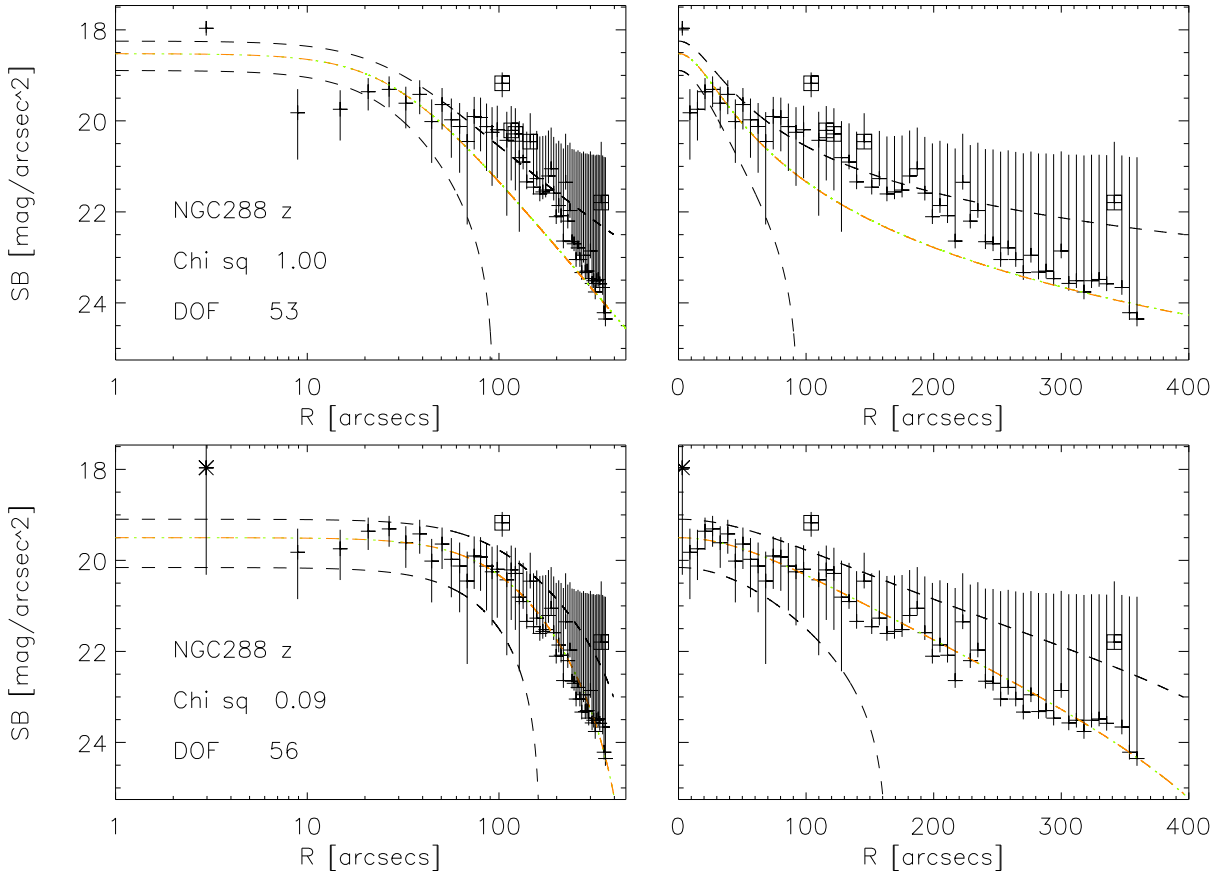

Figure 5.2: Surface brightness distribution in z for NGC 288 in the z-band. The left panel focuses on the inner region of the cluster, while the right panel gives details on the outer regions. The King models we fit are shown as dotted (green) and dashed (orange) lines (for two alternative definitions of concentration: dotted green corresponds to $c = log(r_t/r_c)$, dashed orange to $c = r_t/r_c$). The dashed lines show the 3-sigma deviation of the model, with squares representing the data points that have been clipped iteratively. The upper panel shows the fit with natural $(1/\sigma)$, the lower panel shows the fits with adjusted weight for the SB point indicated with an asterisk. See text for more details.

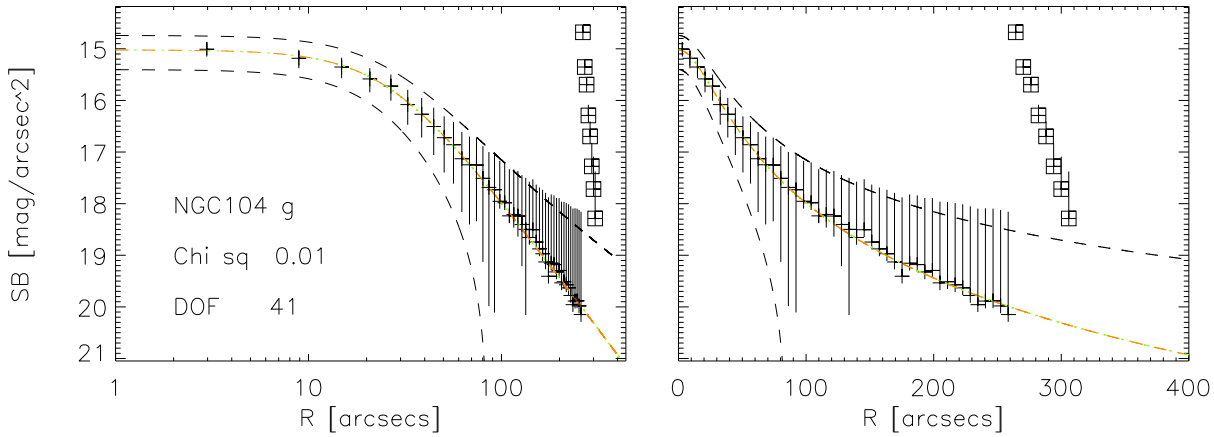

Figure 5.3: SB distribution of NGC104 in the g-band. Legend as in Fig. 5.2. The spike in the outer region is caused by an artefact on the CCD boarder. The cluster is not centred well on the CCD.

Table 5.1: Extract of the King parameter table based on CTIO SB profiles. Central SB uncertainties are pure bootstrapping uncertainties and do not include calibration uncertainties, neither the systematic error introduced in chapter 3.

ID	Filter	μ_0 $[\mathrm{mag}/''^2]$	$\sigma(\mu_0)$	r_c $[']$	$\sigma(r_c)$	c	$\sigma(c)$	r_h $[']$	$\sigma(r_h)$	Model mag	Aper mag
NGC104	g	14.796	0.005	0.429	0.004	4.479	0.030	1.436	0.007	5.542	5.526
NGC104	z	13.819	0.009	0.565	0.008	1.449	1.320	1.307	0.009	4.330	4.356
NGC288	g	20.286	0.011	1.693	0.054	0.782	1.459	1.946	0.040	9.321	9.268
NGC288	r	19.899	0.010	1.849	0.048	0.630	0.505	1.935	0.033	8.873	8.803
NGC288	i	19.655	0.012	1.958	0.087	0.630	1.559	1.947	0.059	8.603	8.482
NGC288	z	19.534	0.019	1.987	0.346	0.582	1.628	1.749	0.244	8.632	8.486
NGC362	g	15.070	0.002	0.175	0.000	2.316	0.381	0.967	0.008	7.400	7.354
NGC362	r	14.390	0.001	0.159	0.000	2.295	0.172	0.918	0.008	6.897	6.843
NGC362	i	14.087	0.001	0.158	0.000	2.917	0.252	1.082	0.007	6.495	6.437
NGC362	z	13.904	0.002	0.160	0.000	2.606	0.376	0.886	0.007	6.412	6.353

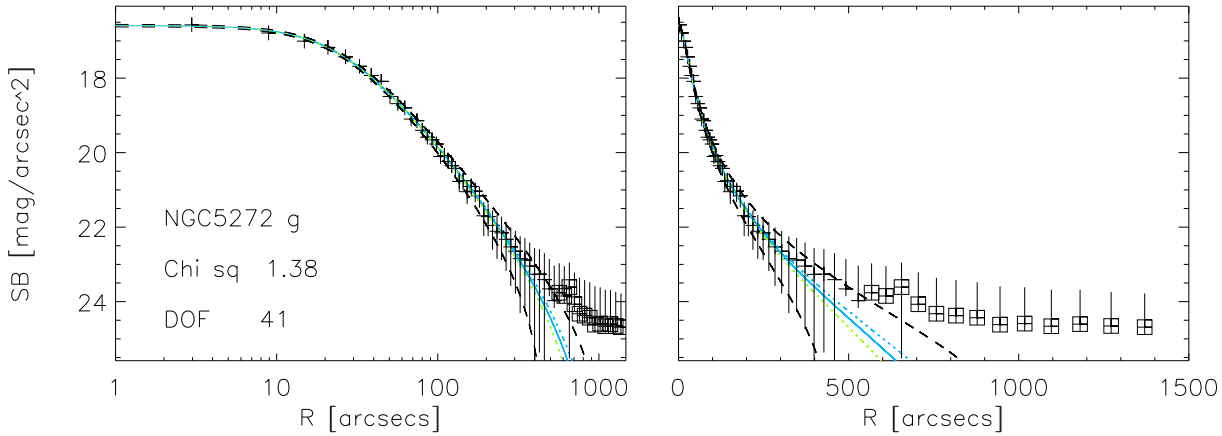

Figure 5.4: g-band SB distribution of NGC5272. The blue dotted line presents the first iteration fit, before the sigma-clipping. The squares indicate the clipped SB points. The blue solid line presents the final King profile. The green dotted line presents the model fit when limiting the SB to points out to $\sim 4.2'$ (representing the minimal CTIO FoV).

5.3.1 Clusters with SDSS data

Several clusters have been observed by the SDSS, with a few in common with our CTIO observations. These data allow us to study how the smaller field of view of the CCD on the CTIO 0.9m affects our determination of King model parameters. The dataset is the same as used in chapter 3, with the addition of NGC 5904 and NGC 6341. For each of these clusters we produce a wide field image, reaching well beyond the tidal radius, by stitching together several SDSS stripes with MONTAGE, although this may lead to potential problems with matching sky levels across observations taken in different conditions. The resulting surface brightness profile (and King model) for NGC 5272 is shown in Fig. 5.4 and reaches to $\sim 20'$.

On the other hand, this sometimes results in unphysical values for the sky: in the i image of NGC 5466 there is a sky gradient (as shown in Fig. 5.1). Some bands, especially u, are also much shallower and this results in apparent colour gradients as the fit is biased towards low scale lengths (Peng et al. 2002, 2010). Even when wide-field data are available, estimating the tidal radius can be difficult (e.g., Jordán et al. 2009).

Effects of a limited field of view

Because SDSS data potentially reach to any radius of interest, we can use SDSS photometry to explore how the smaller field of view of the CTIO 0.9m CCD affects our determination of model parameters. We use the SDSS mosaics to determine the surface brightness profile and fit this to a King model. We then artificially restrict the field to radii of $4.2'$ (the smallest coverage we have) and $6.5'$, to estimate the influence of the field of view on the model fits.

In Fig. 5.5 we compare the fits to the g-band profile of NGC 5053 for the full and limited radii.

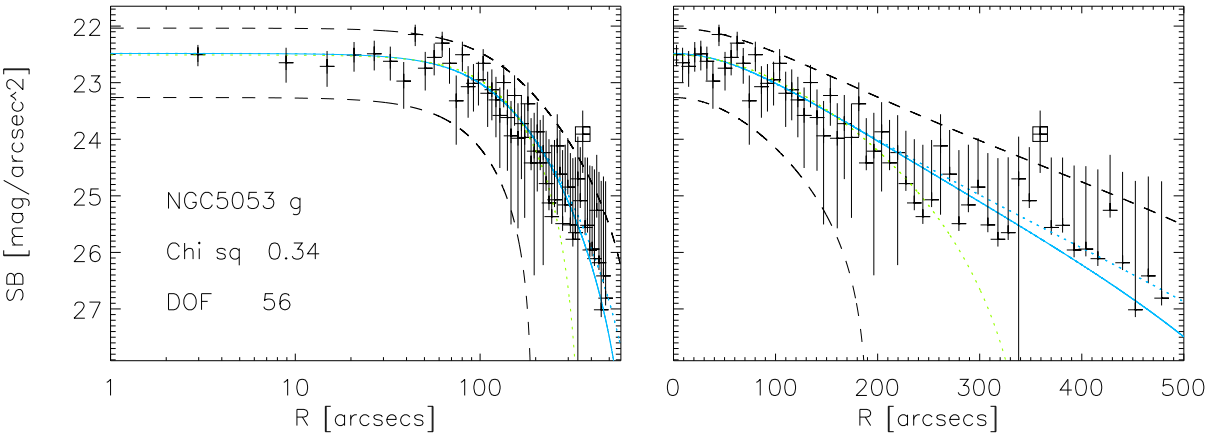

Figure 5.5: SB distribution of NGC5053. Legend as in Fig. 5.4.

While the outer regions show a large discrepancy, with respect to the smaller aperture radii, the King model fits behave reasonably well. We show all other clusters and their fits (similar to the above figure) in the on-line appendix.

Fig. 5.6 presents a comparison of the core radii obtained with the full FOV and the limited 'CTIO-style' profiles. There is generally good agreement between these two quantities and this suggests that the core radius is well determined. However, it is clear that the scatter is much larger for the 4.2 arc minute FOV than for the full CTIO FOV. This illustrates that it is important to exploit the entire CTIO FOV. Some poor or sparse clusters with very poor fits have r_c values outside the plot range, as indicated in the figure caption. Note that the core radii of NGC 5053 based on the 4.2 arc minute FOV show significant scatter, while the values for the full ($6.5'$) CTIO profiles compare much better to the ones obtained with the entire SDSS FOV.

Fig. 5.7 presents a comparison of the concentration parameter values based on the full mosaicked SDSS frame and the artificially truncated profiles. There is reasonably good agreement between the SDSS (full mosaic) and the parameters derived from a smaller field of view, with some exceptions. When using the full CTIO FOV we obtain generally more consistent results. Please note that Pal 4 (i-band) and NGC 7078 (g and r-band) are not within the range plotted in the left-hand panel of Fig. 5.7. The r-band concentration obtained for NGC 7078 is also outside the plot range of the right-hand panel. For both the 4.2 and 6.5 arc minute FOV, the resulting concentrations of some clusters were infinite for some filters. These concentrations are not presented in the figure. Recently, den Brok et al. (2013) published a line-of-sight velocity and proper motion study of NGC 7078. Their best axisymmetric Jeans models includes a central dark mass, originated by a high concentration of stellar remnants at the cluster centre. Moreover, they conclude that the mass concentration is significantly higher than the current literature values and classify it as a core-collapsed cluster without central IMBH.

Fig. 5.8 shows a comparison of the core radii based on the SDSS and CTIO data (taking the median of the r_c in case of multiple observations). In general, these compare well. The only

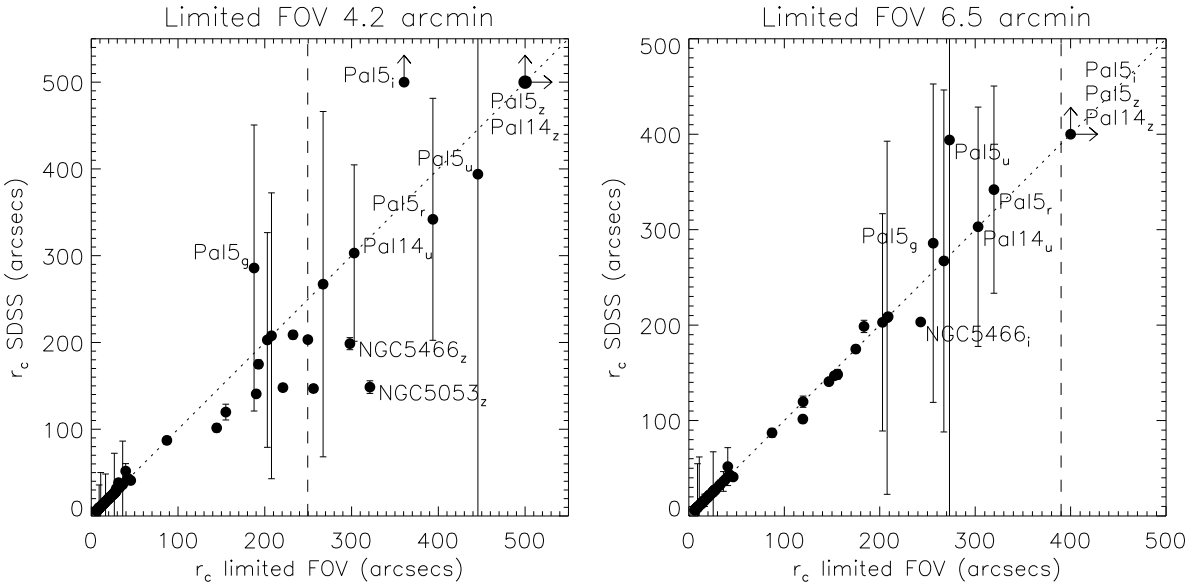

Figure 5.6: Comparison of the core radii r_c based on the full mosaicked FOV and artificially limited SB profiles of 4.2 and 6.5 arc minutes (left and right panel, respectively). The artificial cuts limiting the SB profile radius are indicated with the dashed lines. The dotted line represents a one-to-one correspondence. It is clear that the scatter is reduced using the 6.5′ FOV, stressing the importance of using the entire CTIO FOV. Outliers are generally faint sparse clusters. See text for more details.

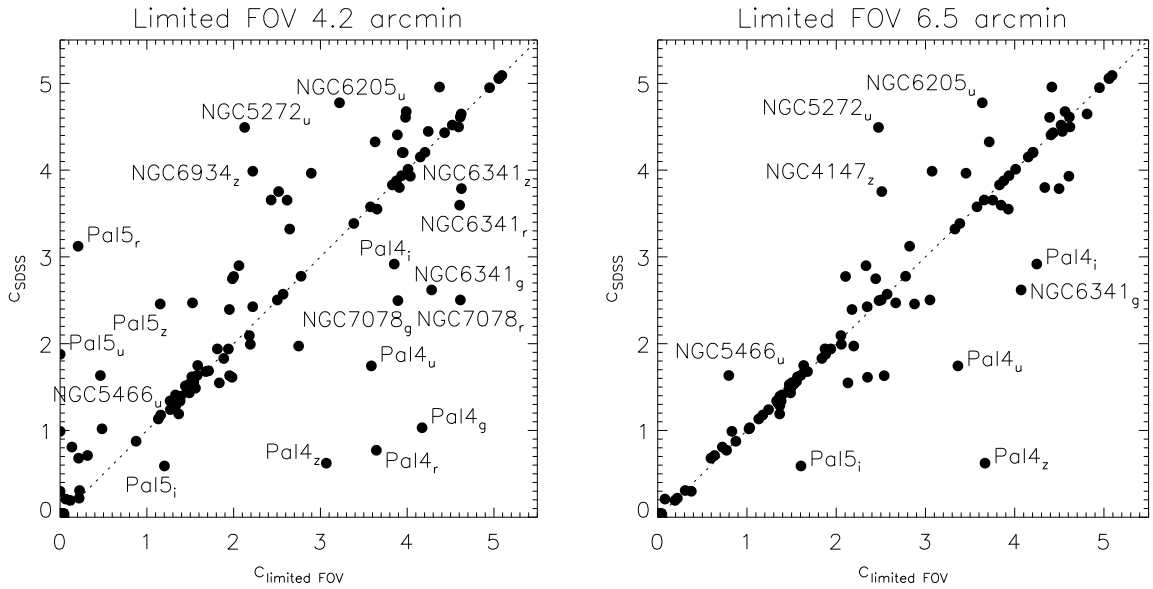

Figure 5.7: Comparison of the concentrations c based on the full mosaicked FOV and an artificial limited SB profile. The dotted line represents a one-to-one correspondence. The bootstrap uncertainties for the concentrations can be large and are not shown for clarity. See text for more details.

discrepant core radius is found for the core-collapsed cluster Pal 3. The fit to the CTIO z-band SB profile is very poor, causing the large difference between the obtained values. However, the z-band fit for SB profile based on June 6 2004 data compares reasonably well to the obtained values for the other bands (with $r_c \sim 0.17'$). Only the results based on the June 5 2004 data are highly discrepant (with $r_c \sim 1.1'$). Nevertheless, taking the median over both nights still

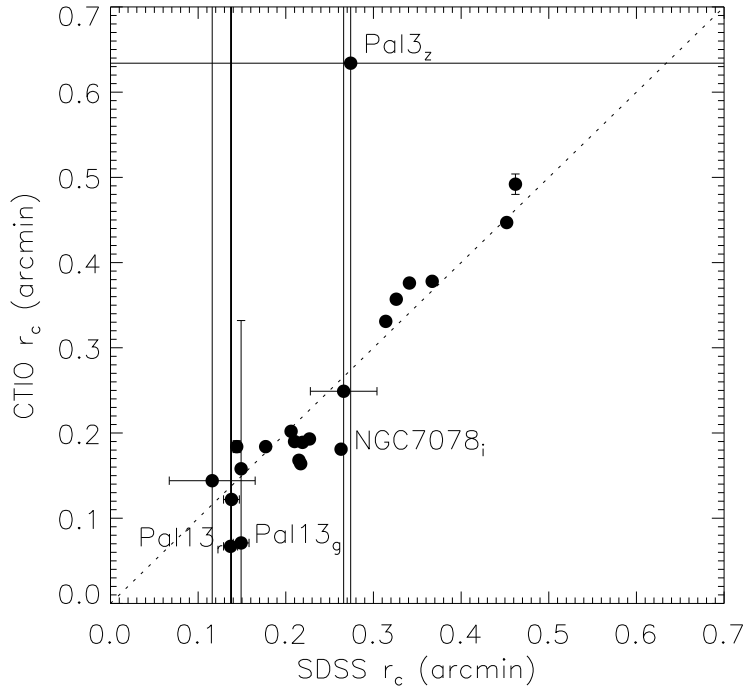

Figure 5.8: Comparison of the core radii r_c based on the full mosaicked SDSS FOV and on the CTIO data (taking the median value in case of multiple observations). The asterisks present the results for the g-band, the filled circles present the z-band results. The r_c compare generally well, with Pal 3 and Pal 13 as exceptions. The dotted line represents a one-to-one correspondence.

results in an unrealistic value $r_{c,z} \sim 0.6'$ for this cluster (as the GC was only observed on those 2 nights). The large error bar is representative for the uncertainty on this value. Note that Pal 3 is only marginally brighter than the sky contribution to the flux. The discrepant r_c value is based on a 60s exposure, while longer exposures for g (270s) and z (410s) taken on June 6 2004 result in a more accurate sky determination and SB profile.

Fig. 5.9 shows how well the concentrations compare for GCs with both SDSS and CTIO data. It is clear that the concentration is poorly constrained for some of the sparse clusters (like Pal 13). For NGC 7078 we find large discrepancies in the concentrations measured using different filters for both SDSS- and CTIO-based profiles. This cluster is listed as a core-collapsed cluster by Harris (1996), indicating that it is hard to fit a King model to the SB profile. Moreover, Fig. 5.7 illustrated that our limited FOV can affect the SB profile fits for this GC (with different values for the concentration in the r- and i-bands).

5.3.2 Comparison with previous work

We now compare our results with previous determinations of integrated magnitudes and structural parameters from the literature. In Fig. 5.10 we show our half-light radii (in the g and z bands) vs. the values in the Harris (1996) compilation. For smaller clusters ($r_h \lesssim 1'$), the data fall close to the 45-degree line, albeit with somewhat large scatter. For clusters subtending a

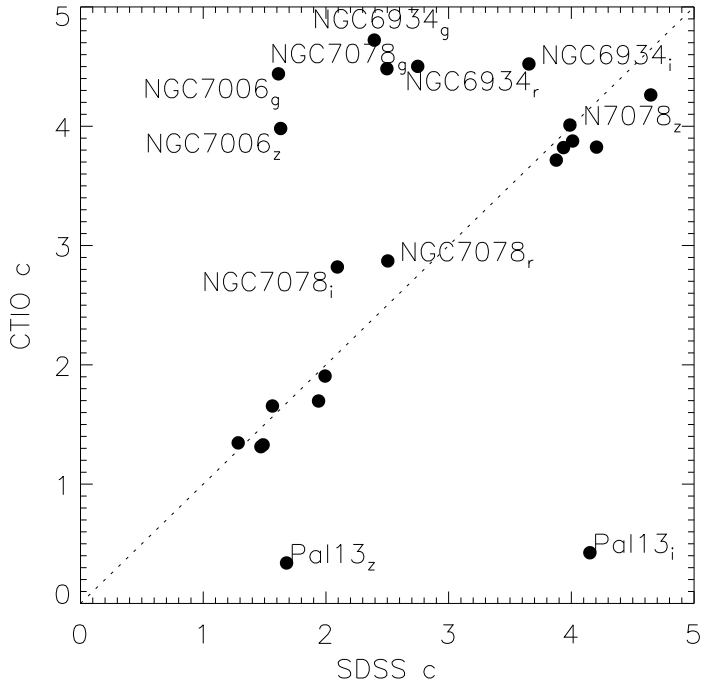

Figure 5.9: Comparison of the concentrations based on CTIO and SDSS data. The dotted line represents the one-to-one correspondence.

larger angle on the sky, we find that our r_h are systematically lower, probably because of our poorer value of r_t.

As an additional check, we selected a representative subsample of CTIO clusters and fitted Sérsic profiles in pixel space with BUDDA, developed by de Souza et al. (2004); Gadotti (2008). In Fig. 5.11 a BUDDA fit of a g'-band observation of NGC 2808 is presented. The blue line presents the Sérsic profile, with the related effective radius r_e given by the red line. As a reference, the orange line presents the King half-light radius r_h as given by Harris (1996). The horizontal light-blue line presents the saturation level of the CCD. Again, we found that generally the effective Sérsic radius (equivalent to the radius encompassing half of the cluster light) was significantly smaller (about a factor three) than the literature values. Note that both approaches suffer from the sky determination issues related to the limited FOV of the CTIO data.

Fig. 5.12 compares our core radii (based on the g- and z-bands) with those listed in the Harris (1996) compilation. With some exceptions for poor clusters (as shown in the figure) the match between the two datasets is very good.

Fig. 5.13 compares the concentrations with the literature (Harris 1996). In general, our estimates of the concentration are higher than what was previously estimated. Miocchi et al. (2013) note several instances where surface brightness profiles return excess luminosity in the core, which is not seen in their (star-count based) profiles. Of course, the concentration index depends on both the core and tidal radius, and we have seen how in our case this latter value is more poorly

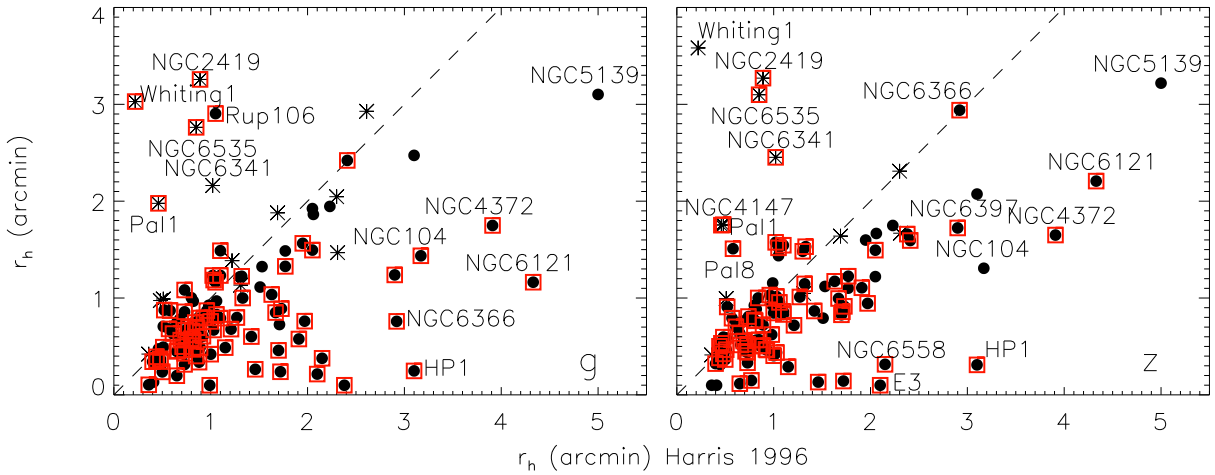

Figure 5.10: Comparison of the half-light radii r_h between our results (for the g- and z-band) and the literature (Harris 1996). Filled circles are values based on CTIO SB profiles, supplemented with SDSS values represented by asterisks. The dashed line indicates the one-to-one correspondence. Core-collapsed clusters, for which infinite concentrations were used to make the fit or for which $c \geq 3$, are indicated with red boxes. In general, our r_h estimate for large clusters is lower than the value known in the literature. See text for more details.

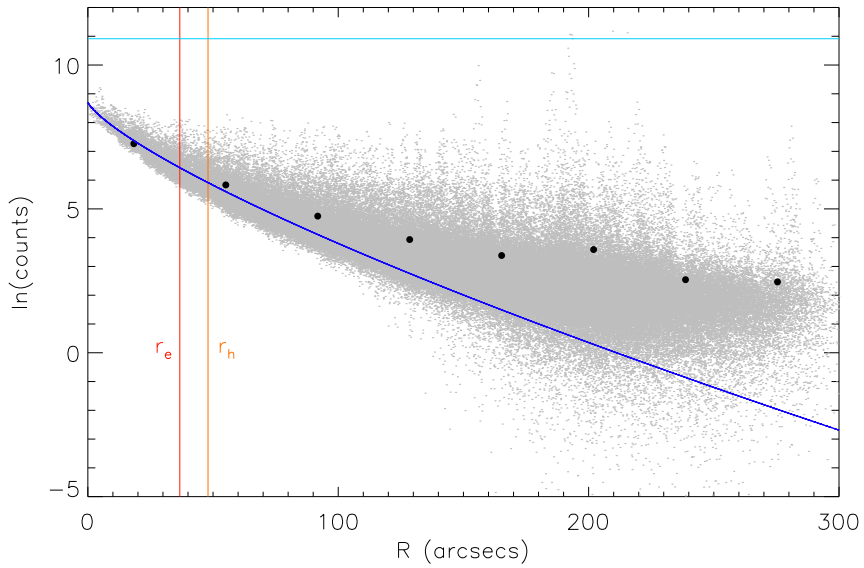

Figure 5.11: Radial profile of NGC 2808: the blue line shows the fit of a Sérsic profile with BUDDA (de Souza et al. 2004; Gadotti 2008). The orange line presents the King profile half-light radius r_e (Harris 1996), the red line presents the Sérsic effective radius r_e from the BUDDA fit. The saturation level is presented by the light-blue line. The black dots give the mean values of the flux within annuli with r_e widths.

estimated, with a bias to smaller values, which would result in higher concentrations.

We now integrate the King profiles numerically to compute a model magnitude within the half-light radius (for each observation separately). We show an extract of the table containing the median model and aperture magnitudes for all observations and all filters in Table 5.1 for the CTIO data. The SDSS-based model and aperture magnitudes can be found on the G2C2 web-

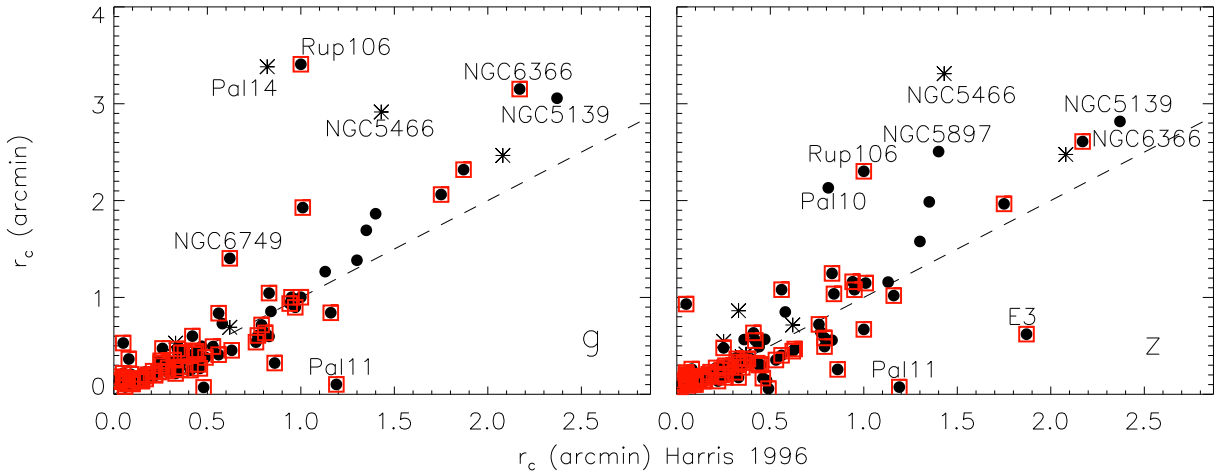

Figure 5.12: Comparison of the core radii r_c between our results (for the g- and z-band) and the literature (Harris 1996). Legend as in Fig. 5.10. In general, our r_c compare well to the literature values. Error bars are not presented for clarity. See text for more details.

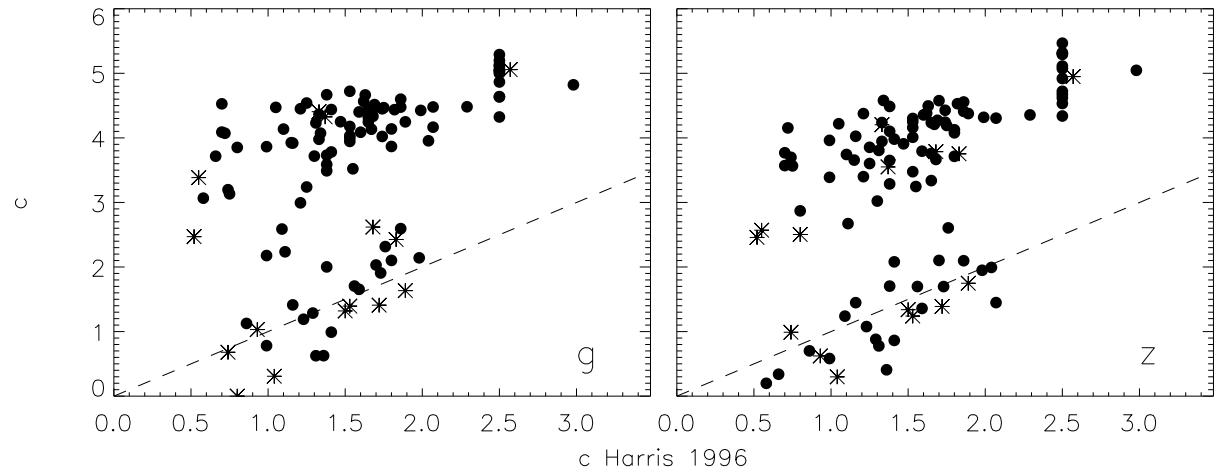

Figure 5.13: Comparison of the concentrations c obtained for the g- and z-band data and the literature (Harris 1996). Filled circles are parameter values based on CTIO data, which is supplemented with SDSS data, represented by asterisks.

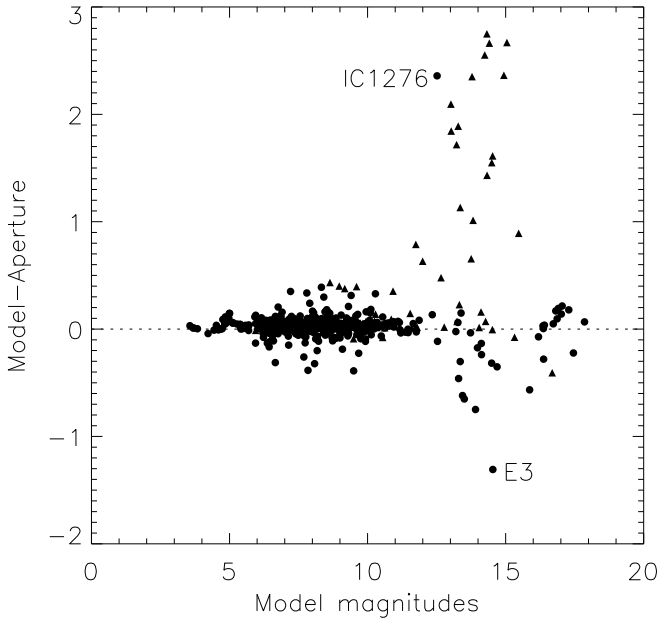

Figure 5.14: Magnitude difference between model and aperture magnitudes (within r_h) as a function of the model magnitude (for all available filters). Filled circles are used for CTIO-based results, filled triangles are used for SDSS based results. The magnitude differences for the SDSS data are higher, because of the higher fraction of poor clusters (including e.g. Pal 1, Pal 3, Pal 13). SDSS i- and z-band magnitudes for Pal 14 and all magnitude differences for Pal 5 are not included in this plot (r_h was so unrealistically high, causing apertures larger than the FOV). The dotted line indicates zero difference.

site[2]. In chapter 3, we presented aperture magnitudes based on the half-light radii listed in Harris (1996). As our half-light radii differ from those shown in Harris (1996), we do not compare these magnitudes, but compare the model and aperture magnitudes in Fig. 5.14. For data on the CTIO 0.9m there is good agreement, while SDSS data show larger scatter: this is chiefly due to photometry for some sparse objects such as Pal 1, Pal 3, Pal 14 and Pal 15. We show a histogram of Δ mag (model – aperture) in Fig. 5.15 for data taken at the CTIO 0.9m. The median magnitude difference is ~ 0.03 mag.

5.3.3 Comparison to structural parameters based on star count density profiles

In contrast to SB profiles, star count profiles are not biased by the presence of sparse, bright stars (Noyola & Gebhardt 2006). Therefore, the latter are accepted as the most reliable way to determine structural parameters. However, our CTIO and SDSS data does not have the required resolution to derive such radial stellar density profiles. Based on a combination of high-resolution HST observations and ground-based observations, Miocchi et al. (2013) were able to construct star count profiles and derived structural parameters for 26 Galactic GCs. In this section, we will compare our King parameters, which are based on model fits to SB profiles,

[2] www.G2C2.ugent.be

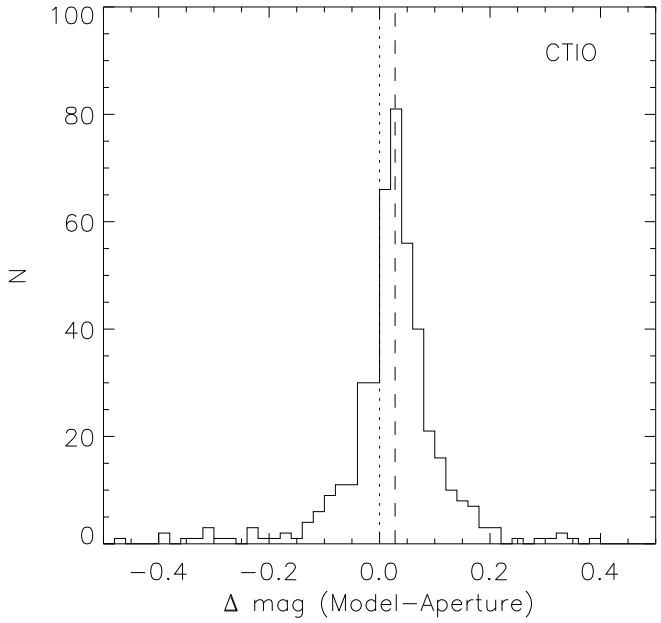

Figure 5.15: Histogram of the magnitude differences between model and aperture magnitudes (within r_h). The dotted line indicates zero difference, the dashed line indicates the median magnitude difference. See text for more details.

to their King model parameters.

Fig. 5.16 presents a comparison between our King model concentrations and the concentrations derived by Miocchi et al. (2013), based on King model fits to star count density profiles. It is clear that for more than half of the clusters we get similar concentrations, while for some clusters we obtain much higher concentrations than Miocchi et al. (2013). Similar conclusions were drawn based on Fig. 5.13, when comparing the concentrations with the Harris catalog. In the discussion following this section, we will further investigate this result.

Fig. 5.17 compares our newly derived core radii with the core radii derived by Miocchi et al. (2013) based on King model fits to star count density profiles. In general, these compare well, with some exceptions which are indicated in the figure. For NGC 288, we were forced to alter the weight of the central SB point, as was discussed before and illustrated in Fig. 5.2. Pal 14 is a very faint GC with available SDSS data. The King model fit obtained for this cluster is not highly reliable. For NGC 5466, SDSS data is used to determine the SB profile, which showed a dip towards the centre, hindering the King model fit. Note that Miocchi et al. (2013) did not use HST data for the central region of NGC 5466, as this was one of the least dense objects of their sample.

Fig. 5.18 shows a comparison between our King model r_h and the effective radii r_e derived by Miocchi et al. (2013) based on star count density profiles. Although the scatter is reasonably large, the general agreement is acceptable good. Some strong outliers are indicated. Note that Miocchi et al. (2013) did not obtain a very satisfying King model fit for NGC 2419, but, that

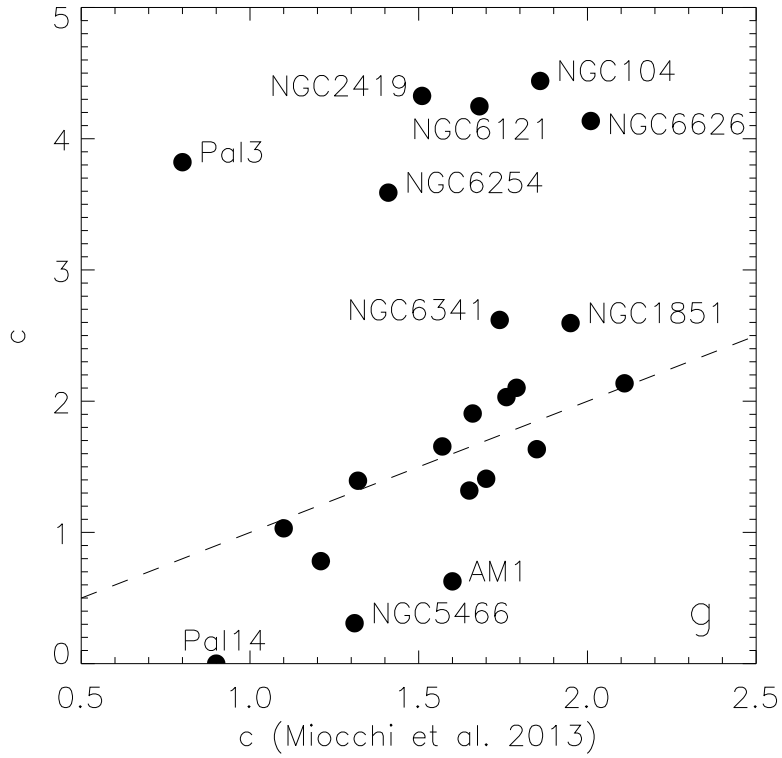

Figure 5.16: Comparison between our King model concentrations and the concentrations based on King model fits to star count density profiles (Miocchi et al. 2013). The dashed line indicates the one-to-one correspondence.

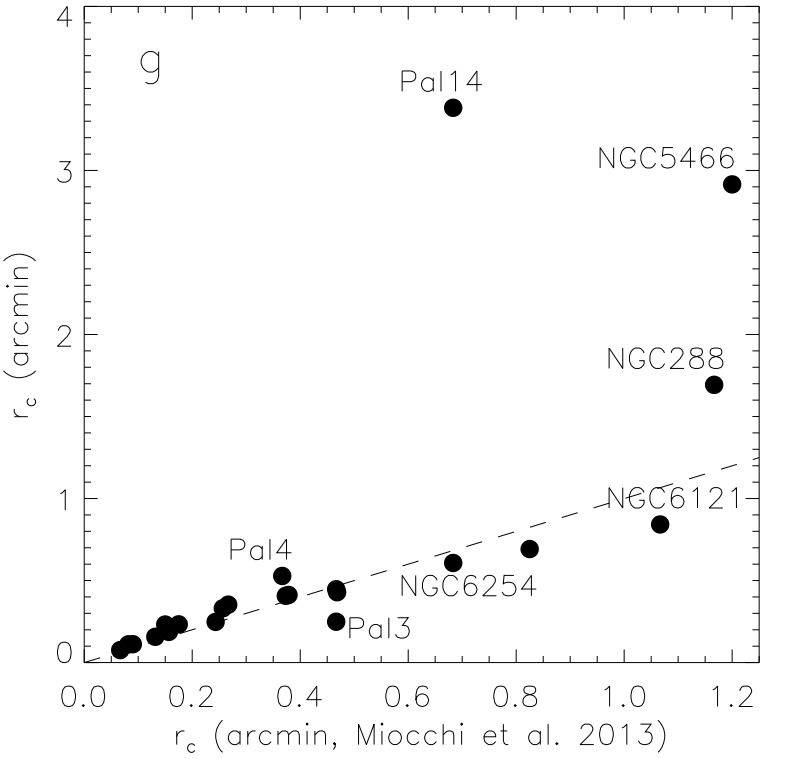

Figure 5.17: Comparison between our King model r_c and the core radii based on King model fits to star count density profiles (Miocchi et al. 2013). The dashed line indicates the one-to-one correspondence.

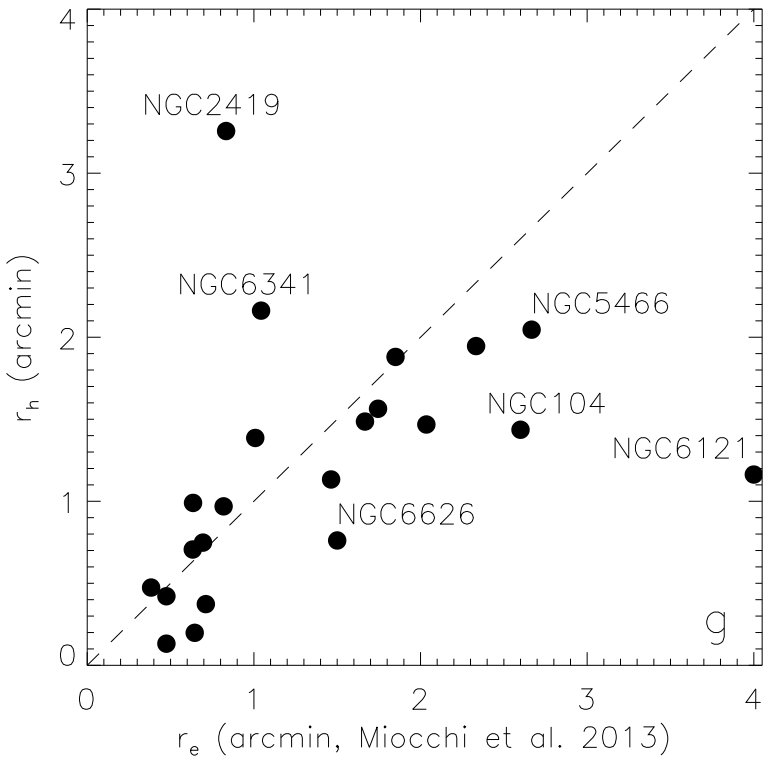

Figure 5.18: Comparison between our King model r_h and the effective radii based on King model fits to star count density profiles (Miocchi et al. 2013). The dashed line indicates the one-to-one correspondence.

their error bars indicate that the given value is somehow an upper limit, which would result in even larger differences with our resulting r_h.

5.4 Discussion

We can now explore correlations between structural parameters and the position of globular clusters within the Galaxy, as well as with stellar populations.

5.4.1 Correlations with the Galactocentric distance

van den Bergh et al. (1991) and McLaughlin (2000) have proposed the existence of a relation between the effective radius and the Galactocentric distance. As shown by Madrid et al. (2012) this relation arises from tidal truncation of globular clusters, while recently Ernst & Just (2013) provide a more theoretical approach on the implications of the correlation between the half-mass and the galactocentric radius. Miocchi et al. (2013) recover this correlation and show that it does not depend on other cluster properties, confirming its likely dynamical origin.

Fig. 5.19 shows the observed correlation between the half-light radius vs. Galactocentric dis-

tance in our data. Based on a robust fit, we find

$$log(r_h) = -1.76 + 0.57 \times log(R_{\rm GC}) \tag{5.2}$$

for the g-band (in reasonable agreement with the empirical power law found by van den Bergh et al. 1991 and in excellent agreement with the scaling relation found by Miocchi et al. 2013) and

$$log(r_h) = -1.04 + 0.38 \times log(R_{\rm GC}) \tag{5.3}$$

for the z-band. Some clusters orbiting the galaxy beyond 40 kpc have lower r_h than predicted by the general trend, consistent with the predictions of Madrid et al. (2012). The scatter on the relation is large, but some clusters are even stronger outliers. For Pal 5 and Pal 14 the SB profile fits are very poor, resulting in unrealistic r_h. Nevertheless, for NGC 2419 the fit looks good and the discrepant r_h value is probably caused by an overestimation of the limiting radius, due to the high concentration estimate. Nevertheless, recent simulations of Madrid et al. (2012) show that extended star clusters can form at large Galactocentric distances while remaining bound to the host galaxy. NGC 2419 could be an example of such a cluster.

To detect correlations between the deviation to the general trend and other parameters, we define

$$D = -1.76 + 0.57 \times log(R_{\rm GC}) - log(r_h) \tag{5.4}$$

for the g-band (and a similar definition for the z-band), following van den Bergh (2012). We searched for correlations between this new parameter and age, HB index and [Fe/H], but did not find statistically significant trends, hence confirming the findings of van den Bergh (2012).

As a final check we plot the distance to the general trend as a function of the absolute magnitude in Fig. 5.20. Surprisingly we find a statistically significant trend for both g- and z-band, opposite to recent results from the literature (van den Bergh 2012; Miocchi et al. 2013). The best robust fits are given by

$$D_{Mg} = 0.52 + (0.08 \pm 0.01) \times M_g \tag{5.5}$$

and

$$D_{Mz} = 0.63 + (0.09 \pm 0.01) \times M_z \tag{5.6}$$

Nevertheless, it should be noted that the clusters determining the general trend have rather poor fits, hence we are cautious to draw strong conclusions based on this result.

The simulations of Madrid et al. (2012) show that the half-mass radius of individual star clusters can vary significantly over a Hubble time. Moreover, the shorter the relaxation times, the more pronounced the variation. Fig. 5.21 presents the correlation between the median relaxation time (Harris 1996) and absolute value of D. We do not see a clear trend or a larger scatter on the

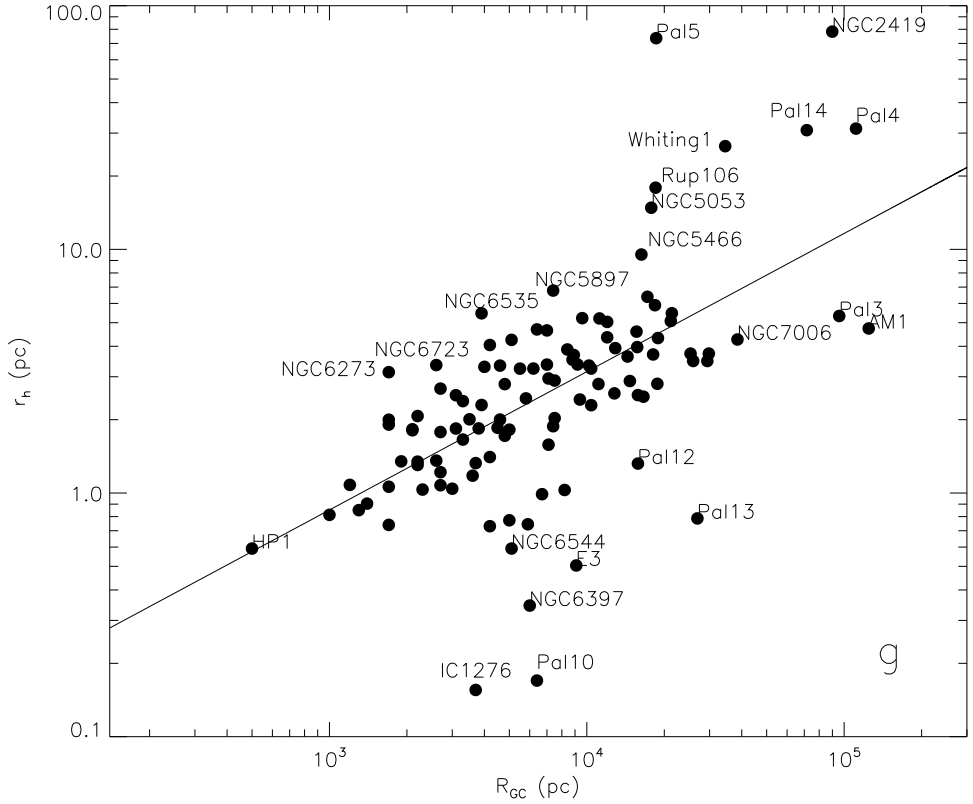

Figure 5.19: Correlation between the half-light radius r_h and the Galactocentric distance $R_{\rm GC}$. The best robust fit is presented by a solid line and given in Eqs. 5.2.

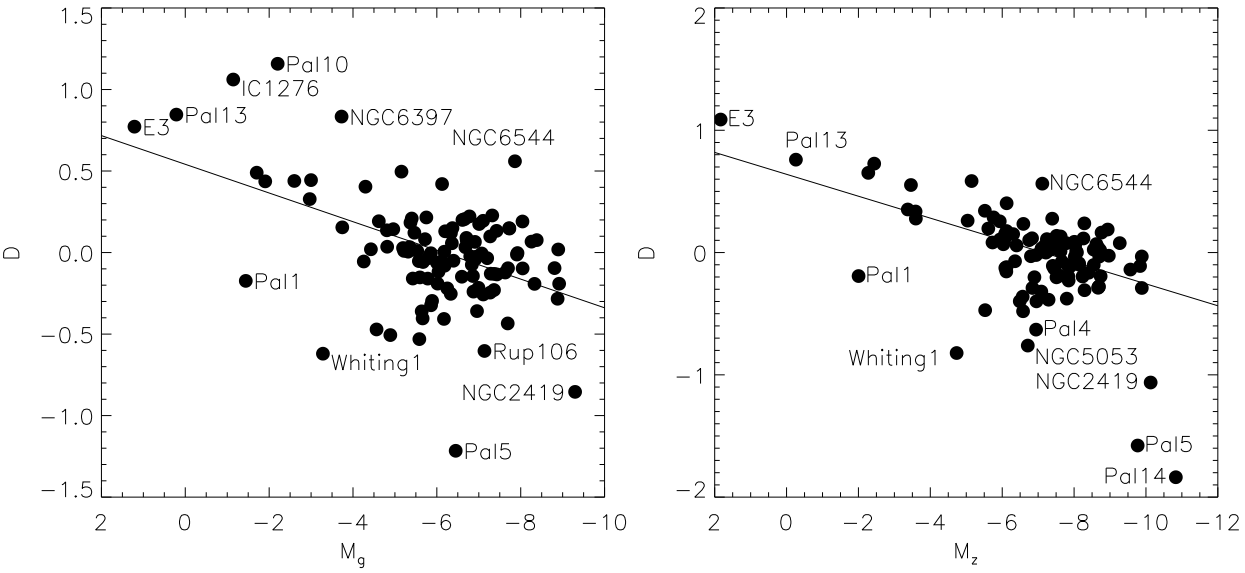

Figure 5.20: Correlation between the absolute magnitude and the distance D to the general trend between r_h and r_{GC} (as defined in Eqs. 5.2 and 5.3). The statistically robust fit is given by a solid line and is given in Eqs. 5.5 and 5.6. Note that the clusters determining the trend are generally faint clusters with poor fits.

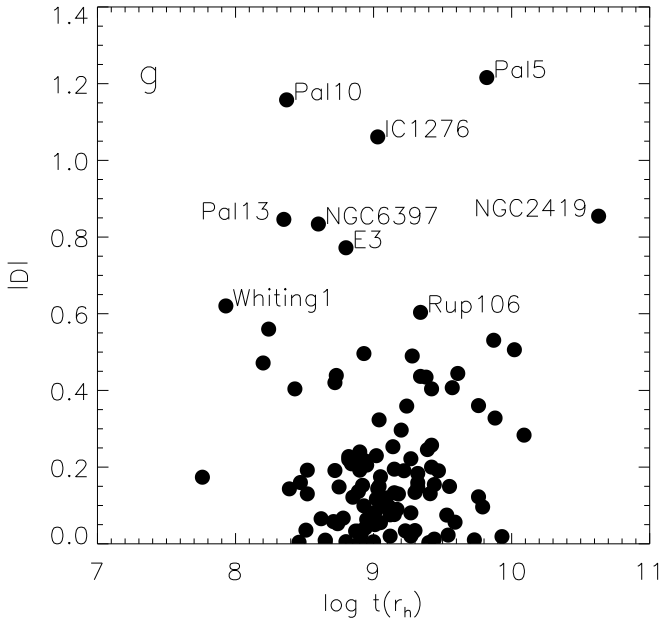

Figure 5.21: Correlation between the absolute value of D (as defined in Eq. 5.4) and the median relaxation time $t(r_h)$ (Harris 1996).

R_{GC}-r_h relation for GCs with shorter relaxation times. Hence, we exclude that these variations are the principal origin of the scatter in the R_{GC}-r_h relation.

5.4.2 PCC vs non-PCC

The core radius and concentration of a cluster can be taken as a broad measure of its dynamical evolution. This in turn may influence the formation of stellar exotica such as blue stragglers, cataclysmic variables, millisecond pulsars and intermediate-mass black holes. In Trager et al. (1995) the distribution of core radii of globular clusters was found to be bimodal, with about 20% of clusters showing central light excesses consistent with core collapse. Cusps and similar excess light features appear to be relatively common in globular clusters in our Galaxy (Vesperini & Trenti 2010) and the Large Magellanic Cloud (Mackey & Gilmore 2003b). However, for NGC 1851 and NGC 6205 (M 13) the previously encountered central cusp (Noyola & Gebhardt 2006) is not confirmed based on our SB profiles, in agreement with the stellar density profiles of Miocchi et al. (2013).

In Fig. 5.22 we plot the concentration distribution. We see evidence for a bimodal or long-tailed distribution, irrespective of filter. Based on this we select all clusters with $c > 3$ as having central light excesses (i.e. post-core collapsed, PCC hereafter): several of these objects are classified as core-collapsed objects by Trager et al. (1995), although the fraction of objects with $c > 3$ is much larger (about 2/3 as opposed to 1/5 of clusters with core collapse). However, Miocchi et al. (2013) find that a number of clusters with excess central light in their surface brightness profiles, do not show such excess in star count profiles. One interesting case is

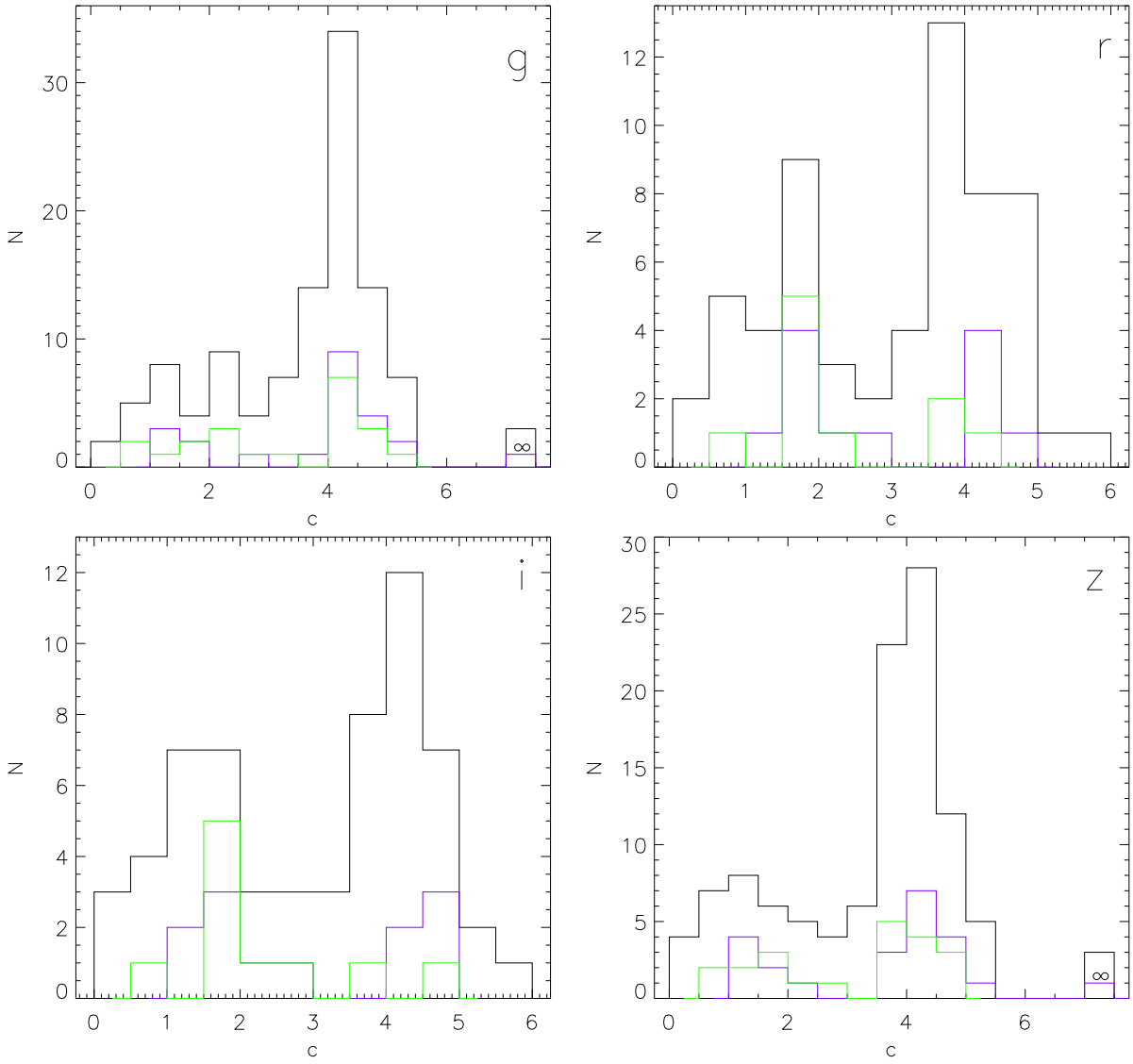

Figure 5.22: Histograms of the *griz* concentrations. Infinite concentrations (for g and z) are here presented as $c = 7$. Purple histograms represent GCs containing pulsars, the distribution of GCs hosting X-ray sources (Verbunt & Lewin 2006) are shown with green histograms.

NGC 362, which we do not regard as core collapsed while it is so classified in Harris (1996). Vesperini & Trenti (2010) detected a central cusp and argue that this cluster is undergoing a phase of core collapse, while Dalessandro et al. (2013) suggest the same on the basis of its double blue straggler sequence (with the innermost blue stragglers having formed by stellar collisions, as opposed to the more common binary evolution channel).

In Fig. 5.23 we show the r_c distribution for the g and z filters. PCC clusters preferentially have small core radii, while non-PCC clusters have a larger fraction of clusters with higher r_c. This is a consequence of the properties of the King models: the core radius is the radius where the light drops to half of the central flux density (in the limit of infinite concentration), hence the more concentrated a cluster, the smaller the core radius. For clusters with a flat central SB profile

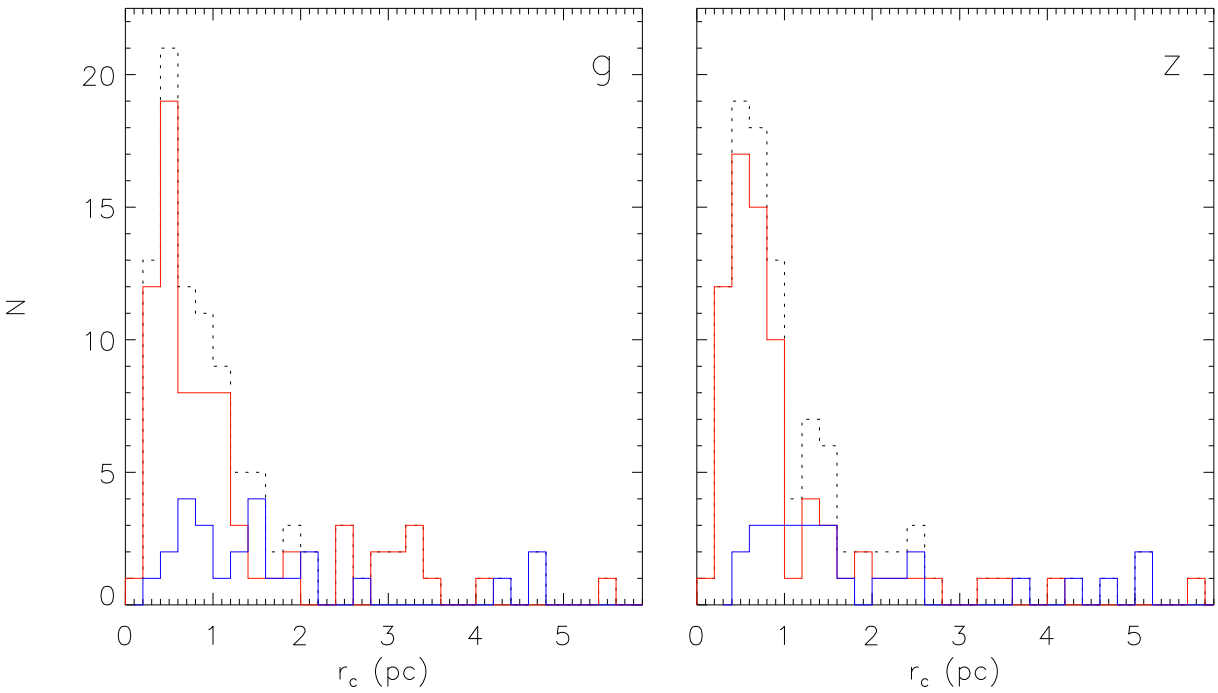

Figure 5.23: The g and z distribution of the core radii, setting the plot range to focus on the bulk of the sample (excluding faint and hard-to-model clusters AM 1, NGC 2419, Pal 3, Pal 4, Rup 106, NGC 5053, NGC 5466, Pal 5, NGC 5897 and Pal 14 in both g and z). The black dotted histogram presents all clusters, while the red and blue histograms represent PCC and non-PCC clusters, respectively.

(read: non-PCC), larger radii have to be reached to reach the radius at which the flux is only half of the central SB. We do not find clear signs for bimodality, opposite to the Trager et al. (1995) results. The median r_c amounts $\sim$ 0.83pc for both g- and z-band.

Fig. 5.24 presents the distribution of the half-light radii for the g- and z-bands. It is clear that PCC span a broader range of possible half-light radii, with a peak towards small half-light radii. For almost all non-PCC clusters r_h is larger than 2 pc, reflecting their flat SB profiles. We find a median r_h of 2.5 pc for both g- and z-band, which is in reasonable agreement with $r_h \sim$ 3pc found for extragalactic GCs in the Virgo and Fornax clusters of galaxies (Jordán et al. 2005; Masters et al. 2010). However, it indicates again that our r_h might be slightly underestimated.

Standard dynamical models of GCs make clear predictions of the evolution of the ratio between the core and the half-light ratio (see Miocchi et al. 2013 and references therein). Fig. 5.25 presents the distribution of the ratio between the core and the half-light radii. We find a peaked distribution centred at $r_c/r_h \sim 0.4$, with an strong extended tail, but do not recover the bimodal distribution as found by Miocchi et al. (2013), who found a peak in their r_c/r_h distribution at about 0.3 (in agreement with that expected from simulations of cluster dynamical evolution).

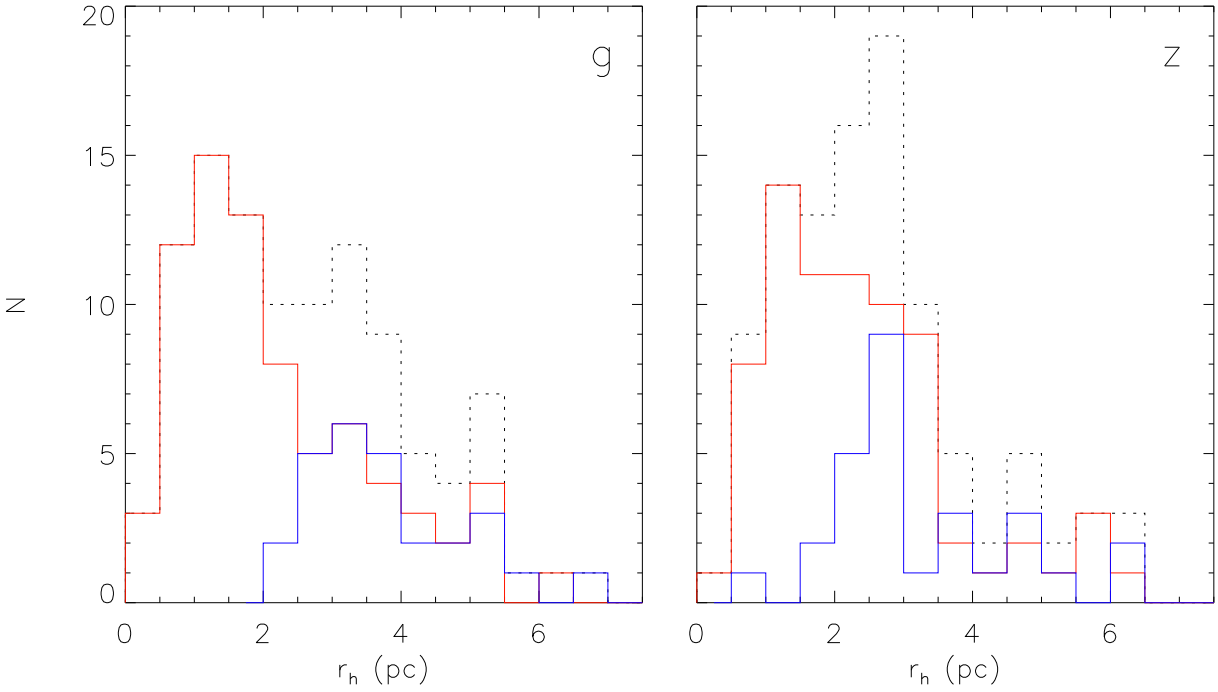

Figure 5.24: The g and z distribution of the half-light radii, setting the plot range to focus on the bulk of the sample (excluding faint and hard-to-model clusters Whiting 1, NGC 2419, Pal 4, Rup 106, NGC 5053, NGC 5466, Pal 5 and Pal 14 in both g and z). Legend as in Fig. 5.23.

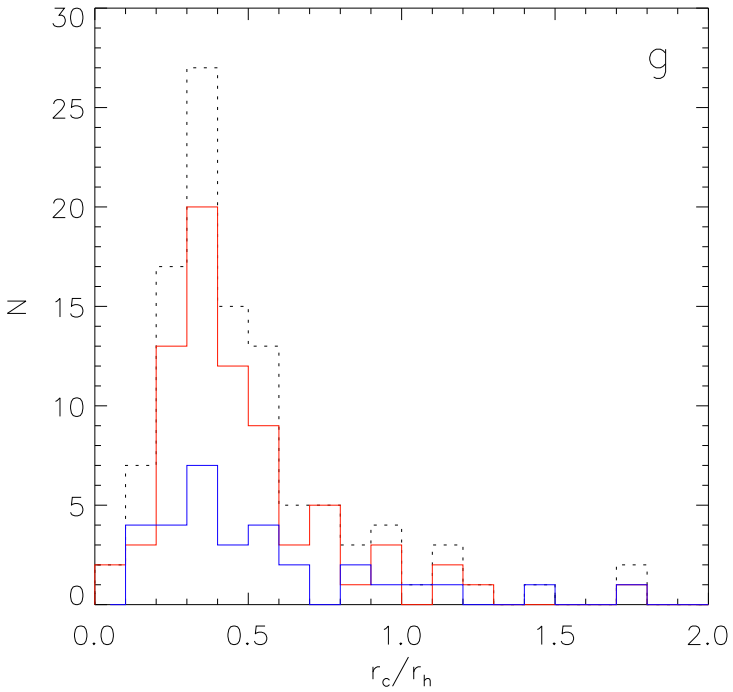

Figure 5.25: Distribution of the ratio between the core and the half-light radii. Some strong outliers are excluded by the plotting range. Legend as in Fig. 5.23.

5.4.3 Connection to pulsars and X-ray sources

Currently 28 Galactic GCs are known to contain pulsars[3]. For 23 such GCs we present structural parameters. The purple histogram in Fig. 5.22 shows the concentration distribution of GCs containing pulsars. We find that the concentration distribution of clusters containing pulsars is similar to the distribution of the entire sample: about 21% of the GCs host pulsars, for both high ($c \geq 3$) and low ($c < 3$) concentration clusters. This confirms the results of Camilo & Rasio (2005), who found that pulsars do not necessarily appear in more dense GCs, opposite to the low-mass X-ray binaries (LMXB), which are situated preferentially in dense GCs. Hence, the question which LMXB are progenitors of the GC milli-second pulsars remains a matter of debate.

Nevertheless, in the same figure, the green histograms present the distributions of the GCs hosting low-luminosity X-ray sources (Verbunt & Lewin 2006, their Table 8.2). For 21 GCs of their sample we present structural parameters. Again we find both high- and low-concentration clusters hosting low-luminosity X-ray sources. Although selection effects are strong for such small samples, it seems as if a higher fraction of the low-concentration clusters hosts such sources: $\sim$ 25% of low concentration ($c < 3$) clusters have known low luminosity X-ray sources, while only 15% of the high-concentration ($c \geq 3$) GCs host such objects.

5.4.4 Correlation of the concentration with the Galactic latitude, GC age, HB morphology, mass function and [Fe/H]

From these data we recover the correlation between concentration and distance from the Galactic plane. This is similar to the correlation between core radius and Galactocentric distance (van den Bergh 2012). Clusters with enhanced central densities are found to lie closer to the plane in Fig. 5.26, irrespective of colour. This is expected to occur from tidal shocks, that both accelerate core collapse and increase tidal evaporation (Gnedin et al. 1999; Madrid et al. 2012).

In Fig. 5.27 we present the age distributions of PCC and non-PCC clusters. We find a correlation between the age of the stellar populations and the degree of central density enhancement, in the sense that younger clusters tend to have flatter cores. This is not surprising as the core collapse process may extend over a Hubble time for clusters well away from the Galactic plane (Madrid et al. 2012). These younger clusters may be examples of systems recently accreted by our Galaxy, possibly from disrupted dwarf galaxies, rather than formed within the Milky Way at early epochs (Dotter et al. 2011). Nevertheless, Madrid et al. (2012) find that the observed correlations between structural parameters and current position within the Galaxy do not actually imply an accretion origin.

In the quest of finding other correlations between the derived structural parameters and the other

[3] http://www.naic.edu/ pfreire/GCpsr.html

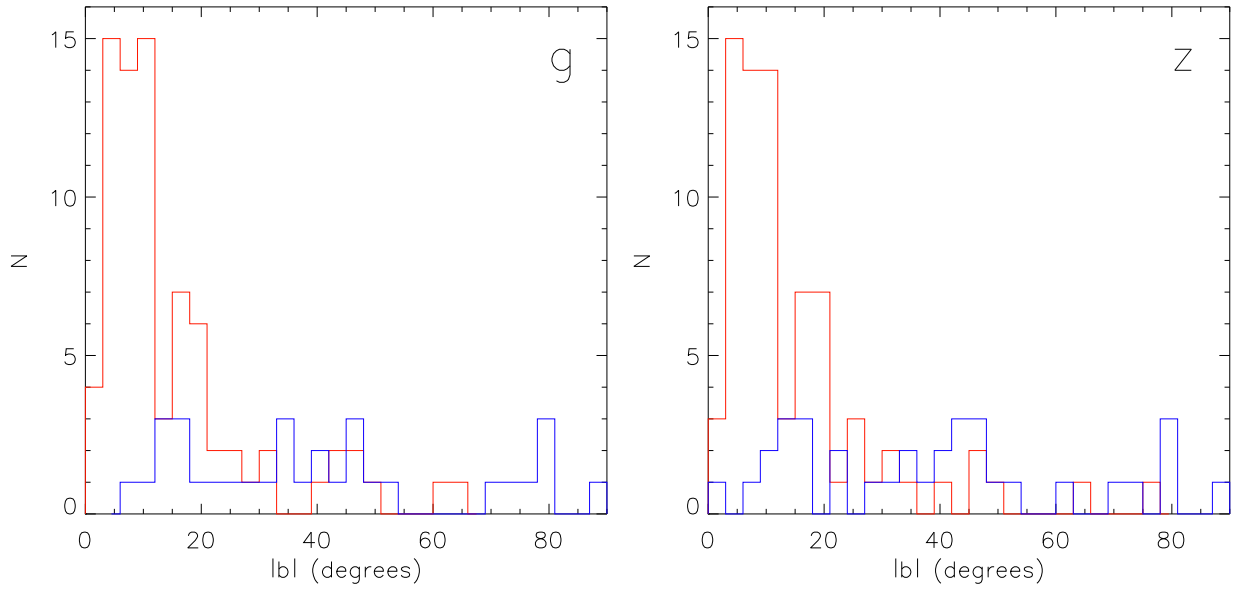

Figure 5.26: Histograms of the absolute Galactic latitude b (in degrees) for core-collapsed ($c \geq 3$, red histogram) and non core-collapsed (blue histogram) GCs. It is clear that the core-collapsed clusters are located towards the Galactic disk, while the non core-collapsed clusters are preferentially residing in the outer halo of the Galaxy.

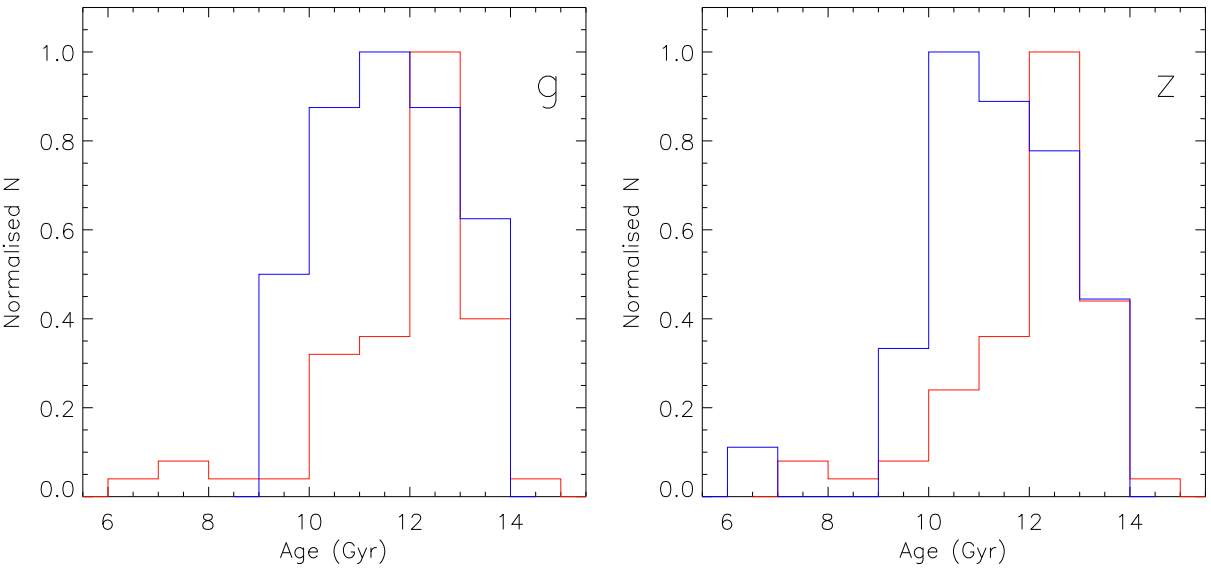

Figure 5.27: Normalised histograms of the ages (Forbes & Bridges 2010) for core-collapsed and non core-collapsed GCs. Legend as in Fig. 5.26. Core-collapsed clusters are preferentially old, while non-core-collapse clusters have a higher fraction of younger clusters.

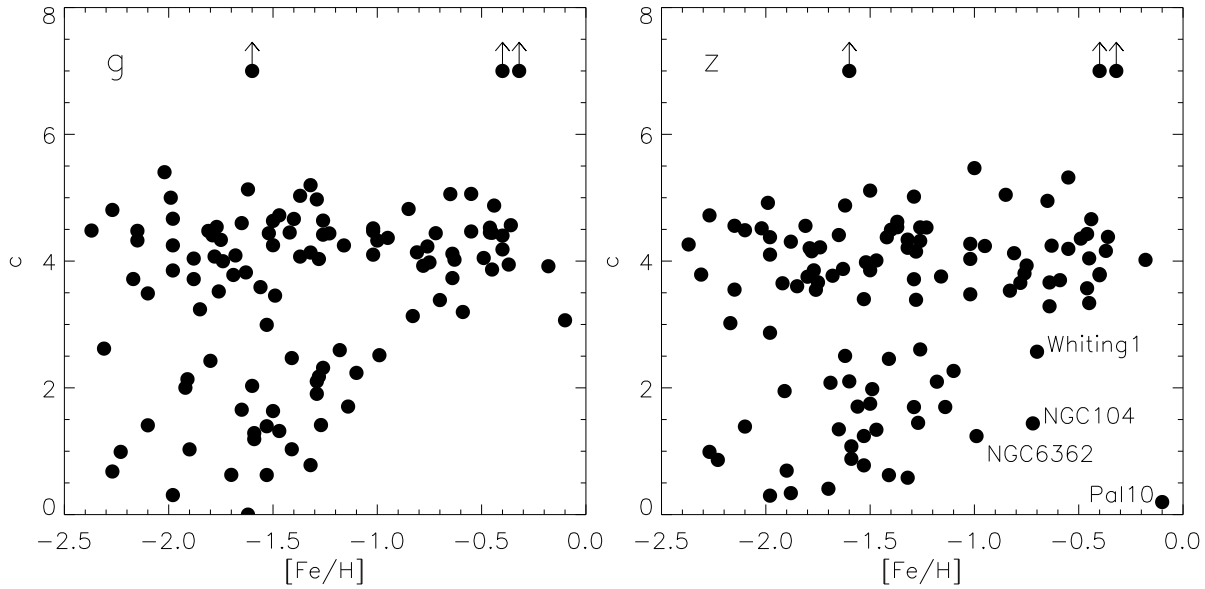

Figure 5.28: Correlation between concentration c and metallicity [Fe/H]. Metal-poor clusters ([Fe/H]$\lesssim -1$) span a wide range of concentrations, while the GCs of intermediate metallicity (-1 <[Fe/H]< 0) span a much smaller range. Arrows indicate cluster fits with infinite concentrations.

cluster properties, we search in Fig. 5.28 for correlations between the concentration and the metal abundance [Fe/H] (Harris 1996). It is clear that metal-poor clusters ([Fe/H]$\lesssim -1$) span a wide range of concentrations, while the GCs of intermediate metallicity (-1 <[Fe/H]< 0) span a much smaller range. The former clusters are distributed over the whole Galaxy, while the latter preferentially reside in the Galactic bulge.

We also investigated if a correlation exists between the concentration and the HB morphology, but did not find any statistically significant trend.

We also looked for correlations between the present-day mass function (MF) and the concentration (in order to compare our observational values with the model predictions of Trenti et al. 2010, their Fig. 11). We use the MF slopes of Hamren et al. (2013) and adopt their MF definition, being a single-sloped power law MF in the form $dN/dm \sim m^{-(1+\alpha)}$ (implying $\alpha = +1.35$ for the classic Salpeter (1955) MF)). The results are given in Fig. 5.29. GCs with bottom-light mass-functions seem to have preferentially high concentrations. This could be caused by the tidal stripping of these clusters by the Milky Way disk, removing preferentially low-mass stars (as mass segregation is moving more massive stars towards the cluster centre by dynamical friction). The concentration determination for these surviving sparse clusters is very sensitive to few bright central RGB stars, as will become clear in Section 5.4.5. Direct comparison to Trenti et al. (2010) is not straightforward, as their models do not include GCs with concentrations as high as found in the current study.

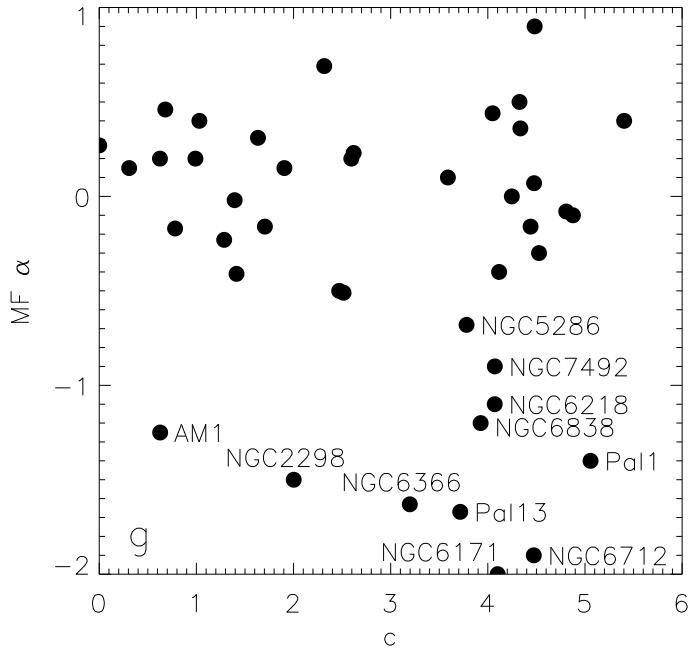

Figure 5.29: Correlation between the present-day mass function (MF) slope and the concentration.

Correlation between the concentration and the dynamical-age family

Ferraro et al. (2012) pointed out that the GC dynamical evolution history not only depends on the chronological age, but also on the internal cluster environment. The 21 GCs included in their study were subdivided in three families: dynamically young (Family I, with no internal mass segregation effects), intermediate (Family II) and dynamically old GCs (Family III). We use the King model concentration as a proxy of the internal evolution of the cluster and look for trends between this parameter and the dynamical age of the GCs.

The current study includes 18 of the 21 GCs of the Ferraro et al. (2012) sample. The median concentration of Family I (including NGC 2419, NGC 5139 and Pal14) amounts $c \sim 0.63$. However, note that for both Pal 14 and NGC 2419, the concentration is poorly defined, so only for NGC 5139 the concentration is reliable. Family II (11 GCs in our subsample: NGC 104, NGC 288, NGC 5024, NGC 5272, NGC 6121, NGC 6205, NGC 6229, NGC 6254, NGC 6341, NGC 6388, NGC 7089) has a wide spread of concentrations, with a median concentration of $c \sim 1.7$. The dynamically old (Family III) subsample (four GCs in our subsample) has a median concentration of $c \sim 3.2$, with $c > 2$ for all four clusters. Although the concentration is poorly constrained by our data and the sample size is too small to do statistics, we conclude that the evolution of the median values of the different families provides still an indication of the relation between the concentration and the dynamical age.

5.4.5 Colour Gradients

In galaxies, colour gradients are interpreted as a metallicity gradient (Tamura & Ohta 2000; La Barbera et al. 2010a). If colour gradients exist in GCs, these would not be linked with the metallicity, as these objects have a largely homogenous metallicity (although variations in light element abundances are omnipresent). However, if dynamical processes affect stellar populations, for instance through the creation of blue stragglers in cluster cores (Ferraro & Lanzoni 2009) or stripping of red giants to produce AGB-manque stars (Pasquato et al. 2013), the formation of cataclysmic variables, millisecond pulsars and intermediate mass black holes, we might be able to detect the presence of these objects through colour variations as a function of radius. Djorgovski & Piotto (1993) found that post core-collapse clusters are bluer in their centre and there were no colour gradients in the opposite direction. Djorgovski et al. (1991) found no blue cores in clusters with flat inner profiles, confirming the correlation between internal dynamics and stellar populations. This was attributed to the stripping of red giants in cluster cores to produce extended HBs (Pasquato et al. 2013) and the formation of blue stragglers by stellar collisions.

However Sohn et al. (1996) found colour gradients even in clusters that fitted the King profile and suggested that internal dynamics may produce extended HBs and lead to colour gradients. Sohn et al. (1998) also found both red and blue cores in both normal and post core-collapse clusters. For example, unlike Djorgovski et al. (1991), Sohn et al. (1998) detects a red core in NGC2808, as we do with our data.

Red and blue cores

We find general flatness of the gradients beyond the half-light radius, which is kind of expected as we do not expect strong stellar population gradients. However, stronger inclinations are apparent closer to the cluster centre. To study the colour of the cluster cores and to seek for correlations with other GC parameters, we define a new parameter

$$\Delta_{g-z} = (g-z)_{r_c} - (g-z)_{r_h}, \tag{5.7}$$

which is negative for blue cores and positive for red cores.

In Fig. 5.30 we present the distribution of this newly defined parameter, which is rather symmetric, with a small tail for red cores. Clusters with extremely positive values ($\Delta_{g-z} > 0.5$) are Pal 3, Pal 5 and Terzan 7, extremely negative values ($\Delta_{g-z} < 0.3$) are found for Whiting 1, AM 1, E 3 and Pal 14. All these clusters are sparse and faint GCs, with hard-to-model SB profiles.

The clusters in the 'red core tail' ($0.3 \leq \Delta_{g-z} \leq 0.5$) are NGC 4833, NGC 6584, NGC 6638,

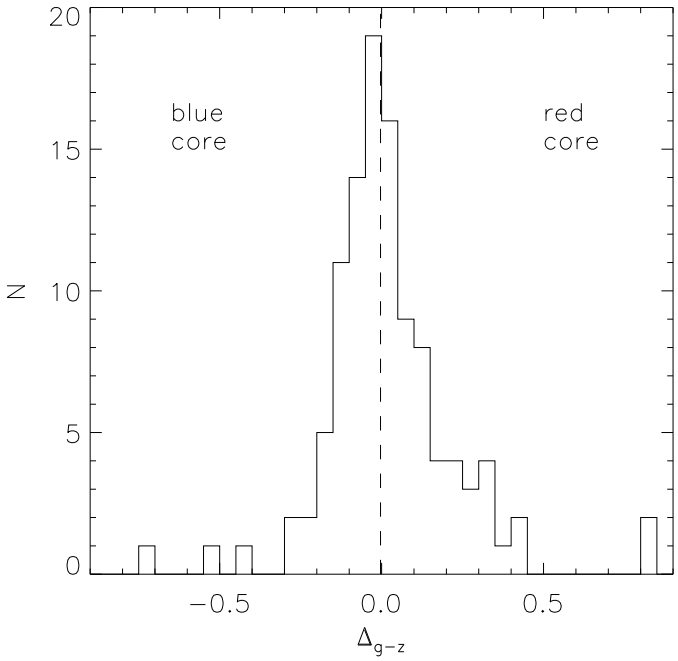

Figure 5.30: Distribution of Δ_{g-z} (defined in Eq. 5.7). The dashed line represents the median value of Δ_{g-z}. Two strong outliers are outside the plotting range: E 3 ($\Delta_{g-z} \sim -1.6$) and Pal 5 ($\Delta_{g-z} \sim 4.1$).

NGC 6779, Pal 10, NGC 6981 and Pal 12. We now will summarise some details on the SB profiles of those particular clusters.

- NGC 4833: the cluster centre is located on a RGB star by the cluster centre algorithm. Moreover, a different bright star was selected for g and z-bands, hence the profiles are not directly comparable. For the g-band, weighting of the central SB point was needed. The z-band SB profile is poorly defined. For all available filters, this cluster is PCC (i.e. $c > 3$). In the GC CMD, some disk contamination is present. Nevertheless, the cluster was centred on a member RGB star.
- NGC 6584: the cluster centre algorithm positioned the cluster centre close to one of the brightest RGB stars, causing a stronger spike in the z-band than in the g-band SB profile. It also explains the very red cluster core. For all available filters, this cluster is found to be PCC (i.e. $c > 3$).
- NGC 6638: shows a stronger spike in the z-band than in g-band SB profile, resulting in a red core. For all available filters, this cluster is PCC (i.e. $c > 3$). The CMD of this cluster suffers significant contamination of disk stars, but, based on the CMD, we could confirm the cluster is centred on a member RGB star (hence excluding the cluster was centred on a foreground disk star).
- NGC 6779: the cluster is centred on one of the brightest RGB stars, resulting in a stronger central peak the longer the central wavelength of the filter. For all filters, the concentration is higher than 3, hence the GC is classified as PCC.

- Pal 10: SB profiles are poorly constrained for this faint sparse GC. Again, the cluster was centred on a RGB GC member, causing the red peak towards the cluster centre. The CMD elucidates that the disk contamination is very strong. Note that the z-band concentration is very poorly constrained, while $c > 3$ for gri pass bands.
- NGC 6981: shows a stronger spike in the z-band than in g-band SB profile, resulting in a red core. This is again a consequence of the centring of the cluster on a member RGB star. For all available filters, this cluster is PCC (i.e. $c > 3$).
- Pal 12: The SB profiles are poorly defined for this faint sparse cluster, which is centred on a member RGB star. This again explains the red cluster core.

As a summary of the above findings, we conclude that the presence of RGB stars close to the cluster centre complicates the direct interpretation of the cluster SB profiles. Some of these clusters are reasonably well resolved, even close to the centre and reveal a well-populated RGB. The cluster centre algorithm locates the centre close to or on top of one of the RGB stars, which results in a strong red SB peak. This issue is of particular importance in rather sparse clusters. Note that some clusters also suffer from contaminants residing in the disk. Based on the CMDs, we could exclude that the cluster was erroneously centred on a foreground disk star. However, it is clear that the strong red peak does rather represent the centring on the RGB star than the overall GC profile.

Centre determination based on RGB stars

The bias introduced by RGB stars was one of the main drivers for Miocchi et al. (2013) to work with star count density profiles: in this study, the authors point out that both the centre position and the SB profile can be heavily affected by a couple of RGB stars. Hence, our findings above confirm their suspicions. Moreover, it was already found in section 3.3.1 that the GC centres based on the roaming procedure did not always compare well with the HST-based centres determined by Goldsbury et al. (2010). However, this did not strongly affect the aperture magnitudes presented in that chapter. In this section we will scrutinise the influence of the centre determination on the SB profiles, the derived King parameters and the colours of the cores.

Miocchi et al. (2013) determined the cluster centroid by taking the mean of the positions of all stars, weighted by their luminosity. Under the assumption that the RGB stars are representative of the cluster light distribution, we compute a new cluster centre taking the median of the positions of the RGB stars selected based on their position in the cluster CMD. Fig. 5.31 illustrates the effects of the different centroid for NGC 4833: for the alternative RGB-based centre, the SB profile is much less peaked towards the centre and is a better representation of the overall cluster distribution. The concentration parameter is still very poorly constrained, especially for

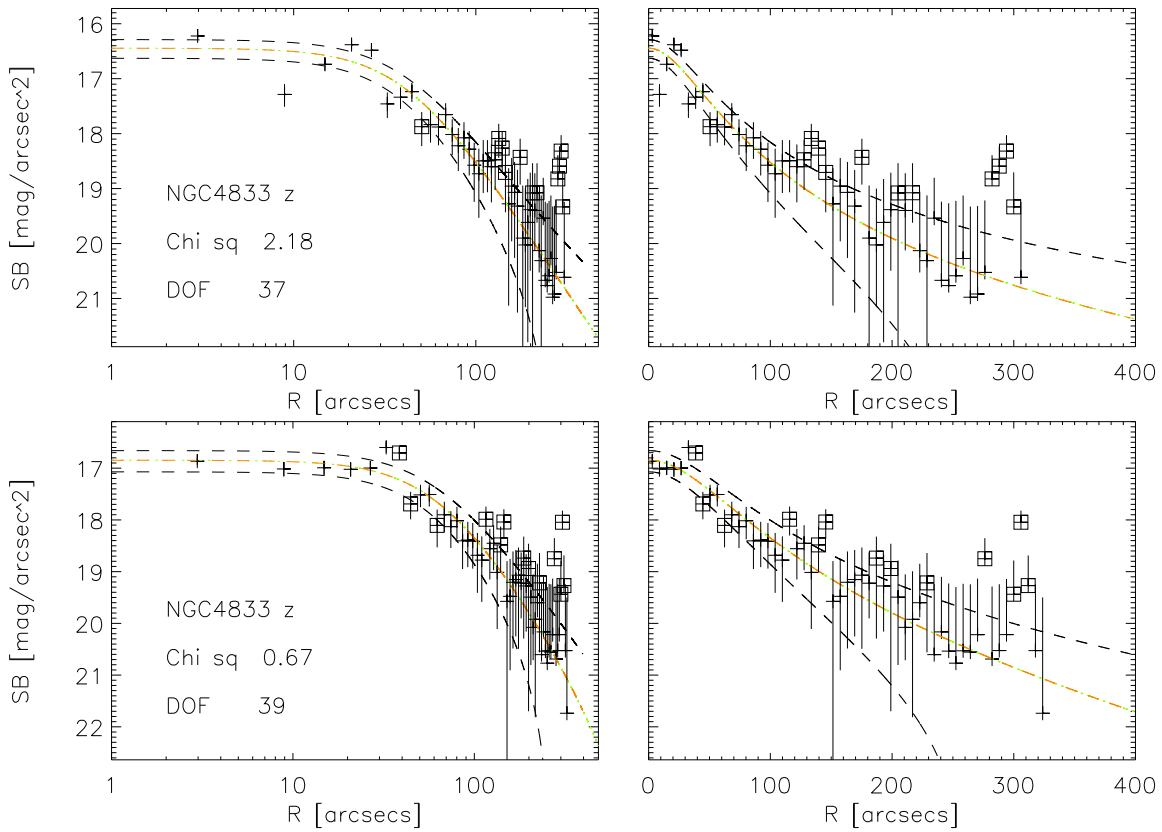

Figure 5.31: z-band SB distributions of NGC 4833. For the upper panel, the SB profile was determined using the centre obtained by the roaming procedure (Bellazzini 2007). The lower panel gives the SB profile using the RGB-based centre. The left panel focuses on the inner region of the cluster, while the right panel gives details on the outer regions.

the z-band profile, but $\Delta_{g-z} \sim -0.1$, so the strong red peak disappeared. The same holds for NGC 6584 (with also $\Delta_{g-z} \sim -0.1$).

For NGC 6981, the SB profiles with the RGB-based centre do not show the strong red peak towards the centre ($\Delta_{g-z} \sim 0.1$). Also for NGC 6779, no red peak was apparent when using the RGB-derived cluster centre ($\Delta_{g-z} \sim -0.2$).

For Pal 10, especially the g-band profile is very poorly constrained when using the other centre determination, because the cluster is so faint in this filter due to the high Galactic extinction. Nevertheless, the strong red core is not apparent anymore based on this new profile fit ($\Delta_{g-z} \sim -0.1$).

For Pal 12, only 29 RGB stars could be selected to make a new estimate of the cluster centre. However, even for this cluster, the extremely red core not present anymore in the SB profile with the RGB-based centre, with $\Delta_{g-z} \sim 0.04$. The uncertainties on the newly-derived parameters are very large, resulting in r_c and c not significantly different from zero for the z-band observations.

Note that for NGC 288, we again needed to adjust the weight of the central SB point for the

RGB-based SB profile. However, in this case the central SB point was about a magnitude fainter than the SB (opposite to the SB profile shown in Fig. 5.2). It is clear that this cluster is hard to model. Also for NGC 6864, we needed to adjust the weight of one of the more central SB points to obtain a King profile fit that is representing the outskirts of the cluster reasonably well.

However, this approach did not work well for NGC 6638 (for which we could only derive a very scattered CMD). For NGC 6626, the RGB-centring method resulted in less smooth SB profiles than when using the roaming procedure. This cluster demonstrates that the RGB-centring method is not solving all SB profile issues. It is clear that for some clusters, SB profiles representing the stellar count densities are hard to determine.

We now will compare the King parameters based on the RGB-centred SB profiles (listed on the G2C2 website[4]) with the parameters based on the roaming procedure SB profiles. Fig. 5.32 compares the King model concentrations of the SB profiles based on the different centring procedures. The large error bars indicate that it it hard to constrain the concentration based on our data. For some of the 'red core tail' GCs, the concentration is drastically different between both methods, while for the control sample, the concentrations compare reasonably well. For NGC 5927, we need to weight the central point of the SB profile based on the roaming centre, while this is not necessary for the RGB-based centre. This explains the concentration difference between both profiles.

Fig. 5.33 compares the King model r_c of the SB profiles based on the roaming procedure and the RGB centring procedure. For the SB profiles based on the RGB centring, the peak close to the cluster centre is generally not present anymore. This results in lower central SB values. As a consequence, r_c (which is the radius at which the profile flux is half of the central SB) is typically larger for SB profiles without a central peak. The r_c of the control sample GCs (marked as green squares) compare reasonably well, with the exception of NGC 288 and NGC 5927. The origin of these offsets was explained above.

Fig. 5.34 compares r_h of King fits to SB profiles obtained with the roaming and RGB centres. For the control sample, the resulting r_h compares well. For the 'red core tail' GCs (see Section 5.4.5), r_h is typically larger for RGB-based profiles. This is expected, as the absence of a central peak implies that larger radii need to be reached to encompass half of the cluster light.

Finally, in Fig 5.35 we compare the central surface brightnesses based on both centring methods. It is clear that RGB-based central SBs are generally fainter than the roaming procedure SBs, due to the absence of a central SB increase. Almost all 'red core tail' GCs suffer this effect, while also a significant fraction of the control sample is affected by this issue. NGC 5927 (z-band) is the only cluster for which the RGB-derived central SB is much brighter than the roaming procedure value.

[4] www.G2C2.ugent.be

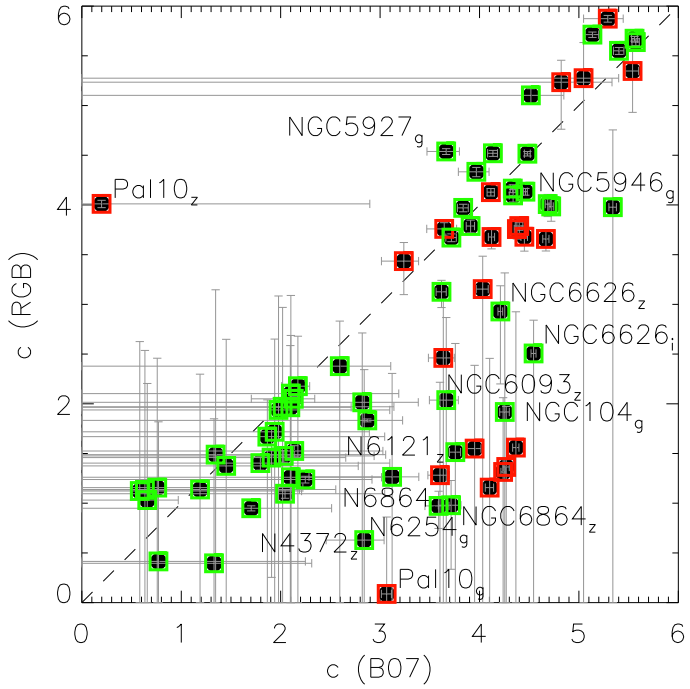

Figure 5.32: Comparison of the concentration c based on SB profiles obtained with the roaming procedure centre (Bellazzini 2007, B07) and with RGB-based centres. The red squares indicate the 'red core tail' clusters (see Section 5.4.5), while green squares indicate the control sample. See text for more details.

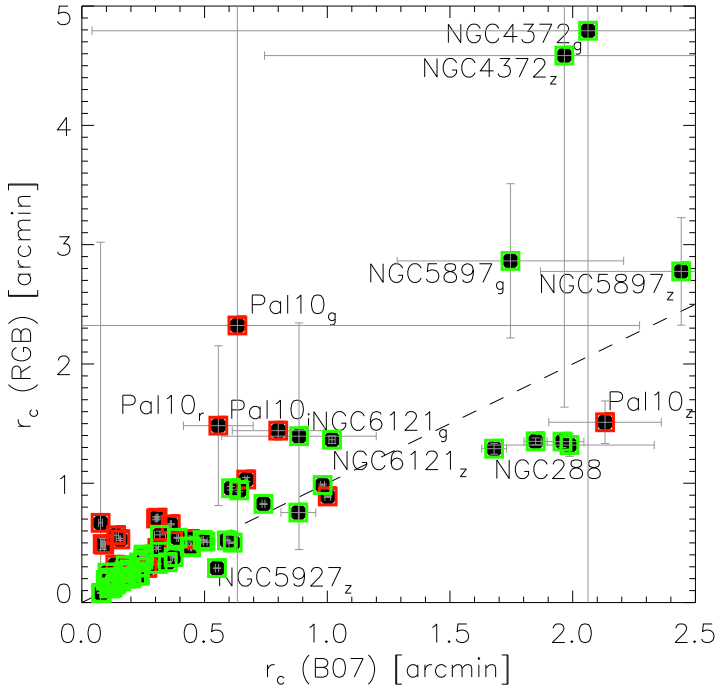

Figure 5.33: Comparison of the core radii r_c based on SB profiles obtained with the roaming procedure centre (Bellazzini 2007, B07) and with RGB-based centres. Legend as in Fig. 5.32. See text for more details.

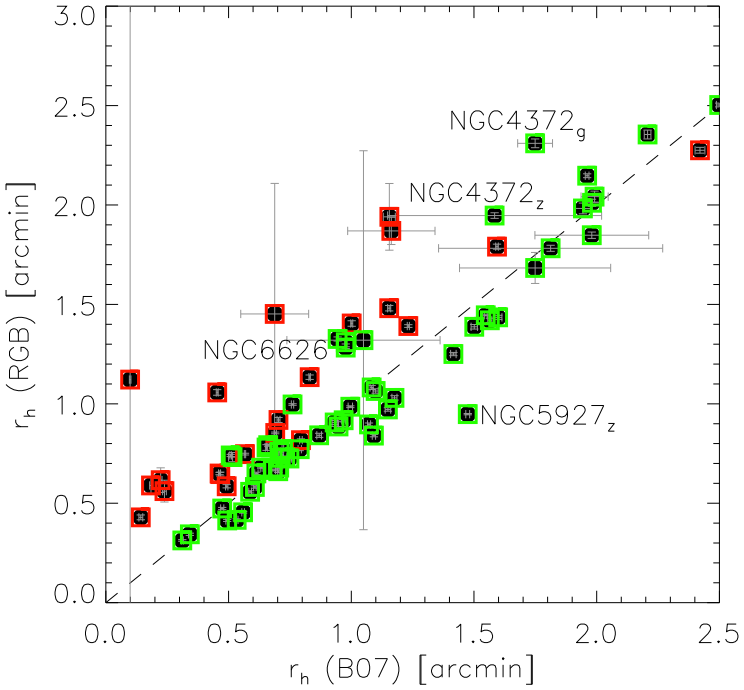

Figure 5.34: Comparison of the half-light radii r_h based on SB profiles obtained with the roaming procedure centre (Bellazzini 2007, B07) and with RGB-based centres. Legend as in Fig. 5.32. See text for more details.

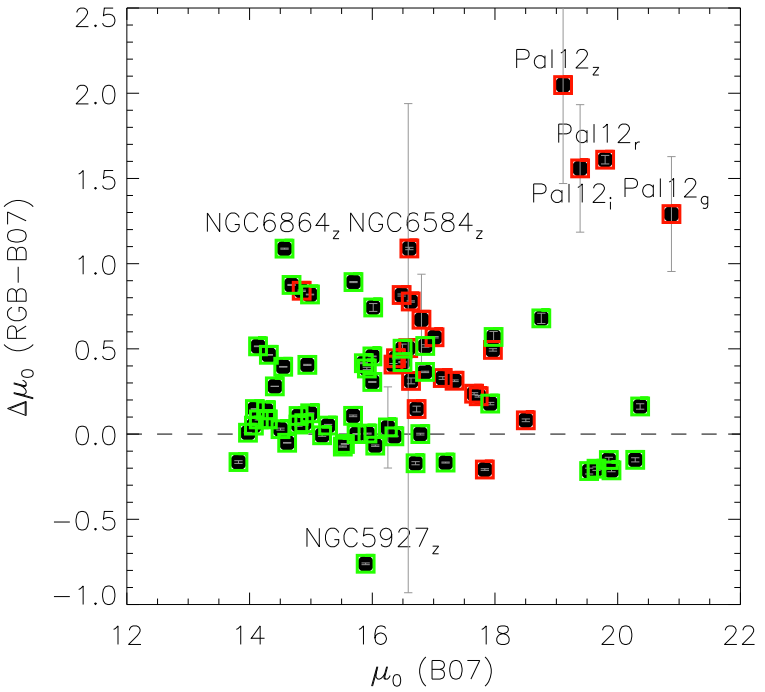

Figure 5.35: Comparison of the central SB based on SB profiles obtained with the roaming procedure centre (Bellazzini 2007, B07) and with RGB-based centres. Legend as in Fig. 5.32. See text for more details.

Parameter comparison of RGB-centred SB profiles with stellar count density parameters

In the previous section we confirmed the results of Miocchi et al. (2013) who demonstrated that the SB profiles of some clusters have cusps that disappear when using the star counts method. We demonstrated that the centre determination can play a key role in the accurate determination of the SB profile. However, we still need to check if the newly derived King parameters based on the RGB-centred profiles compare better to Miocchi et al. (2013) than the parameters derived from SB profiles centred by the roaming procedure (Bellazzini 2007). Note that it was not possible to derive an RGB-based centre for AM 1 and Pal 3: the CMDs of those clusters were of too poor quality to determine the RGB.

For the SDSS subsample, we did not use the roaming algorithm to determine the centre, but used the centre listed in Harris (1996). For this reason, we limit the comparison of the King parameters based on the RGB-centred SB profiles to the CTIO subsample.

Fig. 5.36 presents a comparison for r_c determinations based on g-band SB profiles. This figure is similar to Fig. 5.17, where we presented the comparison for r_c based on SB profiles derived with the roaming procedure. As noted before, SDSS clusters (including NGC 2419, NGC 5466, NGC 6341 and Pal 14) are not included in the figures of this section. For NGC 104, NGC 288 and NGC 5904, the comparison with Miocchi et al. (2013) is remarkably better when using RGB-centred SB profiles. The opposite is true for NGC 1904, NGC 6121, NGC 6254, NGC 6626 and NGC 6864.

In Fig. 5.37 we make a similar comparison of the half-light radii based on RGB-centred SB profiles with the effective radii listed by Miocchi et al. (2013) (similar as Fig. 5.18 for the SB profiles based on the roaming procedure). The agreement for NGC 6626 and NGC 7089 is better for the RGB-centred SB profiles, while for the other clusters the difference with Miocchi et al. (2013) is similar or bigger (NGC 104, NGC 5904 and NGC 6254).

Finally, in Fig. 5.38 we make a comparison of the concentrations based on RGB-centred SB profiles with the results of Miocchi et al. (2013) (similar as Fig. 5.16). It is clear that the RGB-centre-based concentrations for NGC 104 and NGC 6254 are in much better agreement with the latter study, while for NGC 6121 and NGC 6626 the discrepancy remains very large. Note again that this figure only includes CTIO-based results, hence excluding e.g. Pal 14, NGC 2419 and NGC 5466. Moreover, we remind the reader again that it was not possible to obtain RGB-centred SB profiles for Pal 3 and AM 1.

To conclude this section, we state that it is hard to study colour gradients, especially close to the cluster centre, because only a couple of stochastically distributed RGB stars can alter the SB profiles and originate colour gradients. This is especially true for low-density clusters, but can also affect clusters as bright as NGC 104: RGB stars and poor centring can affect the resulting

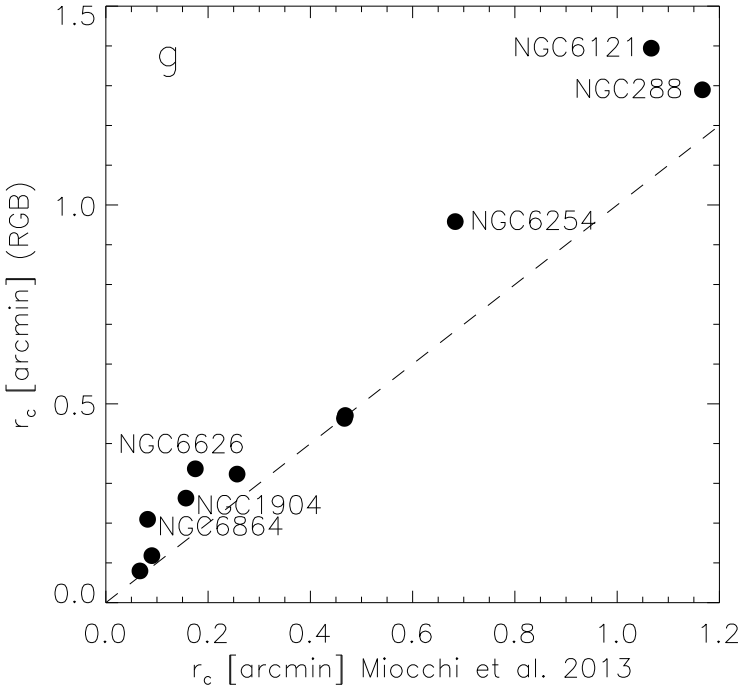

Figure 5.36: Comparison between our King model r_c (CTIO-only RGB-centred SB profiles) and the core radii based on King model fits to star count density profiles (Miocchi et al. 2013). The dashed line indicates the one-to-one correspondence.

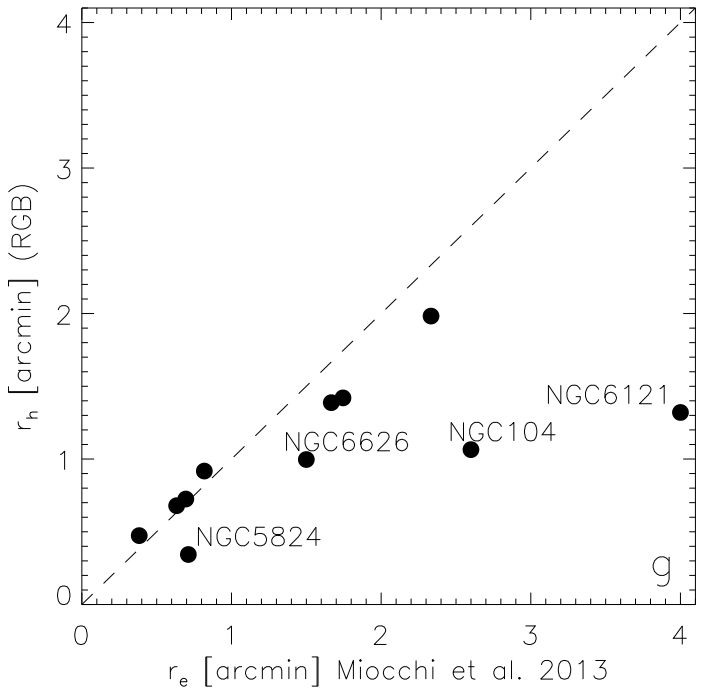

Figure 5.37: Comparison between our King model r_h (CTIO-only RGB-centred SB profiles) and the effective radii based on King model fits to star count density profiles (Miocchi et al. 2013). The dashed line indicates the one-to-one correspondence.

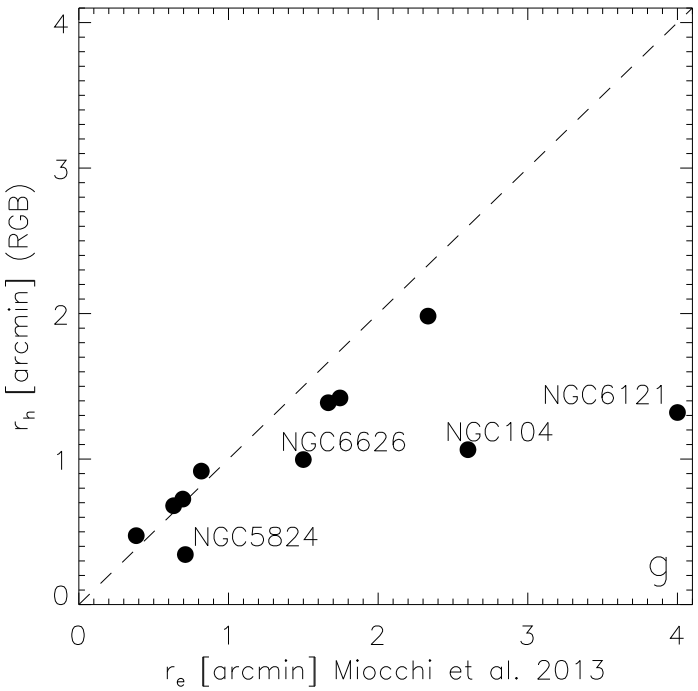

Figure 5.38: Comparison between our King model concentrations (CTIO-only RGB-centred SB profiles) and the concentrations based on King model fits to star count density profiles (Miocchi et al. 2013). The dashed line indicates the one-to-one correspondence.

King parameters drastically. This impedes straightforward interpretation of colour gradients as found in this chapter and in Sohn et al. (1996, 1998).

Correlation between core colour and other cluster parameters

At the moment we use the parameters based on SB profiles for which the centre was determined by the roaming procedure, not on the RGB-based procedure. The previous section revealed some issues with this parameter, which is in some cases not very reliable because of the strong influence of few RGB stars on the final central gradient. However, we still try to recover relations between this parameter and other GC properties. We plot Δ_{g-z} as a function of the HB index in Fig. 5.39. Pal 5 has a very poor fit and falls outside the plotting range. Some other outliers are indicated, the issues regarding the SB profiles of these GCs are discussed above.

When making a robust fit to all the data points, we find no statistically significant relation. The HB index becomes insensitive to the HB morphology for very blue and very red HBs (Catelan et al. 2001, and references therein), which are the ranges which are best populated in our GC sample. Motivated by this argument, we restrict the HB index range to $[-0.9, 0.9]$ and exclude the clusters mentioned above. Again we do not find a statistically significant relation. Note that the positive correlation which is apparent by eye would be contrary to physical expectations, as

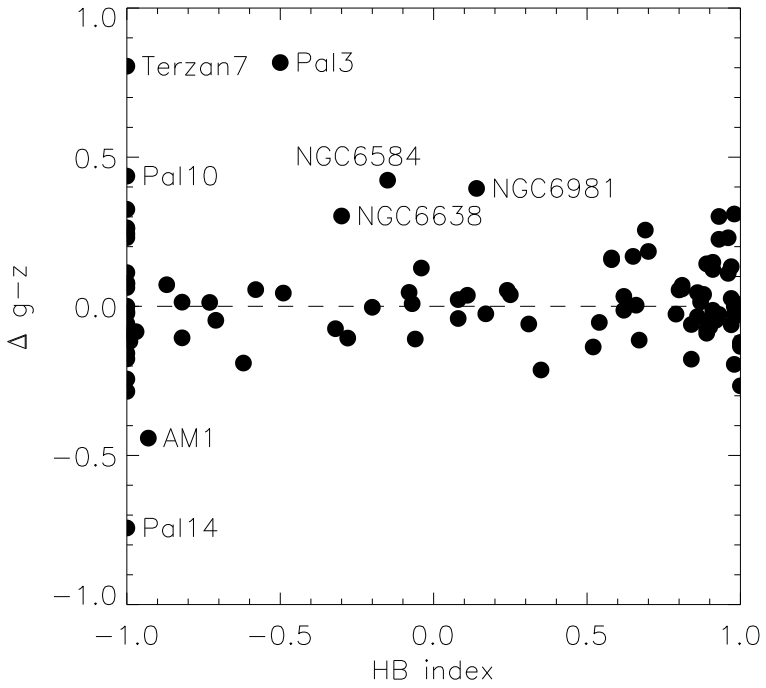

Figure 5.39: Correlation of Δ_{g-z} (as defined in Eq. 5.7) and the HB index (Mackey & van den Bergh 2005). The dashed line indicates $\Delta_{g-z} = 0$. The plot range is excluding Pal 5, which has a very poor SB profile fit.

it would imply bluer cores correspond to redder HBs. We also searched for correlations between concentration c, metallicity [Fe/H] and age with Δ_{g-z}, but did not find statistically significant trends. We think the colour difference Δ_{g-z} is largely caused by the by-chance inclusion of RGB stars close to the cluster centre, hence we do not expect it to correlate with any of the above parameters.

5.5 Conclusions

In this chapter we used the photometric data presented in chapter 3 to derive structural King model parameters for 111 GCs. We investigate the influence of a limited FOV (which is the case for the CTIO data) on the obtained structural parameters. Moreover, we illustrate how randomly distributed red giant stars can affect the centre determination and discuss the related consequences considering the SB profiles and the resulting King model fits.

We compare our parameters to previous work and find reasonably good agreement for the core radii. Nevertheless, for the concentration parameter we find discrepant values, which can be related to the effects of RGB stars.

We investigate correlations between the structural parameters and the position of GCs within the Galaxy, as well as with stellar populations. We confirm the relation between the half-light radius and the Galactrocentric distance. Moreover, we give a new definition for core-collapsed

clusters ($c > 3$). We find that those high-concentration cluster reside preferentially close to the Galactic disk and are preferentially old. Low sample sizes impede to draw strong conclusions on the links between structural parameters and exotic stellar populations such as pulsars and X-ray sources. Finally, we study colour gradients in GCs, which are generally flat in the outer regions of the cluster. Towards the cluster centre, stronger colour gradients can be present, which are mostly caused by by-chance inclusions of RGB stars and therefore do not necessarily represent radial stellar population differences.

Colour-magnitude diagrams

6

6.1 Introduction

Recent studies of GC colour-magnitude diagrams (CMD) exploiting HST data were mainly aimed at the recovery of multiple stellar populations (see e.g. Piotto et al. 2007). These discoveries put an end to the general consensus that GCs are single stellar populations. Moreover, anti-correlations in the abundances of light elements add further evidence for extended enrichment histories (Gratton et al. 2012a,b).

Another application of CMDs is the study of differential extinction, which can be severe near the Galactic centre (Alonso-García et al. 2011). Correcting for these differential reddening effects allows to construct high-quality CMDs with tighter sequences. This leads to a more accurate determination of ages, metallicities and distances based on isochrone fitting, which are important for models of the formation and evolution of the Milky Way.

Because the CMDs were only shortly introduced in section 1.3.2, we now give a more profound context of the stellar evolution. Fig. 6.1 presents a CMD of NGC 288 based on our CTIO data (constructed as described in Section 3.3.3), indicating the different stages of the stellar life. Unfortunately, our data do not have the required resolution and photometric accuracy to study different generations of stars.

After spending most of their lives in the main sequence (MS), burning hydrogen in their core, intermediate-mass stars (0.5 to 10 $M_{\odot}$) leave the MS at the main sequence turn-off (MSTO). They grow in size, move along the sub-giant branch (SGB) and become red giants with inert cores: red giant branch (RGB) stars have inactive cores made of helium, inside a hydrogen burning shell. After the He-flash, which occurs when the temperature and pressure in the core are high enough to ignite He fusion, the stars move to the horizontal branch (HB), where they burn He in the core and hydrogen in a shell. Some of these HB stars are pulsating and are denoted RR Lyrae variables. When the stars have depleted the helium at the core, they continue their life as AGB stars, which host an inactive carbon and oxygen core, while burning He and hydrogen in a shell around it (see e.g. Alonso-García et al. 2011).

Blue stragglers (BS) are main-sequence stars that are brighter and hotter than the stars at the MSTO (as can be seen in Fig. 6.1). These stars are believed to have formed after mass-transfer from a companion star in close binary systems (see e.g. Santana et al. 2013 and references therein). Mateo et al. (1990) proposed an alternative scenario for the formation of BSs through merged close binaries.

The metallicity of a GC stellar population is the main driver for variations in the HB morphology, with more metal-poor clusters having bluer HBs. However, the chemical composition alone cannot explain all the variations observed in the HB morphology, hence at least one second parameter is needed to account for the HB variety. This is one of the long-standing problems in

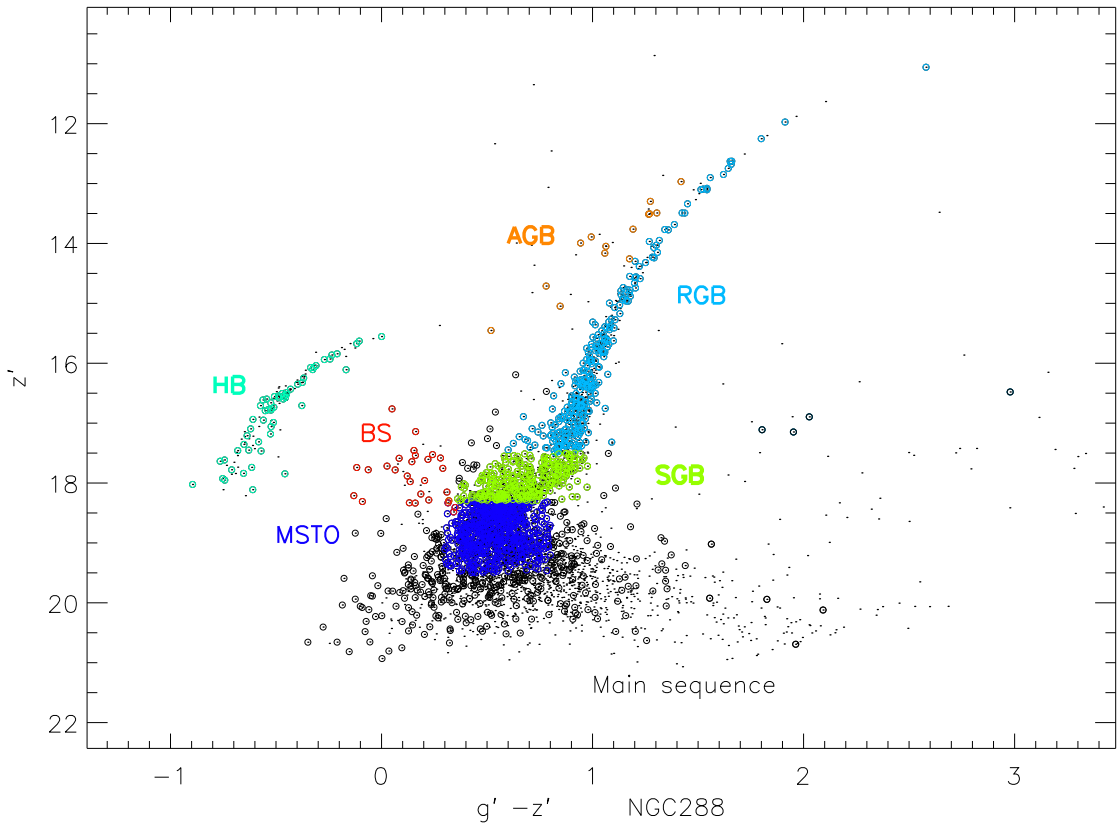

Figure 6.1: CMD of NGC 288 based on our CTIO data, equivalent to the Hertzsprung-Russel diagram presented in Fig. 1.11. The principal stages of stellar life are indicated: horizontal branch (HB), main sequence turn-off (MSTO), red giant branch (RGB), asymptotic giant branch (AGB), sub giant branch (SGB), blue stragglers (BS). The expected location of the main sequence is also indicated. However, the CMD is too shallow to recover the main sequence.

stellar astrophysics and is often referred to as the "Second Parameter Problem" (e.g. Sandage & Wildey 1967; van den Bergh 1967). Searle & Zinn (1978) proposed age as the second parameter in a hierarchical formation scenario and suggested that metal-poor GCs showing red HBs formed by gradually accreting 'protogalactic fragments'. Over the years, helium abundances were designated as responsible for the differences in CMD morphology, not only for different shapes of the HB, but also for the existence of multiple main sequences (Norris 2004; Piotto et al. 2005; Lee et al. 2007). Recently, Gratton et al. (2010) confirmed the He abundance variation as the most likely candidate causing the variety of the observed HB morphologies and express the necessity for a third parameter to explain all the variation in the HB morphology. However, high-resolution spectroscopic observations of Moehler et al. (2011) show that a significant fraction of extreme HB (EHB) stars in ωCen are helium-poor and their theoretical evolutionary models show that the EHB stars can be formed by an independent formation mode. For a recent discussion on the topic, we refer the interested reader to Dotter et al. (2010) and Dotter (2013).

Lee et al. (2007) demonstrated that GCs hosting an extremely hot HB are more massive than

normal GCs and have different kinematics. They suggested that these EHB GCs could have a unique origin, implying that heterogeneous origins of GCs exist. It is important to understand the formation mechanisms and properties of the EHB stars. It is generally accepted that hot HB stars are responsible for the ubiquitous UV upturn in elliptical galaxies (Code & Welch 1979; Faber 1983; Burstein et al. 1988; Yi et al. 1997, 2011). These galaxies host old metal-rich populations and where not expected to contain a large population of hot stars. Different models have been proposed and it is still unknown whether these stars are metal-poor or metal-rich, which has important implications for stellar evolutionary models and the formation history of galaxies.

The constructed CMDs proved to be useful in several applications throughout this thesis: they were indispensable to clean out foreground non-member stars when determining the GC colours in chapter 3. This resulted in highly reduced scatter in the CMR presented in chapter 4 (see e.g. Fig. 4.15). Note that models of Yoon et al. (2006) consider the HB morphology as one of the prime causes of the non-linearity of the CMR. Moreover, they were used in chapter 5 to determine an alternative location for the cluster centre, which turned out to be important for the determination of the SB profiles. In the same chapter, we tested the claim of Pasquato et al. (2013), who proposed a correlation between GC core collapse and horizontal branch morphology in Galactic GCs. In chapter 7, we present a large observational campaign, which focuses on the influence of extreme HB stars on the age determination of these systems. This again illustrates that CMDs are an important source of information on these intriguing systems.

The current chapter will give an overview of some other projects based on the CMDs, that are still work in progress. These include our approach on the long-standing problem of the second parameter problem. Future work based on the CMDs will include the comparison of stellar population models (based on the known cluster age and metallicity) to best-fit isochrones (see e.g. Rosenberg et al. 1999 for a similar approach based on the $UBVRI$ filter set) and will address the differential reddening issue for a large GC sample (see Alonso-García et al. 2011 for pioneering work on this topic).

6.2 Double HB in NGC 6569

Based on VISTA Via Lactea (VVV) NIR data, Mauro et al. (2012) discovered double HBs in NGC 6569 and NGC 6440. Unfortunately, our data set only includes NGC 6569. Fig 6.2 shows their JK Hess diagrams of the HB area of NGC 6569: it shows the relative density of the occurrence of stars at differing CMD positions. It is clear that the two HB subpopulations split in magnitude at the same colour. The luminosity of the HB ($\Delta V(HB - MSTO)$) is an age indicator (e.g. Vandenberg et al. 2013), because the turn-off moves gradually down the main sequence as the cluster ages. Hence, the observed split may be interpreted as an iron abundance

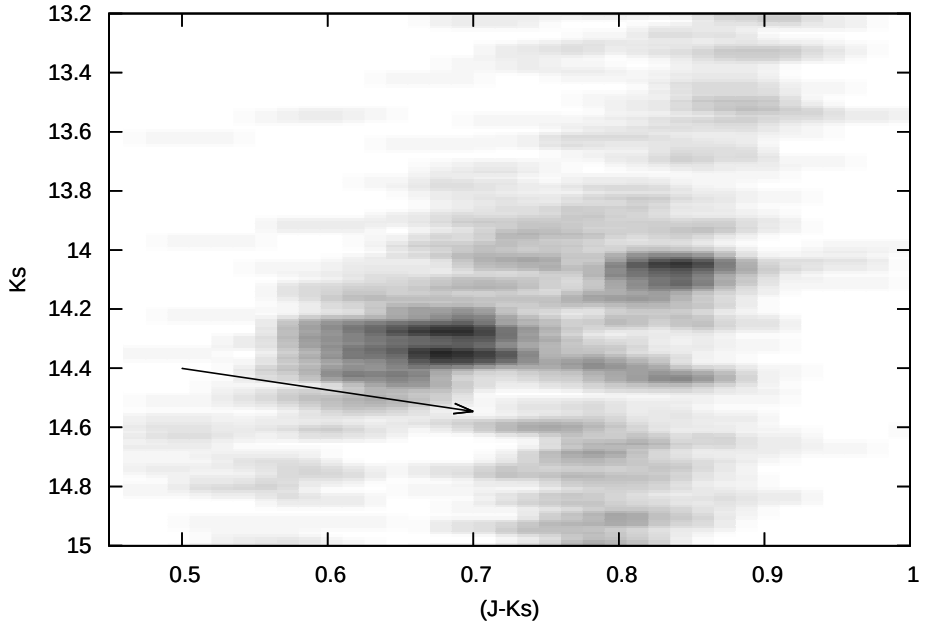

Figure 6.2: $(J - K_s; K_s)$ Hess diagrams of the HB area of NGC 6569 (taken from Mauro et al. 2012). The arrow indicates the reddening effects.

or age difference (because of the degeneracy with respect to age and metallicity). They exclude the split HB is the result of a helium difference but are not conclusive on the origin of this feature, because simulated HBs of Catelan & de Freitas Pacheco (1996) and Dorman et al. (1989) are very different compared to the observed HB split.

Our optical CMD, which is presented in Fig. 6.3, also reveals some evidence of a double HB, which motivated us to study this cluster in more detail. As a first check, we decided to take a closer look at the spatial distribution of the selected stars on the chip, which is presented in Fig. 6.4. We ascertain that the HB stars of interest are distributed quite randomly, which serves as a first indication that the apparent offset between the two branches is not originated by differential reddening effects. However, Alonso-García et al. (2011) show that the extinction along the line of sight can be patchy, hence we cannot fully exclude that the differential reddening is the origin of the apparent separation between the different HBs.

In collaboration with Roger Cohen, we crossmatched our CTIO optical data with NIR data of the VISTA Variables in the Via Lactea (VVV) to check whether we could recover the double HB feature discovered in the NIR data.

We took two approaches to the problem. First we selected the stars based on the g and z filters as presented in the left panel of Fig. 6.5. The right panel shows the JK CMD, using the colour-coding of the left-hand panel. It is clear that the separate sequences in the optical CMD are mixed-up in the NIR CMD. Fig. 6.6 shows CMDs for other filter combinations, which do not show a clear distinction between the positions of the optically-selected split HB stars. This

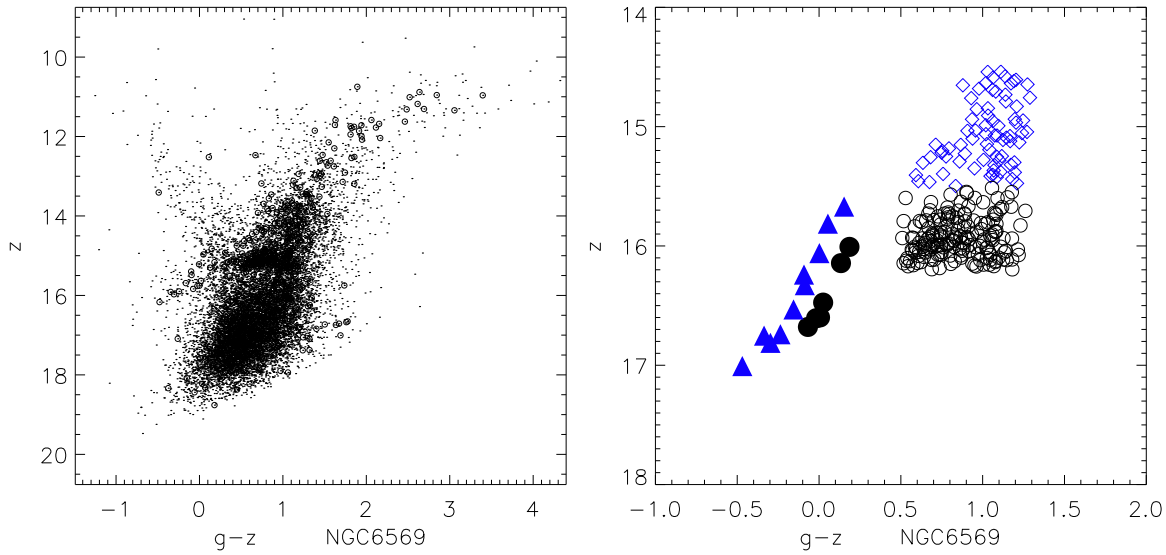

Figure 6.3: Left panel: gz CMD of NGC 6569. Open circles are stars within the half-light radius, dots are stars over the entire CCD. The disk contamination is clearly apparent. Right panel: zoom on the HB region, with the selection of the two candidate sub-HBs indicated with filled triangles and circles. The two proposed HB subpopulations are indicated with black and blue colours.

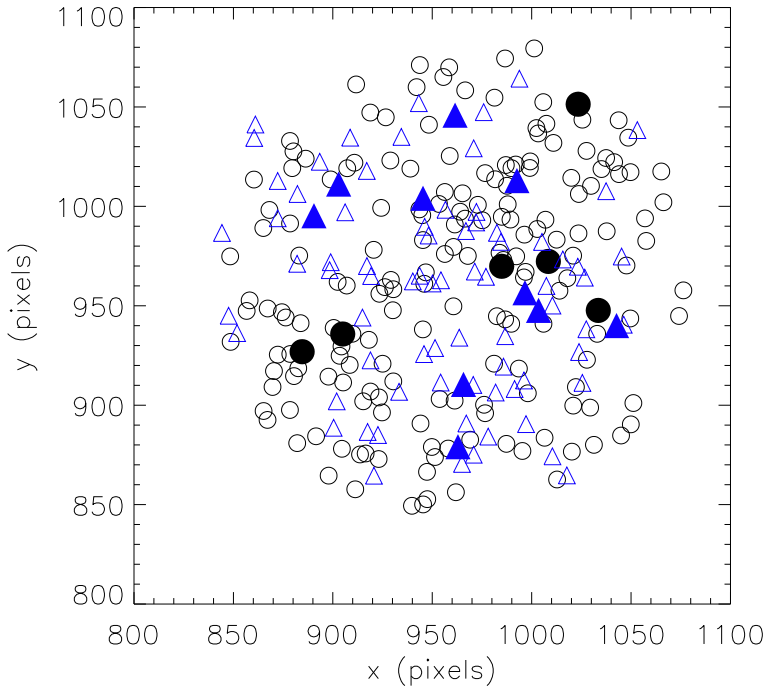

Figure 6.4: NGC 6569: distribution of the HB stars within the half-light radius in the xy-plane of the CCD. Legend as in the right panel of Fig. 6.3. Filled triangles and circles are distributed randomly across the plane, making differential reddening effects less probable to cause the CMD offset. However, Alonso-García et al. (2011) show that extinction along the line of sight can be patchy.

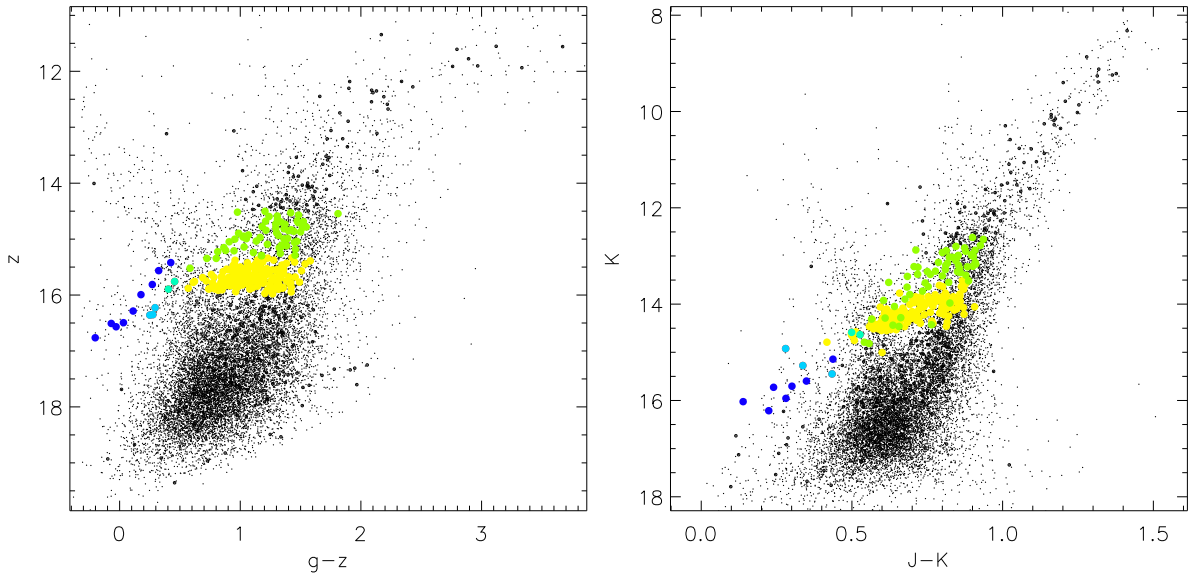

Figure 6.5: The left panel presents the gz CMD of NGC 6569: circles are stars within r_h, dots are stars from the entire field. Coloured filled circles are different HB selections of stars within the half-light radius. The right-hand panel presents the JK CMD, using the same colour-coding.

could be due to differential reddening, which affects the g- and z-band stronger than K-band observations.

As a second approach, we used the colour-magnitude selection from Mauro et al. (2012) to select our HB regions for NGC 6569 (presented in Fig. 6.7). The right-hand panel shows the corresponding optical CMD. The NIR-selected HB is not confirmed in the pure optical CMD, as the stars of the different HB subsamples mix up. Fig. 6.8 shows the CMDs for other filter combinations. Note that for the CMDs including one optical and one NIR filter, the different HB subpopulations are reasonably well separated. Nevertheless, based on optical data alone, we cannot separate the HB in distinct subpopulations.

At this point, we cannot draw any strong conclusions based on optical data only. First we need to gain more insight in the differential reddening in order to directly interpret the optical CMD presented in Fig. 6.5.

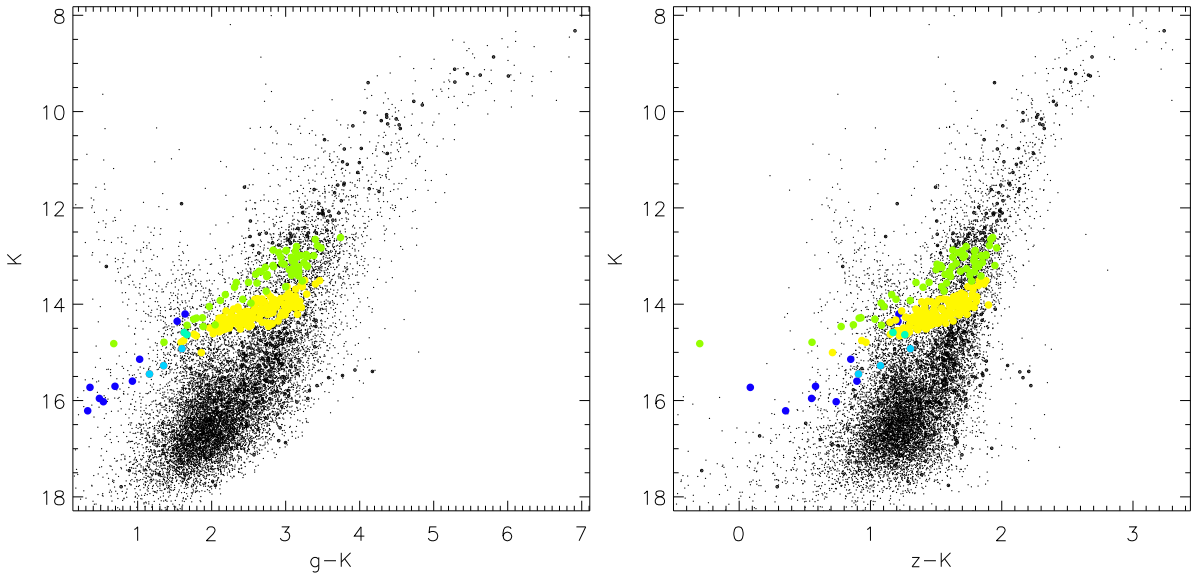

Figure 6.6: gK and zK CMDs of NGC 6569. Legend as in Fig. 6.5.

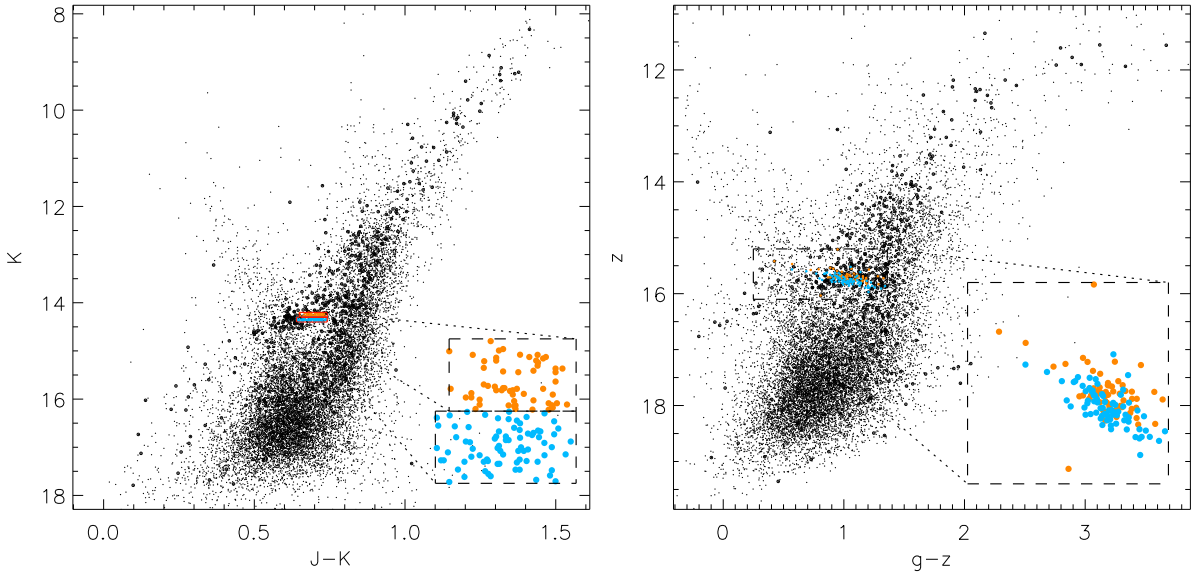

Figure 6.7: JK and gz CMDs of NGC 6569. Circles are stars within r_h, dots are stars from the entire field. Coloured filled circles are different HB selections of stars within the half-light radius (Mauro et al. 2012).

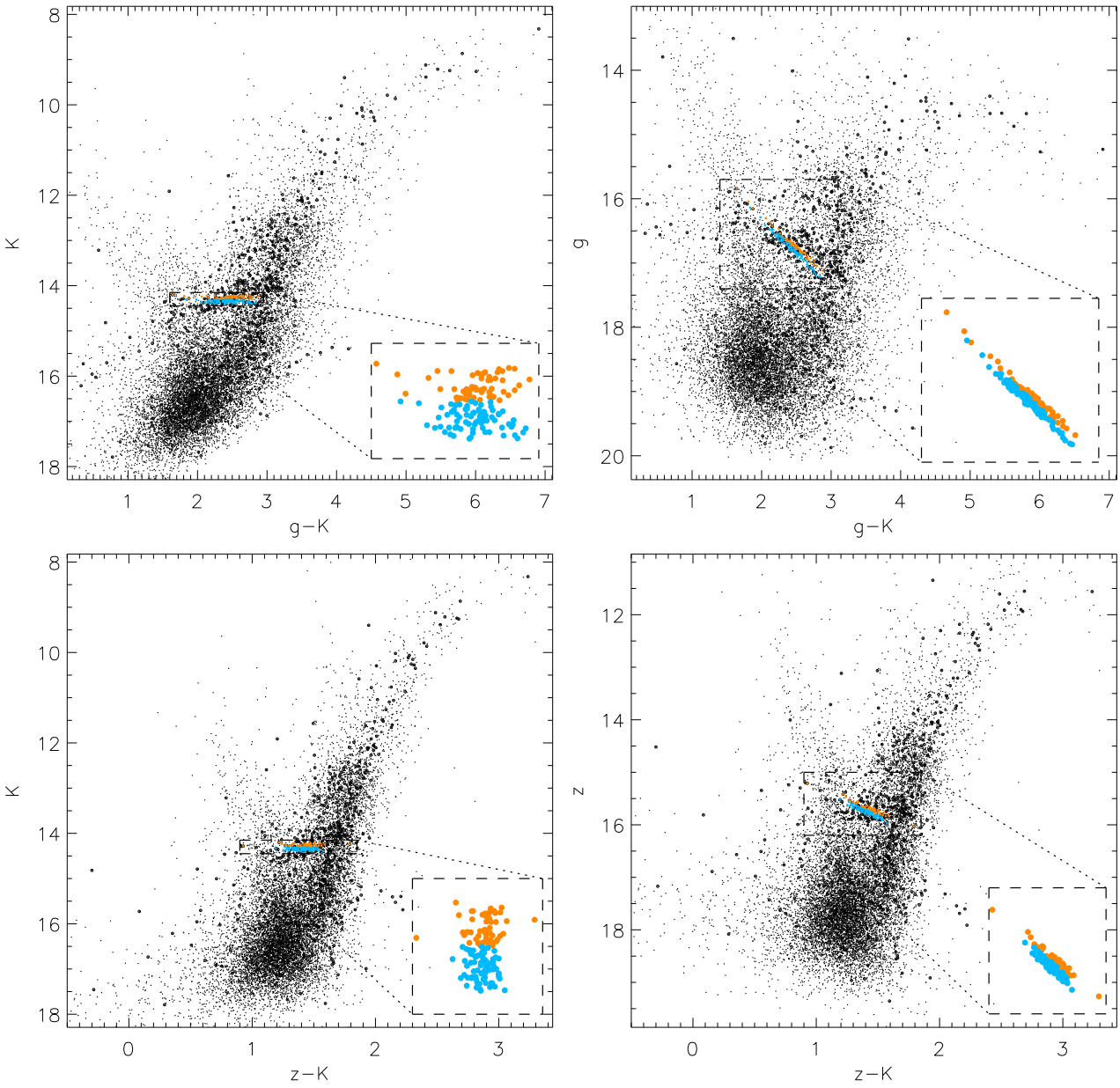

Figure 6.8: CMDs of NGC 6569 for different filter combinations. Legend as in Fig. 6.7. Note that both populations, selected based on JK colours, are pretty well separated in both CMDs.

6.3 Second-parameter problem

The morphology of a GC CMD can reveal important insights on the residing stellar populations and their properties. One of the well-studied CMD sequences is the HB, for which its morphology seems to be related to the cluster metallicity. However, the metal abundance alone cannot account for all the HB variability observed in different clusters: about 50 years ago, the "second parameter problem" was born (Sandage & Wildey 1967; van den Bergh 1967).

Fig. 6.9 presents our CTIO-based CMDs for NGC 288 and NGC 362, a typical second parameter pair: while these clusters have similar metallicity ([Fe/H]~ -1.3), the horizontal branch morphology is very different: NGC 288 has an extended blue HB, while NGC 362 has a very red HB.

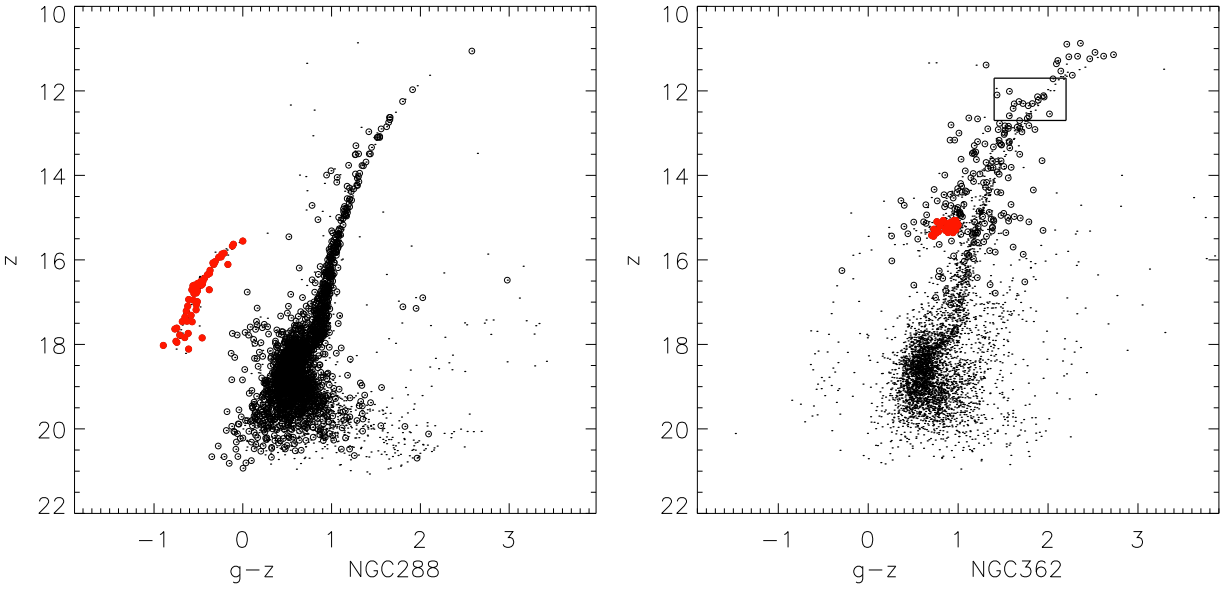

Figure 6.9: CMDs for NGC 288 and NGC 362, the best-studied second parameter pair. Open circles are stars within r_h, dots are stars from the entire field. The HBs are indicated with red filled circles. See text for more details.

Several GC properties have been proposed as candidate second parameters, but so far no such parameter has been found that gives satisfying results for all clusters. Age (e.g., Searle & Zinn 1978; Chaboyer et al. 1996) and He abundance (Hartwick 1968) are the most frequently used second-parameter candidates. However, other less well-studied candidates exist, including environment (Buonanno et al. 1997), stellar rotation (Peterson et al. 1995), CNO abundance (Lee et al. 1994) and mass loss (Yong et al. 2000). Section 6.4 presents our approach on the study of mass loss during the RGB and AGB phase. For recent reviews on the topic, we refer to Brodie & Strader (2006) and Dotter et al. (2010). Dotter (2013) stresses the importance of the use of more than one HB metric, as it is impossible to capture all the HB features in just one parameter. This will probably result in the need of more than one "second parameter", which

need to reflect global cluster parameters (like metallicity and age) and other parameters like e.g. mass loss (Yi et al. 1998) or helium enrichment (Chung et al. 2011).

Note that the UV upturn in elliptical galaxies is ascribed to this extremely blue HB stars as well (see e.g. Dorman et al. 1995; Brown et al. 2008), hence it is of fundamental importance to understand the details on the formation and evolution of the HB stars.

Recently, Kunder et al. (2013) expressed the need to study wide-field CMDs and cumulative fractions of (E)HB stars to study the role of helium as the second parameter affecting the HB morphology. In their study on M 22 (NGC 6656) they found suggestions that the EHB stars are less centrally concentrated than the blue HB stars. This is in contrast to theoretical predictions: one expects the He-enriched second generation of stars close to the GC centre, as the enriched residuals of first generation stars will be concentrated close to the centre of the cluster potential, where the second generation will be born. Hence, the results of Kunder et al. (2013) indicate that helium is not responsible for the morphology discrepancies. For another study on radial gradients of different sub-populations in GCs, we refer the interested reader to Monelli et al. (2013).

We decided to use our CMDs based on wide-field photometry (presented in chapter 3) to tackle the long-standing second parameter problem.

Before continuing the discussion on the second parameter problem, we draw the attention to the kink in the AGB of NGC 362, which is indicated with a box in Fig. 6.9. This feature suggests the presence of dust shells in the atmosphere of these stars, which makes them really look redder (so cooler) than expected, due to the dust extinction. As this transition is not really smooth (almost looks like a step-function, at least for the brightest stars), it could enable to study the chemistry of the dust. Boyer et al. (2009) studied the mass loss of RGB stars in the same cluster. Recently, we contacted their group to check if they have spectra for these stars, as they also have FLAMES and UVES observations (McDonald & van Loon 2007). However, their group suspects that the observed kink is just a stochastic effect (Iain McDonald, private communication).

6.3.1 Sample selection

Some of the clusters with interesting HB properties are listed by Lee et al. (2007). Their list of 28 EHB GCs was the initial sample for this project. We determined wide-field CMDs and radial cumulative fractions for 8 GCs from their subsample of clusters with strongly extended HB (NGC 2808, NGC 5139, NGC 5986, NGC 6093, NGC 6205, NGC 6273, NGC 7078 and NGC 7089) and 9 GCs from their subsample of clusters with moderately extended or bimodal HB distributions (NGC 1851, NGC 1904, NGC 4833, NGC 5904, NGC 6229, NGC 6402, NGC 6681, NGC 6723 and NGC 6864).

At this point, some GCs listed by Lee et al. (2007) are not included for a variety of reasons:

- Too shallow and scattered CMDs (NGC 2419, NGC 6715)
- Too much contamination, coinciding with the HB region, scattered CMD (NGC 5824, NGC 6388, NGC 6441). Note that NGC 6388 and NGC 6441 would be interesting to study as second parameter pair (see e.g. Dalessandro et al. 2013)
- NGC 6712: too much contamination, coinciding with the HB region, would need proper motions to clean.
- NGC 6626: z-band observation was heavily saturated. For the same reason, no z-band magnitude was listed in Chapter 3.
- No data available for NGC 6266, NGC 6656, NGC 6752 and NGC 6522.

Some additional clusters were included in the sample, because they exhibit an interesting HB morphology or they form second parameter pairs (in some cases with one of the above clusters). The reasons for inclusion are:

- extended HB morphology: NGC 5024, NGC 5272, NGC 6218, NGC 6121 (hosting a bimodal HB, as noted by e.g. Monelli et al. 2013) and NGC 6341. Note that NGC 6341 and NGC 7078 form an interesting pair to study (e.g. Dalessandro et al. 2013).
- intermediate HB morphology while very metal-poor: NGC 5053 has a HB index of 0.52 (Mackey & van den Bergh 2005) and [Fe/H]~ -2.27. Note that the metallicity of this cluster is similar to the Fe abundance in NGC 7078 ([Fe/H]~ -2.37, HB index$=0.67$), while the HB extension is very different in both clusters. Hence, this cluster pair is interesting to study the 2nd parameter problem.
- NGC 6171 has a metallicity comparable to NGC 6723, while the HB morphologies are quite different (HB indices equal -0.73 and -0.08, respectively). Therefore, this pair of clusters might provide some additional insights in the second-parameter problem (see e.g. Smith & Hesser 1986).
- NGC 288 and NGC 362 is a classical second parameter pair (with [Fe/H] ~ -1.3; see Fig. 6.9). NGC 362 is known to contain a primarily red HB, although some blue HB stars have been discovered (Moehler et al. 2000). These authors found that blue HB stars in NGC 362 show continuity with the dominant red HB population and suggest that the blue HB subpopulation originates from red giants with unusually high mass loss.

6.3.2 Treating incompleteness issues

Our CMDs are derived from data observed with ground-based small telescopes (both SDSS and CTIO 0.9m telescope). Therefore, these suffer from incompleteness, especially close to the

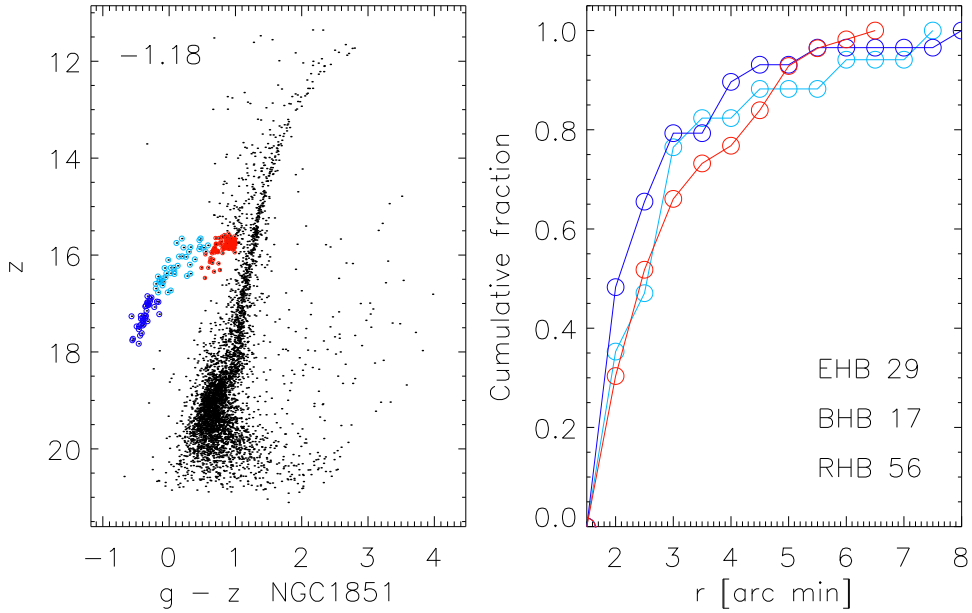

Figure 6.10: NGC 1851: cumulative fraction of HB regions. EHB stars are indicated with dark blue, the blue HB is indicated with light blue, the reddest part of the HB is indicated with red.

cluster centre. To overcome this issue, we first determine an inner and outer radius, between which we believe the CMDs are not biased with respect to different magnitude ranges.

The principal goal of the current project is to study the HB morphology. Therefore, we determine the annuli only taking into account the magnitude range of the HB and consider radii where star counts seem to be (reasonably) complete for the HB magnitude range. For example, for NGC 1851 (Figs. 6.10 and 6.11) EHB stars do not reach fainter than $z \sim 18$, which is considered as the limiting magnitude affecting the completeness of the stars of interest. For this cluster, we adopt an inner limit of 1.5 arcmin and an outer limit of 8 arcmin. Due to saturation issues affecting the SDSS data (see Fig. 3.9), bright stars will be incomplete (as DAOPHOT does not include these in the analysis).

As an example of our data, Fig. 6.10 presents the CMD and corresponding cumulative fractions for NGC 1851. EHB stars are indicated with dark blue, the blue HB is indicated with light blue, the reddest part of the HB is indicated with red. The cluster metallicity [Fe/H] is believed to be the main contributor to the different HB morphologies. Therefore, it is included in the CMDs in the top left corner of the figure (obtained from Harris 1996, 2010 edition). We conclude that the cumulative fractions for the different HB sections are comparable for this cluster.

A similar analysis studying the CMDs and cumulative fractions was performed for 26 GCs. In general, our data do not show that EHB stars are less centrally concentrated, thus, we do not find evidence against helium being the second parameter affecting the HB morphology. Our results do not confirm the suggestions of Kunder et al. (2013).

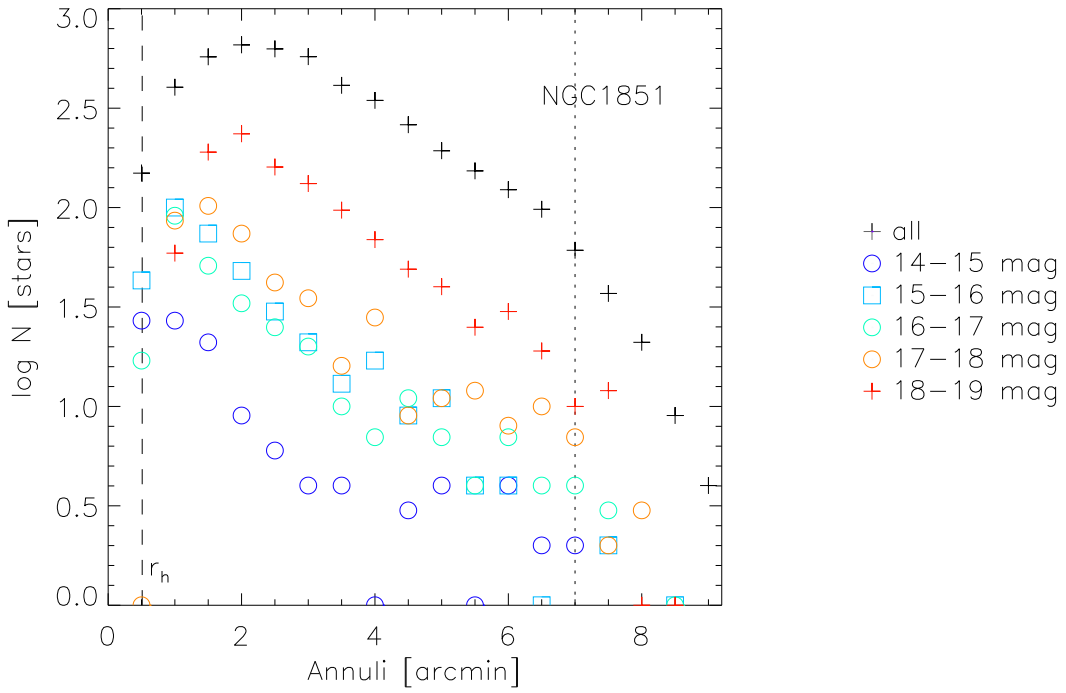

Figure 6.11: NGC 1851: radial distribution of stars. The half-light radius r_h is indicated with the dashed line, the dotted line represents the radius where part of the annulus is outside the field of view.

6.4 Mass-loss during RGB and AGB

In section 6.3 we linked stellar mass-loss to the second parameter problem. Yong et al. (2000) studied mass loss on the HB and found that mass loss causes HB stars to evolve to be hotter (bluer) and fainter. Moreover, to account for the observed HB colours and morphology, Iben & Rood (1970) proposed a scenario that RGB mass loss increases with metallicity (although questioned by Carraro et al. 1996). The project described in this section presents another approach on the second parameter problem and will concentrate on the mass loss of giant stars. Here we will only present the basic ideas, as the collaboration with Iain McDonald was started only recently.

Although stars lose mass during the entire stellar evolution, they experience their strongest mass loss (which is frequently described by "Reimers' law"; Reimers 1975, 1977) during the AGB and RGB phase. Willson (2000) reviewed our current understanding on mass loss processes. The amount of mass-loss not only determines the type of the stellar remnant, but can also alter the post-RGB track in the Hertzsprung-Russel diagram. Moreover, it can also change the mass, chemical state, composition and mineralogy of the material returned to the ISM (McDonald et al. 2011). Dupree et al. (2009) describe how a star's hot ($\sim$ 10000K) chromosphere emits atomic gas at low mass-loss rates, while more intense but shorter pulsation-driven mass loss ejects a mostly cool dusty wind (van Loon et al. 1999).

One can determine the stellar mass based on three observables, if one knows the distance and reddening (as described in McDonald et al. 2011). From high-resolution spectroscopy, one can derive the gravity g. Combined with the cluster distance, the bolometric luminosity L can be obtained from the integrated spectral energy distribution (SED). Moreover, one needs the effective surface temperature T_{eff}, which can be determined based on spectroscopy, photometric colours or SEDs. Based on these observables, the stellar radius can be derived based on the Stefan-Boltzmann law for black body radiation and Newtonian gravity:

$$R^2 = \frac{L}{4\pi\sigma T_{eff}^4} = \frac{GM}{g}. \tag{6.1}$$

Combining both formulas, one can obtain an expression for the stellar mass:

$$M = \frac{gL}{4\pi\sigma T_{eff}^4 G}. \tag{6.2}$$

Although straightforward in theory, it is in practice not easy to determine the stellar mass, because it is difficult to determine the parameters (especially the gravity g) accurately. Therefore, only relative differences in mass are studied (with resulting masses subject to the same systematic uncertainties). Using the above method, McDonald et al. (2011) measured the relative difference between the masses of RGB and AGB stars in ωCen, which provides insight on the mass-loss during the RGB and AGB phase of stellar evolution. They found the bulk of the mass loss occurs on the RGB, while one-third of the mass is lost during the AGB phase. They obtain an estimate for a mass loss rate of $10^{-8} M_{\odot} yr^{-1}$ during the RGB phase, higher than the Reimers' law mass-loss rate of $1.9 \times 10^{-9} M_{\odot} yr^{-1}$.

Their results are based on data for the metal-poor GC ωCen only ([Fe/H]~ -1.7). We believe the accuracy of this result can be improved when applied to other clusters with different HB morphologies and metallicities. Based on their spectroscopy and our homogeneous CMDs, we are making a similar analysis for e.g. NGC 104 ([Fe/H]~ -0.72, HB~ -0.99), NGC 362 ([Fe/H]~ -1.26, HB~ -0.87), NGC 2808 ([Fe/H]~ -1.14, HB~ -0.49) and NGC 4372 ([Fe/H]~ -2.17, HB~ 1) (with metallicities taken from Harris 1996 and HB indices obtained from Mackey & van den Bergh 2005). We are optimistic this might enable us to relate metallicity, initial stellar mass or initial abundance to RGB mass-loss and could provide physical constraints on models for HB stars. The project is in an infant stage, so no preliminary results are presented here.

Outlook: GCs under the scanner to reveal the ages of distant galaxies

7

7.1 Introduction

For unresolved extragalatic objects, integrated colours and spectra provide the only available information on the ages and metallicities of their stellar populations. These can only be calibrated with reference to the only unequivocally datable stellar populations in the Milky Way: colour-magnitude diagrams of open and globular clusters. Unfortunately, there is a fundamental ambiguity in this procedure, as the most commonly used photometric and spectroscopic indices are well known to be degenerate with respect to age and metallicity (Worthey et al. 1994) but additionally they are also degenerate versus blue horizontal branch stars (BHB) and other hot stellar populations present even in old systems (e.g. de Freitas Pacheco & Barbuy 1995; De Propris 2000; Schiavon et al. 2004 (hereafter S04)). This is demonstrated in Fig. 7.1, taken from Percival & Salaris (2011): it shows an old stellar population, superposed with different HB morphologies. It is clear that the latter have a strong impact on the H_β estimate, resulting in strong implications on the age determination of these systems (S04, Cenarro et al. 2008) and hence on theories of galaxy formation.

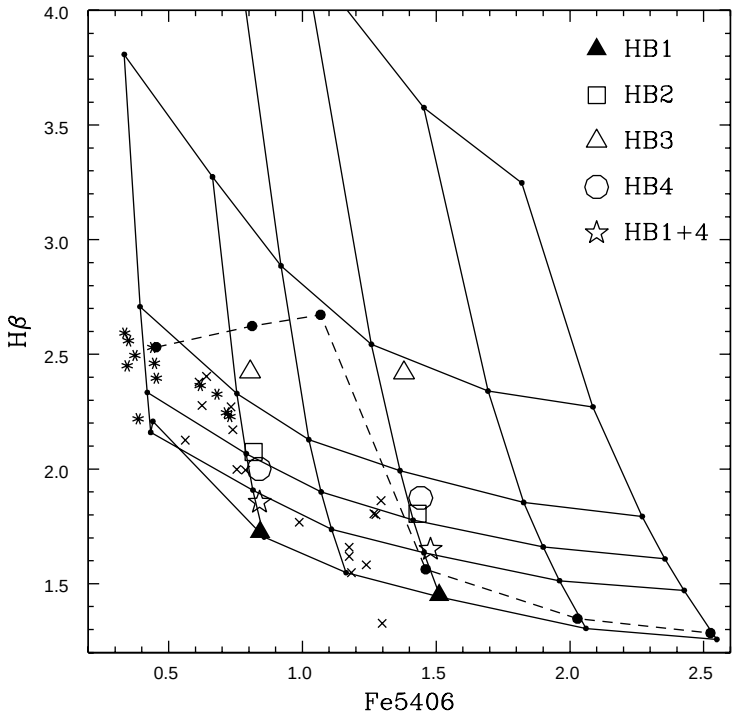

Figure 7.1: Hβ versus Fe5406 α-enhanced grid (taken from Percival & Salaris 2011; their Fig. 2). The underlying grid presents SSP ages of 1.25, 2, 6, 8, 10 and 14 Gyr (from top to bottom) and [Fe/H]$=$ $-1.84, -1.31, -1.01, -0.70, -0.29$ and $+0.05$ (left to right). Crosses and asterisks are observational data for Galactic GCs from S05 (with asterisks denoting clusters with blue HBs). Variations in the shape of the HB strongly affect ages and metallicities derived by Lick indices: e.g. for lower metallicity models, at [Fe/H]~ -1.3, the peak in Hβ implies an age around 5-6 Gyr, whereas for the solar metallicity case, the inferred age is < 3 Gyr (with an underlying population of 14 Gyr).

In this thesis, we presented a homogeneous catalog of integrated photometry of the Milky Way's globular cluster system. We will extend our dataset with archival NUV and FUV Galaxy Evolution Explorer (GALEX) data for 45 GCs, to probe the exotic hot He-burning HB stars and blue stragglers that are likely the dominant UV flux (O'Connell 1999). Moreover, population models suggest that FUV photometry may have the potential to constrain age spreads within a galaxy, while age differences between clusters are considered as one of the most significant second parameters affecting HB morphology (see section 6.3) and can be probed via UV colours. Our resulting homogeneous CMDs (supplemented with data from the literature) allow us to carefully determine the ages of the GCs and locate the hot stars in the HB. By measuring UV-optical colours we will be able to verify the effects of old hot stars on the integrated spectra of elliptical-like stellar populations and in particular the effects of hot HB stars and blue stragglers on integrated ages. With GALEX median imaging survey (MIS) data available for half the sky, this will provide an invaluable calibration for determining more reliable age estimates for the unresolved stellar populations in extragalactic systems.

Adding a suite of integrated spectra at Lick resolution for a homogeneous sample of GCs makes our photometric catalog even more valuable. The Lick/IDS indices were introduced by Worthey et al. (1994) in their pioneering work on old stellar populations and are now widely used (e.g., Falcón-Barroso et al. 2011). First attempts to collect integrated spectra of Galactic GCs have been made (e.g., Zinn & West 1984; Cohen et al. 1998; Puzia et al. 2002; Beasley et al. 2004), but were limited to a small fraction of the known Galactic GC sample. The most comprehensive effort to date was made by Schiavon et al. 2005 (S05 hereafter): these authors presented a library of integrated spectra of 40 Galactic globular clusters. Unfortunately, this library includes less than half of the 45 GCs with existing GALEX data and all but one of the missing clusters have [Fe/H] $\lesssim -0.5$, which are the clusters expected to show the effect of blue horizontal-branch stars on the Balmer lines (S04). This is an important drawback for this sample. Furthermore, the resulting spectra of the S05 library are based on the core regions only, yet clear evidence of color gradients is seen in the UV and *griz* photometry. Finally, the S05 sample does not include more than 40 GCs (without GALEX data) for which we do have the *griz* photometry.

With this motivation, our team embarked on a project to expand our purely photometric GC catalog. We obtained integrated spectra at Lick resolution for a homogeneous sample of GCs, covering the bulk of the southern clusters. This large observational effort was performed using the VLT/FORS2 instrument, with a total observing time of about 80 hours (obtained during a period of two years in observing periods P89, P90 and P91). In the next sections the sample selection and observations will be briefly described. Finally, we will present a preliminary spectrum for one of our many target clusters.

7.2 Sample selection

This large observational effort was performed in service mode. Due to limitations on the duration of the observing blocks, we had to limit our sample to GCs bright enough we could obtain spectra with the required S/N based on observations lasting no longer than one hour. This resulted in a pool of more than 100 GCs, which we subdivided in three subsamples according to their priority.

Priority I clusters were the GCs with available GALEX data which are not in the S05 library. GCs which are not part of the S05 library and do not have GALEX data were listed as priority II: for these clusters we can still compare the Balmer strengths and ages obtained from CMDs with the corresponding values from the integrated spectra. Finally, priority III was assigned to clusters which are included in the S05 library, which enables to directly compare our integrated spectra with their spectral library.

7.3 Observations

The observations were performed at the ESO/Paranal observatory, with the VLT/FORS2 instrument. Spread over three observing periods (between P89 and P91), we obtained data for all our program clusters in about 80 hours of observing time. For our scientific needs, we only required grey time without seeing restrictions, which made this program an excellent bad-weather program to fill the observational queues when observing conditions are mediocre. Nevertheless, we could not observe with full moon, as the blue part of the spectrum with the Balmer lines is essential for this project.

To provide a robust measure of the integrated light of each globular cluster, the spectra were obtained by drift-scanning. Moving the slit back and forth across each cluster yields spatially integrated spectra, eliminating the effects of radial gradients as well as stochastic effects from chance inclusion of one or more luminous RGB stars within a single slit position (e.g., Kennicutt 1992). This observing method is illustrated in Fig. 7.2. Though straightforward in theory, the drift-scanning technique turned out to be an observational challenge.

In section 2.2, we required a separate observation to accurately remove the telluric lines from the NIR spectra obtained for the Fornax ETG project. Similarly, we now need a separate sky spectrum, which is indispensable to properly remove the [OII]3727 emission line from the spectra. For our scientific goals, we need S/N of 30-40 in the Balmer line region at 4000Å, summing the spectra over 2 half-light radii (S04). We chose the 1.31 arcsec slit, the 600B+22 grism, standard resolution on the MIT CCD and 2×2 binning. This was perfect for our needs: it results in spectra with 7.8Å (FWHM) resolution, whereas the Lick/IDS resolution is 8-11Å (FWHM).

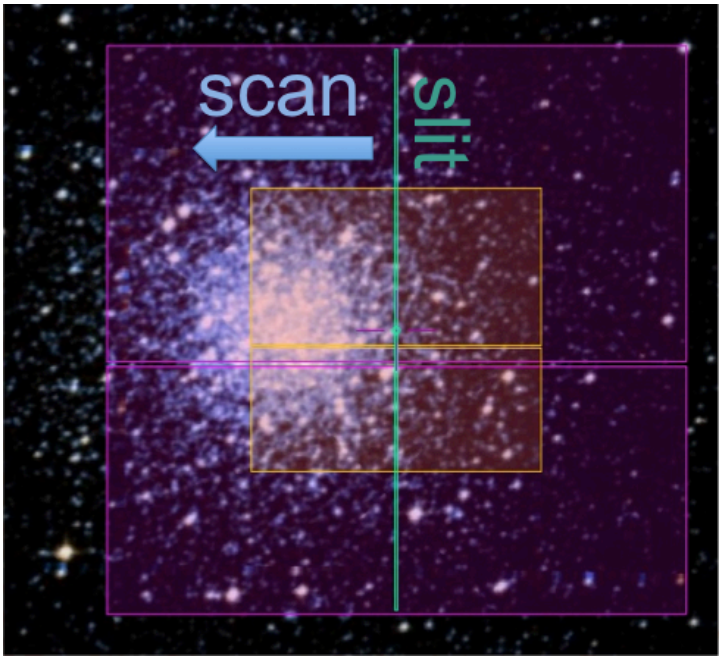

Figure 7.2: Image of NGC 4590 to illustrate the drift-scanning technique applied for the VLT/FORS2 observations.

7.4 Main goals

Combining the spectroscopic data obtained for this project with the photometry presented in this thesis, we will be able to compare CMD-based ages and Balmer strengths with the estimates of both based on integrated spectra. These latter measurements are biased by the BHB and blue straggler stars, which results in younger estimated ages and broader Balmer lines (De Propris 2000, S04, Cenarro et al. 2008). We will use the integrated NUV/FUV$-g$ colour as an estimate for the presence of these hot stars and relate this colour to the discrepancy between the real CMD-based ages (Balmer strengths) and the biased integrated spectra ages (Balmer strengths, resp.). This relation will enable to correct ages and line strengths, based on integrated spectra, for the bias introduced by hot stars in any unresolved stellar population.

In their pioneering work on old stellar populations, Worthey et al. (1994) introduced the Lick/IDS indices, which are now widely used (e.g., Falcón-Barroso et al. 2011). We will use the integrated spectra to determine the Lick/IDS chemical abundances (e.g., Ca4227, G4300, CN_1, CN_2 and NaD) extending our homogeneous photometric catalog of Galactic GCs which will be useful for stellar populations synthesis models (e.g., Maraston 2005; Graves & Schiavon 2008).

Fig. 7.3 presents the VLT/FORS2 spectrum of NGC 104. Although the data reduction is still not optimised (as it is now performed by the FORS2 data reduction pipeline), the spectral features of interest (e.g. several Balmer lines) are clearly present. This preliminary result is definitely encouraging for the remainder of this project.

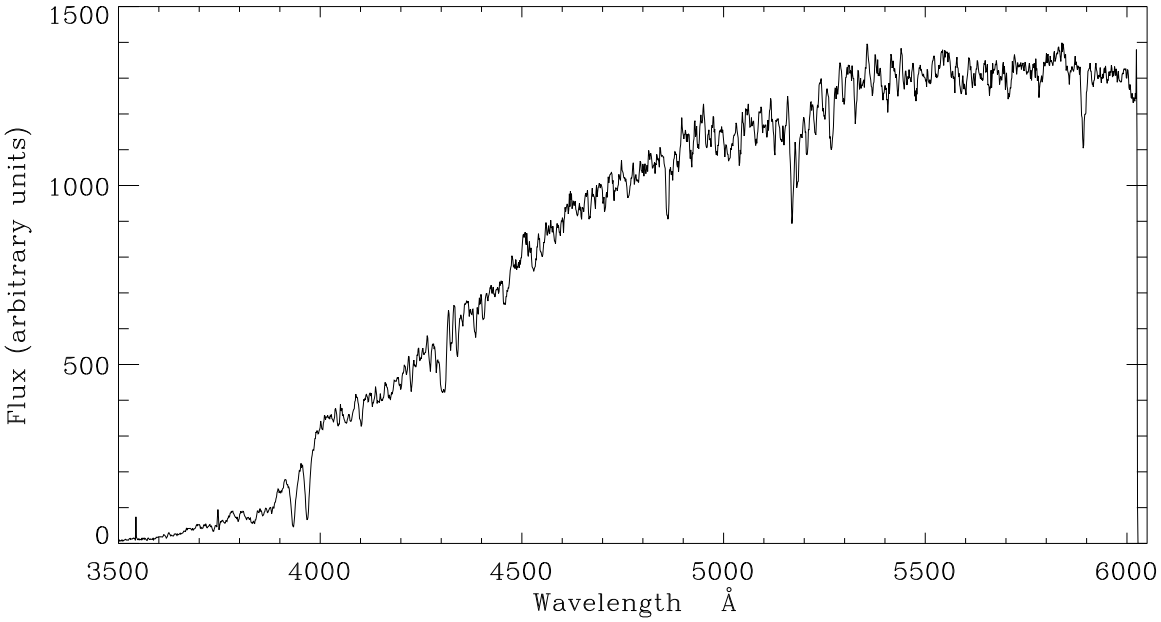

Figure 7.3: NGC 104: VLT/FORS2 spectrum from our sample based on P89 observations.

8 Summary

In this PhD thesis, we explore two different aspects of galaxies, both of which hold important clues about their structure, formation and evolution.

Several fundamental extragalactic scaling relations (like the fundamental plane and Faber-Jackson relation) and other properties (like the black hole mass) of galaxies rely on the use of the velocity dispersions. However, it was not clear if the dust in early-type galaxies significantly affects the determination of this parameter, hence undermining the reliability of the correlations between optical velocity determinations and the related physical properties. Chapter 2 answers this question: we determine the velocity dispersions of ETGs in the Fornax cluster, based on new near-infrared spectra obtained with the ISAAC instrument on the VLT. These NIR spectra are hardly affected by dust attenuation and hence enable to obtain an unbiased estimate of the velocity dispersions. For the first time, we are able to make a homogeneous comparison between NIR velocity dispersions and optical values from the literature. As shown in Fig. 8.1, we find that the dust in these largely optically-thin systems does not strongly alter the velocity dispersion determination. As a consequence, we can keep using the velocity dispersions based on optical data with peace of mind.

From chapter 3 onwards, we choose another approach to study the formation and evolution of galaxies. We leave the distant extra-galactic objects behind us and fully concentrate on the study of the globular cluster (GC) system of our own galaxy, the Milky Way. Current catalogs of Galactic GC photometry are based on dated filter systems, are inhomogeneous and based on

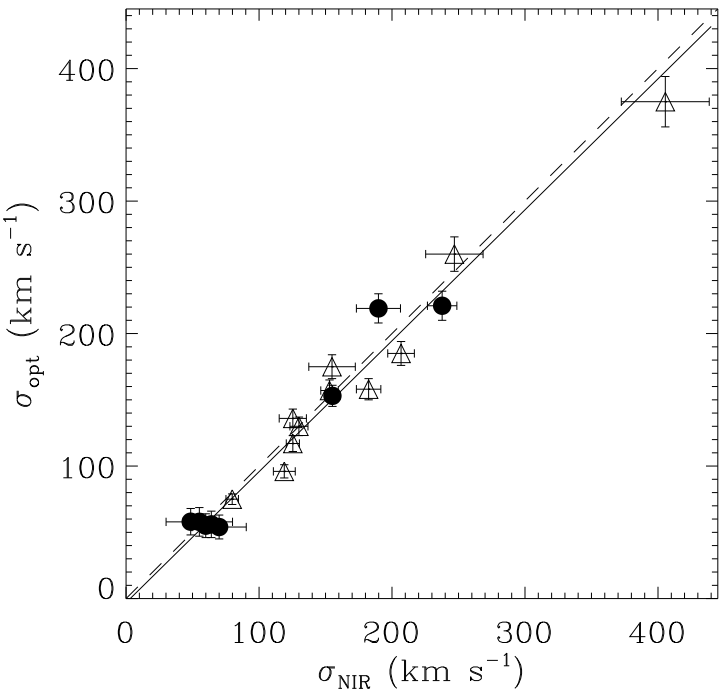

Figure 8.1: Correlation between the dispersion measured from the CO band head and the optical dispersion (Kuntschner 2000). The dashed line shows where two measurements are equal, the solid line is the best-fitting line, given by equation 2.2.

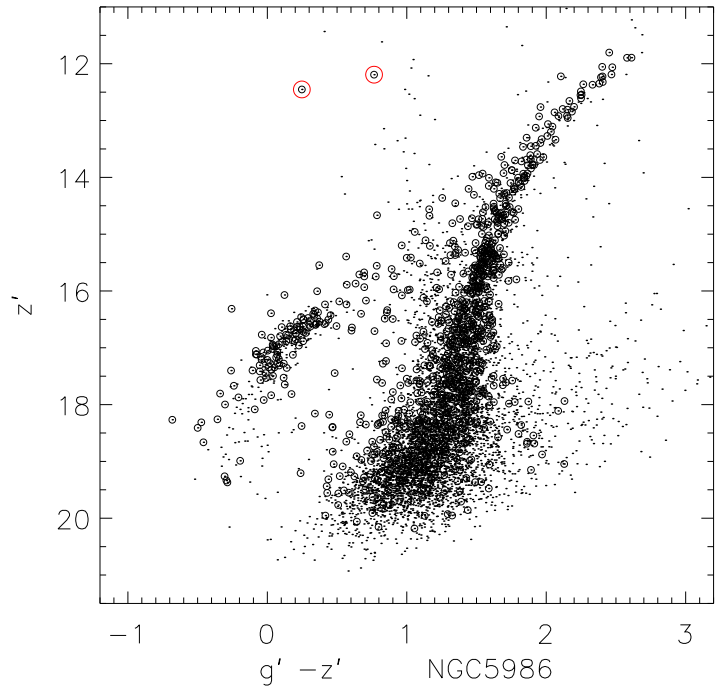

Figure 8.2: NGC 5986: open circles are stars within r_h, dots are stars from the entire field. The two bright isolated stars in the CMD (indicated with red circles) were selected as candidate outliers. Their proper motions confirmed these stars are not cluster member. Therefore, they were cleaned out when performing the aperture photometry.

different methods and instruments. As a service to the astronomical community, we provide a homogeneous catalog of SDSS photometry for a large subset of the Galactic GC system.

Chapter 3 gives an overview of the basic data reduction steps applied to our data and discusses issues related to the cluster centroids and the sky determination, which can be complicated in these crowded fields. In order to obtain clean representative GC colours, which are essential in the next chapter, we clean contaminating foreground stars by a technique involving the cluster colour-magnitude diagrams and the stellar proper motions (illustrated in Fig. 8.2). It is the first time this technique was applied for such an ample GC sample. As the main result of this chapter, we present the currently largest homogeneous SDSS photometry catalog of the Galactic Globular Cluster system.

In chapter 4, we use the clean SDSS colours obtained in the previous chapter and improve existing colour-metallicity relations (CMRs). We do not only use the standard [Fe/H] metal abundance, but also present CMRs based on the Calcium Triplet metallicity scale, a new metallicity indicator currently gaining interest in the astronomical community (e.g. Foster et al. 2010; Usher et al. 2012). We find that the CMRs are non-linear for both metallicity indicators: Fig. 8.3 demonstrates our results for the [Fe/H] abundance. We discuss the origin of the scatter in the CMR and look for links with other GC properties like the HB morphology, the age and the initial mass function. We find a clear correlation between the CMR scatter and the extinction

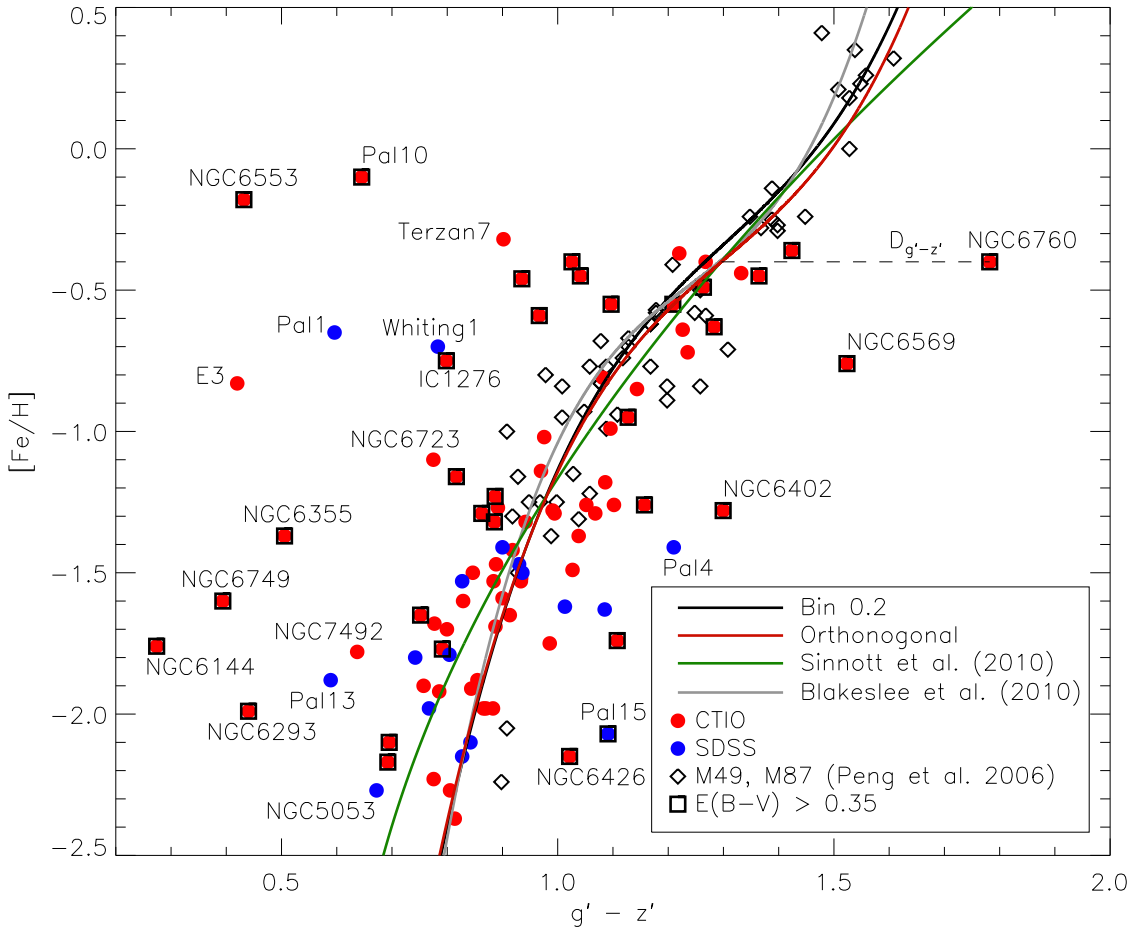

Figure 8.3: [Fe/H] as a function of $g' - z'$ for our sample of Galactic GCs and data of extragalactic GCs from the literature. Clusters from our CTIO and SDSS samples are represented with filled circles, while literature data of M 49 and M 87 (Peng et al. 2006) is represented by diamonds. The black line presents the CMR derived for all low-reddening GCs, fitting colours binned by metallicity bins of 0.2 (as given by Eq. 4.7). The red line is the final CMR (given by Eq. 4.8) obtained by minimizing the orthogonal distance. The grey and green lines present CMRs from the literature (Blakeslee et al. 2010; Sinnott et al. 2010).

estimates, which can be poorly defined especially close to the Galactic disk. Finally, we discuss the colour bimodality and its link to metallicity bimodality, which is complicated by the non-linear nature of the CMRs.

In chapter 5 we supplement the photometric Galactic GC catalog with structural parameters. These are useful indicators of the GC evolution and are closely related to the position in the Galaxy. Because our CTIO data do not cover the entire spatial extent of most of our sample GCs, we first study the influence of a limited field-of-view on the determination of the King model parameters. Thereafter, we compare our derived parameters with the literature, based on both SB profiles and stellar count density profiles. We give a new definition for core-collapsed clusters and find a clear correlation with the position in the Galaxy, which is shown in Fig. 8.4: core-collapsed clusters are located towards the Galactic disk, while non core-collapsed clusters

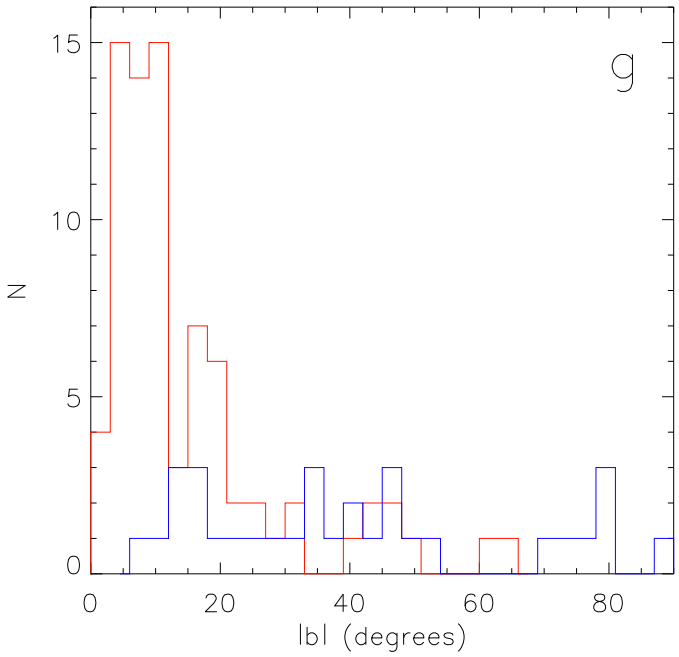

Figure 8.4: Histograms of the absolute Galactic latitude b (in degrees) for core-collapsed ($c \geq 3$, black histogram) and non core-collapsed (red histogram) GCs. It is clear that the core-collapsed clusters are located towards the Galactic disk, while the non core-collapsed clusters are preferentially residing in the outer halo of the Galaxy.

are mostly populating the outer halo. This was predicted by theoretical models (Gnedin et al. 1999; Madrid et al. 2012), but not yet confirmed by observations. Further, we seek correlations between the obtained structural parameters and other cluster properties that are related to the high stellar densities in GCs (including HB morphology, milli-second pulsars, X-ray sources). Finally, we show that colour gradients can be vastly affected by a few central RGB stars, which makes it hard to interpret the gradients and to relate them to stellar subpopulations in GCs.

In chapter 6 some projects are presented based on the colour-magnitude diagrams (CMDs) as an illustration of the scientific output we expect from these diagrams. Although this is still work in progress, some preliminary results are presented regarding the double HB discovered by Mauro et al. (2012) in NGC 6569, our cumulative fraction approach on the the long-standing second-parameter problem and the mass-loss in RGB and AGB stars.

Chapter 7 presents a large observational project started during the course of this PhD thesis. We obtained VLT/FORS2 drift-scan spectra for the bulk of the southern GCs, making it the largest homogeneous spectroscopic sample to date of such objects. We plan to use these spectroscopic data to obtain spectroscopic age estimates, which can be biased due to the effects of extremely hot HB stars. However, using the unbiased age estimates based on the CMDs, we will be able to calibrate this effect using FUV/NUV-optical colours. This relation will enable to improve current age estimates of unresolved elliptical-like stellar populations.

Nederlandse samenvatting

9

Het is al moeilijk om je een imaginair beeld te maken van onze eigen Melkweg, die miljarden sterren zoals onze eigen Zon herbergt. Dan is het misschien nog lastiger om je voor te stellen dat er in het Universum nog miljarden gelijkaardige sterrenstelsels bestaan. Deze gravitationeel gebonden systemen bestaan naast sterren ook uit gas, stof en een mysterieuze donkere materie component. Hoewel deze laatste de meest massieve component is van sterrenstelsels, tasten sterrenkundigen nog steeds in het duister als het gaat over de herkomst of eigenschappen ervan.

Dit doctoraatsonderzoek bestudeerde de vorming en evolutie van sterrenstelsels vanuit twee verschillende perspectieven.

Het eerste deel, uitgevoerd aan de Universiteit van Gent, richtte zich tot het onderzoeken van de zogenaamde 'vroegtype' sterrenstelsels. Verschillende belangrijke relaties (zoals het fundamenteel vlak en de Faber-Jackson relatie) en moeilijk te bepalen eigenschappen (zoals de massa van het zwarte gat, dat in (bijna) elk sterrenstelsel aanwezig is), steunen op het gebruik van de snelheidsdispersie parameter. Deze meet de statistische dispersie van de snelheden van sterren ten opzichte van de gemiddelde bewegingssnelheid van het stelsel. Ondanks het belang van deze parameter, was het nog niet duidelijk welke invloed het interstellair medium (zoals banden van stof) heeft op de bepaling ervan. Uiteraard ondermijnt de onzekere nauwkeurigheid gerelateerd aan de bepaling van deze parameter de betrouwbaarheid van de relaties die erop steunen. Hoofdstuk 2 werkt deze twijfel weg: we bepaalden de snelheidsdispersies van vroegtype sterrenstelsels in de Fornax cluster en gebruikten daarvoor nabij-infrarode spectroscopie, gebaseerd op waarnemingen met het ISAAC instrument van de Very Large Telescope. In optische golflengtes blokkeert en verstrooit het aanwezige stof het licht van de sterren, terwijl in het nabij-infrarode golflengtegebied dit niet het geval is. Dus konden we, en dat voor de eerste keer, een homogene vergelijking maken van de optische en nabij-infrarode snelheidsdispersies, om zo de nauwkeurigheid van optische observaties te testen. We vonden dat het interstellair medium in deze stellaire systemen geen waarneembare invloed heeft op de bepaling van de snelheidsdispersies. Dit belangrijke resultaat word getoond in figuur 9.1: algemeen is er geen verschil tussen de snelheidsdispersies bepaald op basis van optische en nabij-infrarode spectroscopische data. Dit was niet volledig onverwacht, aangezien deze vroegtype sterrenstelsels algemeen geen grote hoeveelheden stof bevatten. We besluiten dat we de snelheidsdispersies die bepaald werden gebaseerd op optische data met een gerust gemoed kunnen blijven gebruiken.

Vanaf hoofdstuk 3 kiezen we voor een andere benadering in de studie van sterrenstelsels. We concentreren ons op ons eigen sterrenstelsel, de Melkweg, en wel in het bijzonder op compacte bolvormige sterrengroepen. Deze worden beschouwd als de bouwstenen van sterrenstelsels, aangezien vele verbanden tussen de structurele eigenschappen van bolhopen en die van de sterrenstelsels die hen herbergen erop wijzen dat hun formatie en evolutie nauw samengingen. Met moderne telescopen is het mogelijk om de sterren in deze bolvormige sterrenhopen apart waar te nemen, waardoor we zelfs de eigenschappen van deze bijzondere sterrenfamilies

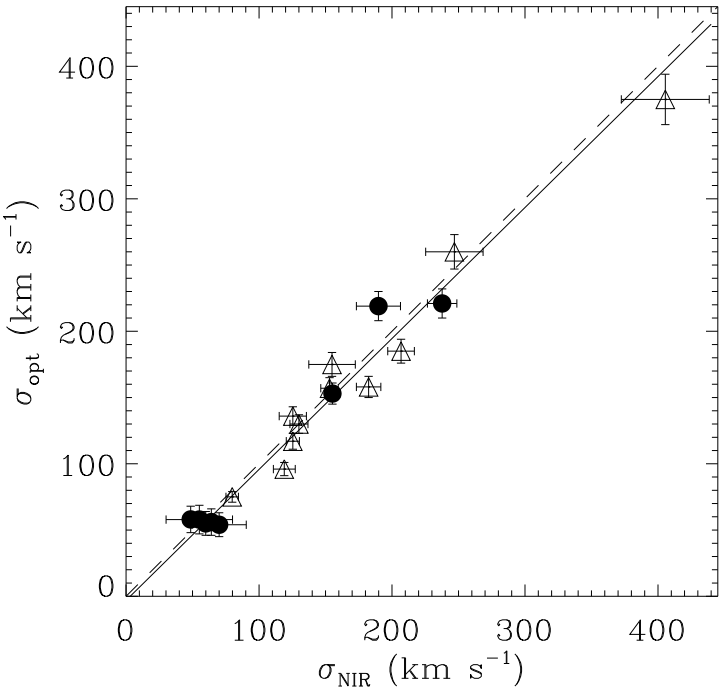

Figure 9.1: Correlatie tussen de snelheidsdispersies gebaseerd op optische (Kuntschner 2000) and nabij-infrarode data. De gestreepte lijn toont waar de twee metingen gelijk zijn. De volle lijn geeft de beste fit voor onze data, zoals die werd gegeven in vergelijking 2.2.

kunnen bestuderen. In verafgelegen sterrenstelsels kunnen we de bolvormige sterrenhopen wel waarnemen, maar is het onmogelijk om de sterren te selecteren. Daarom kunnen we vele eigenschappen van deze sterrenclusters enkel in onze Melkweg bestuderen en zijn ze onmisbaar voor de ijking van verafgelegen bolhopen.

Uiteraard is het dan ook belangrijk om deze schalingsrelaties te verkrijgen voor het standaard SDSS (Sloan Digital Sky Survey) filtersysteem. Bestaande catalogen van Galactische bolhopen zijn gebaseerd op verouderde filtersystemen, zijn niet homogeen en gebaseerd op verschillende methodes en instrumenten. Om dit probleem uit de wereld te helpen, was het primaire doel van dit project een homogene cataloog op te stellen voor een groot deel van de Galactische bolhopen, en, dit gebaseerd op het SDSS filter systeem.

In hoofdstuk 3 bespreken we de observaties en data reductie die noodzakelijk waren voor dit project. De observaties voor dit project werden uitgevoerd over een tijdspanne van verschillende jaren op het CTIO (Cerro Tololo Interamerican Observatory) observatorium in Chili, met een 0.9m telescoop. Aangezien een belangrijk deel van de Melkweg enkel waarneembaar is tijdens de winter vanop het zuidelijk halfrond, werden een aanzienlijk deel van onze observaties niet genomen tijdens kwaliteitsvolle condities: cirruswolken kunnen de fotometrische correctheid aantasten, wat de observaties onbruikbaar maakt voor ons doel. Voor de noordelijke clusters konden we een beroep doen op SDSS data.

We bespreken de bepaling van het centrum van de cluster in detail en gaan verder in op de

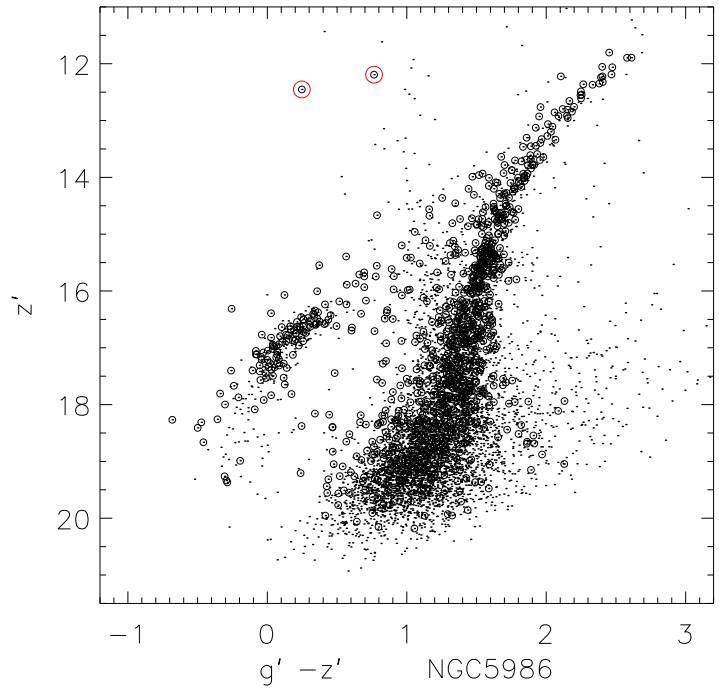

Figure 9.2: Kleur-magnitude diagram van NGC 5986: open cirkels zijn sterren binnen de half-licht straal van de sterhoop, de puntjes tonen sterren uit het hele beeldveld. De twee heldere geïsoleerde sterren zijn kandidaat vervuilers. We controleerden hun snelheidseigenschappen en bevestigden dat deze sterren inderdaad tot de Melkweg behoren, en, niet tot de bolvormige sterhoop. Daarom beslisten we het licht van deze sterren te verwijderen bij de bepaling van de lichtkracht van de bolhoop.

bijdrage van achtergrondstraling. De nauwkeurige bepaling van deze straling is niet eenvoudig, aangezien vele van onze sterhopen het volledige beeldveld van onze observaties vullen, en, we dus geen 'cluster-vrij' deel in ons beeld hebben dat kan dienen voor de bepaling van de achtergrondstraling.

Niet enkel de achtergrondstraling speelt een rol in de foutenmarge van de resultaten. Sterren die behoren tot de schijf van de Melkweg kunnen soms samenvallen met de gezichtslijn van de cluster, wat ervoor zorgt dat ze bijdragen tot de totale schijnbare lichtkracht, hoewel ze niet behoren tot de cluster. Om deze lichtvervuiling te verhelpen, passen we een techniek toe die voorgrond-kandidaat sterren selecteert op basis van hun kleur en lichtkracht. Als deze sterren snelheidseigenschappen hebben die niet overeenkomen met die van de sterhoop, dan verwijderen we de bijdrage in flux van deze vervuilende ster. Deze techniek wordt geïllustreerd in Fig. 9.2. Het is de eerste keer dat deze techniek werd toegepast op zo'n uitgebreide set van Galactische bolhopen. Zo bepalen we magnitudes en kleuren van deze bolvormige objecten die vrij zijn van vervuilende sterren uit de schijf van de Melkweg. Deze cataloog is op de dag van vandaag de meest uitgebreide fotometrische cataloog van de Galactische bolhopen en zal gebruikt kunnen worden voor een grote verscheidenheid aan sterrenkundige projecten.

In hoofdstuk 4 gebruiken we onze cataloog van kleuren en magnitudes om bestaande relaties tussen het metaalgehalte en de kleuren te verbeteren. We gebruiken hierbij niet enkel de abun-

dantie in ijzer, die zowat de standaard vormt in dergelijk onderzoek, maar ook de abundantie in calcium. Deze laatste is een relatief nieuwe indicator voor de chemische eigenschappen van een stellaire populatie, die recent meer en meer interesse opwekte in de sterrenkundige literatuur (bv. Foster et al. 2010; Usher et al. 2012). We vinden dat de kleur-metalliciteit relaties duidelijk niet lineair zijn voor beide indicatoren van de chemische eigenschappen: in Fig. 9.3 tonen we de relatie tussen de $g - z$ kleur en de ijzer eigenschappen van de clusters. Dit heeft een belangrijk gevolg: de kleuren van sterhopen in verafgelegen sterrenstelsels hebben vaak een bimodale verdeling. Vaak wordt deze bimodale verdeling in kleur gelinkt met een bimodale verdeling in metaalgehalte, wat belangrijke gevolgen heeft voor de theorieën voor de vorming van sterrenstelsels. Maar, verschillende publicaties hebben aangetoond dat het mogelijk is een bimodale kleurdistributie te verkrijgen op basis van een unimodale metalliciteitdistributie als de relatie tussen beide niet-lineair is (Yoon et al. 2006; Richtler 2006).

De verstrooiing in de kleur-metalliciteit relatie is niet verwaarloosbaar. Verschillende mogelijke oorzaken die gelinkt zijn met de eigenschappen van de stellaire populatie (zoals leeftijd, aanwezigheid van extreem-hete sterren en de massa verdeling van de sterren) kunnen een rol spelen in deze verstrooiing, maar geen duidelijk verband werd gevonden. We vonden echter wel een duidelijk verband met de onzekerheid in de schatting van de extinctie als gevolg van het stof dat aanwezig is in de schijf van de Melkweg en tonen ook dat de verstrooiing rond de relatie merkbaar kleiner is dankzij de techniek die de voorgrond sterren wegwist. Dit hoofdstuk eindigt met een uitgebreide discussie over de bimodaliteit in kleur en metaalgehalte en illustreert dat de interpretatie van deze verdelingen bemoeilijkt wordt door het niet-lineaire karakter van de kleur-metalliciteit relatie.

We zijn niet enkel geïnteresseerd in de kleuren en magnitudes van de bolhopen: de vorm en structurele eigenschappen van deze objecten zijn nuttige indicatoren in de studie van hun evolutie en zijn nauw gelinkt met de lokatie in de Melkweg. Daarom breiden we in hoofdstuk 5 de fotometrische cataloog uit met structurele parameters. Omdat het beeldveld van onze CTIO data niet de volledige cluster omvat, gebruiken we eerst de SDSS data om de invloed te bestuderen die deze beperkte beelden hebben op de gefitte parameters. Daarna definiëren we clusters met centraal gepiekte kernen en vinden een nauwe correlatie met de Galactische breedtegraad, zoals wordt getoond in figuur 9.4. Dit verband werd voorspeld door theoretische modellen (Gnedin et al. 1999; Madrid et al. 2012), maar werd hiervoor nog niet bevestigd door observaties. Omdat de stellaire dichtheid in deze clusters heel erg hoog is en een invloed kan hebben op de stellaire evolutie, zochten we verder naar correlaties tussen de structurele parameters en de eigenschappen van welbepaalde objecten, waaronder pulsars en Röntgenbronnen. We eindigen dit hoofdstuk met een discussie over de invloed van centraal gelegen rode reuzen op de structurele profielen en hun invloed op de interpretatie van kleur gradiënten.

In hoofdstuk 6 stellen we enkele projecten voor die gebaseerd zijn op diagrammen van kleuren en magnitudes van de stellaire populaties. Dit is grotendeels lopend onderzoek, maar tracht

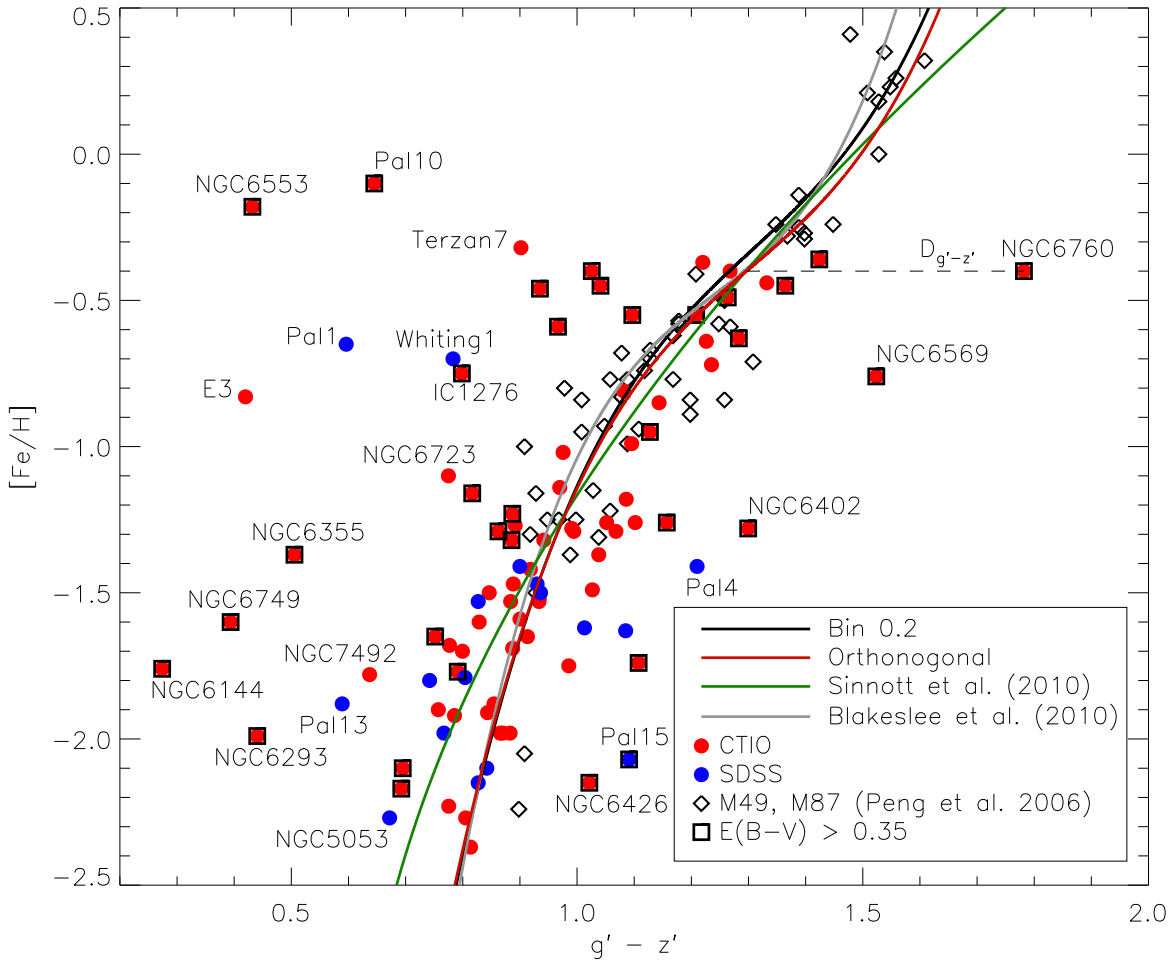

Figure 9.3: [Fe/H] als functie van de $g' - z'$ kleur voor Galactische bolhopen, aangevuld met bolhopen gelegen in andere nabije sterrenstelsels. De Galactische sterhopen afkomstig uit onze CTIO and SDSS data set worden weergegeven met gevulde cirkels, terwijl de extragalactische sterhopen (uit M 49 en M 87) worden getoond als ruiten (data afkomstig uit Peng et al. 2006). Voor sommige clusters werd de kleurbepaling bemoeilijkt door de stofbanden die aanwezig zijn in de Melkweg: deze objecten worden aangeduid met een kader. De lijnen tonen verschillende kleur-metalliciteit relaties: de rode lijn geeft onze beste fit die we bekwamen door de loodrechte afstand tussen de relatie en de datapunten te minimaliseren (zie vergelijking 4.8). De grijze en groene lijn geven relaties tussen kleur en metalliciteit die reeds gepubliceerd werden in de literatuur (Blakeslee et al. 2010; Sinnott et al. 2010).

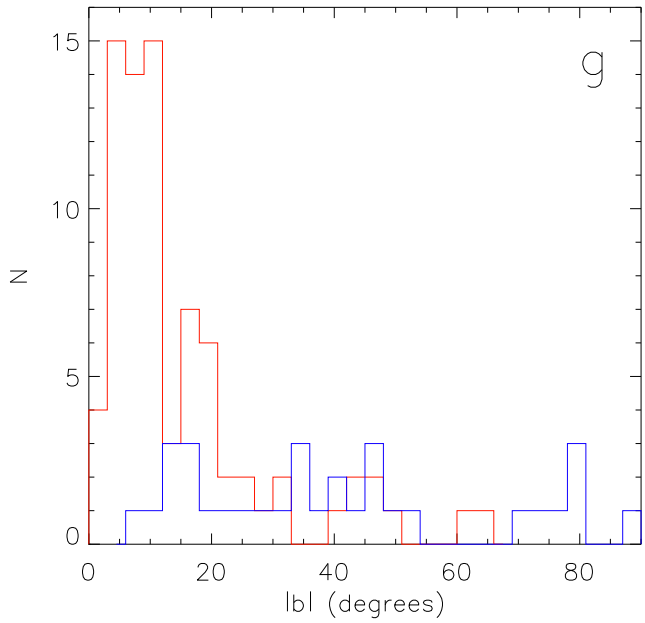

Figure 9.4: Histogram voor de verdeling van de afstand tot de MW schijf (gelijkwaardig aan de Galactische breedtegraad) voor clusters met een centraal gepiekte kern (zwart) en zonder sterke centrale verhoging in lichtkracht (rood). Het is duidelijk dat de eerste groep dicht bij de Galactische schijf vertoeft, terwijl de laatste groep hoofdzakelijk in de halo van onze Melkweg te vinden is.

een idee te geven over de wetenschappelijke resultaten die we verwachten. Deze voorlopige resultaten omvatten een studie van bijzondere eigenschappen van de dubbele horizontale tak die werd ontdekt door Mauro et al. (2012) en geven onze benadering van het lang-bestaande "2e parameter" probleem. Verder geven we een korte inleiding van een project dat zich zal concentreren op het massa-verlies van sterren tijdens de verschillende fases van het stellair leven.

Hoofdstuk 7 stelt een groot observationeel project voor, dat werd gestart tijdens dit doctoraatsonderzoek. We observeerden een groot deel van de zuidelijke bolhopen met VLT/FORS2. Zo bekwamen we een homogene spectroscopische dataset voor deze clusters die uitgebreider en completer is dan wat beschikbaar is in de literatuur. We weten dat leeftijdsschattingen gebaseerd op spectroscopische waarnemingen een vertekend beeld geven van de echte leeftijd van deze objecten, omdat ze aangetast kunnen worden door extreem hete sterren. De enige correcte leeftijdsschattingen zijn gebaseerd op kleur-magnitude diagrammen, die we voorstelden in het vorig hoofdstuk. We zullen dit effect onderzoeken door de leeftijden gebaseerd op fotometrie te vergelijken met schattingen gebaseerd op spectroscopie en dit effect kalibreren aan de hand van een kleur gebaseerd op ultraviolette en optische waarnemingen. Deze relatie zal de huidige leeftijdsschattingen verbeteren voor stellaire populaties zoals elliptische galaxiën, waarvoor het niet mogelijk is de sterren apart te bestuderen en we enkel beschikken over geïntegreerde eigenschappen.

List of scientific contributions

A

Refereed scientific contributions:

- Vanderbeke, J., Baes, M., Romanowsky, A. J., & Schmidtobreick, L. 2011, MNRAS, 412, 2017, ”Optical and near-infrared velocity dispersions of early-type galaxies”
- Tappert, C., Vogt, N., Schmidtobreick, L., Ederoclite, A., & Vanderbeke, J. 2013, MNRAS, 431, 92, ”Life after eruption - II. The eclipsing old nova V728 Scorpii”
- Vanderbeke, J., West, M. J., De Propris, R., Peng, E. W., Blakeslee, J. P., Jordán, A., Côté, P., Gregg, M., Ferrarese, L., Takamiya, M., Baes, M. 2014, MNRAS, 437, 1725: ”G2C2 I: Homogeneous SDSS photometry for Galactic GCs”
- Vanderbeke, J., West, M. J., De Propris, R., Peng, E. W., Blakeslee, J. P., Jordán, A., Côté, P., Gregg, M., Ferrarese, L., Takamiya, M., Baes, M. 2014, MNRAS, 437, 1734: ”G2C2 - II. Integrated colour-metallicity relations for Galactic globular clusters in SDSS passbands”

Non-refereed scientific contributions:

- Vanderbeke, J. 2011, in Fornax, Virgo, Coma et al., Stellar Systems in High Density Environments, 54P, ”A New Look at the Galactic Globular Cluster System”
- Vanderbeke, J. 2011, in Fornax, Virgo, Coma et al., Stellar Systems in High Density Environments, 55P, ”Optical and near-infrared velocity dispersions of early-type galaxies”
- Vanderbeke, J., Baes, M., Romanowsky, A. J., & Schmidtobreick, L. 2011, Boletín de la Asociación Argentina de Astronomía La Plata Argentina, 54, 341, ”Optical and near-infrared velocity dispersions of early-type galaxies”
- Vanderbeke, J., West, M., Côté, P., Peng, E., Blakeslee, J., Jordán, A., Gregg, M., Takamiya, M., Baes, M. 2011, Boletín de la Asociación Argentina de Astronomía La Plata Argentina, 54, 163, ”New look at the Galactic Globular Cluster System”

Bibliography

Ahn, C. P., Alexandroff, R., Allende Prieto, C., et al. 2012, ApJS, 203, 21

Alamo-Martínez, K. A., Blakeslee, J. P., Jee, M. J., et al. 2013, ArXiv e-prints

Alexander, P. E. R. & Gieles, M. 2013, MNRAS, 432, L1

Alonso-García, J., Mateo, M., Sen, B., et al. 2012, AJ, 143, 70

Alonso-García, J., Mateo, M., Sen, B., Banerjee, M., & von Braun, K. 2011, AJ, 141, 146

Alves-Brito, A., Hau, G. K. T., Forbes, D. A., et al. 2011, MNRAS, 417, 1823

Armandroff, T. E. & Da Costa, G. S. 1991, AJ, 101, 1329

Armandroff, T. E. & Zinn, R. 1988, AJ, 96, 92

Armstrong, R. D. & Tam Kung, M. 1978, J. R. Stat. Soc., Ser. C, 27, 363

Ashman, K. M. & Zepf, S. E. 1992, ApJ, 384, 50

Baes, M., Clemens, M., Xilouris, E. M., et al. 2010, A&A, 518, L53

Baes, M. & Dejonghe, H. 2000, MNRAS, 313, 153

Baes, M. & Dejonghe, H. 2001, ApJ Letters, 563, L19

Baes, M. & Dejonghe, H. 2002, MNRAS, 335, 441

Baes, M., Dejonghe, H., & De Rijcke, S. 2000, MNRAS, 318, 798

Bassino, L. P., Faifer, F. R., Forte, J. C., et al. 2006, A&A, 451, 789

Beasley, M. A., Brodie, J. P., Strader, J., et al. 2004, AJ, 128, 1623

Bedin, L. R., Piotto, G., Anderson, J., et al. 2004, ApJ Letters, 605, L125

Begeman, K. G., Broeils, A. H., & Sanders, R. H. 1991, MNRAS, 249, 523

Bellazzini, M. 2007, A&A, 473, 171

Bellazzini, M., Dalessandro, E., Sollima, A., & Ibata, R. 2012, MNRAS, 423, 844

Bellazzini, M., Ferraro, F. R., & Buonanno, R. 1999, MNRAS, 307, 619

Bellazzini, M., Ferraro, F. R., & Ibata, R. 2002, AJ, 124, 915

Benacquista, M. J. & Downing, J. M. B. 2013, Living Reviews in Relativity, 16, 4

Bender, R., Saglia, R. P., & Gerhard, O. E. 1994, MNRAS, 269, 785

Bernardi, M., Sheth, R. K., Annis, J., et al. 2003, AJ, 125, 1866

Bevington, P. R. & Robinson, D. K. 1992, Data reduction and error analysis for the physical sciences

Bianchini, P., Varri, A. L., Bertin, G., & Zocchi, A. 2013, ApJ, 772, 67

Blakeslee, J. P., Cantiello, M., & Peng, E. W. 2010, ApJ, 710, 51

Blakeslee, J. P., Cho, H., Peng, E. W., et al. 2012, ApJ, 746, 88

Blom, C., Forbes, D. A., Brodie, J. P., et al. 2012a, MNRAS, 426, 1959

Blom, C., Spitler, L. R., & Forbes, D. A. 2012b, MNRAS, 420, 37

Bochanski, J. J., Hawley, S. L., Covey, K. R., et al. 2010, AJ, 139, 2679

Bochanski, J. J., Willman, B., West, A. A., Strader, J., & Chomiuk, L. 2013, ArXiv e-prints

Boselli, A., Eales, S., Cortese, L., et al. 2010, PASP, 122, 261

Boyer, M. L., McDonald, I., van Loon, J. T., et al. 2009, ApJ, 705, 746

Bradford, J. D., Geha, M., Muñoz, R. R., et al. 2011, ApJ, 743, 167

Bressan, A., Marigo, P., Girardi, L., et al. 2012, MNRAS, 427, 127

Brodie, J. P. & Huchra, J. P. 1990, ApJ, 362, 503

Brodie, J. P. & Huchra, J. P. 1991, ApJ, 379, 157

Brodie, J. P. & Strader, J. 2006, ARA&A, 44, 193

Brodie, J. P., Strader, J., Denicoló, G., et al. 2005, AJ, 129, 2643

Brown, T. M., Smith, E., Ferguson, H. C., et al. 2008, ApJ, 682, 319

Buonanno, R., Corsi, C., Bellazzini, M., Ferraro, F. R., & Pecci, F. F. 1997, AJ, 113, 706

Burkert, A. & Tremaine, S. 2010, ApJ, 720, 516

Burstein, D., Bertola, F., Buson, L. M., Faber, S. M., & Lauer, T. R. 1988, ApJ, 328, 440

Caldwell, N., Schiavon, R., Morrison, H., Rose, J. A., & Harding, P. 2011, AJ, 141, 61

Caloi, V. & D'Antona, F. 2005, A&A, 435, 987

Camilo, F. & Rasio, F. A. 2005, in Astronomical Society of the Pacific Conference Series, Vol. 328, Binary Radio Pulsars, ed. F. A. Rasio & I. H. Stairs, 147

Cantiello, M. & Blakeslee, J. P. 2007, ApJ, 669, 982

Capaccioli, M., Ortolani, S., & Piotto, G. 1991, A&A, 244, 298

Cappellari, M. 2013, ArXiv e-prints

Cappellari, M. & Emsellem, E. 2004, PASP, 116, 138

Cappellari, M., Emsellem, E., Bacon, R., et al. 2007, MNRAS, 379, 418

Cappellari, M., McDermid, R. M., Alatalo, K., et al. 2013, MNRAS, 432, 1862

Cardelli, J. A., Clayton, G. C., & Mathis, J. S. 1989, ApJ, 345, 245

Carraro, G. 2005, ApJ Letters, 621, L61

Carraro, G., Girardi, L., Bressan, A., & Chiosi, C. 1996, A&A, 305, 849

Carraro, G., Zinn, R., & Moni Bidin, C. 2007, A&A, 466, 181

Carretta, E., Bragaglia, A., Gratton, R. G., et al. 2009, A&A, 505, 117

Catelan, M. 2009, Astroph. & Space Science, 320, 261

Catelan, M., Bellazzini, M., Landsman, W. B., et al. 2001, AJ, 122, 3171

Catelan, M., Borissova, J., Ferraro, F. R., et al. 2002, AJ, 124, 364

Catelan, M. & de Freitas Pacheco, J. A. 1996, PASP, 108, 166

Cenarro, A. J., Cervantes, J. L., Beasley, M. A., Marín-Franch, A., & Vazdekis, A. 2008, ApJ Letters, 689, L29

Chaboyer, B., Demarque, P., Kernan, P. J., & Krauss, L. M. 1998, ApJ, 494, 96

Chaboyer, B., Demarque, P., & Sarajedini, A. 1996, ApJ, 459, 558

Chies-Santos, A. L., Larsen, S. S., Cantiello, M., et al. 2012, A&A, 539, A54

Chies-Santos, A. L., Larsen, S. S., Kuntschner, H., et al. 2011a, A&A, 525, A20

Chies-Santos, A. L., Larsen, S. S., Wehner, E. M., et al. 2011b, A&A, 525, A19

Chung, C., Yoon, S.-J., & Lee, Y.-W. 2011, ApJ Letters, 740, L45

Clark, L. L., Sandquist, E. L., & Bolte, M. 2004, AJ, 128, 3019

Clemens, M. S., Jones, A. P., Bressan, A., et al. 2010, A&A, 518, L50+

Code, A. D. & Welch, G. A. 1979, ApJ, 228, 95

Cohen, J. G. 2004, AJ, 127, 1545

Cohen, J. G., Blakeslee, J. P., & Côté, P. 2003, ApJ, 592, 866

Cohen, J. G., Blakeslee, J. P., & Ryzhov, A. 1998, ApJ, 496, 808

Cohen, J. G., Hsieh, S., Metchev, S., Djorgovski, S. G., & Malkan, M. 2007, AJ, 133, 99

Cohen, J. G. & Kirby, E. N. 2012, ApJ, 760, 86

Cohen, J. G. & Melendez, J. 2005, AJ, 129, 1607

Cohn, H. 1980, ApJ, 242, 765

Conroy, C. & van Dokkum, P. G. 2012, ApJ, 760, 71

Contreras Peña, C., Catelan, M., Grundahl, F., Stephens, A. W., & Smith, H. A. 2013, ArXiv e-prints

Contreras Ramos, R., Clementini, G., Federici, L., et al. 2013, ApJ, 765, 71

Correnti, M., Bellazzini, M., Dalessandro, E., et al. 2011, MNRAS, 417, 2411

Cortese, L., Ciesla, L., Boselli, A., et al. 2012, A&A, 540, A52

Corwin, Jr., H. G., Buta, R. J., & de Vaucouleurs, G. 1994, AJ, 108, 2128

Côté, P., Blakeslee, J. P., Ferrarese, L., et al. 2004, ApJS, 153, 223

Côté, P., Djorgovski, S. G., Meylan, G., Castro, S., & McCarthy, J. K. 2002a, ApJ, 574, 783

Côté, P., Marzke, R. O., & West, M. J. 1998, ApJ, 501, 554

Côté, P., Marzke, R. O., West, M. J., & Minniti, D. 2000, ApJ, 533, 869

Côté, P., McLaughlin, D. E., Cohen, J. G., & Blakeslee, J. P. 2003, ApJ, 591, 850

Côté, P., McLaughlin, D. E., Hanes, D. A., et al. 2001, ApJ, 559, 828

Cote, P., Richer, H. B., & Fahlman, G. G. 1991, AJ, 102, 1358

Côté, P., West, M. J., & Marzke, R. O. 2002b, ApJ, 567, 853

Couture, J., Harris, W. E., & Allwright, J. W. B. 1990, ApJS, 73, 671

Dalessandro, E., Ferraro, F. R., Massari, D., et al. 2013, ArXiv e-prints

Davies, J. I., Baes, M., Bendo, G. J., et al. 2010, A&A, 518, L48+

Davies, J. I., Bianchi, S., Baes, M., et al. 2013, MNRAS, 428, 834

De Angeli, F., Piotto, G., Cassisi, S., et al. 2005, AJ, 130, 116

de Freitas Pacheco, J. A. & Barbuy, B. 1995, A&A, 302, 718

De Looze, I., Baes, M., Parkin, T. J., et al. 2012, MNRAS, 423, 2359

De Marchi, G., Paresce, F., & Pulone, L. 2007, ApJ Letters, 656, L65

De Propris, R. 2000, MNRAS, 316, L9

de Souza, R. E., Gadotti, D. A., & dos Anjos, S. 2004, ApJS, 153, 411

de Vaucouleurs, G. 1955, AJ, 60, 126

de Vaucouleurs, G. 1959, Handbuch der Physik, 53, 275

den Brok, M., van de Ven, G., van den Bosch, R., & Watkins, L. L. 2013, ArXiv e-prints

Desroches, L., Quataert, E., Ma, C., & West, A. A. 2007, MNRAS, 377, 402

Djorgovski, S. & Davis, M. 1987, ApJ, 313, 59

Djorgovski, S. & Piotto, G. 1993, in Astronomical Society of the Pacific Conference Series, Vol. 50, Structure and Dynamics of Globular Clusters, ed. S. G. Djorgovski & G. Meylan, 203

Djorgovski, S., Piotto, G., Phinney, E. S., & Chernoff, D. F. 1991, ApJ Letters, 372, L41

Doeleman, S. S., Fish, V. L., Schenck, D. E., et al. 2012, Science, 338, 355

Dorman, B., O'Connell, R. W., & Rood, R. T. 1995, ApJ, 442, 105

Dorman, B., Vandenberg, D. A., & Laskarides, P. G. 1989, ApJ, 343, 750

Dotter, A. 2013, Mem. S.A. It., 84, 97

Dotter, A., Sarajedini, A., & Anderson, J. 2011, ApJ, 738, 74

Dotter, A., Sarajedini, A., Anderson, J., et al. 2010, ApJ, 708, 698

Dotter, A., Sarajedini, A., & Yang, S.-C. 2008, AJ, 136, 1407

Dressler, A., Lynden-Bell, D., Burstein, D., et al. 1987, ApJ, 313, 42

Dupree, A. K., Smith, G. H., & Strader, J. 2009, AJ, 138, 1485

Ebneter, K. & Balick, B. 1985, AJ, 90, 183

Elson, R. A. W., Fall, S. M., & Freeman, K. C. 1987, ApJ, 323, 54

Emsellem, E., Cappellari, M., Krajnović, D., et al. 2007, MNRAS, 379, 401

Ernst, A. & Just, A. 2013, MNRAS, 429, 2953

Faber, S. M. 1983, Highlights of Astronomy, 6, 165

Faber, S. M. & Jackson, R. E. 1976, ApJ, 204, 668

Faifer, F. R., Forte, J. C., Norris, M. A., et al. 2011, MNRAS, 416, 155

Falcón-Barroso, J., Sánchez-Blázquez, P., Vazdekis, A., et al. 2011, A&A, 532, A95

Ferguson, H. C. 1989, AJ, 98, 367

Ferrarese, L. & Merritt, D. 2000, ApJ Letters, 539, L9

Ferraro, F. R. & Lanzoni, B. 2009, in Revista Mexicana de Astronomia y Astrofisica Conference Series, Vol. 37, Revista Mexicana de Astronomia y Astrofisica Conference Series, 62–71

Ferraro, F. R., Lanzoni, B., Dalessandro, E., et al. 2012, Nature, 492, 393

Ferraro, F. R., Paltrinieri, B., Rood, R. T., & Dorman, B. 1999, ApJ, 522, 983

Ferraro, F. R., Possenti, A., Sabbi, E., et al. 2003, ApJ, 595, 179

Forbes, D. A. & Bridges, T. 2010, MNRAS, 404, 1203

Forbes, D. A., Brodie, J. P., & Grillmair, C. J. 1997, AJ, 113, 1652

Foster, C., Forbes, D. A., Proctor, R. N., et al. 2010, AJ, 139, 1566

Foster, C., Spitler, L. R., Romanowsky, A. J., et al. 2011, MNRAS, 415, 3393

Fraix-Burnet, D., Dugué, M., Chattopadhyay, T., Chattopadhyay, A. K., & Davoust, E. 2010, MNRAS, 1098

Frank, M. J., Hilker, M., Baumgardt, H., et al. 2012, MNRAS, 423, 2917

Fregeau, J. M. & Rasio, F. A. 2007, ApJ, 658, 1047

Fukugita, M., Ichikawa, T., Gunn, J. E., et al. 1996, AJ, 111, 1748

Fusi Pecci, F., Ferraro, F. R., Corsi, C. E., Cacciari, C., & Buonanno, R. 1992, AJ, 104, 1831

Gadotti, D. A. 2008, MNRAS, 384, 420

Gaffney, N. I., Lester, D. F., & Doppmann, G. 1995, PASP, 107, 68

Gaffney, N. I., Lester, D. F., & Telesco, C. M. 1993, ApJ Letters, 407, L57

Galleti, S., Bellazzini, M., Buzzoni, A., Federici, L., & Fusi Pecci, F. 2009, A&A, 508, 1285

Gao, S., Jiang, B.-W., & Zhao, Y.-H. 2007, ChJAA, 7, 111

Gavazzi, G., Boselli, A., Scodeggio, M., Pierini, D., & Belsole, E. 1999, MNRAS, 304, 595

Gebhardt, K., Bender, R., Bower, G., et al. 2000, ApJ Letters, 539, L13

Geisler, D., Wallerstein, G., Smith, V. V., & Casetti-Dinescu, D. I. 2007, PASP, 119, 939

Gerhard, O. 2002, Space Science Reviews, 100, 129

Gieles, M., Baumgardt, H., Heggie, D. C., & Lamers, H. J. G. L. M. 2010, MNRAS, 408, L16

Gnedin, O. Y., Lee, H. M., & Ostriker, J. P. 1999, ApJ, 522, 935

Goldsbury, R., Richer, H. B., Anderson, J., et al. 2010, AJ, 140, 1830

Gomez, H. L., Baes, M., Cortese, L., et al. 2010, A&A, 518, L45+

Goudfrooij, P. & de Jong, T. 1995, A&A, 298, 784

Goudfrooij, P., Gilmore, D., Whitmore, B. C., & Schweizer, F. 2004, ApJ Letters, 613, L121

Grabhorn, R. P., Cohn, H. N., Lugger, P. M., & Murphy, B. W. 1991, in Astronomical Society of the Pacific Conference Series, Vol. 13, The Formation and Evolution of Star Clusters, ed. K. Janes, 392

Graham, A. W. 2002, MNRAS, 334, 859

Graham, A. W. 2008, ApJ, 680, 143

Gratton, R. G., Carretta, E., & Bragaglia, A. 2012a, aapr, 20, 50

Gratton, R. G., Carretta, E., Bragaglia, A., Lucatello, S., & D'Orazi, V. 2010, A&A, 517, A81

Gratton, R. G., Lucatello, S., Carretta, E., et al. 2012b, A&A, 539, A19

Graves, G. J. & Schiavon, R. P. 2008, ApJS, 177, 446

Grillmair, C. J., Freeman, K. C., Irwin, M., & Quinn, P. J. 1995, AJ, 109, 2553

Grillmair, C. J. & Smith, G. H. 2001, AJ, 122, 3231

Gültekin, K., Richstone, D. O., Gebhardt, K., et al. 2009, ApJ, 698, 198

Guzman, R., Lucey, J. R., & Bower, R. G. 1993, MNRAS, 265, 731

Hamren, K. M., Smith, G. H., GuhaThakurta, P., et al. 2013, ArXiv e-prints

Harris, W. E. 1991, ARA&A, 29, 543

Harris, W. E. 1996, AJ, 112, 1487

Harris, W. E. & Harris, G. L. H. 2002, AJ, 123, 3108

Harris, W. E., Harris, G. L. H., & McLaughlin, D. E. 1998, AJ, 115, 1801

Harris, W. E. & van den Bergh, S. 1981, AJ, 86, 1627

Hartwick, F. D. A. 1968, ApJ, 154, 475

Hawarden, T. G., Longmore, A. J., Tritton, S. B., Elson, R. A. W., & Corwin, Jr., H. G. 1981, MNRAS, 196, 747

Heasley, J. N., Janes, K. A., Zinn, R., et al. 2000, AJ, 120, 879

Heggie, D. & Hut, P. 2003, The Gravitational Million-Body Problem: A Multidisciplinary Approach to Star Cluster Dynamics

Heggie, D. C. & Hut, P. 1996, in IAU Symposium, Vol. 174, Dynamical Evolution of Star Clusters: Confrontation of Theory and Observations, ed. P. Hut & J. Makino, 303

Heitsch, F. & Richtler, T. 1999, A&A, 347, 455

Hilker, M., Infante, L., & Richtler, T. 1999, A&A Supl., 138, 55

Hubble, E. P. 1926, ApJ, 64, 321

Hurley, J. R. & Shara, M. M. 2012, MNRAS, 425, 2872

Ibata, R., Nipoti, C., Sollima, A., et al. 2013, MNRAS, 428, 3648

Iben, Jr., I. & Rood, R. T. 1970, ApJ, 161, 587

Jordán, A., Blakeslee, J. P., Côté, P., et al. 2007, ApJS, 169, 213

Jordán, A., Côté, P., Blakeslee, J. P., et al. 2005, ApJ, 634, 1002

Jordán, A., Peng, E. W., Blakeslee, J. P., et al. 2009, ApJS, 180, 54

Jordi, K., Grebel, E. K., Hilker, M., et al. 2009, AJ, 137, 4586

Kaviraj, S., Rowlands, K., Alpaslan, M., et al. 2013, MNRAS, 435, 1463

Kennicutt, Jr., R. C. 1992, ApJS, 79, 255

Kim, S., Yoon, S.-J., Chung, C., et al. 2013, ArXiv e-prints

King, I. 1962, AJ, 67, 471

King, I. R. 1966, AJ, 71, 64

Kissler-Patig, M., Brodie, J. P., Schroder, L. L., et al. 1998, AJ, 115, 105

Kissler-Patig, M., Kohle, S., Hilker, M., et al. 1997, A&A, 319, 470

Koch, A., Grebel, E. K., Odenkirchen, M., Martínez-Delgado, D., & Caldwell, J. A. R. 2004, AJ, 128, 2274

Kormendy, J. & Bender, R. 1996, ApJ Letters, 464, L119

Kormendy, J. & Bender, R. 2009, ApJ Letters, 691, L142

Kormendy, J., Fisher, D. B., Cornell, M. E., & Bender, R. 2009, ApJS, 182, 216

Krajnović, D., Karick, A. M., Davies, R. L., et al. 2013, MNRAS, 433, 2812

Krauss, L. M. & Chaboyer, B. 2003, Science, 299, 65

Kroupa, P. 1998, in Astronomical Society of the Pacific Conference Series, Vol. 134, Brown Dwarfs and Extrasolar Planets, ed. R. Rebolo, E. L. Martin, & M. R. Zapatero Osorio, 483

Kruijssen, J. M. D., Pelupessy, F. I., Lamers, H. J. G. L. M., et al. 2012, MNRAS, 421, 1927

Kunder, A., Stetson, P. B., Cassisi, S., et al. 2013, ArXiv e-prints

Kundu, A. & Whitmore, B. C. 1998, AJ, 116, 2841

Kuntschner, H. 2000, MNRAS, 315, 184

La Barbera, F., De Carvalho, R. R., De La Rosa, I. G., et al. 2010a, AJ, 140, 1528

La Barbera, F., Lopes, P. A. A., de Carvalho, R. R., de la Rosa, I. G., & Berlind, A. A. 2010b, ArXiv e-prints

LaMassa, S. M., Heckman, T. M., Ptak, A., et al. 2012, ApJ, 758, 1

Larsen, S. S., Brodie, J. P., Huchra, J. P., Forbes, D. A., & Grillmair, C. J. 2001, AJ, 121, 2974

Law, D. R. & Majewski, S. R. 2010, ApJ, 718, 1128

Leaman, R., VandenBerg, D. A., & Mendel, J. T. 2013, ArXiv e-prints

Lee, J.-W. & Carney, B. W. 2006, AJ, 132, 2171

Lee, Y.-W. 1990, ApJ, 363, 159

Lee, Y.-W., Demarque, P., & Zinn, R. 1994, ApJ, 423, 248

Lee, Y.-W., Gim, H. B., & Casetti-Dinescu, D. I. 2007, ApJ Letters, 661, L49

Leeuw, L. L., Sansom, A. E., Robson, E. I., Haas, M., & Kuno, N. 2004, ApJ, 612, 837

Lester, D. F. & Gaffney, N. I. 1994, ApJ Letters, 431, L13

Lewis, M. S., Liu, W. M., Paust, N. E. Q., & Chaboyer, B. 2006, AJ, 131, 2538

Lin, D., Irwin, J. A., Webb, N. A., Barret, D., & Remillard, R. A. 2013, ArXiv e-prints

Lotz, J. M., Miller, B. W., & Ferguson, H. C. 2004, ApJ, 613, 262

Lützgendorf, N., Kissler-Patig, M., Gebhardt, K., et al. 2013, A&A, 552, A49

Lyubenova, M., Kuntschner, H., & Silva, D. R. 2008, A&A, 485, 425

Mackey, A. D. & Gilmore, G. F. 2003a, MNRAS, 345, 747

Mackey, A. D. & Gilmore, G. F. 2003b, MNRAS, 338, 85

Mackey, A. D. & Gilmore, G. F. 2004, MNRAS, 355, 504

Mackey, A. D. & van den Bergh, S. 2005, MNRAS, 360, 631

Madrid, J. P., Hurley, J. R., & Sippel, A. C. 2012, ApJ, 756, 167

Majewski, S. R., Kunkel, W. E., Law, D. R., et al. 2004, AJ, 128, 245

Mancone, C. & Sarajedini, A. 2008, AJ, 136, 1913

Maraston, C. 2005, MNRAS, 362, 799

Marín-Franch, A., Aparicio, A., Piotto, G., et al. 2009, ApJ, 694, 1498

Marino, A. F., Milone, A. P., & Lind, K. 2013, ApJ, 768, 27

Marks, M., Kroupa, P., Dabringhausen, J., & Pawlowski, M. S. 2012, MNRAS, 422, 2246

Mashchenko, S. & Sills, A. 2005a, ApJ, 619, 243

Mashchenko, S. & Sills, A. 2005b, ApJ, 619, 258

Massey, R., Kitching, T., & Richard, J. 2010, Reports on Progress in Physics, 73, 086901

Masters, K. L., Jordán, A., Côté, P., et al. 2010, ApJ, 715, 1419

Mateo, M., Harris, H. C., Nemec, J., & Olszewski, E. W. 1990, AJ, 100, 469

Mateu, C., Vivas, A. K., Zinn, R., Miller, L. R., & Abad, C. 2009, AJ, 137, 4412

Mauro, F., Moni Bidin, C., Cohen, R., et al. 2012, ApJ Letters, 761, L29

McDonald, I., Johnson, C. I., & Zijlstra, A. A. 2011, MNRAS, 416, L6

McDonald, I. & van Loon, J. T. 2007, A&A, 476, 1261

McDonald, I., Zijlstra, A. A., Rajoelimanana, A. F., & Johnson, C. I. 2013, MNRAS, 429, L65

McLaughlin, D. E. 2000, ApJ, 539, 618

McLaughlin, D. E. & van der Marel, R. P. 2005, ApJS, 161, 304

Michard, R. 2005, A&A, 441, 451

Michard, R. & Prugniel, P. 2004, A&A, 423, 833

Mieske, S., Jordán, A., Côté, P., et al. 2006, ApJ, 653, 193

Mieske, S., Jordán, A., Côté, P., et al. 2010, ApJ, 710, 1672

Milgrom, M. 1983, ApJ, 270, 365

Miller, B. W., Lotz, J. M., Ferguson, H. C., Stiavelli, M., & Whitmore, B. C. 1998, ApJ Letters, 508, L133

Milone, A. P., Piotto, G., Bedin, L. R., et al. 2012, A&A, 537, A77

Miocchi, P., Lanzoni, B., Ferraro, F. R., et al. 2013, ApJ, 774, 151

Moehler, S., Dreizler, S., Lanz, T., et al. 2011, A&A, 526, A136

Moehler, S., Landsman, W. B., & Dorman, B. 2000, A&A, 361, 937

Moffat, J. W. 2005, Journal of Cosmology and Astroparticle Physics, 5, 3

Moffat, J. W. & Toth, V. T. 2008, ApJ, 680, 1158

Monelli, M., Milone, A. P., Stetson, P. B., et al. 2013, MNRAS, 431, 2126

Monet, D. G., Levine, S. E., Canzian, B., et al. 2003, AJ, 125, 984

Moore, B. 1996, ApJ Letters, 461, L13

Moorwood, A., Cuby, J., Biereichel, P., et al. 1998, The Messenger, 94, 7

Muratov, A. L. & Gnedin, O. Y. 2010, ApJ, 718, 1266

Norris, J. E. 2004, ApJ Letters, 612, L25

Nowak, N., Saglia, R. P., Thomas, J., et al. 2008, MNRAS, 391, 1629

Nowak, N., Saglia, R. P., Thomas, J., et al. 2007, MNRAS, 379, 909

Noyola, E. & Gebhardt, K. 2006, AJ, 132, 447

O'Connell, R. W. 1999, ARA&A, 37, 603

Odenkirchen, M., Grebel, E. K., Rockosi, C. M., et al. 2001, ApJ Letters, 548, L165

Olszewski, E. W., Saha, A., Knezek, P., et al. 2009, AJ, 138, 1570

Ortolani, S., Renzini, A., Gilmozzi, R., et al. 1995, Nature, 377, 701

Ostrov, P., Geisler, D., & Forte, J. C. 1993, AJ, 105, 1762

Pahre, M. A., Djorgovski, S. G., & de Carvalho, R. R. 1995, ApJ Letters, 453, L17+

Pasquato, M., Raimondo, G., Brocato, E., et al. 2013, A&A, 554, A129

Patat, F. & Carraro, G. 2001, MNRAS, 325, 1591

Paust, N. & Chaboyer, B. 2011, in Bulletin of the American Astronomical Society, Vol. 43, American Astronomical Society Meeting Abstracts #217, 152.14

Paust, N. E. Q., Aparicio, A., Piotto, G., et al. 2009, AJ, 137, 246

Paust, N. E. Q., Reid, I. N., Piotto, G., et al. 2010, AJ, 139, 476

Peacock, M. B., Zepf, S. E., Maccarone, T. J., & Kundu, A. 2011, ApJ, 737, 5

Peebles, P. J. E. & Dicke, R. H. 1968, ApJ, 154, 891

Peng, C. Y., Ho, L. C., Impey, C. D., & Rix, H.-W. 2002, AJ, 124, 266

Peng, C. Y., Ho, L. C., Impey, C. D., & Rix, H.-W. 2010, AJ, 139, 2097

Peng, E. W., Ford, H. C., & Freeman, K. C. 2004, ApJ, 602, 705

Peng, E. W., Jordán, A., Côté, P., et al. 2006, ApJ, 639, 95

Percival, S. M. & Salaris, M. 2011, MNRAS, 412, 2445

Perrett, K. M., Bridges, T. J., Hanes, D. A., et al. 2002, AJ, 123, 2490

Peterson, R. C., Rood, R. T., & Crocker, D. A. 1995, ApJ, 453, 214

Pickles, A. J. 1998, PASP, 110, 863

Pilbratt, G. L., Riedinger, J. R., Passvogel, T., et al. 2010, A&A, 518, L1

Piotto, G., Bedin, L. R., Anderson, J., et al. 2007, ApJ Letters, 661, L53

Piotto, G., Villanova, S., Bedin, L. R., et al. 2005, ApJ, 621, 777

Pota, V., Forbes, D. A., Romanowsky, A. J., et al. 2013, MNRAS, 428, 389

Press, W. H. & Schechter, P. 1974, ApJ, 187, 425

Pritzl, B. J., Armandroff, T. E., Jacoby, G. H., & Da Costa, G. S. 2002, AJ, 124, 1464

Pritzl, B. J., Armandroff, T. E., Jacoby, G. H., & Da Costa, G. S. 2004, AJ, 127, 318

Pritzl, B. J., Armandroff, T. E., Jacoby, G. H., & Da Costa, G. S. 2005, AJ, 129, 2232

Prugniel, P. & Simien, F. 1996, A&A, 309, 749

Pulone, L., De Marchi, G., Covino, S., & Paresce, F. 2003, A&A, 399, 121

Puzia, T. H., Kissler-Patig, M., Thomas, D., et al. 2005, A&A, 439, 997

Puzia, T. H., Saglia, R. P., Kissler-Patig, M., et al. 2002, A&A, 395, 45

Reed, B. C., Hesser, J. E., & Shawl, S. J. 1988, PASP, 100, 545

Reimers, D. 1975, Memoires of the Societe Royale des Sciences de Liege, 8, 369

Reimers, D. 1977, A&A, 61, 217

Rejkuba, M. 2012, Astroph. & Space Science, 341, 195

Rhode, K. L. 2012, AJ, 144, 154

Ribeiro, A. L. B. & Dantas, C. C. 2010, ArXiv e-prints

Richtler, T. 2006, Bulletin of the Astronomical Society of India, 34, 83

Roberts, M. S. & Haynes, M. P. 1994, ARA&A, 32, 115

Rosenberg, A., Saviane, I., Piotto, G., & Aparicio, A. 1999, AJ, 118, 2306

Rosenberg, A., Saviane, I., Piotto, G., Aparicio, A., & Zaggia, S. R. 1998, AJ, 115, 648

Rowlands, K., Dunne, L., Maddox, S., et al. 2012, MNRAS, 419, 2545

Rubin, V. C. & Ford, Jr., W. K. 1970, ApJ, 159, 379

Rubin, V. C., Thonnard, N., & Ford, Jr., W. K. 1978, ApJ Letters, 225, L107

Sakari, C. M., Venn, K. A., Irwin, M., et al. 2011, ApJ, 740, 106

Salaris, M. & Weiss, A. 1998, A&A, 335, 943

Salinas, R., Jílková, L., Carraro, G., Catelan, M., & Amigo, P. 2012, MNRAS, 421, 960

Salpeter, E. E. 1955, ApJ, 121, 161

Sandage, A., Sandage, M., & Kristian, J. 1975, Galaxies and the Universe

Sandage, A. & Wildey, R. 1967, ApJ, 150, 469

Santana, F. A., Muñoz, R. R., Geha, M., et al. 2013, ApJ, 774, 106

Saviane, I., da Costa, G. S., Held, E. V., et al. 2012, A&A, 540, A27

Saviane, I., Piotto, G., Fagotto, F., et al. 1998, A&A, 333, 479

Schiavon, R. P., Rose, J. A., Courteau, S., & MacArthur, L. A. 2004, ApJ Letters, 608, L33

Schiavon, R. P., Rose, J. A., Courteau, S., & MacArthur, L. A. 2005, ApJS, 160, 163

Schlafly, E. F. & Finkbeiner, D. P. 2011, ApJ, 737, 103

Schweizer, F. 1982, ApJ, 252, 455

Searle, L. & Zinn, R. 1978, ApJ, 225, 357

Sharples, R. M., Zepf, S. E., Bridges, T. J., et al. 1998, AJ, 115, 2337

Siegel, M. H., Majewski, S. R., Cudworth, K. M., & Takamiya, M. 2001, AJ, 121, 935

Silge, J. D. & Gebhardt, K. 2003, AJ, 125, 2809

Silge, J. D., Gebhardt, K., Bergmann, M., & Richstone, D. 2005, AJ, 130, 406

Silk, J. 2012, Comptes Rendus Physique, 13, 724

Silk, J., Di Cintio, A., & Dvorkin, I. 2013, ArXiv e-prints

Silva, D. R., Kuntschner, H., & Lyubenova, M. 2008, ApJ, 674, 194

Sinnott, B., Hou, A., Anderson, R., Harris, W. E., & Woodley, K. A. 2010, AJ, 140, 2101

Smecker-Hane, T. A. & McWilliam, A. 2002, ArXiv Astrophysics e-prints

Smith, G. H. & Hesser, J. E. 1986, PASP, 98, 838

Smith, J. A., Tucker, D. L., Chen, B., et al. 2000, in Bulletin of the American Astronomical Society, Vol. 32, American Astronomical Society Meeting Abstracts, 1424

Smith, J. A., Tucker, D. L., Kent, S., et al. 2002, AJ, 123, 2121

Smith, M. W. L., Gomez, H. L., Eales, S. A., et al. 2012, ApJ, 748, 123

Sofue, Y. 2012, Publications of the Astronomical Society of Japan, 64, 75

Sohn, Y.-J., Byun, Y.-I., & Chun, M.-S. 1996, Astroph. & Space Science, 243, 379

Sohn, Y.-J., Byun, Y.-I., Yim, H.-S., Rhee, M.-H., & Chun, M.-S. 1998, Journal of Astronomy and Space Sciences, 15, 1

Sollima, A., Martínez-Delgado, D., Valls-Gabaud, D., & Peñarrubia, J. 2011, ApJ, 726, 47

Spitler, L. R. & Forbes, D. A. 2009, MNRAS, 392, L1

Stetson, P. B. 1987, PASP, 99, 191

Stetson, P. B. 1994, PASP, 106, 250

Stoehr, F., Fraquelli, D., Kamp, I., et al. 2007, Space Telescope European Coordinating Facility Newsletter, 42, 4

Strader, J., Brodie, J. P., Cenarro, A. J., Beasley, M. A., & Forbes, D. A. 2005, AJ, 130, 1315

Strader, J., Brodie, J. P., Spitler, L., & Beasley, M. A. 2006, AJ, 132, 2333

Strader, J., Romanowsky, A. J., Brodie, J. P., et al. 2011, ApJS, 197, 33

Tamura, N. & Ohta, K. 2000, AJ, 120, 533

Temi, P., Brighenti, F., & Mathews, W. G. 2007, ApJ, 660, 1215

Temi, P., Brighenti, F., Mathews, W. G., & Bregman, J. D. 2004, ApJS, 151, 237

Tonini, C. 2013, ApJ, 762, 39

Toomre, A. 1978, in IAU Symposium, Vol. 79, Large Scale Structures in the Universe, ed. M. S. Longair & J. Einasto, 109–116

Trager, S. C., Djorgovski, S., & King, I. R. 1993, in Astronomical Society of the Pacific Conference Series, Vol. 50, Structure and Dynamics of Globular Clusters, ed. S. G. Djorgovski & G. Meylan, 347

Trager, S. C., King, I. R., & Djorgovski, S. 1995, AJ, 109, 218

Trenti, M., Vesperini, E., & Pasquato, M. 2010, ApJ, 708, 1598

Trimble, V. 1987, ARA&A, 25, 425

Trouille, L. & Chaboyer, B. 2002, in Bulletin of the American Astronomical Society, Vol. 201, American Astronomical Society Meeting Abstracts, 710

Usher, C., Forbes, D. A., Brodie, J. P., et al. 2012, MNRAS, 426, 1475

van den Bergh, S. 1967, AJ, 72, 70

van den Bergh, S. 1975, ARA&A, 13, 217

van den Bergh, S. 2012, ApJ, 746, 189

van den Bergh, S., Demers, S., & Kunkel, W. E. 1980, ApJ, 239, 112

van den Bergh, S. & Mackey, A. D. 2004, MNRAS, 354, 713

van den Bergh, S., Morbey, C., & Pazder, J. 1991, ApJ, 375, 594

van der Marel, R. P. & van Dokkum, P. G. 2007, ApJ, 668, 756

van Dokkum, P. G. 2001, PASP, 113, 1420

van Dokkum, P. G. & Franx, M. 1995, AJ, 110, 2027

van Loon, J. T., Groenewegen, M. A. T., de Koter, A., et al. 1999, A&A, 351, 559

Vandenberg, D. A., Brogaard, K., Leaman, R., & Casagrande, L. 2013, ArXiv e-prints

Vanderbeke, J., Baes, M., Romanowsky, A. J., & Schmidtobreick, L. 2011, MNRAS, 412, 2017

Vanderbeke, J., West, M. J., De Propris, R., et al. 2014a, MNRAS, 437, 1725

Vanderbeke, J., West, M. J., De Propris, R., et al. 2014b, MNRAS, 437, 1734

Verbunt, F. & Lewin, W. H. G. 2006, Globular cluster X-ray sources, ed. W. H. G. Lewin & M. van der Klis, 341–379

Veron-Cetty, M. & Veron, P. 1988, A&A, 204, 28

Vesperini, E. & Chernoff, D. F. 1994, ApJ, 431, 231

Vesperini, E. & Trenti, M. 2010, ApJ Letters, 720, L179

Vickers, J. J., Grebel, E. K., & Huxor, A. P. 2012, AJ, 143, 86

Vlahakis, C., Dunne, L., & Eales, S. 2005, MNRAS, 364, 1253

Wang, S. & Ma, J. 2013, AJ, 146, 20

Webbink, R. F. 1985, in IAU Symposium, Vol. 113, Dynamics of Star Clusters, ed. J. Goodman & P. Hut, 541–577

West, M. J., Côté, P., Marzke, R. O., & Jordán, A. 2004, Nature, 427, 31

Whitmore, B. C. & Schweizer, F. 1995, AJ, 109, 960

Whitmore, B. C., Sparks, W. B., Lucas, R. A., Macchetto, F. D., & Biretta, J. A. 1995, ApJ Letters, 454, L73

Willson, L. A. 2000, ARA&A, 38, 573

Wilson, A. G. 1955, PASP, 67, 27

Wilson, C. D., Cridland, A., Foyle, K., et al. 2013, ApJ Letters, 776, L30

Wilson, C. P. 1975, AJ, 80, 175

Winge, C., Riffel, R. A., & Storchi-Bergmann, T. 2009, ApJS, 185, 186

Wise, M. W. & Silva, D. R. 1996, ApJ, 461, 155

Wise, M. W. & Silva, D. R. 1997, in Astronomical Society of the Pacific Conference Series, Vol. 116, The Nature of Elliptical Galaxies; 2nd Stromlo Symposium, ed. M. Arnaboldi, G. S. Da Costa, & P. Saha, 364–+

Witt, A. N., Thronson, Jr., H. A., & Capuano, Jr., J. M. 1992, ApJ, 393, 611

Worthey, G., Faber, S. M., Gonzalez, J. J., & Burstein, D. 1994, ApJS, 94, 687

Yi, S., Demarque, P., & Oemler, Jr., A. 1997, ApJ, 486, 201

Yi, S., Demarque, P., & Oemler, Jr., A. 1998, ApJ, 492, 480

Yi, S. K., Lee, J., Sheen, Y.-K., et al. 2011, ApJS, 195, 22

Yong, H., Demarque, P., & Yi, S. 2000, ApJ, 539, 928

Yoon, S.-J., Lee, S.-Y., Blakeslee, J. P., et al. 2011a, ApJ, 743, 150

Yoon, S.-J., Sohn, S. T., Lee, S.-Y., et al. 2011b, ApJ, 743, 149

Yoon, S.-J., Yi, S. K., & Lee, Y.-W. 2006, Science, 311, 1129

York, D. G., Adelman, J., Anderson, Jr., J. E., et al. 2000, AJ, 120, 1579

Zacharias, N., Monet, D. G., Levine, S. E., et al. 2005, VizieR Online Data Catalog, 1297, 0

Zepf, S. E. & Ashman, K. M. 1993, MNRAS, 264, 611

Zepf, S. E., Beasley, M. A., Bridges, T. J., et al. 2000, AJ, 120, 2928

Zhu, G., Blanton, M. R., & Moustakas, J. 2010, ArXiv e-prints

Zinn, R. 1985, ApJ, 293, 424

Zinn, R. & West, M. J. 1984, ApJS, 55, 45

Zitrin, A., Broadhurst, T., Coe, D., et al. 2011, ApJ, 742, 117